

# Value-added chitosan scaffolds for biomedical applications

Kho, Shu Hui

2019

Kho, S. H. (2019). Value-added chitosan scaffolds for biomedical applications. Doctoral thesis, Nanyang Technological University, Singapore.

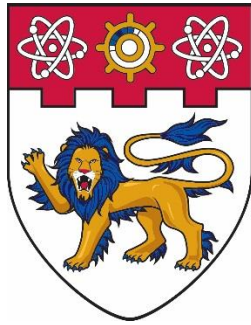
<https://hdl.handle.net/10356/137100>

<https://doi.org/10.32657/10356/137100>

---

This work is licensed under a Creative Commons Attribution-NonCommercial 4.0 International License (CC BY-NC 4.0).

*Downloaded on 09 Apr 2024 12:20:21 SGT*



**NANYANG  
TECHNOLOGICAL  
UNIVERSITY**  

---

**SINGAPORE**

**VALUE-ADDED CHITOSAN SCAFFOLDS  
FOR BIOMEDICAL APPLICATIONS**

**KHO SHU HUI**  
**Interdisciplinary Graduate School**  
**NTU Institute for Health Technologies (HealthTech NTU)**

# **VALUE-ADDED CHITOSAN SCAFFOLDS FOR BIOMEDICAL APPLICATIONS**

**KHO SHU HUI**

**Interdisciplinary Graduate School  
NTU Institute for Health Technologies (HealthTech NTU)**

A thesis submitted to the Nanyang Technological University in partial  
fulfillment of the requirement for the degree of  
Doctor of Philosophy

**2019** (*Year of Submission of Thesis*)

## Statement of Originality

I hereby certify that the work embodied in this thesis is the result of original research, is free of plagiarised materials, and has not been submitted for a higher degree to any other University or Institution.

17<sup>th</sup> October 2019

.....

Date



.....

Kho Shu Hui



## Supervisor Declaration Statement

I have reviewed the content and presentation style of this thesis and declare it is free of plagiarism and of sufficient grammatical clarity to be examined. To the best of my knowledge, the research and writing are those of the candidate except as acknowledged in the Author Attribution Statement. I confirm that the investigations were conducted in accord with the ethics policies and integrity standards of Nanyang Technological University and that the research data are presented honestly and without prejudice.

17<sup>th</sup> October 2019

.....  
Date

  
.....  
Professor Liu Xuewei

## Authorship Attribution Statement

This thesis does not contain materials from papers published in peer-reviewed journals where I was the first and/or corresponding author.

17<sup>th</sup> October 2019

.....

Date



.....

Kho Shu Hui

## Acknowledgements

This whole Ph.D. journey would not have been possible with the support of several key figures in my life. Firstly, I would like to express my immense gratitude to my main supervisor, Professor Liu Xuewei, for his constant encouragement, unwavering support, as well as providing numerous opportunities for me to step out of my comfort zone to learn and improve.

I would also like to take this opportunity to thank my co-supervisor, Assoc. Prof. Duan Hongwei, and my mentor, Assoc. Prof. Luo Dahai, for their insightful advices and guidance provided. I would also like to extend my gratitude to Professor Yoon Ho Sup for providing many enlightening ideas and for the opportunity to work in collaboration with his group. I too, would like to thank Professor Mary Chan-Park for providing several opportunities during the earlier part of my Ph.D. journey for me to engage with collaborators from other industries, as well as a chance to work with her group.

I would like to express my heartfelt gratitude to Interdisciplinary Graduate Programme (IGP) and NTU Institute of Health Technologies (HealthTech NTU) for presenting me with the privilege to embark on this Ph.D. programme, as well as NTU for supporting me financially in this journey.

I would like to also express my appreciation to my collaborating partners, Nguyen for supplying the initial batches of proteins, Dr. Tan Yu Jia for her mentorship when I first started this journey, and Dr. Guo Zhong whom have helped me immensely during discussions as well as learning skills from him. I am eternally grateful for the opportunity to be able to work in different laboratories, and to experience different lab cultures, and most importantly, a vital source of friendship. Everyone in our group are harmonious, thereby creating a fun environment to work in. In particular, I would like to thank Dr. Mallick, Dr. William, Dr. Leng Wei Lin, Dr. Leow Yu Hui, Mr. Das Mrinmoy and Mr. Desmond Lin for always providing a listening ear as well as great advices; Dr. Toh Hui Ting, Dr. Ngow Yeen Shian, Mr. Jonathan Tan and Mr. Yoo Jun Yeob for creating such a positive environment for me to handle my biological experiments in SBS, as well as them readily providing their guidance whenever I need them; Ms. Zhang Kaixi, Ms. Wang Liping, Mr. Zhong Wenbin, and Dr. Xiong Qirong, for always providing necessary aid when I encountered difficulties during bacterial studies. I am also grateful to friends I have made in IGP, Mr. William Ong and Ms. Kathy Wong, whom have provided very strong emotional support throughout this journey.

I would like to express my deepest gratitude to Mr. He Jingxi, whom are always very encouraging and motivational, and never failed to help me see the light at the end of the tunnel. Last but not least, I would like to thank my parents, brother and grandparents for their unconditional love and support, as well as to my friends for being always understanding and simply be there for me during tough and stressful periods.

## Table of contents

<i>Acknowledgements</i> .....	<i>I</i>
<i>Table of contents</i> .....	<i>II</i>
<i>List of Figures</i> .....	<i>V</i>
<i>List of Schemes</i> .....	<i>XIII</i>
<i>List of Tables</i> .....	<i>XVI</i>
<i>Summary</i> .....	<i>XVII</i>
<b><i>Chapter 1 / Natural Polysaccharides and Chitosan in Biomedical Applications</i></b> .....	<b><i>1</i></b>
1.1   Polymeric Sugars from Nature and Their Advantages in Biomedical Applications .....	1
1.2   Chitosan, a Semisynthetic Polysaccharide Derived from Chitin .....	4
1.2.1   Degree of Deacetylation (DD) of Chitosan .....	4
1.2.2   Chitosan's Molecular Weight (MW) .....	5
1.2.3   Bioactivities of Chitosan .....	5
1.2.4   Biomedical Applications of Chitosan-Based Materials .....	8
1.3   References .....	13
<b><i>Chapter 2 / Dual-Responsive Targeted rSML-A Delivery System Utilizing a Chitosan Scaffold</i></b> .....	<b><i>20</i></b>
Abstract .....	20
2.1   Introduction .....	21
2.1.1   General Overview of Cancer .....	21
2.1.2   Proteins as Drugs, such as Mistletoe Lectin, for Cancer Therapeutics .....	22
2.1.3   Challenges Faced in Delivery of Bioactive Biomacromolecules .....	25
2.2   Proposed Design and Rationale .....	28
2.2.1   Polyethylene Glycol (PEG) as Hydration Shield .....	29
2.2.2   Active Targeting with Boronic Acid .....	29

2.2.3   Acid-labile Linkage to Aid in Endosomal Escape.....	30
2.2.4   GSH-Responsive Linkage.....	31
2.3   Results and Discussion .....	32
2.3.1   Initial Design: Synthesis, Biological Assays, and Limitations Encountered.....	32
2.3.2   New Model: Proposed Modifications, Synthesis and Biological Assays.....	38
2.4   Conclusion .....	54
2.5   Methods and Materials.....	55
2.5.1   Materials .....	55
2.5.2   Chemical Synthesis.....	55
2.5.3   Expression and Purification of rSML-A from <i>E. coli</i> .....	67
2.5.4   SDS-Polyacrylamide Gel Electrophoresis (SDS-PAGE) Analysis of rSML-A .....	67
2.5.5   <i>In Vitro</i> Biological Assays .....	68
2.6   References.....	71
<b>Chapter 3 / A Facile Synthetic Approach to PGO Derivatives Using Chitosan Scaffolds and Evaluation of the Resultant Modifications .....</b>	<b>78</b>
Abstract.....	78
3.1   Introduction.....	79
3.1.1   General Overview of Antibiotics and Antibiotic Resistance.....	79
3.1.2   Peptidoglycan (PG) in Gram-Positive (G+ve) and Gram-Negative (G-ve) Bacteria .....	82
3.1.3   Reported Studies with PG Substrates and the Challenges Faced During the Journey .....	84
3.2   Proposed Study and Rationale .....	87
3.3   Results and Discussions.....	89
3.3.1   MALDI-TOF MS Analysis and Enzymatic Degradation Assay .....	89
3.3.2   Bacterial Cell Wall Labelling Mechanistic Studies with Our PGO.....	91
3.3.3   Facile and Practical Synthesis of PGO-Derivatives .....	98

3.4   Conclusion .....	101
3.5   Methods and Materials.....	102
3.5.1   Materials .....	102
3.5.2   Lysozyme Degradation Assay .....	102
3.5.3   Labelling of Bacterial Cell Walls with 3-1 @Rhd and STED Microscopy.....	103
3.5.4   Quantifying Intensity of Fluorescence Signals .....	104
3.5.5   Chemical Synthesis of PGO Derivatives .....	105
3.6   References.....	111
<b>Chapter 4   Conclusion and Future Directions .....</b>	<b>116</b>
4.1   Conclusion .....	116
4.2   Future Directions .....	118
4.2.1   Turning Our Delivery System into a Nanotheranostic System.....	10218
4.2.2   A Customizable Targeted Delivery System.....	102
4.2.3   Delivery of A Wide-Variety of Biomacromolecules .....	10320
4.2.4   Investigation of the Mechanisms of Bacterial Cell Wall Biosynthesis .....	10421
4.3   References.....	123
<b>APPENDIX I – MALDI-TOF MS Analysis .....</b>	<b>126</b>
<b>APPENDIX II - Supplementary Data for Chapter 2 .....</b>	<b>136</b>
<b>APPENDIX III Supplementary Data for Chapter 3 .....</b>	<b>147</b>

## List of Figures

**Figure 1.1** | Chemical structures of some naturally occurring polysaccharides (left to right: dextran, hyaluronic acid/hyaluronan, cellulose, chitin). The numbers labelled on dextran represent the generic counting system of carbon atoms in carbohydrates. Anomeric carbon is labelled as

C1.....1

**Figure 1.2** | (a) Increasing antimicrobial activity of 48.5 kDa chitosan against *S. aureus* with chitosan concentration ranging from (1) 0%, (2) 0.25%, (3) 0.5%, (4) 0.75%, (5) 1%, as shown on the culture plate (diameter = 9.5 cm). (b) Increasing antimicrobial activity of chitosan against *S. aureus* with increasing MW, (1) blank, (2) < 5 kDa, (3) 48.5 kDa, (4) 72.5 kDa, (5) 129.0 kDa, (6) 165.7 kDa, as shown on the culture plate (diameter = 9.5 cm) with decreasing number of colonies of bacteria formed. Reprinted with permission from ref. 35.

Copyright (2019), Elsevier. ....6

**Figure 1.3** | (a) Doubling time (calculated from growth curve) of A375 remains the same, while that of SKMEL28 and RPMI 7951 increases when incubated with chitosan coated wells as compared to the control (coated with 0.1% AcOH). (b) Image of the outcome of MTT assay for A375, SKMEL28 and RPMI upon 48 hours incubation with 2 mg/mL chitosan coatings dissolved in 0.1% acetic acid, and 0.1% acetic acid coating as control. (c) Relative cell viabilities of the respective melanoma cell lines upon incubation with 0.1% acetic acid (white bars) and chitosan dissolved in 0.1% acetic acid (black bars). Reprinted with permission from ref. 39. Copyright (2019), Elsevier. ....8

**Figure 1.4** | (a) Illustration on the fabrication of CS-TA-LNPs, in which TPP was added after the three individual components are homogenized. (b) Triplicate experiment on the antimicrobial activity of the individual components (left box, CK = sterile water, CS = 50 µg/mL chitosan, Ta = 50 µg/mL tannin, L = 50 µg/mL lysozyme) and chitosan-based nanomaterials (right box, CK = sterile water, CS NPs = 50 µg/mL chitosan nanoparticles, CS-Ta-LNPs = 50 µg/mL chitosan-tannin-lysozyme nanoparticles). Reprinted with permission from ref. 63. Copyright (2019), Elsevier. ....12

<b>Figure 2.1</b>   A chart representing top 10 principal causes of death in Singapore from 2014 to 2018, shown as a percentage of total number death occurred during the respective years. Numerical values are obtained from ref. 2. ....	<b>21</b>
<b>Figure 2.2</b>   <b>(a)</b> Cartoon plot of mistletoe lectin consisting of A-chain (circled in red) and B-chain connected (circled in blue) by a disulfide bridge. Reprinted with permission from ref. 18. Copyright (2019), Elsevier. <b>(b)</b> A schematic illustration on the mode of action of RIP (indicated as orange star). RIP recognizes and depurinates adenine (A4324) in 28S rRNA of the large ribosomal subunit.....	<b>24</b>
<b>Figure 2.3</b>   <b>(a)</b> Ribosome-inactivating activity of Singapore Mistletoe Lectin (SML) determined by the degree of inhibition of luciferase translation in a rabbit reticulocyte system. IC <sub>50</sub> is $2.81 \pm 0.03$ nM. <b>(b)</b> Ribosome-inactivating activity of rSML-A determined by the degree of inhibition of luciferase translation in a rabbit reticulocyte system. IC <sub>50</sub> is $4.87 \pm 0.01$ nM. Adapted from ref. 27. ....	<b>25</b>
<b>Figure 2.4</b>   Cytotoxic effect of BioPORTER®/rSML-A and SML on <b>(a)</b> HeLa cancer cells and <b>(b)</b> MCF-7/caspase-3 positive cells. Adapted from ref. 27. ....	<b>25</b>
<b>Figure 2.5</b>   Schematic illustration of passive and active targeting of nanoparticle-drug complexes. The endothelial cells are spaced further apart from each other, resulting in the formation of a more permeable vessel. Upon which, nanoparticles are able to passively accumulate and be retained around the tumor site. Active targeting occurs when the nanoparticles are modified with targeting ligands which directs them towards receptors on cancer cells for binding. Reprinted with permission from ref. 30. Copyright (2019), Nature. ....	<b>26</b>
<b>Figure 2.6</b>   Schematic illustrations of bottlenecks encountered for delivery of biomacromolecules. Reprinted with permission from ref. 35. Copyright (2019), Nature. ....	<b>27</b>
<b>Figure 2.7</b>   Our design of rSML-A delivery system. It comprises of biodegradable and biocompatible glycol chitosan backbone modified with a boronic acid targeting ligand and a disulfide linker for covalent conjugation to rSML-A. ....	<b>28</b>



<b>Figure 2.8   (a)</b> Schematic illustration of phenylboronic acid-based micelle in targeting sialic acids, and <b>(b)</b> compilation of its binding affinities towards different sugars such as glucose, mannose, galactose, SA, and Me-SA. Reprinted with permission from ref 44. Copyright (2019), American Chemical Society. ....	<b>30</b>
<b>Scheme 2.1  </b> Schematic illustration of polymer modified with CDM derivative under acidic (right) and basic (left) conditions.....	<b>31</b>
<b>Figure 2.9  </b> Schematic illustration of our initial design of rSML-A delivery system. ....	<b>32</b>
<b>Figure 2.10  </b> Gel image of the SML and SML-A (left), adapted from ref. 27, and the gel image of the recombinant A-chains obtained from collaborator, after being thawed from deep-freeze (right). ....	<b>35</b>
<b>Figure 2.11  </b> Flow cytometry results depicting graphs of fluorescence intensity of PI against Annexin V – FITC channel for MDA-MB-231 after 48 hours incubation with 2-11, GC-BA0-SPDP/rSML-A. Q2 depicts the percentage of dead cells, while Q3 gives the percentage of cells in early apoptosis stage, and Q4 shows the percentage of live cells. ....	<b>35</b>
<b>Figure 2.12  </b> WST-1 assay of MDA-MB-231 (bottom) upon 48 hours incubation (khaki) and 72 hours incubation (blue) with 2-19, GC-BA1-SPDP/rSML-A. The samples were incubated in presence of FBS and glucose.....	<b>37</b>
<b>Figure 2.13  </b> New proposed model of the carrier system, BA-GC-SS/rSML-A. Ratio of BA-PEG linker (grey) and CDM-TEG-SSPy (blue) is 2:1, and it can be varied during the final step of synthesizing the polymer, BA-GC-SSPy.....	<b>38</b>
<b>Scheme 2.6  </b> General schematic illustration of the procedure in induction and purification of the recombinant protein, rSML-A. ....	<b>40</b>
<b>Figure 2.14  </b> Gel images of mixtures in intermediary steps of recombinant protein (rSML-A) purification. L = ladder/marker (values written on the left are in kDa); (-) = before induction, induced = after protein induction; FT = first flow through; W1 = after first wash; W2 = after second wash,; + SUMO protease = after incubation with SUMO protease; 2nd column = after second column; SUMO tag = flow through of second column which contains SUMO tag..	<b>41</b>

<b>Figure 2.15</b>   FPLC chromatogram of rSML-A, and gel image obtained from SDS-PAGE of different fractions collected (insert). .....	<b>41</b>
<b>Figure 2.16</b>   Confocal images (top to bottom: merged, bright field, red channel, DAPI channel) of MDA-MB-231 treated with different substrates (left to right: BioPORTER/rSML-A, 2-30A, 2-30B, rSML-A, rhodamine B, RBS) for 6 hours in blank DMEM (without glucose, FBS, P/S, and phenol red). Scale bar (white) = 5 $\mu$ m for BioPORTER/rSML-A and PBS, and scale bar (white) = 10 $\mu$ m for the rest. ....	<b>43</b>
<b>Figure 2.17</b>   SDS-PAGE gel images of rSML-A in different concentrations (left), crude mixtures of 2-30A and 2-30B (middle) in which each well contains 5 $\mu$ g of rSML-A), and respective solution of 2-30A and 2-30B after washing with PBS twice (right) by ultrafiltration with 50 kDa filter membrane and centrifugation conditions set at 10,000 X g, 5 minutes, 4 °C. ....	<b>44</b>
<b>Figure 2.18</b>   A graphical plot of mean intensity against concentration of rSML-A, with the values of mean intensity of each band (corresponding to their respective amount of rSML-A) recorded using Fiji ImageJ. ....	<b>45</b>
<b>Figure 2.19</b>   WST-8 assay of MDA-MB-231 upon treatment with BioPORTER/rSML-A and 2-30B in triplicate studies. The cell viability percentages shown here were normalized to that of negative control, PBS (cell viability = 100%). Red color-coded bars indicated presence of FBS during incubation while blue color-coded bars indicated absence of FBS in first 4 hours of treatment, according to the standard protocol of BioPORTER® reagent. ....	<b>46</b>
<b>Figure 2.20</b>   Confocal microscopic images (left to right: DAPI, green channel, red channel, bright field, merged) of MDA-MB-231 treated with different substrates conjugated with rhodamine green (top to bottom: 2-30B, 2-30). The cells were subsequently stained with LysoTracker red and DAPI. Scale bar (white) = 5 $\mu$ m. ....	<b>47</b>
<b>Figure 2.21</b>   LC-MS spectrum of modified Aurein 1.2 upon cleavage from Sieber amide resins with TFA/H <sub>2</sub> O/TIPS (v/v 95:2.5:2.5) solution. The peptide was obtained after precipitation with diethyl ether from dried supernatant and resuspended in DI water. ....	<b>49</b>

<b>Figure 2.22</b>   Confocal microscopic images (top to bottom: merged, bright field, red channel, DAPI channel) of MDA-MB-231 (left two columns) and NIH3T3 (right two columns) treated with different substrates (2-30B and 2-30B@A) tagged with rhodamine. Scale bar (white) = 10 $\mu$ m. ....	<b>50</b>
<b>Figure 2.23</b>   Merged confocal microscopic images of (top to bottom) BioPORTER/rSML-A, 2-30B, 2-30B@A, rSML-A, modified Aurein 1.2, sulforhodamine B in different cell lines MDA-MB-231 (left) and NIH3T3 (right). The color blue depicts DAPI staining, while red depicts substrates stained with sulforhodamine chloride. Scale bar (white) = 10 $\mu$ m.....	<b>51</b>
<b>Figure 2.24</b>   WST-8 cell viability assays of (a) 2-30B@A, (b) 2-30B, and (c) 2-29, in MDA-MB-231 cells (dark blue) and NIH3T3 (light blue). The cells were incubated with substrates under normal growth condition, in presence of glucose and FBS for 70 h. The cell viability percentages shown here were normalized to that of negative control, PBS (cell viability = 100%)......	<b>52</b>
<b>Figure 2.25</b>   Compiled z-stack images depicts a three-dimensional view of MDA-MB-231 after 12 hours incubation with our final conjugate, 2-30B@A (red) which most had successfully escaped from the endosomes before lysosomes (green) fusion. Blue color represents nuclei as stained by DAPI. ....	<b>53</b>
<b>Figure 2.26</b>   Image of how the mean intensity values were obtained using Fiji ImageJ (top, left), and values recorded (Area, Mean, IntDen, RawIntDen) are shown in tables above. Mean intensity is obtained by subtracting the mean values from the average of the background. .	<b>68</b>
<b>Figure 3.1</b>   A general schematic illustration on some of the different classes of antibiotics available till 2003. Image adapted from ref. 2.....	<b>79</b>
<b>Figure 3.2</b>   (a) Statistic of new antibiotic approvals from 2000 to 2015. A total of 32 new antibiotic drugs were launched, with two of them used in combinations with existing antibiotics. Reprinted with permission from ref. 1. Copyright (2019), Springer Nature. (b) A list of new first-in-class antibiotics launched from 2000 to 2015. ....	<b>80</b>

<b>Figure 3.3</b>   A schematic illustration of the structure of cell wall in (a) Gram-negative bacteria and (b) Gram-positive bacteria. Reprinted with permission from ref. 16. Copyright (2019), Springer Nature.....	<b>82</b>
<b>Figure 3.4</b>   LC-MS spectrum of the organic layer from lysozyme (40% wt) degradation assay. The metabolites that matches with the m/z signals are shown in the insert. ....	<b>90</b>
<b>Figure 3.5</b>   LC-MS spectra of the organic layer (top) and crude (bottom) lysozyme (10% wt) degradation assay. The metabolites that matches with the m/z signals are shown in the insert. ....	<b>90</b>
<b>Figure 3.6</b>   Schematic illustration of lysozyme degradation (top) and the LC-ESI-TOF MS result obtained from lysozyme (20% wt) degradation assay (bottom). Two major resultant peaks at $t = 0.69$ min and $t = 0.99$ min correspond to the NAG-NAM fragment and the phospholipid respectively. The remaining peaks were from metabolites from the enzyme and the buffer used in the lysozyme degradation assay. ....	<b>91</b>
<b>Figure 3.7</b>   Confocal microscopic image (left), STED confocal microscopic image (middle), and processed STED confocal image (right) of MRSA-BAA40 incubated with 3-1@Rhd (red) and cell surface staining dye, FM 1-43fx. Scale bar = 2 $\mu\text{m}$ . ....	<b>92</b>
<b>Figure 3.8</b>   STED microscopy studies of G+ve bacteria, where green = FM 1-43fx, red = 3-1@Rhd, yellow = region of colocalization of two fluorophores. Scale bar = 2 $\mu\text{m}$ . ....	<b>93</b>
<b>Figure 3.9</b>   STED microscopy studies of G-ve bacteria, where green = FM 1-43fx, red = 3-1@Rhd, yellow = region of colocalization of two fluorophores. Scale bar = 2 $\mu\text{m}$ . ....	<b>94</b>
<b>Figure 3.10</b>   Magnified STED microscopic images of <i>S. aureus</i> and <i>E. faecalis</i> , where green = FM 1-43fx, red = 3-1@Rhd, yellow = region of colocalization of two fluorophores. Scale bar = 1 $\mu\text{m}$ . ....	<b>95</b>
<b>Figure 3.11</b>   Relative fluorescence intensity on bacterial surface after treatment in 3-1@Rhd. A total of at least a hundred bacteria cells from each strain were used for calculation, and the average 3-1@Rhd fluorescence signal per cell was measured for comparison. Chemical	

structures of the different third amino acids found in natural PGs of these 6 strains are shown in insert. ....	96
<b>Figure 3.12</b>   Relative fluorescence intensity on <i>E. faecalis</i> surface after treatment with 3-1 @Rhd, CS-PP@Rhd, PP@Rhd and rhodamine alone (Rhd). A total of at least a hundred bacteria cells from each strain were used for calculation, and the average rhodamine fluorescence signal per cell was measured for comparison. ....	97
<b>Figure 3.13</b>   Schematic illustration on the quantification of fluorescence intensity using Fiji ImageJ.....	105
<b>Figure A1.1</b>   Image scan of selected MALDI-TOF-MS spectra of the pullulan standard (6.2 kDa), for entries u (DD, +heat), v (DD, +heat), w (2nd-Co., +heat), w (DD, +heat). ....	131
<b>Figure A1.2</b>   Image scan of selected MALDI-TOF-MS spectra of the chitosan (< 3 kDa, Carbosynth), for entries t (2nd-Co., -heat), t (DD, -heat), u (2nd-Co., +heat), z (DD, -heat), w (2nd-Co., +heat).....	131
<b>Figure A1.3</b>   Successful MS spectrums pullulan 6.2 kDa (left) chitosan purchased from Carbosynth (right) obtained from different conditions.....	132
<b>Figure A1.4</b>   MALDI-TOF-MS spectrum depicting a distribution of different MW of chitosan, with the peak height corresponding to 1615.7 kDa. ....	132
<b>Figure A2.1</b>   <sup>1</sup> H NMR spectrum of 2-9 in D <sub>2</sub> O. ....	136
<b>Figure A2.2</b>   <sup>1</sup> H NMR spectrum of 2-10 in D <sub>2</sub> O. ....	136
<b>Figure A2.3</b>   <sup>1</sup> H NMR spectrum of 2-20 in CDCl <sub>3</sub> .....	137
<b>Figure A2.4</b>   <sup>13</sup> C NMR spectrum of 2-20 in CDCl <sub>3</sub> .....	137
<b>Figure A2.5</b>   <sup>1</sup> H NMR spectrum of 2-21 in CDCl <sub>3</sub> .....	138
<b>Figure A2.6</b>   <sup>13</sup> C NMR spectrum of 2-21 in CDCl <sub>3</sub> .....	138
<b>Figure A2.7</b>   <sup>1</sup> H NMR spectrum of 2-22 in CDCl <sub>3</sub> .....	139
<b>Figure A2.8</b>   <sup>13</sup> C NMR spectrum of 2-22 in CDCl <sub>3</sub> .....	139
<b>Figure A2.9</b>   <sup>1</sup> H NMR spectrum of 2-23 in CDCl <sub>3</sub> .....	140
<b>Figure A2.10</b>   <sup>13</sup> C NMR spectrum of 2-23 in CDCl <sub>3</sub> .....	140

<b>Figure A2.11</b>   $^1\text{H}$ NMR spectrum of 2-24 in DMSO-d <sub>6</sub> . .....	<b>141</b>
<b>Figure A2.12</b>   $^1\text{H}$ NMR spectrum of 2-25 in DMSO-d <sub>6</sub> . .....	<b>141</b>
<b>Figure A2.13</b>   $^1\text{H}$ NMR spectrum of 2-28 in DMSO-d <sub>6</sub> . .....	<b>142</b>
<b>Figure A2.14</b>   $^1\text{H}$ NMR spectrum of 2-29 in DMSO-d <sub>6</sub> . .....	<b>143</b>
<b>Figure A2.15</b>   $^1\text{H}$ NMR spectrum of 3-2 in DMSO-d <sub>6</sub> . .....	<b>162</b>
<b>Figure A2.16</b>   $^1\text{H}$ NMR spectrum of 3-5 in DMSO-d <sub>6</sub> . .....	<b>162</b>
<b>Figure A2.17</b>   $^1\text{H}$ NMR spectrum of 3-7 in D <sub>2</sub> O. ....	<b>163</b>
<b>Figure A2.18</b>   $^1\text{H}$ NMR spectrum of 3-9 in DMSO-d <sub>6</sub> . .....	<b>163</b>
<b>Figure A2.19</b>   $^1\text{H}$ NMR spectrum of 3-12 in DMSO-d <sub>6</sub> . .....	<b>164</b>
<b>Figure A2.20</b>   $^1\text{H}$ NMR spectrum of 3-14 in D <sub>2</sub> O. ....	<b>164</b>

## List of Schemes

- Scheme 1.1** | Schematic illustration of deacetylation of chitin to obtain chitosan under basic conditions. The degree of deacetylation,  $DD = yx + y$ , varies depending on the conditions used. ....4
- Scheme 2.2** | Synthesis of the boronic acid targeting ligand with, **(a)** octaethylene glycol (OEG) spacer and **(b)** PEG<sub>1000</sub>. Reactions and conditions: a, tosyl chloride, NaOH (1.5 equiv.), THF/H<sub>2</sub>O; b, sodium azide (2 equiv.), ACN; c, TBDMS-Cl (1.1 equiv.), NEt<sub>3</sub> (1.1 equiv.), DMAP (0.1 equiv.), DCM; d, NaH (1.1 equiv.), DMF; e, TBAF (3 equiv.), THF; f, carboxy dimethylmaleic anhydride (1.5 equiv.), HATU (1.5 equiv.), DIPEA (1.5 equiv.), DCM; g, 4-ethynylphenylboronic acid pinacol ester, copper iodide (0.05 equiv.), DIPEA (3 equiv.), DCM; h, NaIO<sub>4</sub> (5 equiv.), NH<sub>4</sub>OAc (5 equiv.), acetone/H<sub>2</sub>O.....33
- Scheme 2.3** | Assembly of the protein carrier. Reactions and conditions: a, DIPEA (3 equiv.), DMAP (0.4 equiv.), DMSO; b, sulfo-LC-SPDP (0.5 equiv.), PBS/DMSO (pH 7.6). .....33
- Scheme 2.4** | Synthesis of GC-BA-SPDP/rSML-A conjugate with different lengths of PEG segment on GC-BA-SPDP. The protein was treated with TCEP at 4°C in PBS for an hour and filtered by 3 kDa membrane prior to conjugation. The protein concentrate was collected and added to the PBS mixture, consisting of respective polymers, GC-BA-SPDP, for 18 hours at 4 °C. ....34
- Scheme 2.5** | Synthesis of the essential components of the carrier, **(a)** protected targeting ligand, BE-PEG and **(b)** acid-labile disulfide linker, CDM-TEG-SSPy. Reactions and conditions: a, tosyl chloride, NaOH (1.5 equiv.), THF/H<sub>2</sub>O; b, sodium azide (2 equiv.), ACN; c, 4-ethynylphenylboronic acid pinacol ester, copper iodide (0.05 equiv.), DIPEA (3 equiv.), DCM; d, potassium thioacetate (2.5 equiv.), NaI (0.1 equiv.), acetone; e, 1. NaOMe (1.5 equiv.), MeOH, 2. dipyridyl disulfide; f, carboxy dimethylmaleic anhydride (1.2 equiv.), HATU (1.25 equiv.), HOAt (1.25 equiv.), DIPEA (1.25 equiv.), DCM. ....39
- Scheme 2.5** | Synthesis of new carrier design from commercially available glycol chitosan. Reactions and conditions: a, phthalic anhydride (5 equiv.), AcOH/H<sub>2</sub>O; b, tosyl chloride (1.5

equiv.), triethylamine (3 equiv.), DMF; c, sodium hydride (1.5 equiv.), 2-20, DMF; d, 1. sodium periodate (5 equiv.), DMF, 2. HCl; e, hydrazine (10 equiv.), methanol; f, 2-23, DIPEA, DMAP, DMF. ....	40
<b>Scheme 2.7</b>   Synthesis of BA-GC-SS/rSML-A (2-30) conjugate. The protein was treated with DTT at 4 °C in PBS for an hour and filtered by 10 kDa membrane prior to conjugation. The protein concentrate was collected and added to the PBS mixture, consisting BA-GC-SSPy (2-29), and incubated for 24 hours at 4 °C. ....	42
<b>Scheme 2.8</b>   (a) Aurein 1.2 peptide sequence with C-terminal modified with LPETGGG (red) to conjugate with GFP-Cre (blue). (b) Proposed design of Aurein 1.2, in which the C-terminal is modified with Cys since it has a thiol end for conjugation to the disulfide linker on the polymeric carrier. ....	48
<b>Scheme 3.1</b>   Synthetic scheme illustrating the biosynthesis of Lipid II from Lipid I which occur at the cytoplasmic membrane. The sugar ring color coded in green is NAG, while the other that is color coded in yellow is NAM. ....	83
<b>Scheme 3.2</b>   General synthetic route of the tetrasaccharide core in Lipid IV by Wong et al. <sup>35</sup> ...	86
<b>Scheme 3.3</b>   A schematic illustration of our ‘top-down’ approach to PGO derivative (3-1) which starts from a chitosan polymer. 3-1 was stained with rhodamine to give 3-1@Rhd, in which each molecule of 3-1 is tagged with at most 1 molecule of rhodamine on the amino group on L-lysine. ....	88
<b>Scheme 3.4</b>   Schematic illustration of rhodamine-labelled substrates for brief SAR study on <i>E. faecalis</i> . ....	97
<b>Scheme 3.5</b>   Synthesis of modified PGOs with peptide attachment on the C2 amino group, 3-7. Reactions and conditions: a, succinic anhydride (0.5 equiv.), DMF; b, H <sub>2</sub> NR (peptide) (1 equiv.), HATU, HOAt, DIPEA, DMF; c, acetic anhydride (5 equiv.), pyridine; d, MeNH <sub>2</sub> , MeOH; e, 1. 1H-tetrazole, dibenzyl <i>N,N</i> -diisopropylphosphoramidite (2 equiv.), 2. tert-butyl hydroperoxide, DCM; f, 1. H <sub>2</sub> , Pd/C, MeOH, 2. <i>n</i> C <sub>14</sub> H <sub>29</sub> OPO(OH) <sub>2</sub> (2 equiv.), DMF, 3. LiOH, MeOH/H <sub>2</sub> O (v/v, 1:1). ....	99



**Scheme 3.6** | Synthesis of modified PGOs with peptide attachment on the C6 hydroxyl group, 3-

14. Reactions and conditions: a, phthalic anhydride (3 equiv.), AcOH/H<sub>2</sub>O; b, NaH, 2-bromopropanoate (0.5 equiv.), DMF; c, H<sub>2</sub>NR (peptide) (1 equiv.), HATU, HOAt, DIPEA, DMF; d, hydrazine, AcOH, MeOH; e, acetic anhydride (5 equiv.), pyridine; f, 1. MeNH<sub>2</sub>, 2. 1H-tetrazole, dibenzyl *N,N*-diisopropylphosphoramidite (2 equiv.), 3. tert-butyl hydroperoxide, DCM; g, 1. H<sub>2</sub>, Pd/C, MeOH, 2. *n*C<sub>14</sub>H<sub>29</sub>OPO(OH)<sub>2</sub> (2 equiv.), DMF, 3. LiOH, MeOH/H<sub>2</sub>O (v/v, 1:1). .....**100**

**Scheme A1.1** | Schematic illustrations of the chemical structures of the matrices (top row) as well as derivatising agent (bottom row) mentioned. ....**128**

## List of Tables

<b>Table 1.1</b>   Relation between chitosan's principal characteristics and its use in biomedical applications. Reprinted with permission from ref. 40. Copyright (2019), Elsevier. ....	<b>9</b>
<b>Table A1.1</b>   List of conditions tried, part 1. Derivatising solution A comprises of 2 mg of 3-AQ dissolved in 1 mL of 2 mM ADP solution. Derivatising solution B is a mixture of 4 mg/mL 2-HPM solution and 4 mM ADP solution (v/v = 1:1), such that upon mixing, the final concentrations of 2-HPM and ADP are halved. Derivatising solution C is a mixture of 10 mg/mL 2-HPM solution and 4 mM ADP solution (v/v = 1:1). Derivatising solution D is a mixture of 20 mg/mL 2-HPM solution and 4 mM ADP solution (v/v = 1:1). ADP solution is a mixture of ADP dissolved in H <sub>2</sub> O/ACN (v/v = 1:1), and 2-HPM solution is a mixture of 2-HPM dissolved in MeOH/AcOH (v/v = 9:1). <sup>\$</sup> Matrix was purchased and used without further purification. <sup>#</sup> MALDI-TOF-MS analysis was carried out in negative mode. <sup>*</sup> Matrix was added till saturation point, in which the solid particles were settled at the bottom and the supernatant was remove for usage. ....	<b>128</b>
<b>Table A1.2</b>   List of conditions tried, part 2. Derivatising solutions B, C and D were the same as described in Table A.1. <sup>\$</sup> Matrix was purchased and used without further purification. <sup>*</sup> Matrix was added till saturation point, in which the solid particles were settled at the bottom and the supernatant was remove for usage. ....	<b>129</b>
<b>Table A1.3</b>   Results obtained from MALDI-TOF-MS analysis of entries a to s, were 'X' = only noise observed, 'S/N' = signal to noise ratio, and 'N.D.' = not determined. ....	<b>130</b>
<b>Table A1.4</b>   Results obtained from MALDI-TOF-MS analysis of entries t to af, were 'X' = only noise observed, 'S/N' = signal to noise ratio, and 'N.D.' = not determined. ....	<b>130</b>
<b>Table A1.5</b>   Results obtained from MALDI-TOF-MS analysis of entries ag to ar, were 'X' = only noise observed, 'S/N' = signal to noise ratio, and 'N.D.' = not determined. ....	<b>132</b>

## Summary

This thesis focuses on the use of chitosan in two different applications. The thesis starts off with a generic introduction on natural sugar polymers, which is followed up by the introduction of the key star of this thesis - chitosan. Important parameters and interesting inherent pharmaceutical properties were discussed too, along with a few applications closely related to the works presented in this thesis.

In the second chapter, chitosan's versatility as well as high biocompatibility were utilised to turn it into a carrier for a bio-macromolecular cargo. The cargo of interest was a species that belonged to the ribosome-inactivating proteins (RIPs), whose generic potency are well known, namely rSML-A. Expression and purification of the recombinant protein was carried out firstly in accordance with a protocol provided by the collaborator, and designs were made to enable the cargo's endosomal escape, which has been a critical limiting factor for efficient cytosolic delivery of biomacromolecules. After several trial and errors, the delivery system has been optimised and fine-tuned, such that the final conjugate, **2-30B@A**, was able to escape the endosome easily before degradation of the cargo by lysosomes. In addition, adding a targeting ligand greatly increased the specificity of the system towards the cells of interest, as opposed to negative controls.

In the third chapter, brief description of the conventional 'bottom-up' approaches in obtaining peptidoglycan oligosaccharides (PGOs) were discussed, along with were several limitations faced. To combat these limitations, an unconventional yet facile 'top-down' approach from chitosan produced a synthetic PGO **3-1**, together with several studies done on the substrates obtained were discussed. From the biological studies conducted, it was determined that PGO obtained via this approach greatly resembled that of the natural PGs, in which the same methodology was used to synthesize PGO derivatives that were not reported to the best of my knowledge.

In the last chapter, a brief summary of the previous chapters was described and concluded the whole thesis.

## Chapter 1 | Natural Polysaccharides and Chitosan in Biomedical Applications

### 1.1 | Polymeric Sugars from Nature and Their Advantages in Biomedical Applications

Nature is a remarkable source of inspiration for any innovations, and she is capable of creating a plethora of complex biological structures in a seemingly effortless manner. An area of particular interest to us is naturally occurring polysaccharides. These polysaccharides are highly diverse as they consist of various chemical compositions and spatial conformations, as well as a wide range of molecular weights. They are made of several repeating monosaccharides of same or different chemical compositions, in which they are generally connected via glycosidic bonds (see **Figure 1.1**). For instance, in the dextran, a polysaccharide made by various bacterial strains, has two types of glycosidic linkages. The predominant linkage is known as  $\alpha$ -(1 $\rightarrow$ 6) glycosidic bond, which is formed between anomeric carbon (C1) and 4<sup>th</sup> hydroxyl group (on C6) of another D-glucose unit. Other possible linkages that result in its complex branched structure, are  $\alpha$ -(1 $\rightarrow$ 2)-,  $\alpha$ -(1 $\rightarrow$ 3)- or  $\alpha$ -(1 $\rightarrow$ 4)- glycosidic bonds (see **Figure 1.1** for  $\alpha$ -(1 $\rightarrow$ 6)- and  $\alpha$ -(1 $\rightarrow$ 3)- linkages in dextran). The formation of these highly specific and complex structures is extremely difficult and tedious in chemical synthesis, as the similar reactivity of the hydroxyl groups, as well as their steric environment, must be taken into consideration.

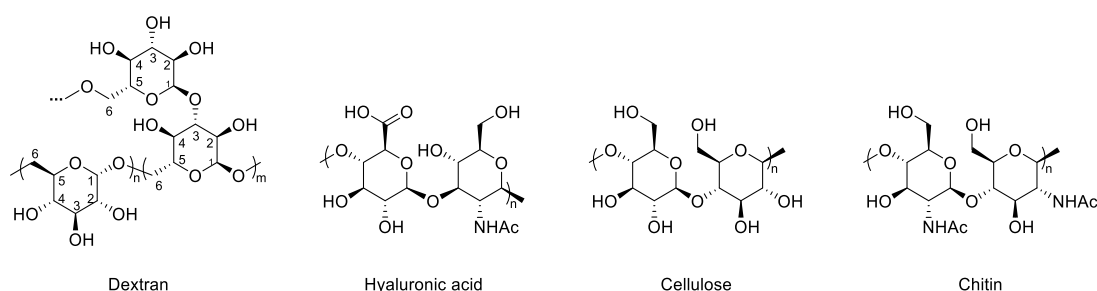


**Figure 1.1** | Chemical structures of some naturally occurring polysaccharides (left to right: dextran, hyaluronic acid/hyaluronan, cellulose, chitin). The numbers labelled on dextran represent the generic counting system of carbon atoms in carbohydrates. Anomeric carbon is labelled as C1.

Cellulose has the same monosaccharide repeating unit as dextran, but the monomers are connected to each other via  $\beta$ -(1 $\rightarrow$ 4) glycosidic linkages in a linear manner. Chitin, on the other

hand, has similar glycosidic linkages as cellulose ( $\beta$ -(1 $\rightarrow$ 4) glycosidic bonds), but has *N*-acetyl-D-glucosamine (NAG) as the repeating unit instead of glucose. Unlike the previous three cases, in which their repeating unit is of the same monosaccharide, hyaluronic acid comprised of repeating units of D-glucuronic acid and *N*-acetyl-D-glucosamine disaccharides. The third hydroxyl group of NAG forms a  $\beta$ -(1 $\rightarrow$ 3) glycosidic linkage with the anomeric carbon of D-glucuronic acid within in the disaccharide, while the fourth hydroxyl group of D-glucuronic acid forms a  $\beta$ -(1 $\rightarrow$ 4) glycosidic linkage with the anomeric carbon of another *N*-acetyl-D-glucosamine. Among the four natural polysaccharides shown in **Figure 1.1**, only hyaluronic acid is negatively charged at physiologically pH due to presence of carboxylic group, while the other three are neutral.

These glycosidic bonds present in the sugar polymers are often easily broken in nature, or in other terms, endowed these natural polysaccharides with biodegradable traits. Dextran can be degraded in mammalian tissues by an enzyme, dextranase.<sup>1</sup> Majority of hyaluronic acid are degraded by hyaluronidase isozyme in tissues and transported to liver endothelial cells in which they are further degraded to glucuronic acid and *N*-acetylglucosamine in lysosomes.<sup>2</sup> Ultimately, they will be converted to CO<sub>2</sub>, H<sub>2</sub>O, and urea upon metabolism. Cellulases, often found in microbes, are a group of enzymes that aid in hydrolysing  $\beta$ -1,4 glycosidic linkages found in cellulose. The key enzymatic activities that ensure complete degradation of cellulose are endoglucanase activity, exoglucanase activity, and  $\beta$ -glucosidases activity.<sup>3-4</sup> Chitin's  $\beta$ -1,4 glycosidic bonds can be hydrolysed with the aid of chitinases, in which mammals including human possess.<sup>5-7</sup>

In the past century, due to their unique structures and chemical compositions, these natural polysaccharides have been extensively studied and have exhibit interesting properties in biomedical and pharmaceutical applications. Dextran, a hydrophilic polysaccharide, has demonstrated its ability in reducing inflammatory response and vascular thrombosis.<sup>8-11</sup> Hyaluronic acid, a key component of extracellular matrix (ECM), is widely diffused in nature. It has shown to aid in wound healing process by promoting fibroblast growth at the wound site and

stimulate collagen production, and it is able to keep tissues hydrated, such as the human eyes.<sup>12-15</sup> Cellulose, found mainly in plant fibers, has poor solubility in water but this makes it an ideal tissue engineering biomaterial such as grafts design or wound healing scaffolds.<sup>16</sup> In past decade, bacterial cellulose is emerging as an alternative due to its practicability in production and has better biocompatibility than cellulose.<sup>17-18</sup> Similarly, bacterial cellulose is often used in wound healing treatment, especially on skins, since it can be easily removed after recovery.<sup>19</sup> After cellulose, chitin is the next most abundant natural polysaccharide, which is found mainly in the shells of crustaceans, such as crabs and shrimps, and insects. Being mechanically strong and biocompatible, chitin is an excellent scaffold in bone engineering, whereby cells are able to grow and distribute in the interconnected porous scaffolds.<sup>20</sup> It is one of the top choices as bone graft substitutes because it can be made into a composite with hydroxyapatite, one of the major bone minerals.<sup>21</sup>

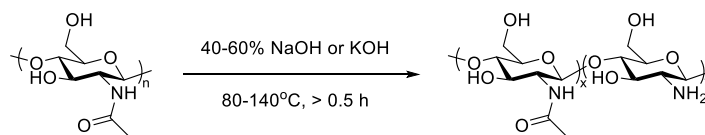
On top of their intriguing pharmaceutical properties and most importantly, their extensively studied biocompatible and biodegradable characteristics, these polysaccharides are generally stable, and they can be chemically modified into a class of smart biopolymers. Smart polymers, or stimuli-responsive polymers, are sensitive to their environment, and they can undergo changes in their structure or chemical compositions upon a change in the environment they are in. Depending on the functional groups present, the stimuli resulting in the change can be either physical or chemical. Physical stimuli include temperature, magnetic field, ultrasound, light, etc, while chemical changes usually result in the change of chemical compositions due to pH changes, or occurrence of oxidation or reduction. These features are highly sought after in biomedical applications, in which more focus will be placed on a derivative of chitin.

## 1.2 | Chitosan, a Semisynthetic Polysaccharide Derived from Chitin

Semisynthetic polysaccharides are obtained by chemical treatment of their naturally occurring counterparts. Chitosan (CS), in this case, is derived from chitin after undergoing deacetylation. Over the past few decades, chitosan has garnered a lot of attention and extensive research has been conducted as it is considered as a class of smart biopolymers with enormous possibilities for structural modifications to carry out desired functions. Upon deacetylation, the reactive amino groups are free for further chemical modifications. Together with the presence of two different hydroxyl groups at C6 and C3 respectively, with the latter being least reactive due to highly hindered environment, one can utilise this difference in reactivities to attach different handles onto the polymer for a wide variety of applications.

### 1.2.1 | Degree of Deacetylation (DD) of Chitosan

Typical deacetylation of chitin uses 40-60% concentrated NaOH or KOH heated at 80 °C - 140 °C for a duration of at least 0.5 hour (see **Scheme 1.1**).<sup>22-23</sup> Strong basic condition is essential due to additional resistance resulted from spatial arrangement of C2-C3 substituents in trans relationship. Methods using strong acids are generally avoided as the polysaccharide will be hydrolysed along with the removal of acetyl groups. Chitosan can also be prepared by enzymatic reaction, using the enzyme, chitin deacetylase. This method of preparation is much less common than chemical removal of the acetyl functional group from chitin.



**Scheme 1.1** | Schematic illustration of deacetylation of chitin to obtain chitosan under basic conditions. The degree of deacetylation,  $DD = \frac{y}{x+y}$ , varies depending on the conditions used.

After deacetylation, the polymer is comprised of two types of monomers, *N*-acetyl-D-glucosamine (GlcNAc) and D-glucosamine (GlcN). Degree of deacetylation (DD) in this case is

the molar fraction of D-glucosamine in the resultant polymer ( $DD = \frac{y}{x+y} * 100\%$ ). One is able to control the degree of deacetylation by varying the parameters shown in **Scheme 1.1**. For instance, by increasing the time and temperature, one is able to obtain a highly deacetylated chitosan ( $DD > 90\%$ ). Several studies have shown that different degree of deacetylation plays an important role in the resulting polymer's physiochemical and biological properties. For instance, once DD reaches 50% or more, the polymer becomes water-soluble in slightly acidic environment (below its  $pK_a$  of 6.2).<sup>24</sup> A study conducted by Rinaudo *et al.* demonstrated that the concentration of proton has to be at least equivalent to the concentration of free amino groups present in order to fully dissolve the chitosan.<sup>25</sup> Protonation of free amino groups on C2 of D-glucosamine units in chitosan thereby results in a pseudo-natural cationic biopolymer. This effect gives rise to its potential in a plethora of biomedical applications and in pH-responsive biopolymers.

### 1.2.2 | Chitosan's Molecular Weight (MW)

Chitosan's molecular weight is largely determined by the methods and conditions of deacetylation. It can be categorized as follow, very high MW ( $> 300$  kDa), high MW (80-300 kDa), low MW (10-80 kDa) and very low MW ( $< 10$  kDa).<sup>26</sup> Different molecular weights affect the resulting properties of chitosan, such as moisture content, tensile strength and crystallinity.<sup>27-28</sup> A study conducted by Nuthanid *et al.* showed that chitosan with very high MW has significantly greater moisture absorption and tensile strength as compared to chitosan with low MW.<sup>29</sup> Xu and Du reported that chitosan with low to high MW has a positive relationship with enhanced protein encapsulation efficiencies, as well as a lower premature release kinetics.<sup>28</sup> Another study compared the stability of the resulting nanoparticle (NP) formed between very low and low MW chitosan, and it was found that the latter has better protection against enzyme degradation.<sup>30</sup>

### 1.2.3 | Bioactivities of Chitosan

Degree of deacetylation and molecular weight are the two most fundamental, and yet highly important parameters in determining chitosan's utility in its bioactivities and potential applications.



In this context, higher emphasis will be placed on two of the more relevant bioactivities, which are antimicrobial and anticancer activities. One of the well-known bioactivities of chitosan is its antibacterial activity, with part of the reason attributing to its pseudo cationic nature. It was proposed that this allows them to interact and disrupt the negatively charged membranes of the microbials, thereby causing the efflux of proteins and cellular contents.<sup>31-34</sup> Andres *et al.* reported that the increasing amount of potassium ions in the growth media observed when mortality rate of *Enterococcus faecalis* increases with increasing concentration of powdered chitosan treated, suggests that the cell wall has been disrupted by chitosan.<sup>33</sup> Zheng and Zu conducted a study on the antimicrobial effect of different molecular weights of chitosan (< 300 kDa) against *Staphylococcus aureus*.<sup>35</sup> It was demonstrated that at a concentration of 0.75% chitosan solution, chitosan with higher MW results in better killing effect (see **Figure 1.2**).

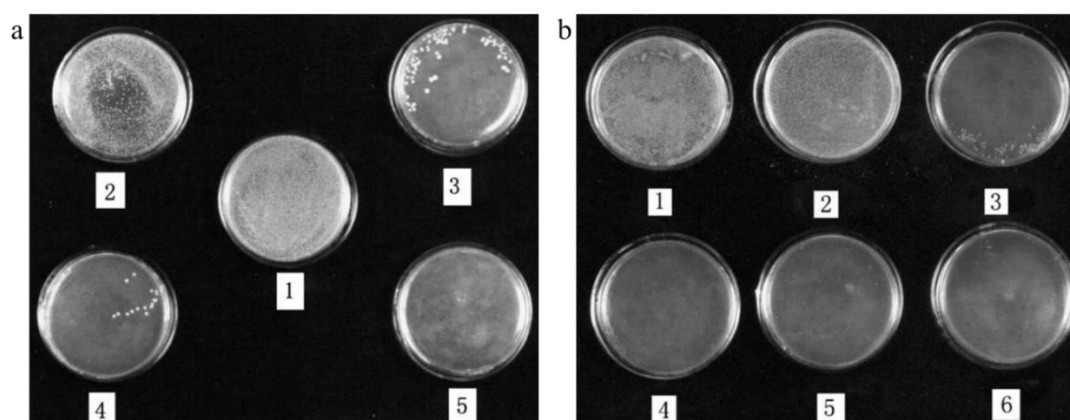


**Figure 1.2** | (a) Increasing antimicrobial activity of 48.5 kDa chitosan against *S. aureus* with chitosan concentration ranging from (1) 0%, (2) 0.25%, (3) 0.5%, (4) 0.75%, (5) 1%, as shown on the culture plate (diameter = 9.5 cm). (b) Increasing antimicrobial activity of chitosan against *S. aureus* with increasing MW, (1) blank, (2) < 5 kDa, (3) 48.5 kDa, (4) 72.5 kDa, (5) 129.0 kDa, (6) 165.7 kDa, as shown on the culture plate (diameter = 9.5 cm) with decreasing number of colonies of bacteria formed. Reprinted with permission from ref. 35. Copyright (2019), Elsevier.

Several studies have shown that chitosan too, possess anticancer/antitumor activity. Earlier studies conducted on hydrolysed chitosan, or chitooligosaccharides (COS), demonstrated that they can induce lymphocyte factor, thereby increasing growth of T-cells, which resulted in increased cytotoxicity and tumor inhibitory effects.<sup>36-37</sup> In another study conducted by Park *et al.*, they demonstrated that very low MW chitosan or COS has much better antitumor activity as compared

to the other end of the spectrum, very high MW chitosan against three different cell lines, HepG2 (liver cancer cells), A549 (lung cancer cells), and PC3 (prostate cancer cells).<sup>38</sup> Different cytotoxic effects were observed too in different cell lines. They reported that very high MW chitosan (1,900 kDa, DD = 98.5%) purchased from Sigma Aldrich has 50% cytotoxic concentration (CC<sub>50</sub>) of 50 µg/mL against HepG2 cells, > 50 µg/mL against A549 cells, and 50 µg/mL against PC3 cells. In comparison, COS obtained from enzymatic hydrolysis of the very high MW chitosan recombinant chitosanase showed much better cytotoxic activity with more than twice the efficacy. Moulin *et al.* showed that chitosan's anticancer properties are dependent on human melanoma cell lines.<sup>39</sup> In their study, they observed that the growth rate of the cell lines, SKMEL28 cells (primary melanoma derived from skin) and RPMI 7951 cells (melanoma derived from metastatic lymph node) were greatly reduced as compared to A375 cells (primary melanoma derived from skin) upon incubation with 2 mg/mL of chitosan (dissolved in 0.1% AcOH) coating on the wells (see **Figure 1.3a**). It was observed that cytotoxicity is the highest in RPMI 7951 cells, followed by SKMEL28 cells, and finally A375 cells upon 48 hours incubation with the same conditions mentioned (see **Figures 1.3b** and **1.3c**). Upon further investigations, they found out that in SKMEL28, induction of apoptosis was probably a result of increment in c-IAP expression, whereas in the case of RPMI 7951, apoptosis induction was through mitochondrial pathway. However, chitosan coatings do not seem to have a significant impact on A375, in which they reported that neither a decrease in growth rate nor apoptosis induction was observed.

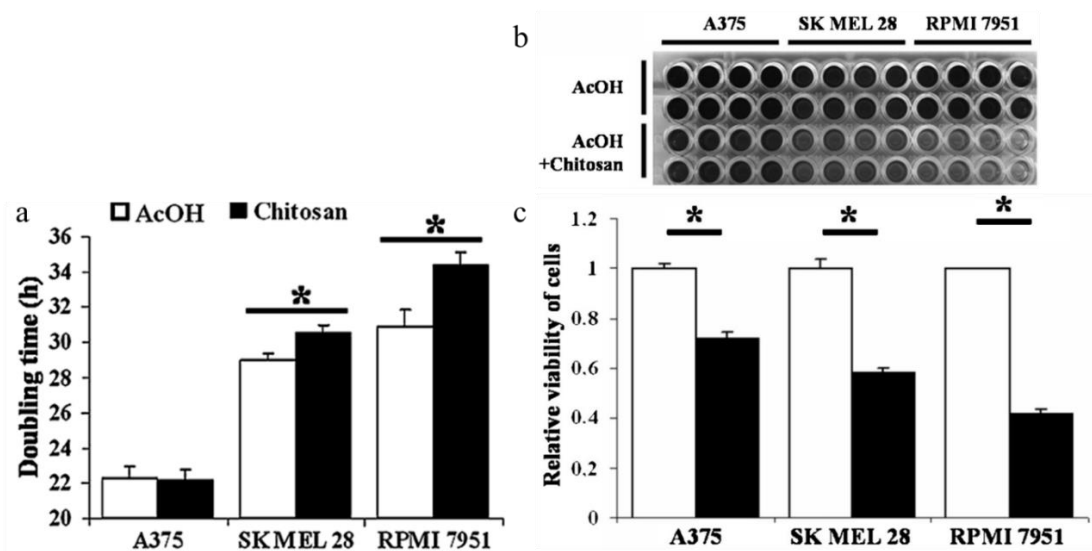


**Figure 1.3** | (a) Doubling time (calculated from growth curve) of A375 remains the same, while that of SKMEL28 and RPMI 7951 increases when incubated with chitosan coated wells as compared to the control (coated with 0.1% AcOH). (b) Image of the outcome of MTT assay for A375, SKMEL28 and RPMI upon 48 hours incubation with 2 mg/mL chitosan coatings dissolved in 0.1% acetic acid, and 0.1% acetic acid coating as control. (c) Relative cell viabilities of the respective melanoma cell lines upon incubation with 0.1% acetic acid (white bars) and chitosan dissolved in 0.1% acetic acid (black bars). Reprinted with permission from ref. 39. Copyright (2019), Elsevier.

#### 1.2.4 | Biomedical Applications of Chitosan-Based Materials

Since the discovery of chitosan more than two centuries ago, numerous researches have been carried out with a plethora of modifications on chitosan to enhance chitosan's intrinsic bioactivities, as well as add on additional features for a variety of biomedical applications. **Table 1.1** summarised the desired characteristics of chitosan that are important to different biomedical applications.<sup>40</sup> In general, for good biocompatibility and low cytotoxicity to healthy cells are highly preferred in most of biomedical applications. Chitosan, originating from a natural polysaccharide, has these advantages. In addition to that, the presence of free amino groups upon deacetylation enables the application of amine chemistry for further modifications of chitosan, in which chitin is not able to provide. This greatly increases the versatility of chitosan as a great biomaterial for many researchers to explore and work with.

Potential Biomedical Applications	Principal Characteristics
Surgical sutures	Biocompatible
Dental implants	Biodegradable
Artificial skin	Artificial skin
Rebuilding of bone	Film forming
Corneal contact lenses	Hydrating agent
Time release drugs for animals and humans	Nontoxic, biological tolerance
Encapsulating material	Hydrolysed by lysozyme
	Wound healing properties
	Efficient against bacteria, viruses, fungi

**Table 1.1** | Relation between chitosan's principal characteristics and its use in biomedical applications. Reprinted with permission from ref. 40. Copyright (2019), Elsevier.

One way to enhance the antimicrobial activity of chitosan is to place a permanent positive charge on the free amino groups, regardless of the environment it is in, by turning the primary amine into a quaternary amine.<sup>41-43</sup> Zhang *et al.* prepared quaternized carboxymethyl chitosan-based silver nanoparticle composite (QCMC-Ag NPs composite), in which both components are known to have good antibacterial activity.<sup>44</sup> In their study, they reported that the efficacy of QCMC-Ag NPs composite against one of the model pathogenic gram-positive bacteria, *Staphylococcus aureus* is better than Ag NPs or QCMC alone. By combining these two components into a composite, it helps to counter the limitations of Ag NPs in which they are generally genotoxic and tend to aggregate easily, and at the same time improve bacteria toxicity. In another study by Pogorielov *et al.*, they demonstrated that in situ preparation of chitosan-Ag NPs against methicillin-resistant *Staphylococcus aureus* (MRSA) has a minimum inhibitory concentration (MIC) 1.2 µg/mL, which is almost six times lower than chitosan alone, and eight times lower than Ag NPs alone.<sup>45</sup>

An interesting biomedical application that make full use of chitosan's antimicrobial activity is its use to aid in healing of wounds. Chitosan also possesses other desirable properties that are necessary as biomaterials for wound healing such as good biodegradability, excellent biocompatibility and low immunogenicity. Chitosan is also structurally similar to a key wound

healing macromolecule found in extracellular matrix (ECM), glycosaminoglycans (GAGs).<sup>46</sup> Degradation of chitosan can help in initiating the making of ECM components for wound repair. There are numerous wound dressings containing chitosan available in the market, such as HidroKi<sup>®</sup>, Patch<sup>®</sup> and KytoCel<sup>®</sup>.<sup>47-48</sup> Recently, Lan *et al.* reported that *N*-succinyl-chitosan (obtained by chemically modifying a portion of chitosan's amino groups with succinic anhydride) more water-soluble than chitosan alone and retain is able to its antibacterial properties.<sup>49</sup> In addition, they demonstrated that *N*-succinyl-chitosan powder greatly shortened the wound healing time required on rabbit's skin as compared to chitosan powder and negative control, and that the modified biopolymer is able reduce bacterial contamination and infection, as well as promote tissue formation.

Another huge area of interest which garnered a lot of attention is the application of chitosan in delivery systems. The cargo to be delivered varies from small molecular drugs to peptide, nucleic acids, and even huge biomacromolecules such as proteins. It can be applicable for a wide range of biomedical applications such as delivering drugs for infection treatment, wound healing and different types of cancer therapeutics and diagnostics.<sup>50-63</sup> Moreover, chitosan-based carriers can be in different forms, such as nanoparticles (NPs), liposomes, micelles, hydrogels and polymers.

Chitosan nanoparticles have often been employed in encapsulating drugs for delivery purposes. In a study conducted by Ali *et al.*, made use of high MW chitosan (120 kDa, DD  $\geq$  85%) to encapsulate an antibiotic, levofloxacin, by ionotropic gelation technique with sodium tripolyphosphate to obtain a nanoparticle-like product, LFX-CS-NPs for treatment of ocular infection.<sup>50</sup> Thereafter, in order to extend corneal residence time, they incorporated LFX-CS-NPs into a sol-gel system. Their results showed enhanced antibacterial activity against *Pseudomonas aeruginosa* and *Staphylococcus aureus*, higher retention of the antibiotic at the cornea, and that it was safe for ocular administration, thereby implying that their formulation for the delivery system is effective for ocular drug delivery. In the context of cancer therapeutics, encapsulation of

hydrophilic drugs such as doxorubicin (DOX) and hydrophobic drugs such as paclitaxel (PTX) and camptothecin (CPT) by chitosan-based nanoparticles have been evaluated in several *in vitro* and *in vivo* studies.<sup>51-54</sup>

Another prominent use of chitosan-based carrier system is in gene delivery for anticancer therapy. Majority of the nucleic acid/chitosan polyplexes formed are based on electrostatic attractions, in which the former tends to be more negatively charged and the latter is more positively charged at slightly acidic environment. Often, this form of encapsulation faced stability issues in blood circulation or microenvironment of tumor, due to presence of numerous negatively charged components (i.e. serum proteins and glycosaminoglycans).<sup>55</sup> This result in a competition between the polyanions and the nucleic acid cargos, which may cause its premature release. In addition, the carrier system may have limitations in cell penetration since its route of entry is via non-specific absorptive endocytosis.<sup>56</sup> These challenges can be overcome with modifications on chitosan. Borchard *et al.* made use of quaternized chitosan to enhance its positive charge for stronger electrostatic interaction with DNA.<sup>57</sup> Strand *et al.* combat the stability issue by glycosylating chitosan to form branched chitosan, before assembling with DNA.<sup>58</sup> Li *et al.* included PEGylation (PEG<sub>2000</sub> and PEG<sub>5000</sub>) in formation of complexes with high MW chitosan (150 kDa, DD  $\geq$  83%) to improve stability.<sup>59</sup> They reported that PEGylated CPC2/pDNA and PEGylated CPC2/siRNA complexes significantly enhance stability at physiological conditions, and better silencing efficiency for the latter. For better cell penetrations, chitosan can be decorated with targeting ligands with respect to prominent receptors found on surfaces of the desired cells. In this way, they are able to enter by receptor mediated endocytosis. To enhance cell penetration, Ren *et al.* incorporated a targeting ligand, folic acid (FA), onto a high MW chitosan (201 kDa, DD  $\geq$  92%), and subsequent modification and complexation with antisense oligodeoxynucleotides to obtain the product, FA-HPCS-asODNs with average size of 181 nm.<sup>60</sup> They demonstrated that folic acid-conjugated hydroxypropyl-chitosan (FA-HPCS) complexed with asODNs enabled targeted delivery to KB-A-1 cells in Balb/c mice with high efficiency.

Chitosan have also been employed in delivery of proteins for a variety of biomedical applications. Yang *et al.* modified very high MW chitosan ( $> 310$  kDa,  $DD \geq 75\%$ ) by cross-linking with lactide and fibrinogen with UV light to form chitosan-lactide-fibrinogen (CLF) hydrogel for delivery of bone morphogenetic protein-2 (BMP-2), a key growth factor in bone regeneration.<sup>61</sup> BMP-2 was first mixed with the chitosan-lactide-fibrinogen solution before UV light was shone to induce simultaneous encapsulation of the protein along with hydrogel formation. Through *in vitro* and *in vivo* studies, they demonstrated the efficacy of their system to deliver the protein and enhanced osteogenesis. Liu *et al.* reported an oral insulin delivery method using insulin-loaded lecithin/chitosan nanoparticles with an average size of 180 nm.<sup>62</sup> *In vivo* studies conducted on diabetic rats showed successful reduction in blood glucose levels with an improved insulin release kinetics. In another study conducted by Wang et al. demonstrated the fabrication of chitosan-tannin-lysozyme nanoparticles (CS-TA-LNPs) via ion crosslinking method with sodium tripolyphosphate (TPP) (see **Figure 1.4a**), and that strong antibacterial performance against *Staphylococcus aureus* was observed (see **Figure 1.4b**).<sup>63</sup>

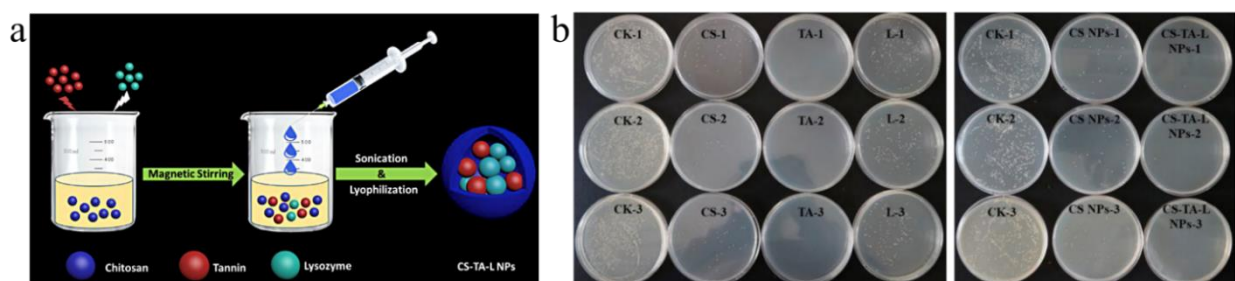


**Figure 1.4** | (a) Illustration on the fabrication of CS-TA-LNPs, in which TPP was added after the three individual components had been homogenized. (b) Triplicate experiment on the antimicrobial activity of the individual components (left box, CK = sterile water, CS = 50 µg/mL chitosan, Ta = 50 µg/mL tannin, L = 50 µg/mL lysozyme) and chitosan-based nanomaterials (right box, CK = sterile water, CS NPs = 50 µg/mL chitosan nanoparticles, CS-Ta-LNPs = 50 µg/mL chitosan-tannin-lysozyme nanoparticles). Reprinted with permission from ref. 63. Copyright (2019), Elsevier.

### 1.3 | References

1. Roberts, J.J.; Martens, P.J. 9 - Engineering Biosynthetic Cell Encapsulation Systems. In *Biosynthetic Polymers for Medical Applications*, Poole-Warren, L.; Martens, P.; Green, R., Eds.; Woodhead Publishing, 2016; pp 205-239.
2. Maiti, S.; Kumari, L. 3 - Smart Nanopolysaccharides for the Delivery of Bioactives. In *Nanoarchitectonics for Smart Delivery and Drug Targeting*, Holban, A.M.; Grumezescu, A.M., Eds.; William Andrew Publishing, 2016; pp 67-94.
3. Wilson D.B., Three Microbial Strategies for Plant Cell Wall Degradation. *Ann. NY Acad. Sci.* **2008**, *1125*, 289-297.
4. Lakhundi, S.; Siddiqui, R.; Khan, N.A., Cellulose Degradation: A Therapeutic Strategy in the Improved Treatment of Acanthamoeba Infections. *Parasit. Vectors* **2015**, *8*, 1-16.
5. Tabata, E.; Kashimura, A.; Kikuchi, A.; Masuda, H.; Miyahara, R.; Hiruma, Y.; Wakita, S.; Ohno, M.; Sakaguchi, M.; Sugahara, Y.; Matoska, V.; Bauer, P.O.; Oyama, F., Chitin Digestibility is Dependent on Feeding Behaviors, which Determine Acidic Chitinase mRNA Levels in Mammalian and Poultry Stomachs. *Sci. Rep.* **2018**, *8*, 1461-1471.
6. Lee, C.G.; Silva, C.A.D.; Cruz, C.S.D.; Ahangari, F.; Ma, B.; Kang, M.-J.; He, C.H.; Takyar, S.; Elias, J.A., Role of Chitin and Chitinase/Chitinase-Like Proteins in Inflammation, Tissue Remodeling, and Injury. *Annu. Rev. Physiol.* **2011**, *73*, 479-501.
7. Koch, B.E.; Stougaard, J.; Spalink, H.P., Keeping Track of the Growing Number of Biological Functions of Chitin and its Interaction Partners in Biomedical Research. *Glycobiology* **2015**, *25*, 469-482.
8. Sun, M.; Mao, J.J., Engineering Dextran-Based Scaffolds for Drug Delivery and Tissue Repair. *Nanomedicine* **2012**, *7*, 1771-1784.
9. Askari, M.; Fisher, C.; Weniger, F.G.; Bidie, S.; Lee, W.P., Anticoagulation Therapy in Microsurgery: A Review. *J. Hand Surg.* **2006**, *31*, 836-846.



10. Booi, D.I., Perioperative Fluid Overload Increases Anastomosis Thrombosis in the Free TRAM Flap Used for Breast Reconstruction. *Eur. J. Plast. Surg.* **2011**, *34*, 81-86.
11. Gombocz, K.; Beledi, A.; Alotti, N.; Kecskés, G.; Gábor, G.; Bogár, L.; Kőszegi, T.; Garai, J., Influence of Dextran-70 on Systemic Inflammatory Response and Myocardial Ischaemia-Reperfusion Following Cardiac Operations. *J. Crit. Care* **2007**, *11*, R87.
12. Gallo, N.; Nasser, H.; Salvatore, L.; Natali, M.L.; Campa, L.; Mahmoud, M.; Capobianco, L.; Sannino, A.; Madaghiele, M., Hyaluronic Acid for Advanced Therapies: Promises and Challenges. *Eur. Polym. J.* **2019**, *117*, 134-147.
13. Litwiniuk, M.; Krejner, A.; Speyrer, M.S.; Gauto, A.R.; Grzela, T., Hyaluronic Acid in Inflammation and Tissue Regeneration. *Wounds* **2016**, *28*, 78-88.
14. Fallacara, A.; Baldini, E.; Manfredini, S.; Vertuani, S., Hyaluronic Acid in the Third Millennium. *Polymers* **2018**, *10*, 701-736.
15. Fallacara, A.; Vertuani, S.; Panozzo, G.; Pecorelli, A.; Valacchi, G.; Manfredini, S., Novel Artificial Tears Containing Cross-Linked Hyaluronic Acid: An *In Vitro* Re-Epithelialization Study. *Molecules* **2017**, *22*, 2104-2116.
16. Manoukian, O.S.; Sardashti, N.; Stedmanm T.; Gailiunas, K.; Ojha, A.; Penalosa, A.; Mancuso, C.; Hobert, M.; Kumbar, S.G. Biomaterials for Tissue Engineering and Regenerative Medicine. In *Encyclopedia of Biomedical Engineering*, Narayan, R., Ed.; Elsevier: Oxford, 2019; pp 462-482.
17. Helenius, G.; Bäckdahl, H.; Bodin, A.; Nannmark, U.; Gatenholm, P.; Risberg, B., *In Vivo* Biocompatibility of Bacterial Cellulose. *J. Biomed. Mater. Res. A* **2006**, *76A*, 431-438.
18. Fu, L.; Zhang, J.; Yang, G., Present Status and Applications of Bacterial Cellulose-Based Materials for Skin Tissue Repair. *Carbohydr. Polym.* **2013**, *92*, 1432-1442.
19. Lin, Y.-K.; Chen, K.-H.; Ou, K.-L.; Liu, M., Effects of Different Extracellular Matrices and Growth Factor Immobilization on Biodegradability and Biocompatibility of Macroporous Bacterial Cellulose. *J. Bioact. Compat. Polym.* **2011** *26*, 508-518.

20. Sharnshina, J.L.; Berton, P.; Rogers, R.D., Advances in Functional Chitin Materials: A Review. *ACS Sustain. Chem. Eng.* **2019**, *7*, 6444-6457.
21. Kumar, P.; Vinitha, B.; Fathima, G., Bone Grafts in Dentistry. *J. Pharm. Bioall. Sci.* **2013**, *5*, S125-S127.
22. Chawla, S.P.; Kanatt, S.R.; Sharma, A.K. 8 - Chitosan. In *Polysaccharides*, Ramawat, K.; Mérillon, JM. Eds.; Springer, 2015; pp 219-246.
23. Yuan, Y.; Chesnutt, B.M.; Haggard, W.O.; Bumgardner, J.D., Deacetylation of Chitosan: Material Characterization and *In Vitro* Evaluation via Albumin Adsorption and Pre-Osteoblastic Cell Cultures. *Materials* **2011**, *4*, 1399-1416.
24. Anraku, M.; Gebicki, J.M.; Iohara, D.; Tomida, H.; Uekama, K.; Maruyama, T.; Hirayama, F.; Otagiri, M., Antioxidant Activities of Chitosans and its Derivatives in *In Vitro* and *In Vivo* Studies. *Carbohydr. Polym.* **2018**, *199*, 141-149.
25. Rinaudo, M.; Pavlov, G.; Desbrières, J., Influence of Acetic Acid Concentration on the Solubilization of Chitosan. *Polymer* **1999**, *40*, 7029-7032.
26. Ragelle, H.; Vandermeulen, G.; Preat, V.J., Chitosan-Based siRNA Delivery Systems. *J. Control. Release* **2013**, *172*, 207-218.
27. Knaul, J.Z.; Kasaai, M.R.; Bui, V.T.; Creber, K.A.M., Characterization of Deacetylated Chitosan and Chitosan Molecular Weight Review. *Can. J. Chem.* **1998**, *76*, 1699-1706.
28. Xu, Y.; Du, Y. Effect of Molecular Structure of Chitosan on Protein Delivery Properties of Chitosan Nanoparticles. *Int. J. Pharm.* **2003**, *250*, 215-226.
29. Nunthanid, J.; Puttipatkhachorn, S.; Yamamoto, K.; Peck, G.E., Physical Properties and Molecular Behavior of Chitosan Films. *Drug Dev. Ind. Pharm.* **2001**, *27*, 143-157.
30. Alameh, M.; Dejesus, D.; Jean, M.; Darras, V.; Thibault, M.; Lavertu, M.; Buschmann, M.D.; Merzouki, A., Low Molecular Weight Chitosan Nanoparticulate System at Low N:P Ratio for Nontoxic Polynucleotide Delivery. *Int. J. Nanomed.* **2012**, *7*, 1399-1414.

31. Rabea, E.I.; Badawy, M.E.-T.; Stevens, C.V.; Smagghe, G.; Steurbaut, W., Chitosan as Antimicrobial Agent: Applications and Mode of Action. *Biomacromolecules* **2003**, *4*, 1457-1465.
32. Kong, M.; Chen, X. G.; Xing, K.; Park, H. J., Antimicrobial Properties of Chitosan and Mode of Action: A State of the Art Review. *Int. J. Food Microbiol.* **2010**, *144*, 51-63.
33. Andres, Y.; Giraud, L.; Gerente, C.; Cloirec, P.L., Antibacterial Effects of Chitosan Powder: Mechanisms of Action. *Environ. Technol.* **2007**, *28*, 1357-1363.
34. Raafat, D.; von Bargen, K.; Haas A.; Sahl, H.-G., Insights into the Mode of Action of Chitosan as an Antibacterial Compound. *Appl. Environ. Microbiol.* **2008**; *74*, 3764-3773.
35. Zheng, L.-Y.; Zhu, J.-F., Study on Antimicrobial Activity of Chitosan with Different Molecular Weights. *Carbohydr. Polym.* **2003**, *54*, 527-530.
36. Suzuki, K.; Mikami, T.; Okawa, Y.; Tokoro, A.; Suzuki, S.; Suzuki, M., Antitumor Effect of Hexa-*N*-Acetylchitohexaose and Chitohexaose. *Carbohydr. Res.* **1986**, *151*, 403-408.
37. Tokoro, A.; Tatewaki, N.; Suzuki, K.; Mikami, T.; Suzuki, S.; Suzuki, M., Growth-Inhibitory Effect of Hexa-*N*-Acetylchitohexaose and Chitohexaose against Meth-A Solid Tumor. *Chem. Pharm. Bull. (Tokyo)* **1988**, *36*, 784-790.
38. Park, J.K.; Chung, M.J.; Choi, H.N.; Park, Y.I., Effects of the Molecular Weight and the Degree of Deacetylation of Chitosan Oligosaccharides on Antitumor Activity. *Int. J. Mol. Sci.* **2011**, *12*, 266-277.
39. Gibot, L.; Chabaud, S.; Bouhout. S.; Bolduc, S.; Auger. F.A.; Moulin, V.J., Anticancer Properties of Chitosan on Human Melanoma are Cell Line Dependent. *Int. J. Biol. Macromol.* **2015**, *72*, 370-379.
40. Rinaudo, M., Chitin and Chitosan: Properties and Applications. *Prog. Polym. Sci.* **2006**, *38*, 603-632.
41. Tan, H.; Ma, R.; Lin, C.; Liu, Z.; Tang, T., Quaternized Chitosan as an Antimicrobial Agent: Antimicrobial Activity, Mechanism of Action and Biomedical Applications in Orthopedics. *Int. J. Mol. Sci.* **2013**, *14*, 1854-1869.

42. Li, P.; Poon, Y.F.; Li, W.; Zhu, H.-Y.; Yeap, S.H.; Cao, Y.; Qi, X.; Zhou, C.; Lamrani, M.; Beuerman, R.W.; Kang, E.-T.; Mu, Y.; Li, C.M.; Chang, M.W.; Jan Leong, S.S.; Chan-Park, M.B., A Polycationic Antimicrobial and Biocompatible Hydrogel with Microbe Membrane Suctioning Ability. *Nat. Mater.* **2011**, *10*, 149-156.
43. Zhao, X.; Li, P.; Guo, B.L.; Ma, P.X., Antibacterial and Conductive Injectable Hydrogels Based on Quaternized Chitosan-Graft-Polyaniline/Oxidized Dextran for Tissue Engineering. *Acta Biomater.* **2015**, *26*, 236-248.
44. Huang, S.Q.; Wang, J.; Zhang, Y.; Yu, Z.M.; Qi, C.S., Quaternized Carboxymethyl Chitosan-Based Silver Nanoparticles Hybrid: Microwave-Assisted Synthesis, Characterization and Antibacterial Activity. *Nanomaterials*, **2016**, *6*, 1-22.
45. Holubnycha, V.; Kalinkevich, O.; Ivashchenko, O.; Pogorielov, M., Antibacterial Activity of In Situ Prepared Chitosan/Silver Nanoparticles Solution Against Methicillin-Resistant Strains of Staphylococcus aureus. *Nanoscale Res. Lett.* **2018**, *13*, 1-8.
46. Shariatnia, Z.; Mazloom, J.A., Chitosan-Based Hydrogels: Preparation, Properties and Applications. *Int. J. Biol. Macromol.* **2018**, *115*, 194-220.
47. Simões, D.; Miguel, S.P.; Ribeiro, M.P.; Coutinho, P.; Mendonça, A.G.; Correia, I.J., Recent Advances on Antimicrobial Wound Dressing: A Review. *Eur. J. Pharm. Biopharm.* **2018**, *127*, 130-141.
48. Kravanja, G.; Primožič, M.; Knez, Ž.; Leitgeb, M., Chitosan-Based (Nano)Materials for Novel Biomedical Applications. *Molecules* **2019**, *24*, 1960-1983.
49. Tang, F.; Lv, L.; Lu, F.; Rong, B.; Li, Z.; Lu, B.; Yu, K.; Liu, J.; Dai, F.; Wu, D.; Lan, G., Preparation and Characterization of N-Chitosan as a Wound Healing Accelerator. *Int. J. Biol. Macromol.* **2016**, *93*, 1295-1303.
50. Aameeduzzafar; Imam, S.S.; Abbas Bukhari, S.N.; Ahmad, J.; Ali, A., Formulation and Optimization of Levofloxacin Loaded Chitosan Nanoparticle for Ocular Delivery: *In Vitro* Characterization, Ocular Tolerance and Antibacterial Activity. *Int. J. Biol. Macromol.* **2018**, *108*, 650-659.

51. Jeong, Y.; Jin, S.G.; Kim, I.Y.; Pei, J.; Wen, M.; Jung, T.Y.; Moon, K.S.; Jung, S., Doxorubicin-Incorporated Nanoparticles Composed of Poly(ethylene glycol)-Grafted Carboxymethyl Chitosan and Antitumor Activity Against Glioma Cells *In Vitro*. *Colloid. Surface. B*. **2010**, 79, 149-155.
52. Yousefpour, P.; Atyabi, F.; Vasheghani-Farahani, E.; Mousavi, A.A.M.; Dinarvand, R., Targeted Delivery of Doxorubicin-Utilizing Chitosan Nanoparticles Surface-Functionalized with Anti-Her2 Trastuzumab. *Int. J. Nanomed.* **2011**, 6, 1977-1990.
53. Kim, J.H.; Kim, Y.S.; Kim, S.; Park, J.H.; Kim, K.; Choi, K.; Chung, H.; Jeong, S.Y.; Park, R.W.; Kim, I.S., Hydrophobically Modified Glycol Chitosan Nanoparticles Carriers for Paclitaxel, *J. Control. Release* **2006**, 111, 228-234.
54. Buyens, K.; De Smedt, S.C.; Braeckmans, K.; Demeester, J.; Peeters, L.; van Grunsven, L.A.; du Jeu, X.M.; Sawant, R.; Torchilin, V.; Farkasova, K., Liposome Based Systems for Systemic siRNA Delivery: Stability in Blood sets the Requirements for Optimal Carrier Design. *J. Control. Release* **2012**, 158, 362-370.
55. Min, K.H.; Park, K.; Kim, Y.-S.; Bae, S.M.; Lee, S.; Jo, H.G.; Park, R.-W.; Kim, I.-S.; Jeong, S.Y.; Kim, K., Hydrophobically Modified Glycol Chitosan Nanoparticles-Encapsulated Camptothecin Enhance the Drug Stability and Tumor Targeting in Cancer Therapy. *J. Control Release* **2008**, 127, 208-218.
56. Nimesh, S.; Thibault, M.M.; Lavertu, M.; Buschmann, M.D., Enhanced Gene Delivery mediated by Low Molecular Weight Chitosan/DNA Complexes: Effect of pH and Serum. *Mol. Biotechnol.* **2010**, 46, 182-196.
57. Thanou, M.; Florea, B.; Geldof, M.; Junginger, H.; Borchard, G., Quaternized Chitosan Oligomers as Novel Gene Delivery Vectors in Epithelial Cell Lines. *Biomaterials* **2002**, 23, 153-159.
58. Strand, S.P.; Issa, M.M.; Christensen, B.E.; Vårum, K.M.; Artursson, P., Tailoring of Chitosans for Gene Delivery Novel Self-Branched Glycosylated Chitosan Oligomers with Improved Functional Properties. *Biomacromolecules* **2008**, 9, 3268-3276.

59. Ping, Y.; Liu, C.; Zhang, Z.; Liu, K.L.; Chen, J.; Li, J., Chitosan-Graft-(PEI- $\beta$ -Cyclodextrin) Copolymers and Their Supramolecular PEGylation for DNA and siRNA Delivery. *Biomaterials* **2011**, *32*, 8328-8341.
60. Wang, J.; Tao, X.; Zhang, Y.; Wei, D.; Ren, Y., Reversion of Multidrug Resistance by Tumor Targeted Delivery of Antisense Oligodeoxynucleotides in Hydroxypropyl-Chitosan Nanoparticles. *Biomaterials* **2010**, *31*, 4426-4433.
61. Kim, S.; Bedigrew, K.; Guda, T.; Maloney, W.J.; Park, S.; Wenke, J.C.; Yang, Y.P., Novel Osteoinductive Photo-Cross-Linkable Chitosan-Lactide-Fibrinogen Hydrogels Enhance Bone Regeneration in Critical Size Segmental Bone Defects. *Acta Biomater.* **2014**, *10*, 5021-5033.
62. Liu, L.; Zhou, C.; Xia, X.; Liu, Y., Self-Assembled Lecithin/Chitosan Nanoparticles for Oral Insulin Delivery: Preparation and Functional Evaluation. *Int. J. Nanomedicine* **2016**, *11*, 761-769.
63. Sun, X.; Jia, P.; Zhe, T.; Bu, T.; Liu, Y.; Wang, Q.; Wang, L., Construction and Multifunctionalization of Chitosan-Based Three-Phase Nano-Delivery System. *Food Hydrocoll.* **2019**, *96*, 402-411.

## **Chapter 2 | Dual-Responsive Targeted rSML-A Delivery System Utilizing a Chitosan Scaffold**

### **Abstract**

Cancer is one of the major public health problems worldwide, and it has landed top in principal causes of death in Singapore for the past decade. Many bioactive compounds used in pharmacotherapy are either too potent to be administered or exhibit unwanted side-effects which limits their clinical application. This calls for the need to enhance selectivity, also known as active-targeting, in addition to passive accumulation in the tumor cells due to angiogenesis. Biomacromolecules such as proteins, offer a whole new therapeutic opportunity to combat against this deadly disease that small molecular drug could not. Till date, the clinical development of bioactive proteins, as potential drug candidates, has been hardly making progress devoid of a strategy for the proteins' efficient and targeted cytosolic delivery. The challenge mainly stemmed from their poor physiochemical stability and little to no permeability across the cellular membranes. A robust and viable delivery strategy entails adequate protection of the protein, which is able to cover the whole journey of circulation until reaching a target cell and releasing the cargo in its native form. A biodegradable and biocompatible chitosan-based delivery system for the targeted cytosolic delivery of a protein of interest, rSML-A (recombinant Singapore Mistletoe Lectin A-chain), is reported herein. In particular, the viability of this targeted system has been demonstrated through straightforward synthetic routes and uptake of the final conjugate into the sialic-acid overexpressed cells (MDA-MB-342) selectively against the control (NIH3T3). The design of a combination of highly specific components was substantiated by promising biological activities observed in this study, and provides an excellent platform for future applications in protein delivery.

## 2.1 | Introduction

### 2.1.1 | General Overview of Cancer

Cancer is a term for diseases that involves cells growing abnormally such as uncontrolled cell growth and retarded cell death. It is one of the major public health problems worldwide, especially when metastatic cancerous cells are able to spread and invade to other parts of the body, such as bones, lungs, brain, and greatly deteriorate our immune system.<sup>1</sup> In Singapore, it has landed top in principal causes of death for the past decade (see **Figure 2.1**).<sup>2</sup>

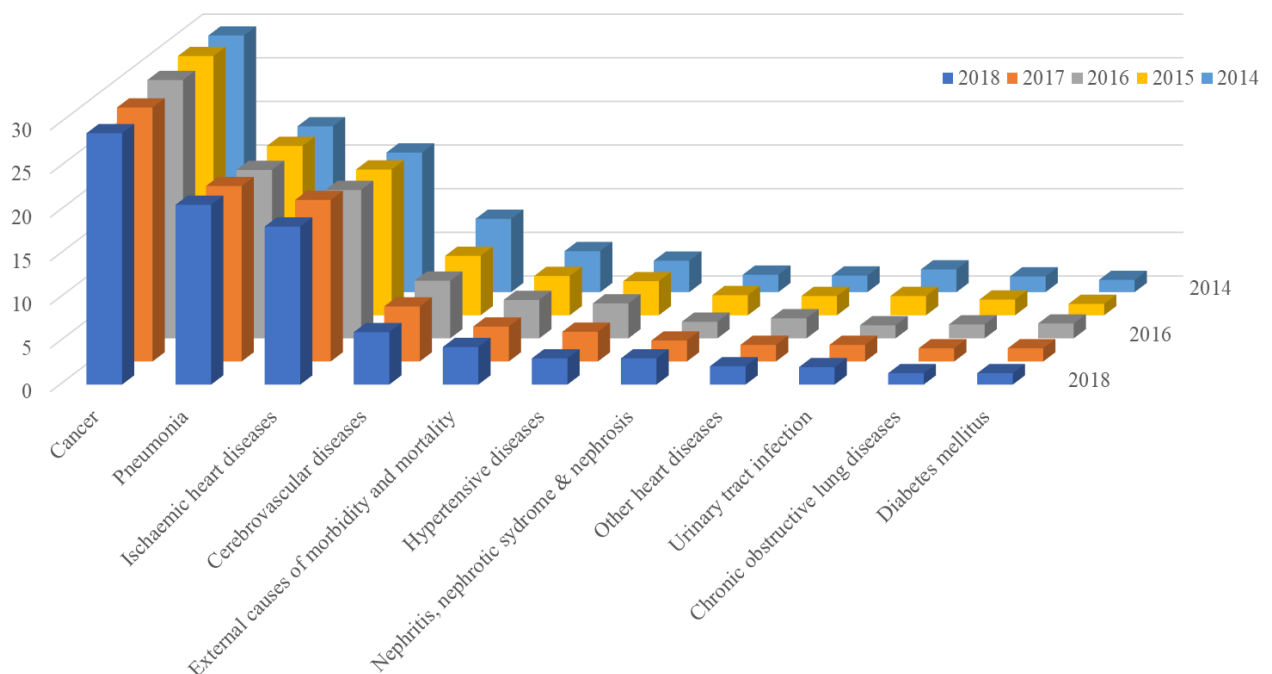


**Figure 2.1** | A chart representing top 10 principal causes of death in Singapore from 2014 to 2018, shown as a percentage of total number death occurred during the respective years. Numerical values are obtained from ref. 2.

Curing cancer completely has always been a very difficult task, as the current biomedical technology allows diagnosis after they have grown to at least the size of a grape, and many would only notice when the symptoms worsened drastically often after metastasis occurred. Removal of the grown tumor involves surgery, which possessed great amount of risks. Hence, non-surgical treatment by making use of nanotechnology is much preferred. In addition, the choice of a suitable



drug to combat cancer is very limited in conventional chemotherapeutics, as adverse effects on patients have to be taken into account. Moreover, acquired or intrinsic multi-drug resistance (MDR) further complicates the situation.

Many bioactive compounds used in pharmacotherapy are either too potent to be administered or exhibit unwanted side-effects which limits their clinical application, which stems from their inability to differentiate between cancer cells and healthy cells.<sup>3</sup> These drugs are usually accumulated passively around the tumor site due to 'leaky' tumor vasculature and retained there as a result of impaired lymphatic drainage.<sup>4</sup> This increased in permeability of the tumor vasculature resulted from the occurrence of sprouting angiogenesis, in which the vessels dilate in response to more vascular endothelial growth factor (VEGF), and subsequent chaotic formation of more vessels to support the rapid growth of the tumor.<sup>5</sup>

Innumerable investigations have been carried out to understand the disease better. Many discoveries made have established that cancerous cells possess unique cellular characteristics in accordance to their respective types, and that these is very useful in differentiating them from the healthy cells.<sup>6-9</sup>

### **2.1.2 | Proteins as Drugs, such as Mistletoe Lectin, for Cancer Therapeutics**

Biomacromolecular drugs, sometimes known as biopharmaceutical drugs, such as nucleic acids and proteins which acts on transcriptional pathways offer new modalities for currently untreatable diseases including cancer. As such, they hold great potentials and promises as novel therapeutics in this area. Protein drugs has novel advantages in cancer therapeutics as compared to small molecular drugs and gene therapy. First of all, they have high potency and specificity in tackling cancer via direct or indirect mechanism.<sup>10-12</sup> Some proteins are able to interact and interfere with definitive signalling pathways, thereby inducing direct cell death of cancer cells. Others can either inhibit tumors by stimulating immuno-response or modulating microenvironment of tumors. Secondly, notably lower IC<sub>50</sub> values are often observed amongst

protein drugs as compared to small molecular drugs, due to their high specificity and potency.<sup>13</sup> Thirdly, they often possess little to no genotoxicity compared to gene therapy, as their mode of actions are based in downstream regulation and do not pose the risk of altering genetic makeup.<sup>14-</sup>

15

Ribosome-inactivating proteins a class of proteins well known for interfering with protein biosynthesis and they are highly potent cytotoxins, and they are considered as anticancer therapeutics, from the clinical point-of-view.<sup>16-17</sup> A particular protein which has caught our attention belongs to this class of highly potent protein, known as mistletoe (*Viscum album*) lectin I (ML-I). It is heterodimeric glycoprotein consisting of a 29 kDa-A-chain and a 34 kDa-B-chain connected by a disulfide bridge (see **Figure 2.2a**).<sup>18</sup> In a study conducted by Bantel *et al.*, it was found that ML-I activates caspase-8/FLICE independently of death receptor signalling and enhances anticancer drug-induced apoptosis at low concentration.<sup>19</sup> A recent study by Kok *et al.*, they demonstrated that which are key steps in cellular uptake of ML-I via high content imaging.<sup>20</sup> First, ML-I interacts with the glycan on cell surface, and both clathrin-dependent and independent internalisation occurs. Next, it is redirected from the endocytic vesicles to Golgi apparatus, and subsequently rerouted to the ER. In addition, they have also demonstrated the pro-apoptotic activity of ML-I, which highlights its potential to eradicate multidrug resistant tumor cells. Furthermore, ML-1 was demonstrated to be safe to healthy cells and without further enhancement of the tumor in long-term treatment.<sup>21</sup> ML-1 was reported to exhibit anticancer properties, and further investigations showed that it stemmed from the A-chain by catalysing irreversible hydrolysis of eukaryotic 28S rRNA's *N*-glycosidic bond at adenine 4324 located in  $\alpha$ -sarcin/ricin loop, thereby inactivating the ribosome and inhibiting crucial protein synthesis (see **Figure 2.2b**), while B-chain is responsible for binding to sugar and enabling the entry of the protein via receptor-mediated endocytosis.<sup>22-23</sup> In another recent study by Lee *et al.*, they observed the down-regulation of c-Myc expression upon treating the mice with ML-I, and that proliferation of liver cancer cells was inhibited.<sup>24</sup>

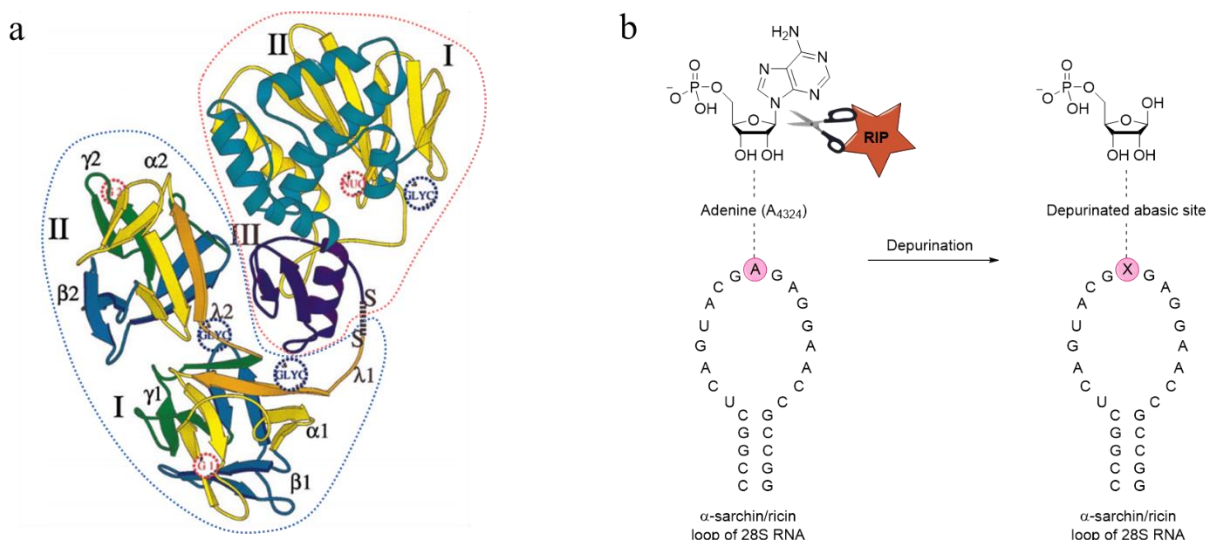


**Figure 2.2** | (a) Cartoon plot of mistletoe lectin consisting of A-chain (circled in red) and B-chain connected (circled in blue) by a disulfide bridge. Reprinted with permission from ref. 18. Copyright (2019), Elsevier. (b) A schematic illustration on the mode of action of RIP (indicated as orange star). RIP recognizes and depurinates adenine (A<sub>4324</sub>) in 28S rRNA of the large ribosomal subunit.

Despite their advantages and potential therapeutic effects, difficulties faced in the isolation and purification of these biologically active proteins from plant extracts slowed down the discovery. Emergence of recombinant protein techniques for therapeutics not only countered the difficulties raised previously, it has also greatly expanded the availability and the extensiveness of effective treatment against a broad range of diseases, including cancer.<sup>25-26</sup>

Our collaborator, Nguyen from Yoon Ho Sup's group., had successfully isolated the recombinant A-chain of the Singapore mistletoe lectin (*viscum ovalifolium*).<sup>27</sup> In their study, they demonstrated that ribosome-inactivating activity of the recombinant Singapore mistletoe lectin A-chain (rSML-A) (using a commercially available cationic lipid-based carrier, BioPORTER®, as the delivery agent) is comparable to SML, with a relatively potent IC<sub>50</sub> value of  $4.87 \pm 0.01$  nM (see **Figure 2.3**). In addition, he carried on with cytotoxicity test on two different cancer cell lines, HeLa (human cervical cancer) cells and MCF-7/caspase-3 positive (human breast cancer) cells, and showed that the rSML-A is the one possessing the cytotoxic activity; and was comparable to the protein as a whole (see **Figure 2.4**).

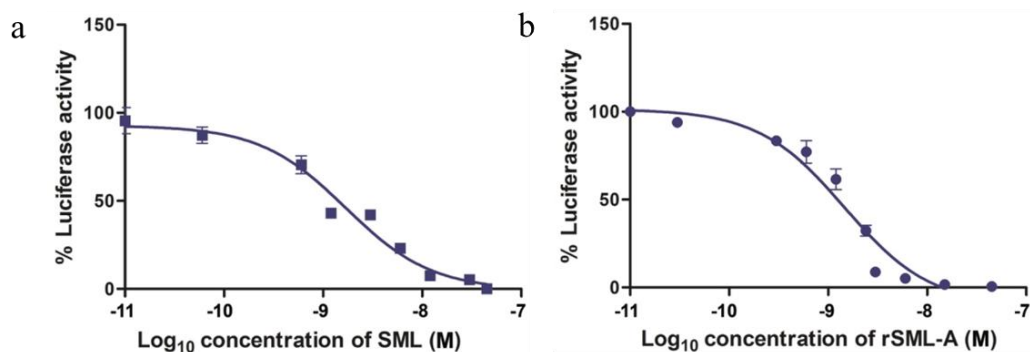


**Figure 2.3** | (a) Ribosome-inactivating activity of Singapore Mistletoe Lectin (SML) determined by the degree of inhibition of luciferase translation in a rabbit reticulocyte system. IC<sub>50</sub> is  $2.81 \pm 0.03$  nM. (b) Ribosome-inactivating activity of rSML-A determined by the degree of inhibition of luciferase translation in a rabbit reticulocyte system. IC<sub>50</sub> is  $4.87 \pm 0.01$  nM. Adapted from ref. 27.

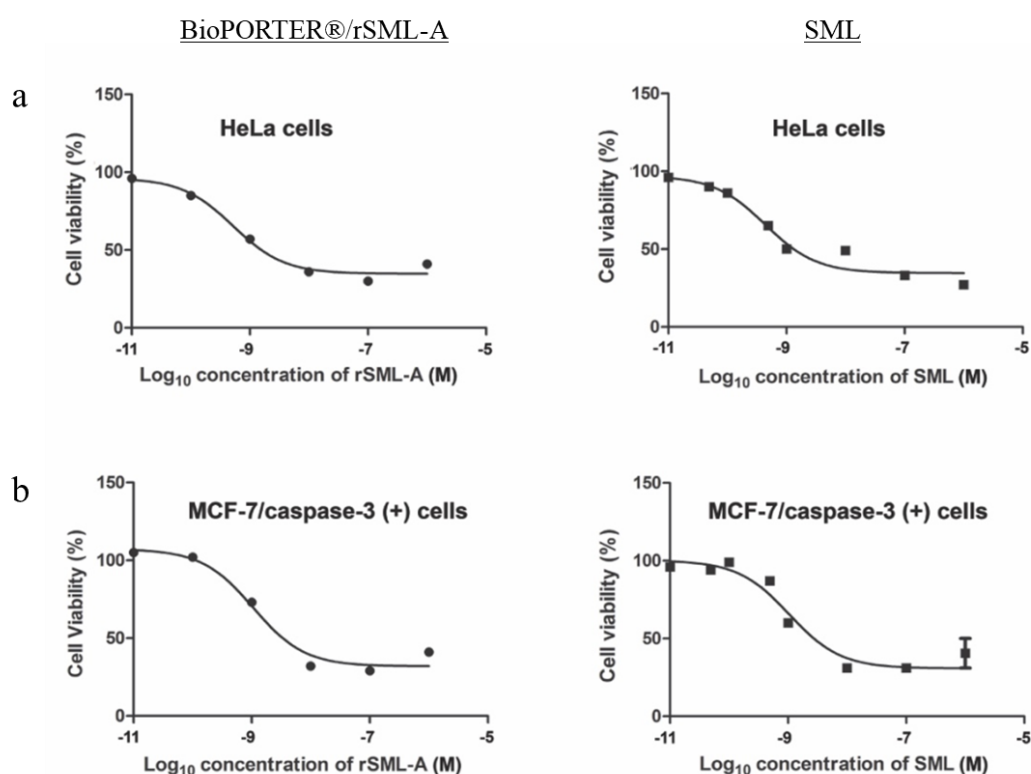


**Figure 2.4** | Cytotoxic effect of BioPORTER®/rSML-A and SML on (a) HeLa cancer cells and (b) MCF-7/caspase-3 positive cells. Adapted from ref. 27.

### 2.1.3 | Challenges Faced in Delivery of Bioactive Biomacromolecules

To classify as a drug candidate, it has to meet the minimum of the numerous requirements, such as efficacy, safety, potency, chemical stability, as well as pharmaceutical developability.<sup>28</sup> These multiparametric requirements often result in bioactive proteins as drug candidates, to be

dropped out from the development pipeline due to various reasonings such as lack of stability, prone to degradation, low efficacy resulting from inability to cross cell membranes, toxicity at non-target site.<sup>29</sup>

This calls for the need to enhance selectivity, also known as active-targeting, in addition to passive accumulation in the cancer cells. As mentioned in earlier, passive-targeting stems from permeable vasculature in which drugs or nanoparticle-drug complexes are able to leak out and passively accumulate around the tumor site (see **Figure 2.5**).<sup>30</sup> Thus, by incorporating a targeting ligand on the NPs, it will direct them towards receptors expressed on cancer cells. Drugs can be released from the nanoparticle (i) in close proximity; (ii) after binding onto receptor on the membrane; or (iii) upon internalisation into the cell.

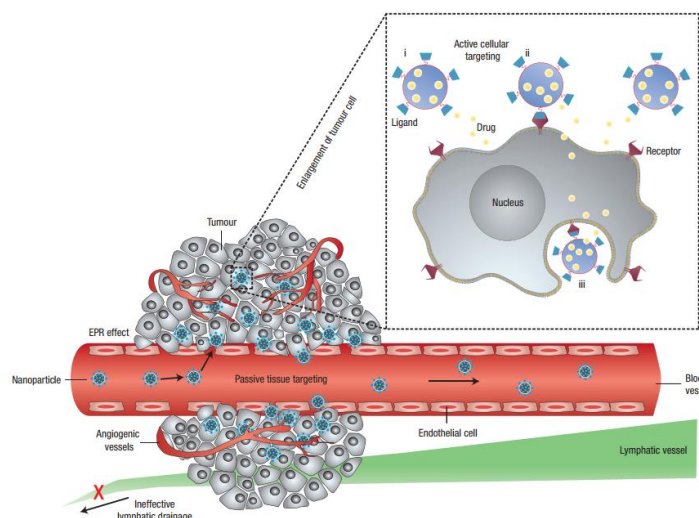


**Figure 2.5** | Schematic illustration of passive and active targeting of nanoparticle-drug complexes. The endothelial cells are spaced further apart from each other, resulting in the formation of a more permeable vessel. Upon which, nanoparticles are able to passively accumulate and be retained around the tumor site. Active targeting occurs when the nanoparticles are modified with targeting ligands which directs them towards receptors on cancer cells for binding. Reprinted with permission from ref. 30. Copyright (2019), Nature.

Although a myriad of nano-systems have been developed in the past two decades to achieve intracellular delivery of these bioactive macromolecules, many have their shortcomings such as absence of active-targeting ligands, high cytotoxicity and/or immunogenic to healthy cells, rapid renal clearance, unable to avoid the macrophages attacks before reaching the target site, and/or

most importantly, the inability to escape the endosome before it fuses with lysosomes that destroys the bioactive macromolecules (see **Figure 2.6** for summary of bottlenecks encountered).<sup>31-35</sup>

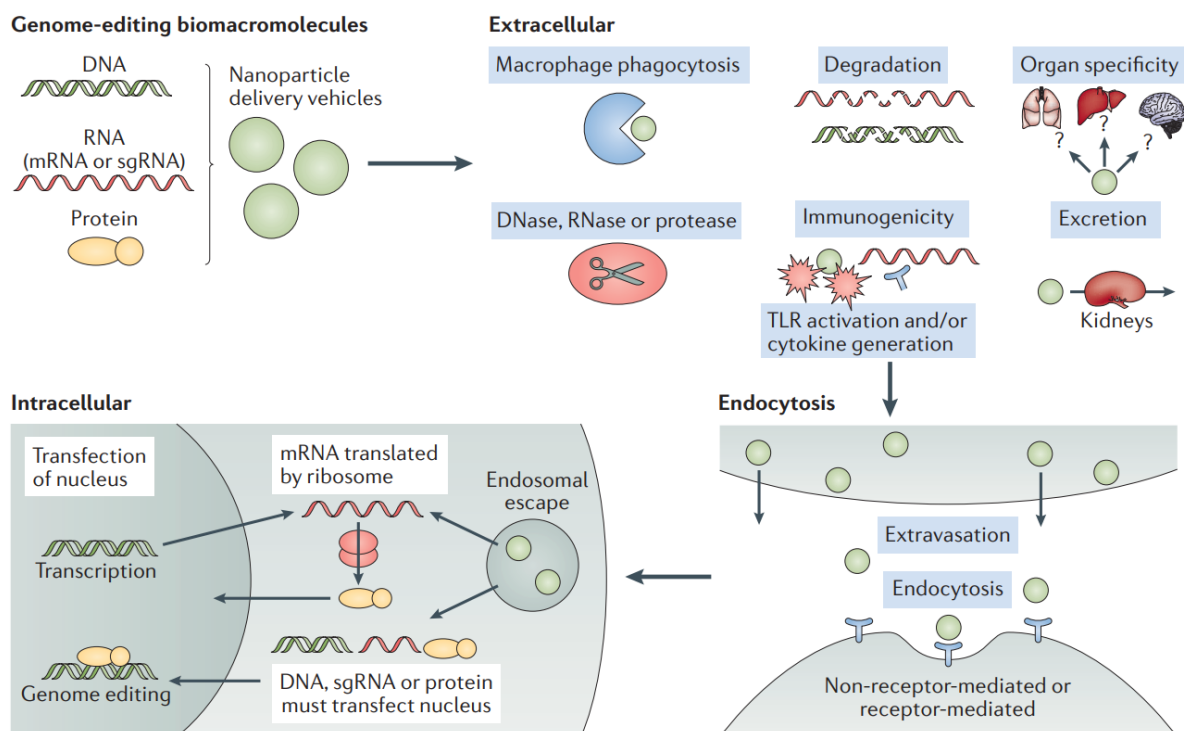


**Figure 2.6** | Schematic illustrations of bottlenecks encountered for delivery of biomacromolecules. Reprinted with permission from ref. 35. Copyright (2019), Nature.

As such, to maximize the therapeutic potential of the bioactive proteins, one would need to take into account of numerous factors in designing a safe nano-system to effectively deliver them and ensure their functionality.

## 2.2 | Proposed Design and Rationale

Till date, the clinical development of bioactive proteins, as potential drug candidates, is hardly making progress devoid of a strategy for the proteins' efficient and targeted cytosolic delivery. The challenge mainly stemmed from their poor physiochemical stability and little to no permeability across the cellular membranes.

A robust and viable delivery strategy entails adequate protection of the protein, which is able to cover the whole journey of circulation until reaching a target cell and releasing the cargo in its native form. To combat the challenges mentioned, we came up with a proposed design of a dual responsive chitosan-based delivery system (see **Figure 2.6**). Advantages of chitosan has been discussed previously, and the versatility of the amino group available allow us to tailor our needs with desired functionality. High MW glycol chitosan (DD > 85%) was used as a scaffold in the design as it provides better solubility in aqueous medium as compared to chitosan.

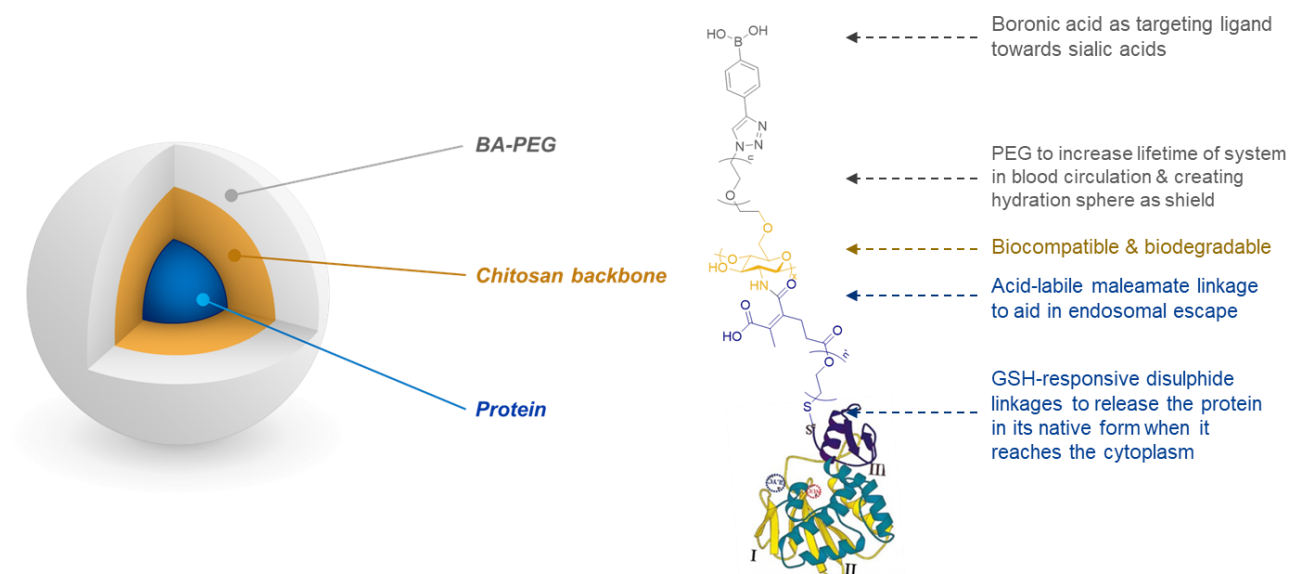


**Figure 2.7** | Our design of rSML-A delivery system. It comprises of biodegradable and biocompatible glycol chitosan backbone modified with a boronic acid targeting ligand and a disulfide linker for covalent conjugation to rSML-A.

### 2.2.1 | Polyethylene Glycol (PEG) as Hydration Shield

In a pioneering work conducted by Abuchowski et al. about 40 years ago, they demonstrated that the plasma half-life of bovine serum albumin increased when they are conjugated to PEG.<sup>36-37</sup> They have also noted an increase in solubility of the protein-polymer complex due to PEG conjugation. Incorporation of poly(ethylene glycol) segment into the system not only aid in preventing recognition by macrophages of the reticuloendothelial system (RES), it helps to increase the lifetime of the system in blood circulation, thereby allowing the systems to accumulate at the targeted site passively; also known as enhanced permeability and retention (EPR) effect.<sup>38</sup> That is because by conjugating PEG onto the protein, it provides steric repulsion, as well as an hydration shield, which helps to reduce immunogenicity of the agent, degradation by proteolytic enzymes, opsonization, and clearance by the phagocyte system.<sup>39-40</sup>

### 2.2.2 | Active Targeting with Boronic Acid

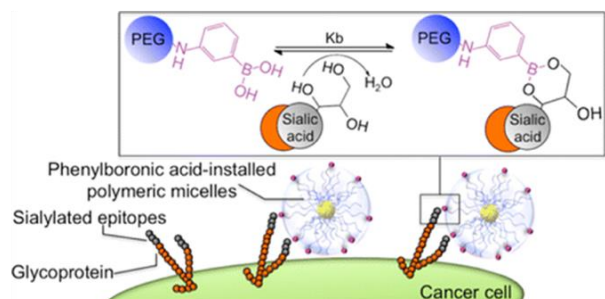
Boronic acids have natural affinity towards sialylated epitopes, such as glycans containing *N*-acetylneuraminic acid (Neu5Ac), which are overexpressed in most of the cancer cells.<sup>41-42</sup> In addition, a study conducted by Kannagi *et al.* showed that the percentage increase in the expression of sialylated antigens is closely related to cancer progression, and the overexpression of glycans such as Sialyl-Lewis<sup>x</sup> and Sialyl-Lewis<sup>a</sup> is the key indication of likelihood of metastases.<sup>43</sup>

In a study conducted by Kataoka *et al.*, they demonstrated that phenylboronic acid modified polymer has much higher binding affinities towards sialic acid compared to other sugars at physiological pH (7.4) and slightly more acidic environment at pH 6.5 (see **Figure 2.8**).<sup>44</sup> They found that the  $pK_a$  of the polymer conjugated with phenylboronic acid ( $pK_a$  9.7) was much higher than that of physiological conditions, which signifies that a large percentage of the trigonal phenylboronic acid at pH 7.4 remains undissociated to sialic acid. Furthermore, phenylboronic acid has two favourable conformations – trigonal planar and tetrahedral – as opposed to non-



aromatic boronates, thereby increasing its affinity for sugars to allow additional B-N or B-O stabilization.<sup>45-46</sup>

a



b

**Table 1. Binding Constants and Rate Coefficients of PBA-PEG-*b*-PLGA and Sugars in Phosphate Buffer pH 7.4 and 6.5<sup>a</sup>**

sugar		pH		$K_b$ 6.5 / $K_b$ 7.4
		7.4	6.5	
glucose	$K_b$ ( $M^{-1}$ )	1.71	0.39	0.29
	$k_q \times 10^{-9}$ ( $M^{-1} s^{-1}$ )	0.18	0.04	—
mannose	$K_b$ ( $M^{-1}$ )	3.95	0.70	0.17
	$k_q \times 10^{-9}$ ( $M^{-1} s^{-1}$ )	0.41	0.07	—
galactose	$K_b$ ( $M^{-1}$ )	5.11	1.11	0.21
	$k_q \times 10^{-9}$ ( $M^{-1} s^{-1}$ )	0.53	0.11	—
NeuSAc (SA)	$K_b$ ( $M^{-1}$ )	12.3	12.7	1.03
	$k_q \times 10^{-9}$ ( $M^{-1} s^{-1}$ )	1.28	1.32	—
MeNeuSAc (Me-SA)	$K_b$ ( $M^{-1}$ )	3.40	6.00	1.76
	$k_q \times 10^{-9}$ ( $M^{-1} s^{-1}$ )	0.35	0.62	—

<sup>a</sup>Determined by steady-state fluorescence quenching measurements;  $\tau_0$  (ns) at pH 7.4 was  $9.62 \pm 49.2$  and at pH 6.5 was  $9.67 \pm 49.2$ .

**Figure 2.8 | (a)** Schematic illustration of phenylboronic acid-based micelle in targeting sialic acids, and **(b)** compilation of its binding affinities towards different sugars such as glucose, mannose, galactose, SA, and Me-SA. Reprinted with permission from ref 44. Copyright (2019), American Chemical Society.

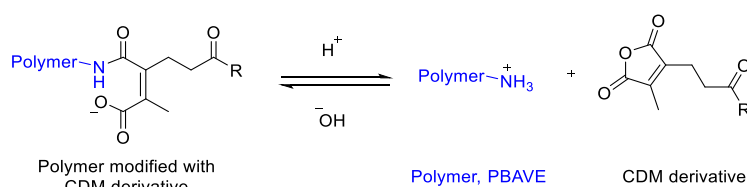
Hence, as an alternative to expensive targeting ligands such antibodies and cell-penetrating peptides, we drawn in by the cost-effectiveness and versatility of phenyl boronic acid as an targeting ligand. We hypothesized that by linking phenyl boronic acid onto our polymeric sugar backbone with a PEG spacer, the hydrophobic core (protein) will result in the self-assembly of the nanoparticle, in which the boronic acids are readily available for binding with sialic acids via multivalency effect. Upon binding, and subsequently brought close enough to the membrane, internalisation for the delivery system will be triggered.

### 2.2.3 | Acid-labile Linkage to Aid in Endosomal Escape

To address one of the major challenges in the nano-carriers systems which would be its ability to escape from the endosome, especially when the cargo to deliver is a biomacromolecule. As a result, the general pathway of internalization would be via endocytosis, in which left unattended will result in degradation of the biomacromolecule cargo upon fusion of late endosomes with

lysosomes. Thus, to avoid this outcome, a pH-sensitive linkage can be attached to our potential “proton-sponge” backbone.

This can be done by introducing an acid-labile maleamate bonds, which can aid in endosomal escape (see **Figure 2.8**).<sup>47</sup> This bond can be formed by reacting the free amino groups of the polymer with carboxylated dimethyl maleic acid (CDM). Cleavage of this acid-labile bond in slightly more acidic endosome would activate the polymer’s innate endosomolytic capabilities by acting as a proton sponge. Subsequent increament in the influx of ions as well as water molecules would lead to swelling, followed by bursting of the endosomes before degradation by lysosomes upon fusion.



**Scheme 2.1** | Schematic illustration of polymer modified with CDM derivative under acidic (right) and basic (left) conditions.

#### 2.2.4 | GSH-Responsive Linkage

In addition, installing a disulfide bond linkage between the protein and polymer-backbone allows freeing of the proteins upon cleavage by the endogenous glutathione (GSH), a tripeptide (H- $\gamma$ -L-Glu-L-Cys-L-Gly-OH), present in the cytosol. It was reported that the GSH levels in cancerous cells are 100- to 1000-fold higher than that of the extracellular environments.<sup>48-49</sup> This usage of redox potential stimuli mechanism, as a result of passive accumulation, has been employed in numerous gene delivery.

## 2.3 | Results and Discussion

### 2.3.1 | Initial Design: Synthesis, Biological Assays, and Limitations Encountered

The initial design utilised a commercially available disulfide linker, sulfo-LC-SPDP, which acts as a bridge between the chitosan backbone and rSML-A (see **Figure 2.9**). Acid-labile CDM group was incorporated such that at acidic endosomal pH, ring closure of maleic anhydride ring will be instigated, and the free amino groups on chitosan will act as proton sponge for endosomal escape mechanism to proceed.

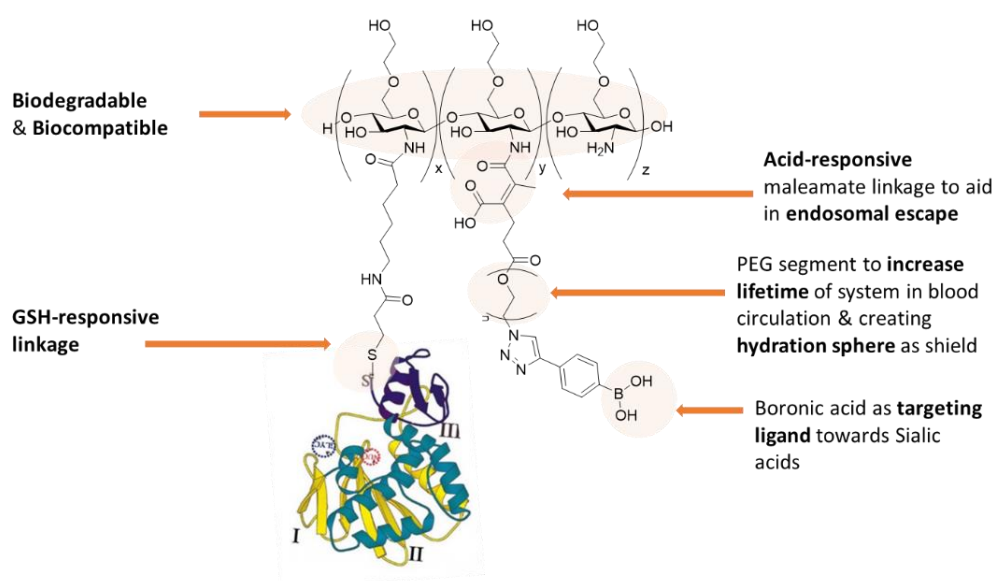
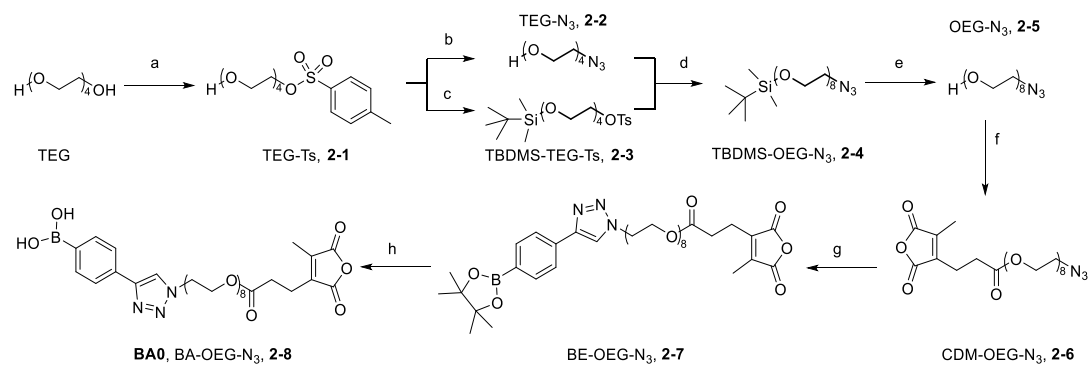


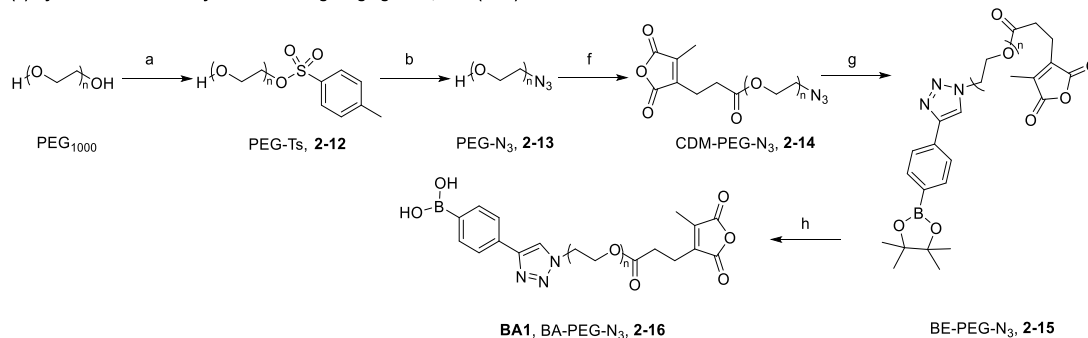
**Figure 2.9** | Schematic illustration of our initial design of rSML-A delivery system.

The boronic acid linker was synthesized as shown in **Scheme 2.2**, with different lengths of PEG (categorized by number of repeating units of the ethylene oxide segment) acting as spacer between boronic acid and carboxy dimethylmaleic anhydride (CDM). Thereafter, it was conjugated onto the glycol chitosan (GC), followed by attachment of the commercially available sulfo-LC-SPDP linker, as shown in **Scheme 2.3**. The product obtained will be termed as GC-BA-SPDP, as both the BA and SPDP linker are connected at the amino end of chitosan. Products obtained after each step was dialysed for three days.

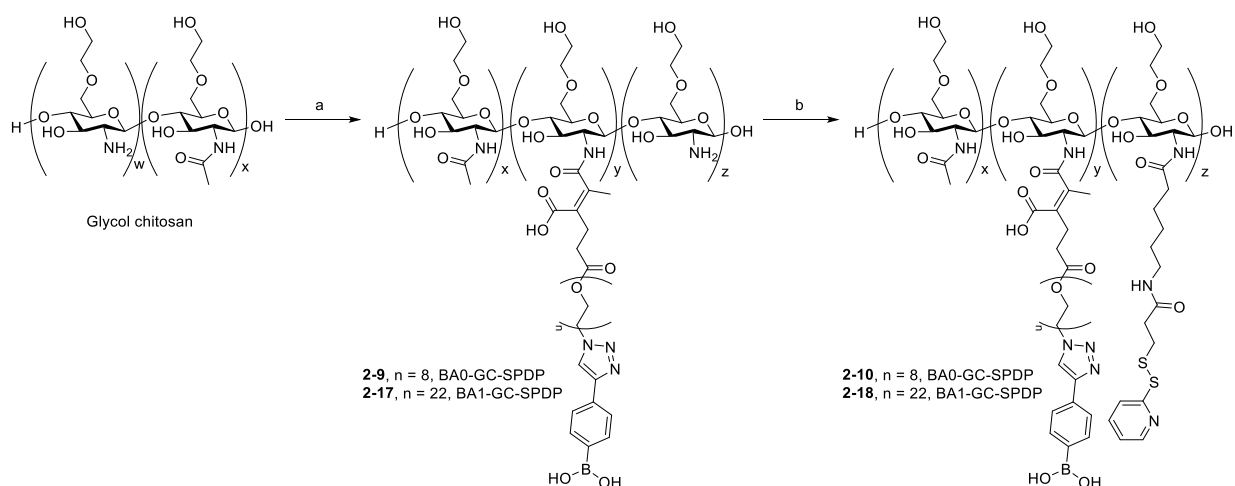
(a) Synthetic scheme of synthesis for targeting ligand 1, BA0 (2-8):



(a) Synthetic scheme of synthesis for targeting ligand 2, BA1 (2-16):

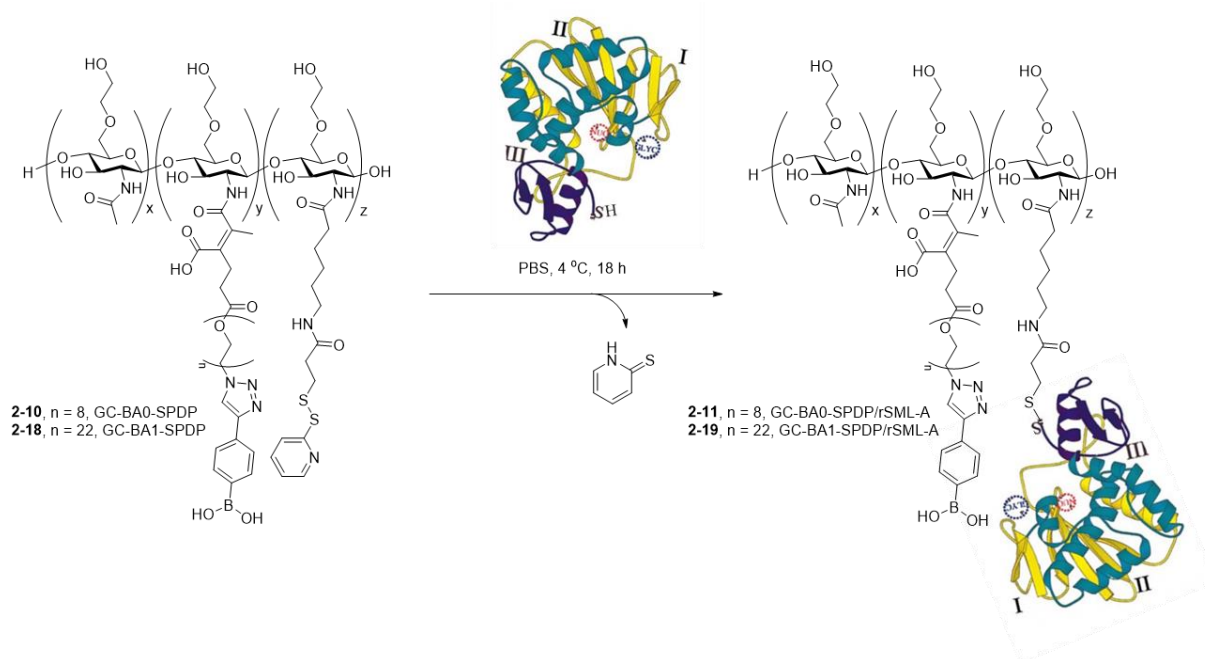


**Scheme 2.2** | Synthesis of the boronic acid targeting ligand with, (a) octaethylene glycol (OEG) spacer and (b) PEG<sub>1000</sub>. Reactions and conditions: a, tosyl chloride, NaOH (1.5 equiv.), THF/H<sub>2</sub>O; b, sodium azide (2 equiv.), ACN; c, TBDMS-Cl (1.1 equiv.), NEt<sub>3</sub> (1.1 equiv.), DMAP (0.1 equiv.), DCM; d, NaH (1.1 equiv.), DMF; e, TBAF (3 equiv.), THF; f, carboxy dimethylmaleic anhydride (1.5 equiv.), HATU (1.5 equiv.), DIPEA (1.5 equiv.), DCM; g, 4-ethynylphenylboronic acid pinacol ester, copper iodide (0.05 equiv.), DIPEA (3 equiv.), DCM; h, NaIO<sub>4</sub> (5 equiv.), NH<sub>4</sub>OAc (5 equiv.), acetone/H<sub>2</sub>O.



**Scheme 2.3** | Assembly of the protein carrier. Reactions and conditions: a, DIPEA (3 equiv.), DMAP (0.4 equiv.), DMSO; b, sulfo-LC-SPDP (0.5 equiv.), PBS/DMSO (pH 7.6).

Thereafter, the lectin was conjugated onto the GC-BA0-SPDP in different weight ratios, (polymer/rSML-A) 5:1, 20:1, 40:1 (see **Scheme 2.3** for reaction scheme). Unreacted rSML-A were removed by ultrafiltration with a 30 kDa filter membrane via centrifugation at 10,000 X g for 8 minutes. The lectin, rSML-A, was obtained from a collaborator at the courtesy of Professor Yoon Ho Sup. The purity of the protein (rSML-A and rKML-A) obtained from the collaborator was checked by SDS-PAGE (see **Figure 2.10**) after being thawed from 3 to 4 years of deep-freeze. A single band slightly above 25 kDa mark indicates that the protein is still pure (with some being dimerized as can be seen slightly above the 50 kDa mark). Meanwhile, the recombinant A-chain of Korean mistletoe lectin (KML-A) was not pure, indicated by appearance of two close bands in very close proximity, and hence, was not used in the studies.



**Scheme 2.4** | Synthesis of GC-BA-SPDP/rSML-A conjugate with different lengths of PEG segment on GC-BA-SPDP. The protein was treated with TCEP at 4 °C in PBS for an hour and filtered by 3 kDa membrane prior to conjugation. The protein concentrate was collected and added to the PBS mixture, consisting of respective polymers, GC-BA-SPDP, for 18 hours at 4 °C.

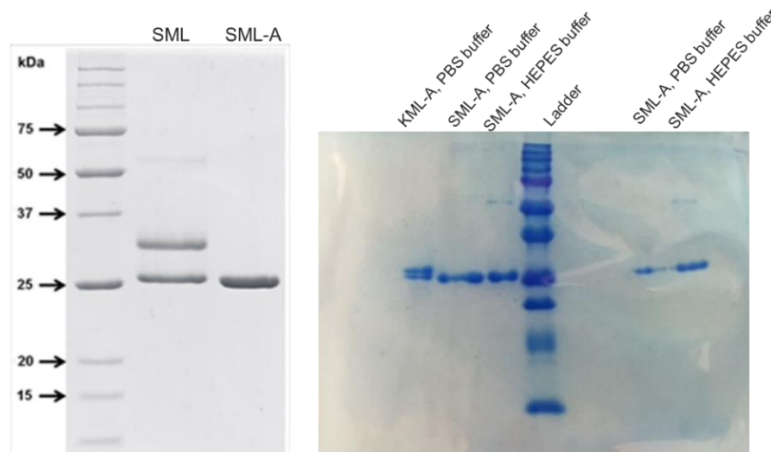


**Figure 2.10** | Gel image of the SML and SML-A (left), adapted from ref. 27, and the gel image of the recombinant A-chains obtained from collaborator, after being thawed from deep-freeze (right).

Apoptosis assay was conducted, since our hypothesis was that the delivery system would help in internalising the rSML-A, and subsequently releasing it in its native form, which in turn would inhibit protein synthesis and result in cell apoptosis and cell death. MDA-MB-231 (ER $\alpha$ -, higher expression of sialic acids), a breast cancer cell line, was chosen as the target of interest and treated with the polymer-protein conjugates for 48 hours incubation. The cells were then harvested, washed with PBS and stained with Annexin V/PI, according to the protocol supplied by the manufacture. Thereafter, the stained cells were analysed by flow cytometry, and the results obtained are show in **Figure 2.11**.

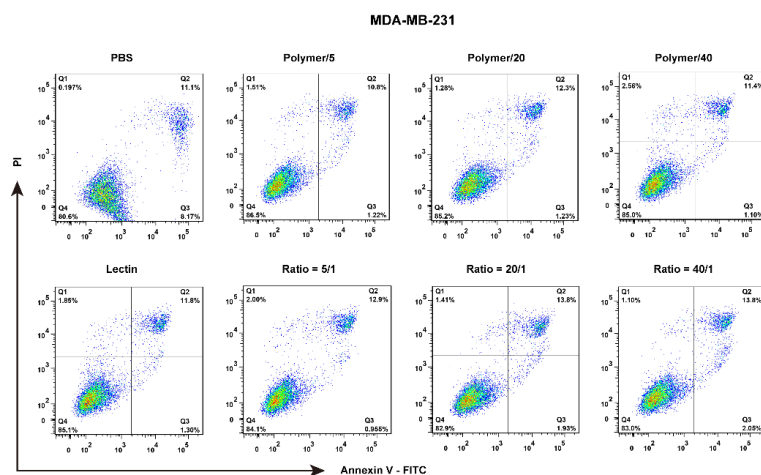


**Figure 2.11** | Flow cytometry results depicting graphs of fluorescence intensity of PI against Annexin V – FITC channel for MDA-MB-231 after 48 hours incubation with **2-11**, GC-BA0-SPDP/rSML-A. Q2 depicts the percentage of dead cells, while Q3 gives the percentage of cells in early apoptosis stage, and Q4 shows the percentage of live cells.

The results obtained from flow cytometry showed that there was not a significant difference despite increasing amount of protein added. This showed that maximum amount of protein has been conjugated at the highest polymer/protein ratio (40:1), and the resultant killing effect were similar. Although the percentage of cells in Q2 and Q3 combined were only slightly higher in polymer-protein conjugates as compared to polymer alone, this showed that a small amount of protein has been delivered. The results implied that induction of apoptotic stage may require a time period of longer than 12 hours of incubation. We hypothesised that steric hindrance resulted from conjugating the 29 kDa protein onto the chitosan backbone result in the targeting ligands (CDM-OEG-BA0) being buried deep within, and thereby obstructing the receptor-mediated endocytosis process.

Thereafter, the effect of longer targeting ligand (PEG<sub>1000</sub> with  $n \approx 22$ ) was studied in a smaller setting by conducting cell cytotoxicity studies and increasing the incubation period. The desired polymeric targeting ligands were synthesized according to **Scheme 2.2(b)**. The final product was purified by dialysis in 1 kDa dialysis tubing. The attachment of the new targeting ligands and sulfo-LC-SPDP on to the chitosan backbone was carried out in a similar manner (see **Scheme 2.3**). The protein, rSML-A, was conjugated onto the polymer in the weight ratio, (polymer/r-SML-A) 40:1 according the conditions shown in **Scheme 2.4**. Unreacted rSML-A were removed by ultrafiltration with a 30 kDa filter membrane via centrifugation at 10,000 X *g* for 8 minutes.

After obtaining the new conjugate, **2-18**, their toxicity profile in breast cancer cells, MDA-MB-231, was studied on a smaller scale. The cells were treated with the polymer-lectin conjugates at different concentrations in serum-containing media (without phenol red). After 48 and 72 hours respectively, the media, along with free conjugates were aspirated, washed twice with PBS, and media containing WST-1 reagent was added to each well and incubated in dark for another hour at 37 °C. TECAN microplate reader was used for absorbance measurement at 450 nm (with reference wavelength set at 650 nm). Transmittance intensities were recorded, and values obtained were normalised in accordance to the control, and subsequently plotted as shown in **Figure 2.12**.

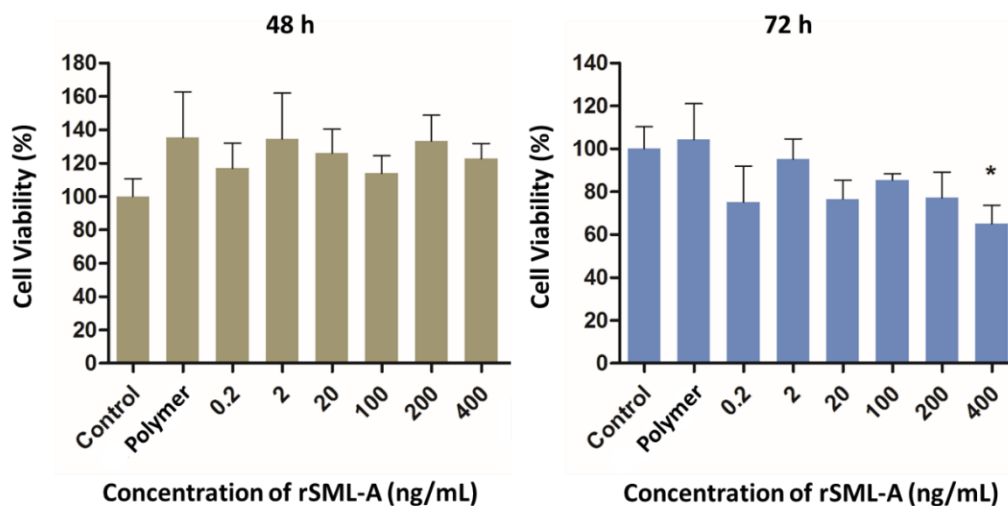


**Figure 2.12** | WST-1 assay of MDA-MB-231 upon 48 hours incubation (khaki) and 72 hours incubation (blue) with **2-19**, GC-BA1-SPDP/rSML-A. The samples were incubated in presence of FBS (2%) and absence of glucose.

The cell viability assays suggested that the initial design of polymer-lectin conjugates do not have significant effects on the cells. We hypothesized that it could be due to inability to escape from the endosome, as both the targeting ligand and disulfide linker (sulfo-LC-SPDP) are connected onto the amino group of the sugar, in which, the disulfide linker forms a stable amide bond which is not easily hydrolysed at endosomal pH (approx. pH 6.5). As a result, the proton-sponge effect of chitosan was limited. In addition, the targeting ligand density may not be sufficient for multi-valent binding advantage, as the amount of targeting ligands to be conjugated has to be carefully tuned such that the SPDP linker can be connected as well. Moreover, LC-SPDP has a long chain of alkyl spacer, which will add on some hydrophobicity factor to the final polymer, this may hinder effective conjugation of rSML-A onto the polymer.



### 2.3.2 | New Model: Proposed Modifications, Synthesis and Biological Assays

Based on the initial design, both the targeting ligands and disulfide linkers (LC-SPDP) compete for the amino groups present on the glycol chitosan backbone. Enhancing the targeting ability will compromise the amount of protein that can be conjugated and delivered. On the other hand, increasing the amount of disulfide linker to maximise the amount of protein that can be conjugated will result in poorer endosomal escape ability. The reason stemmed from the formation of a stable amide bond between commercial LC-SPDP linker and amino group of the chitosan, which in turns, limits the amount of free amine present to aid in escaping from the endosome. Hence, taking into the account of this and all the factors mentioned previously, the rSML-A delivery system has been remodelled as shown in **Figure 2.13** below.

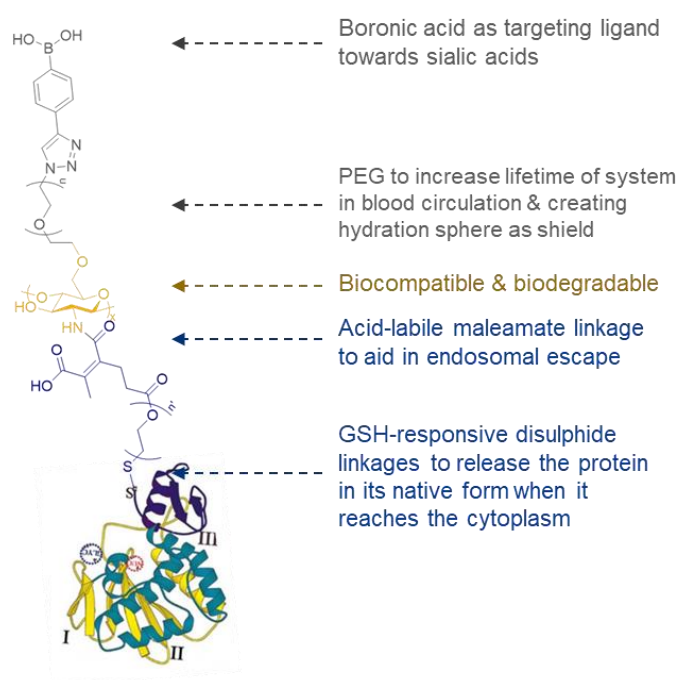
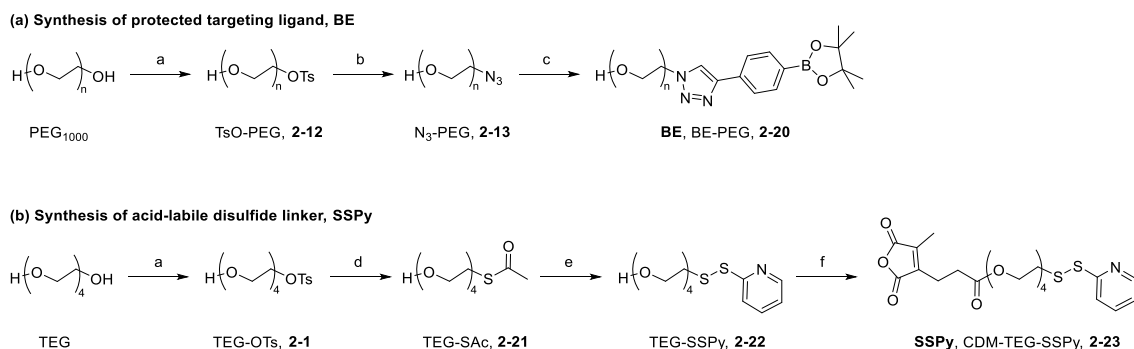


**Figure 2.13** | New model of the carrier system, BA-GC-SS/rSML-A. Ratio of BA-PEG linker (grey) and CDM-TEG-SSPy (blue) is 2:1, and it can be varied during the final step of synthesizing the polymer, BA-GC-SSPy.

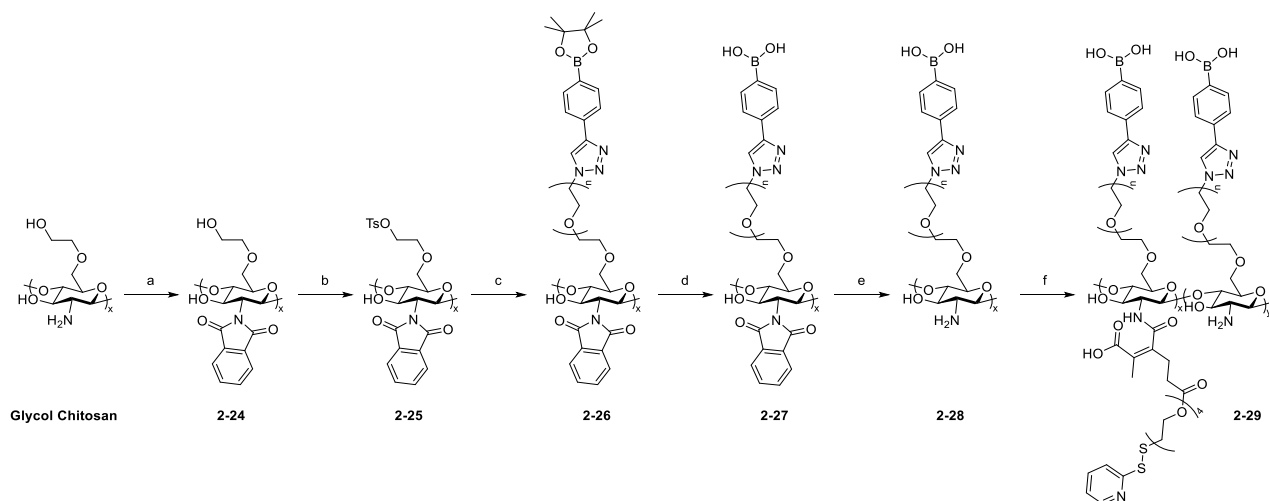
With this, the use of available sites on the glucosamine monomeric units are maximised, such as both the hydroxyl and amino groups for attachment of the two distinctive key components for different purposes respectively. The polyethylene glycol terminals are much more hydrophilic as compared to the protein, which is slightly hydrophobic in comparison, thus this will induce the

formation of a nanoparticle-like complex. The syntheses of the essential components, protected targeting ligand and acid-labile disulfide linker, are relatively straightforward, as shown in **Scheme 2.5**. Another reason to redesign the disulfide linker is because a slightly hydrophilic TEG segment will help to improve the solubility of the final polymer greatly, and that disruption of any nanoparticulate formation prior to conjugation can be easily done by ultrasonication.



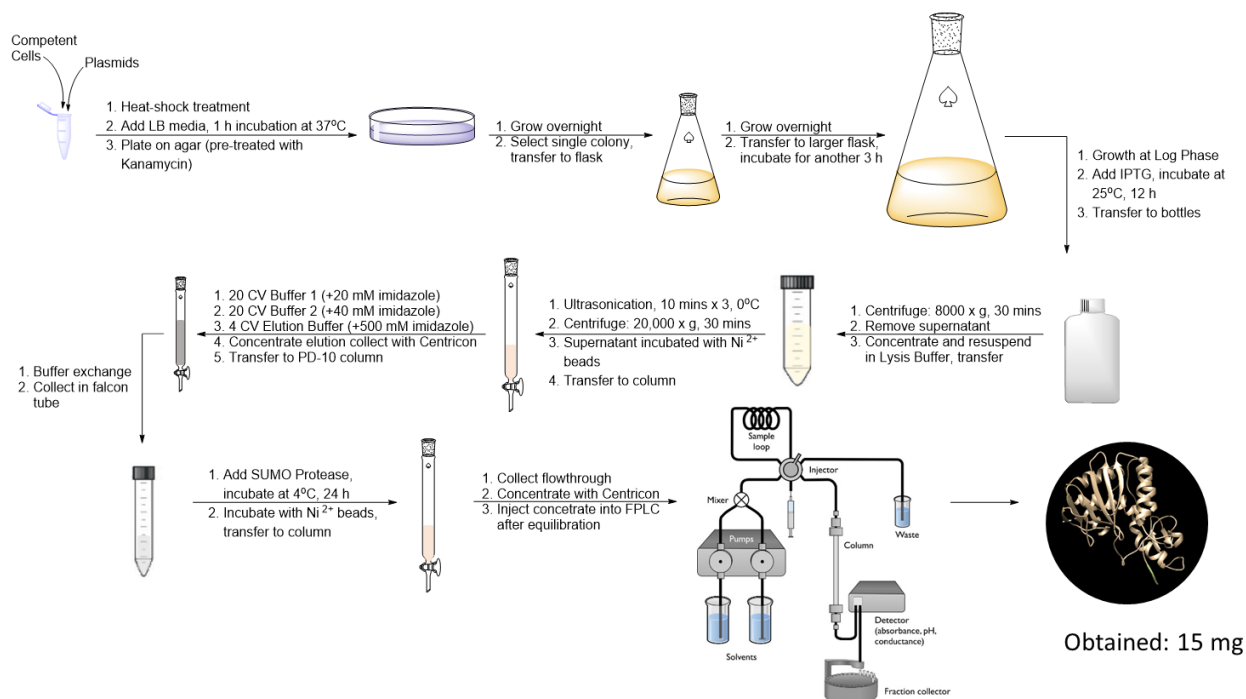
**Scheme 2.5** | Synthesis of the essential components of the carrier, (a) protected targeting ligand, BE-PEG and (b) acid-labile disulfide linker, CDM-TEG-SSPy. Reactions and conditions: a, tosyl chloride, NaOH (1.5 equiv.), THF/H<sub>2</sub>O; b, sodium azide (2 equiv.), ACN; c, 4-ethynylphenylboronic acid pinacol ester, copper iodide (0.05 equiv.), DIPEA (3 equiv.), DCM; d, potassium thioacetate (2.5 equiv.), NaI (0.1 equiv.), acetone; e, 1. NaOMe (1.5 equiv.), MeOH, 2. dipyridyl disulfide; f, carboxy dimethylmaleic anhydride (1.2 equiv.), HATU (1.5 equiv.), HOAt (1.5 equiv.), DIPEA (1.5 equiv.), DCM.

The new carrier was prepared according to **Scheme 2.6** shown in the next page. It is termed as BA-GC-SSPy, with the ‘BA’ placed before ‘GC’ so as to distinguish from the initial design, and also because the targeting ligands (BA) and disulfide linker (SSPy) are now at opposite ends of the glucosamine monomeric units. Solubility of the new carrier was improved greatly, as a stock solution of 50 mg/mL of polymer in water was prepared and can be kept for long period of time without precipitation observed. In contrast, the initial design, GC-BA-SPDP, has a maximum solubility of 1 mg/mL in water.



**Scheme 2.5** | Synthesis of new carrier design from commercially available glycol chitosan. Reactions and conditions: a, phthalic anhydride (5 equiv.), AcOH/H<sub>2</sub>O; b, tosyl chloride (1.5 equiv.), triethylamine (3 equiv.), DMF; c, sodium hydride (1.5 equiv.), **2-20**, DMF; d, 1. sodium periodate (5 equiv.), DMF, 2. HCl; e, hydrazine (10 equiv.), methanol; f, **2-23**, DIPEA, DMAP, DMF.

Meanwhile expression of rSML-A using *E. coli* was carried out, in accordance to protocol reported by our collaborator (see **Scheme 2.6** below), for biological assays.<sup>27</sup> The gel images of the mixture in intermediary steps and in final FPLC purification are shown in **Figures 2.14 and 2.15** respectively.



**Scheme 2.6** | General schematic illustration of the procedure in induction and purification of the recombinant protein, rSML-A.

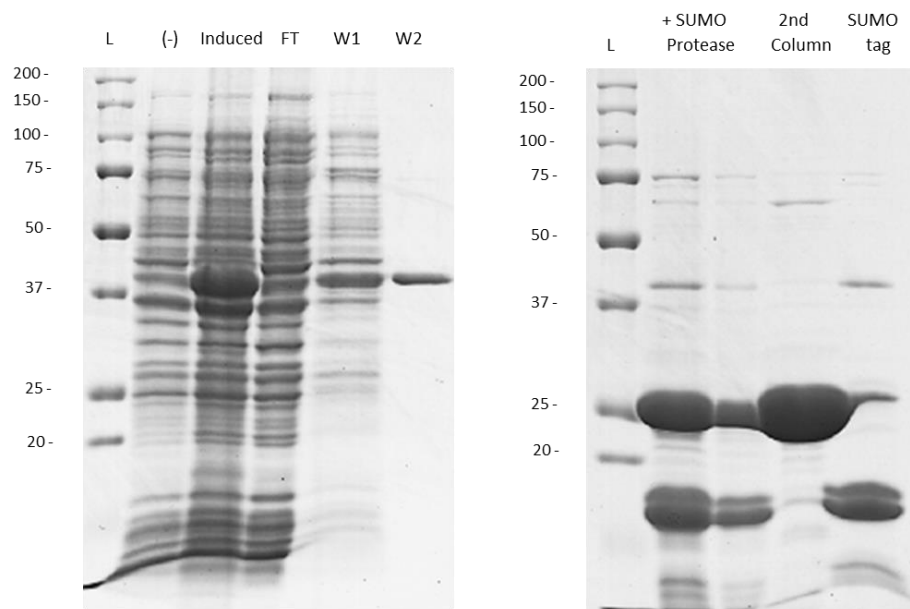


**Figure 2.14** | Gel images of mixtures in intermediary steps of recombinant protein (rSML-A) purification. L = ladder/marker (values written on the left are in kDa); (-) = before induction, induced = after protein induction; FT = first flow through; W1 = after first wash; W2 = after second wash,; + SUMO protease = after incubation with SUMO protease; 2nd column = after second column; SUMO tag = flow through of second column which contains SUMO tag.

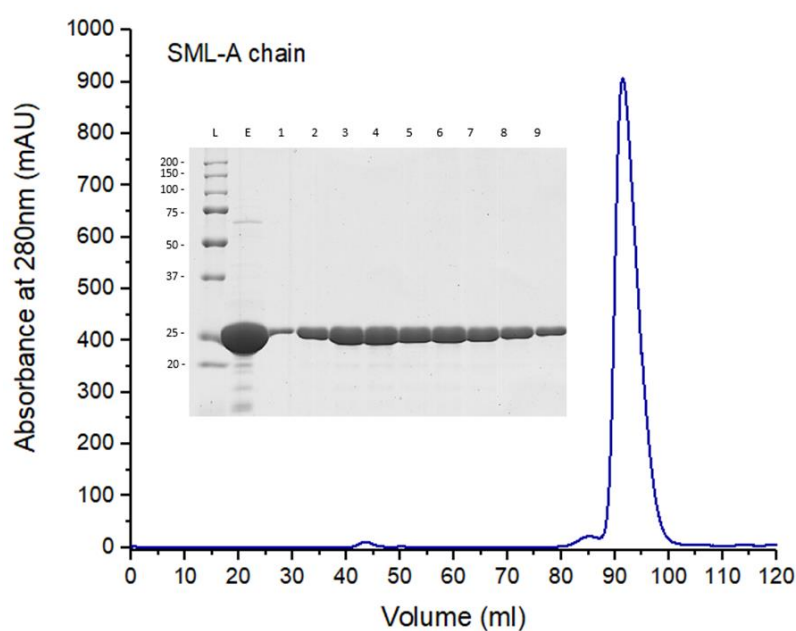
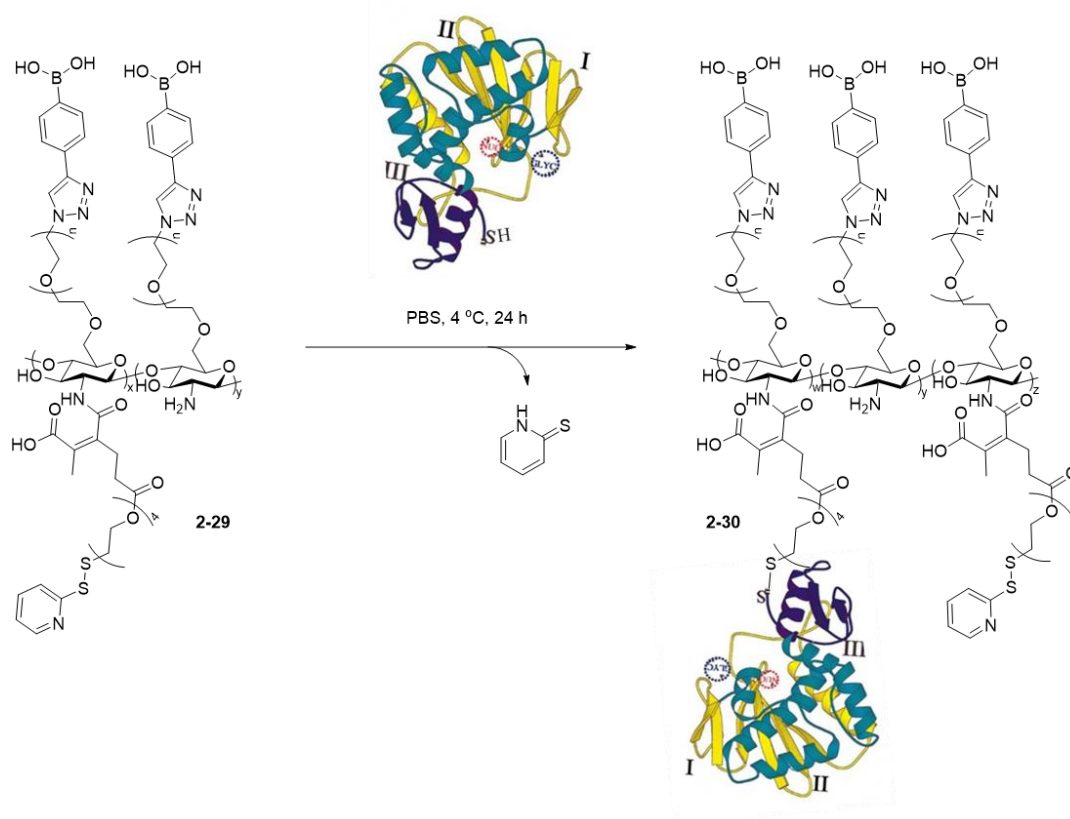


**Figure 2.15** | FPLC chromatogram of rSML-A, and gel image obtained from SDS-PAGE of different fractions collected (insert).

In order to achieve high conjugating efficacy with minimal wastage instead conjugating by a range of weight ratios, it is essential to first understand the spatial requirement of the two key

components in the delivery system, which are the carrier and the cargo (recombinant protein). The hydrodynamic diameter ( $D_H$ ) of rSML-A was estimated to be within 4.5 to 5.5 nm based on the data available from the following proteins: trypsin (23.2 kDa,  $D_H$  = 4.8 nm), glutathione-S-transferase (26 kDa,  $D_H$  = 4.8 nm), carbonic anhydrase I (29 kDa,  $D_H$  = 4.9 nm, Pim-1 (31.5 kDa,  $D_H$  = 5.2 nm) and protein kinase A (40 kDa,  $D_H$  = 5.6 nm).<sup>50-51</sup> The approximate length of pentasaccharide in a linear configuration is approximately 2.2 to 2.4 nm. Considering these factors, the protein was conjugated onto the carrier using two different ratios, 15 sugar units per rSML-A (**2-30A**) and 20 sugar units per rSML-A (**2-30B**), see **Scheme 2.7**. The final conjugate is termed as BA-GC-SS/rSML-A.



**Scheme 2.7** | Synthesis of BA-GC-SS/rSML-A (**2-30**) conjugate. The protein was treated with DTT at 4 °C in PBS for an hour and filtered by 10 kDa membrane prior to conjugation. The protein concentrate was collected and added to the PBS mixture, consisting BA-GC-SSPy (**2-29**), and incubated for 24 hours at 4 °C.

After obtaining the conjugate, a preliminary visual study was conducted to see if the breast cancer cell, MDA-MB-231, is able to uptake the new conjugates, BA-GC-SS/rSML-A<sub>15</sub> (**2-30A**) and BA-GC-SS/rSML-A (**2-30B**). Positive control (BioPORTER/rSML-A) and negative controls

(rSML-A, fluorophore, and PBS) were included in the study. Prior to the treatment, the substrates (**2-30A**, **2-30B**, BioPORTER/rSML-A and rSML-A) were tagged with fluorophore (rhodamine B) by reacting with sulforhodamine B acid chloride according to protocol provided by manufacturer. The cells were first seeded on glass coverslips for 18 hours before incubating with different substrates and PBS for 6 hours in blank DMEM (without glucose, FBS, P/S, and phenol red). Thereafter, the media containing leftover substrates were aspirated and washed thrice with PBS, before DAPI-staining for better visualisation, and then fixed with 4% paraformaldehyde, and subsequently washed thrice with PBS. The coverslips were then carefully removed from the culture plate for visualisation under a confocal microscope. The confocal microscopic images obtained are shown in **Figure 2.16** below.

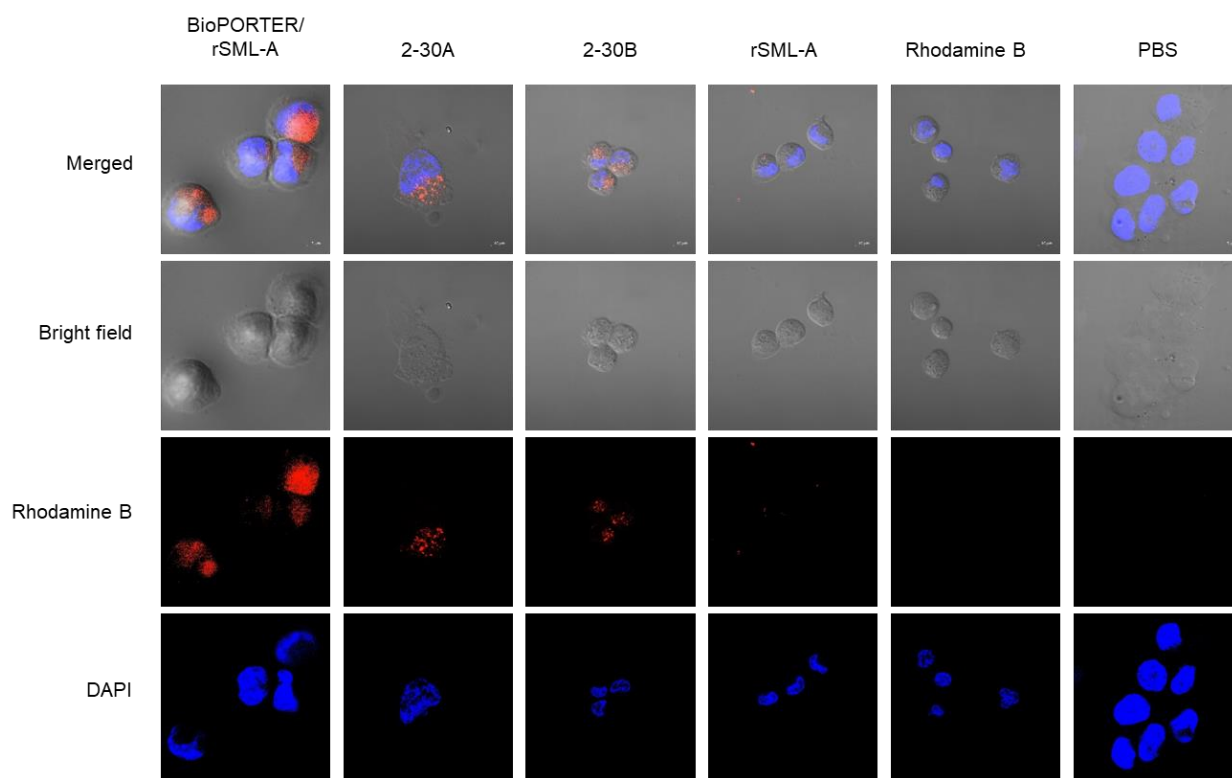


**Figure 2.16** | Confocal images (top to bottom: merged, bright field, red channel, DAPI channel) of MDA-MB-231 treated with different substrates (left to right: BioPORTER/rSML-A, **2-30A**, **2-30B**, rSML-A, rhodamine B, RBS) for 6 hours in blank DMEM (without glucose, FBS, P/S, and phenol red). Scale bar (white) = 5  $\mu$ m for BioPorter/rSML-A and PBS, and scale bar (white) = 10  $\mu$ m for the rest.

Based on the confocal images obtained and upon comparing with the negative controls, it was highly implied that the conjugates (**2-30A** and **2-30B**) were taken up by the breast cancer cells

under the conditions tested. However, there was no significant difference between both of the conjugates. Hence, we postulated that perhaps, in both conjugating ratios, maximum conjugation has already been reached, possibly due to the three-dimensional arrangement of both the protein and the polymer that were not factored in during the theoretical calculation. Thus, SDS-PAGE experiment was carried out without the addition of reducing agent for both crude substrates (obtained after conjugation of protein without further purification) to determine the amount of proteins that were conjugated. In order to do so, SDS-PAGE of rSML-A was first carried out in a series of different amounts as shown in **Figure 2.17** (left). The highest amount of rSML-A ran was 5  $\mu$ g, which was the amount of protein present in 10  $\mu$ L of crude mixture of **2-30A** and **2-30B** respectively. The intensity of each band was recorded using Fiji-ImageJ and plotted in graph as shown in Figure 2.18. The equation of best-fit line was drawn and used to calculate the amount of unreacted protein (x-value). SDS-PAGE without addition of reducing agent was ran for crude mixtures (**Figure 2.17** (middle)) and solutions after washing with PBS twice (**Figure 2.18** (right)).

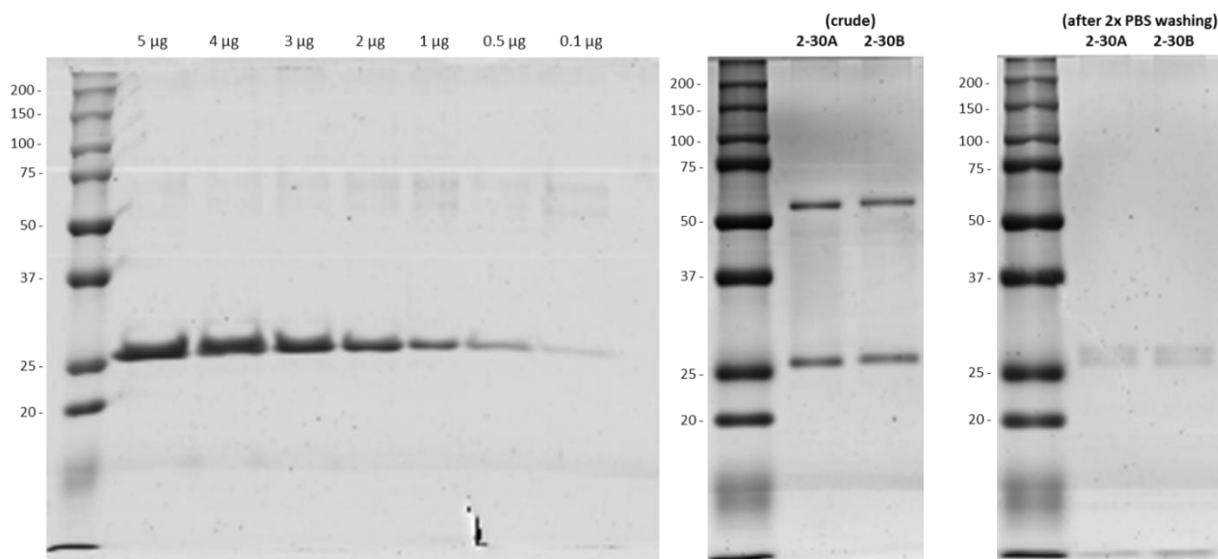


**Figure 2.17** | SDS-PAGE gel images of rSML-A in different concentrations (left), crude mixtures of **2-30A** and **2-30B** (middle) in which each well contains 5  $\mu$ g of rSML-A), and respective solution of **2-30A** and **2-30B** after washing with PBS twice (right) by ultrafiltration with 50 kDa filter membrane and centrifugation conditions set at 10,000 X g, 5 minutes, 4  $^{\circ}$ C.

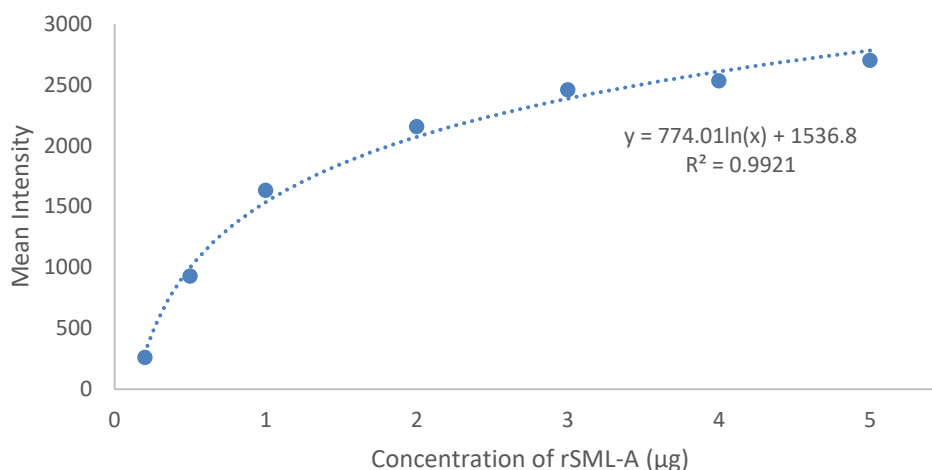


**Figure 2.18** | A graphical plot of mean intensity against concentration of rSML-A, with the values of mean intensity of each band (corresponding to their respective amount of rSML-A) recorded using Fiji ImageJ.

The gel image in **Figure 2.17** (middle) showed the presence of two bands which were wide apart, with the bottom band corresponding to rSML-A which has a molecular weight of 28.9 kDa. Upon closer inspection, it was observed that the top band correspond to a compound which has MW slight greater than 50 kDa, and concluded that there is a very high possibility that it belonged to the dimerised rSML-A (MW = 57.8 kDa). Based on the calculation shown in section 2.5.4, and using this equation to calculate the amount of free rSML-A that were not conjugated:

$$\text{Amount of unreacted protein } (\mu\text{g}) = \text{amount of protein in bottom band} + 2 * \text{amount of protein in top band},$$

the amount of unreacted protein in **2-30A** is 1.9 µg (bottom band = 0.53 µg, top band = 0.68 µg) and the amount of unreacted protein in **2-30B** is 1.5 µg (bottom band = 0.45 µg, top band = 0.53 µg). In other words, the amount of rSML-A conjugated in **2-30A** is 3.1 µg (62% conjugating efficiency) and that in **2-30B** is **3.5 µg** (70% conjugating efficiency). After two times of washing with PBS, the band is hardly visible as shown in **Figure 2.17** (right), in which the amount of unreacted protein left in **2-30A** after washing is 0.81 µg and that in **2-30B** is 0.71 µg.

Thereafter, the cytotoxic effect of **2-30B** (which has a higher conjugating efficiency calculated previously) was studied in breast cancer cells using WST-8 assay, against a well-recognized delivery agent for proteins, BioPORTER®, as positive control, and PBS as negative



control. MDA-MB-231 cells were first seeded on 96-wells plate, 18 hours prior to experiment. The media were then changed to new ones according to the required conditions. Condition 1 was conducted according to the standard protocol of BioPORTER® reagent, which is absence of FBS in first 4 hours of incubation, and subsequently changed to growth media (WST-8 results will be color coded in blue in **Figure 2.19**). Condition 2 was conducted in presence of 2% FBS in the media (WST-8 results will be color coded in red in **Figure 2.19**). After 72 hours of incubation, the media were aspirated, gently washed with PBS thrice, and media containing WST-8 reagent was added. Transmittance values were recorded after an hour of incubation at 37 °C in the incubator (see **Figure 2.19**). Indeed, cell cytotoxicity against breast cancer cells increased with our new design, which indicated that it acts as a better carrier as compared to our initial design. On the side note, BioPORTER/rSML-A treatment in presence of 2% FBS weakened its ability as a carrier system at lower concentrations of rSML-A.

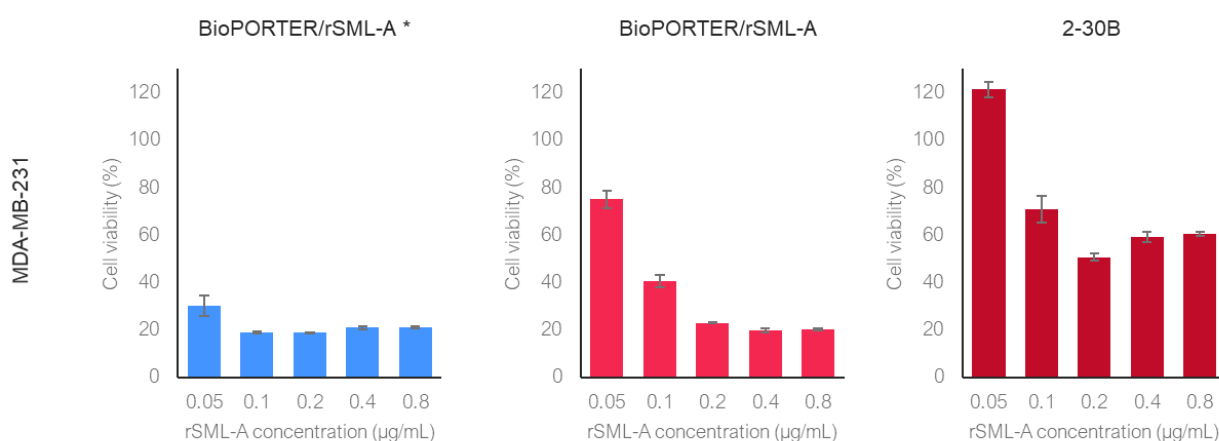


**Figure 2.19** | WST-8 assay of MDA-MB-231 cells upon treatment with BioPORTER/rSML-A and **2-30B** in triplicate studies. The cell viability percentages shown here were normalized to that of negative control, PBS (cell viability = 100%). Red color-coded bars indicated presence of FBS (2%) and absence of glucose during incubation while blue color-coded bars indicated absence of FBS in first 4 hours of treatment, according to the standard protocol of BioPORTER® reagent, before changing to the same conditions as the others.

Although the new design result in improved cytotoxicity against breast cancer cells (< 60% viability at 0.2 µg/mL of rSML-A treated), the efficiency was not as ideal compared to BioPORTER® reagent, despite being exposed to the same treatment conditions. We hypothesized

that perhaps, the endosomal escape ability of the conjugate, **2-30B**, was compromised, since the proteins wrapped in the core would tighten the spherical structure, making it less accessible for hydrolysis of the maleate bonds to occur. Therefore, a lysosomal tracking study was conducted to test the hypothesis (see **Figure 2.20**). The polymeric carrier **2-29** was included in this study as well because we would like to determine if the absence of rSML-A would not have the effect described, and thus it would be able to exhibit its endosomal escape ability. To conduct this study, the substrates **2-30B** and **2-29** were tagged with Rhodamine Green instead of sulforhodamine B acid chloride (red), as the lysotracker available at hand has red fluorescence upon excitation (LysoTracker Red). As per previous experiments, MDA-MB-231 cells were first seeded on glass coverslips 18 hours prior to experiment. After incubating the cells with the substrates for 6 hours, media were aspirated and washed thrice with PBS, before treatment with LysoTracker Red (according to manufacturer's protocol). They were then washed thrice with PBS, and stained with DAPI, and washed thrice again with PBS. The samples were all fixed with 4% paraformaldehyde for 30 minutes and then washed thrice with PBS. The confocal microscopic images obtained are shown in **Figure 2-20** below.

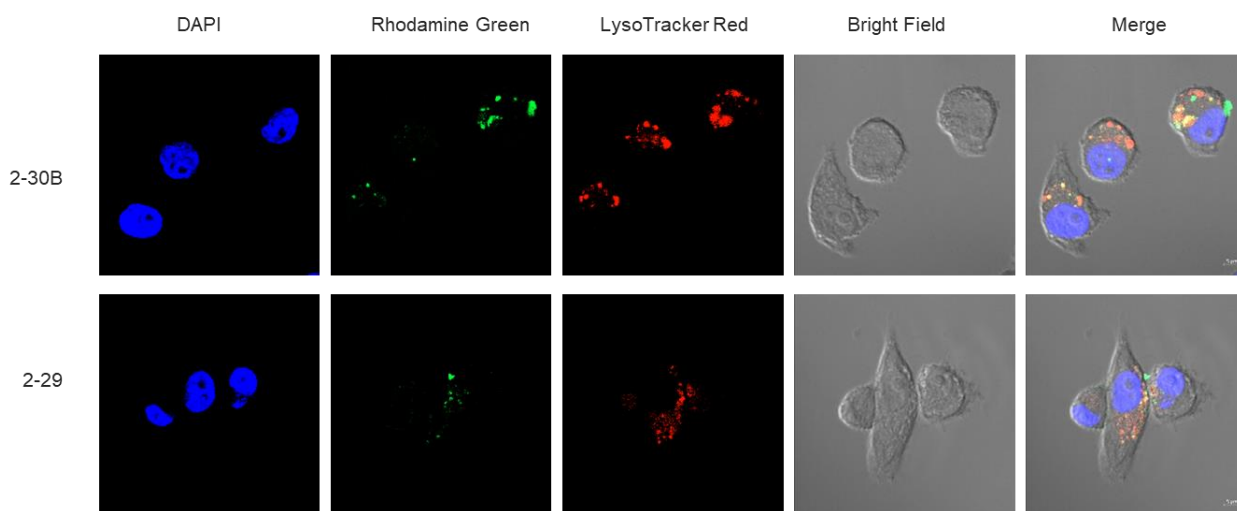
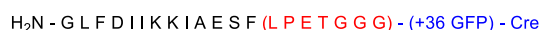


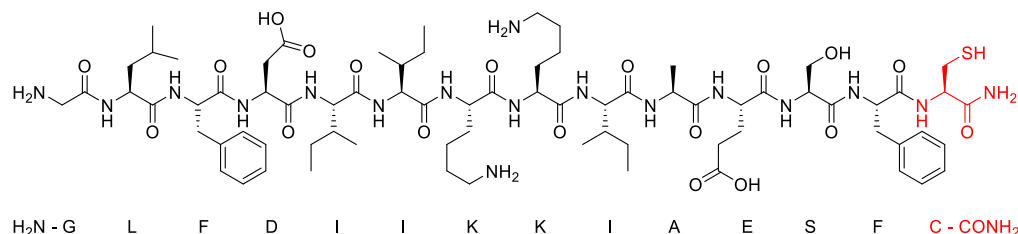
**Figure 2.20** | Confocal microscopic images (left to right: DAPI, green channel, red channel, bright field, merged) of MDA-MB-231 treated with different substrates conjugated with rhodamine green (top to bottom: **2-30B**, **2-29**). The cells were subsequently stained with LysoTracker Red and DAPI. Scale bar (white) = 5  $\mu$ m.

From the confocal microscopic images in **Figure 2.20**, it was observed that majority of the conjugates are stuck within the lysosome (at regions where the red and green coincided). Even the polymeric carrier without its cargo, **2-29**, were stuck in the lysosomes as well. After a quick literature search, we came across an interesting study conducted by Liu *et al.* in 2015.<sup>52</sup> They reported the synthesis of a series of antimicrobial peptides with an additional LPETGG tag at C-terminal for sortase-mediated conjugation +36 GFP, for cytosolic delivery studies in serum-free DMEM for 4 hours. They have found that Aurein 1.2 (GLFDIIKKIAESF) gave the best overall activity in enhancing the endosomal escape, with an increase of the cytosolic protein delivery by up to 5-fold, and that it has no known mammalian cell cytotoxicity. Thus, a slight modification of Aurein 1.2 (see **Scheme 2.8b**) was designed and synthesized to be incorporated it into the delivery system. The thiol end added was to facilitate attachment onto thiol linker on the polymeric carrier.

(a) Peptide sequence for Aurein 1.2 (in black, without the brackets) reproted by Liu *et al.*:



(b) Our design of Aurein 1.2, modified with Cys (shown in red) at C terminal:



**Scheme 2.8** | (a) Aurein 1.2 peptide sequence with C-terminal modified with LPETGGG (red) to conjugate with GFP-Cre (blue). (b) Proposed design of Aurein 1.2, in which the C-terminal is modified with Cys since it has a thiol end for conjugation to the disulfide linker on the polymeric carrier.

Modified Aurein 1.2 was synthesized using conventional solid phase peptide synthesis method with Sieber amide resins, according to standard SPPS protocol. In brief, the resin was pre-soaked in DMF and then activated for the attachment of the first amino acid, Fmoc-Cys(Trt)-OH. Nitrogen gas was bubbled into the mixture to allow constant mixing of the reagents. Thereafter, the amino acid was flushed out and washed twice with DMF, before deprotection of the Fmoc



sulforhodamine), and then incubated with breast cancer cells (MDA-MB-231) and mouse embryonic fibroblasts, NIH3T3, in which the latter acts as a negative control cell line. The incubation conditions were the same as previously described, and subsequently stained with DAPI for better visualisation purposes. The samples were fixed with 4% paraformaldehyde prior to microscopic studies. The confocal microscopic images are shown in **Figure 2.22** and **Figure 2.23**.

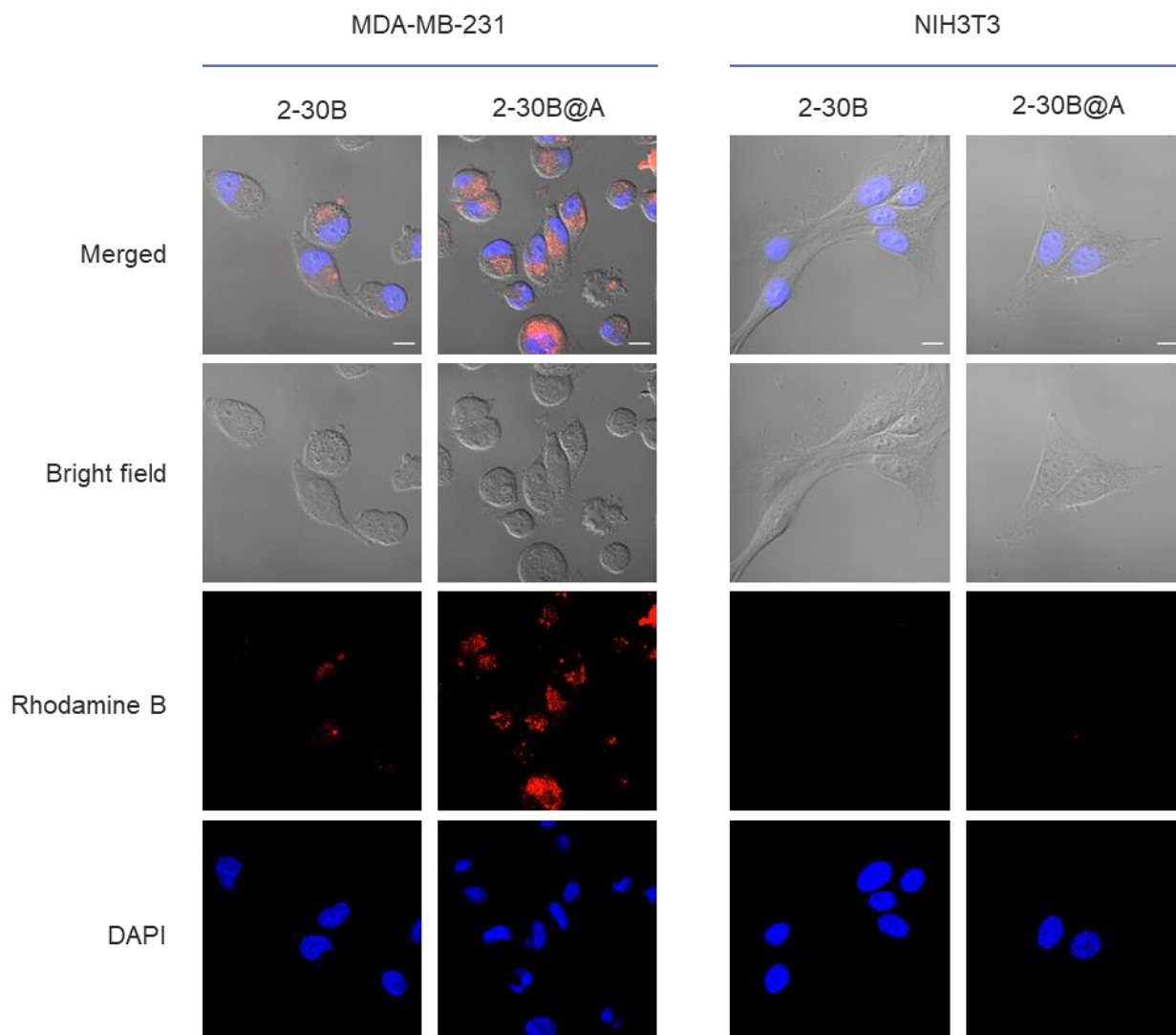


**Figure 2.22** | Confocal microscopic images (top to bottom: merged, bright field, red channel, DAPI channel) of MDA-MB-231 (left two columns) and NIH3T3 (right two columns) treated with different substrates (**2-30B** and **2-30B@A**) tagged with rhodamine. Scale bar (white) = 10  $\mu$ m.

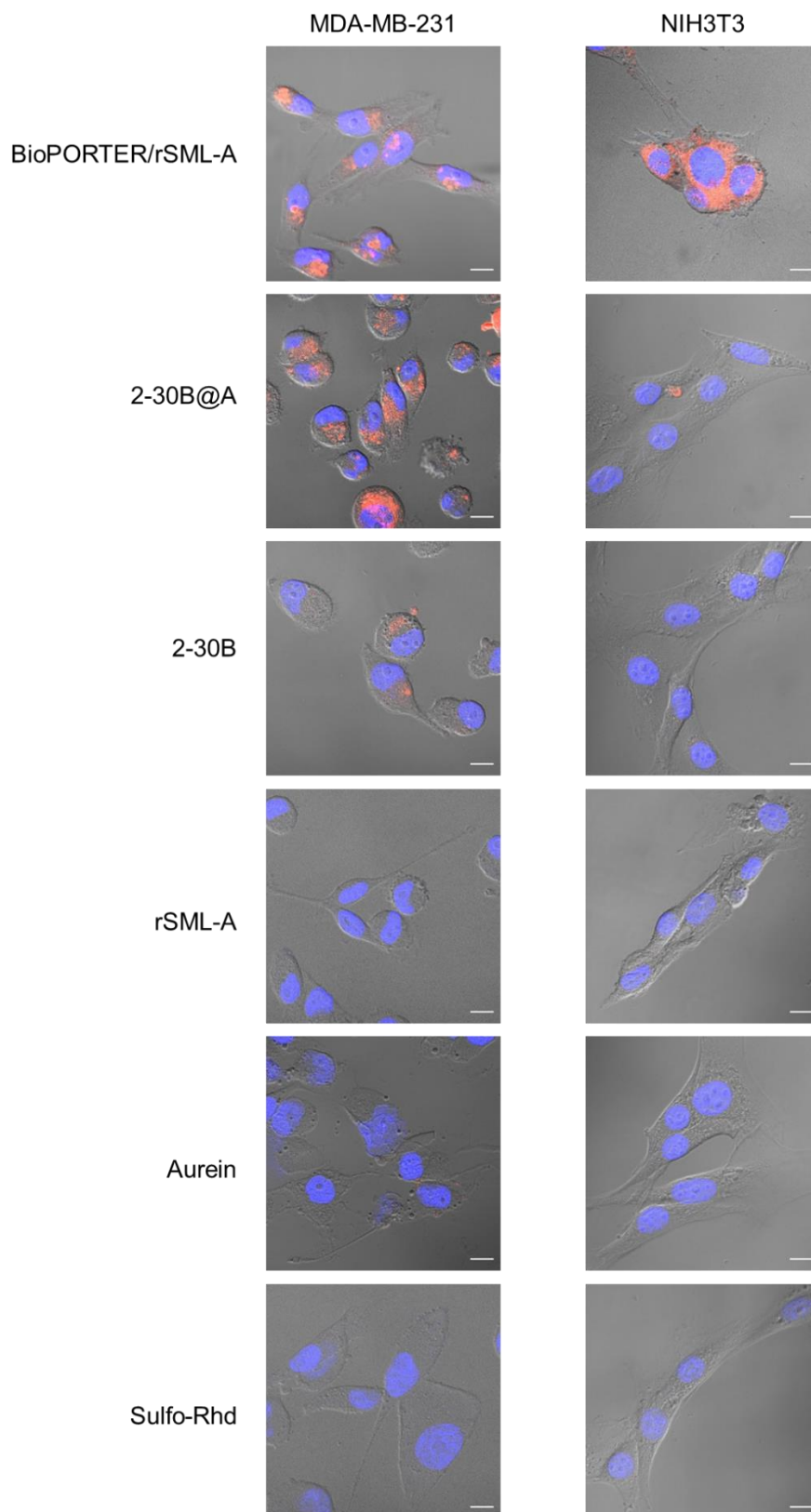


**Figure 2.23** | Merged confocal microscopic images of (top to bottom) BioPORTER/rSML-A, **2-30B**, **2-30B@A**, rSML-A, modified Aurein 1.2, sulforhodamine B in different cell lines MDA-MB-231 (left) and NIH3T3 (right). The color blue depicts DAPI staining, while red depicts substrates stained with sulforhodamine chloride. Scale bar (white) = 10  $\mu$ m.

A significant increment in uptake of **2-30B@A** as compared to **2-30B** was observed visually in the breast cancer cells, MDA-MB-231. Encouraged by the results, cell viability assay was then carried out with the conjugates **2-30B@A** and **2-30B**, along with the polymer carrier **2-29** for comparison study. The conditions of treatment were milder in this study, in which the cells were incubated with our substrates under growth conditions (in presence of 2,250 mg/L of D-glucose and 5% FBS) for 70 hours. Subsequent work-up procedures were the same as previously described, and WST-8 reagent in fresh media were added for an hour of incubation. Thereafter, the transmittance values were recorded and plotted in the charts shown in **Figure 2.24**.

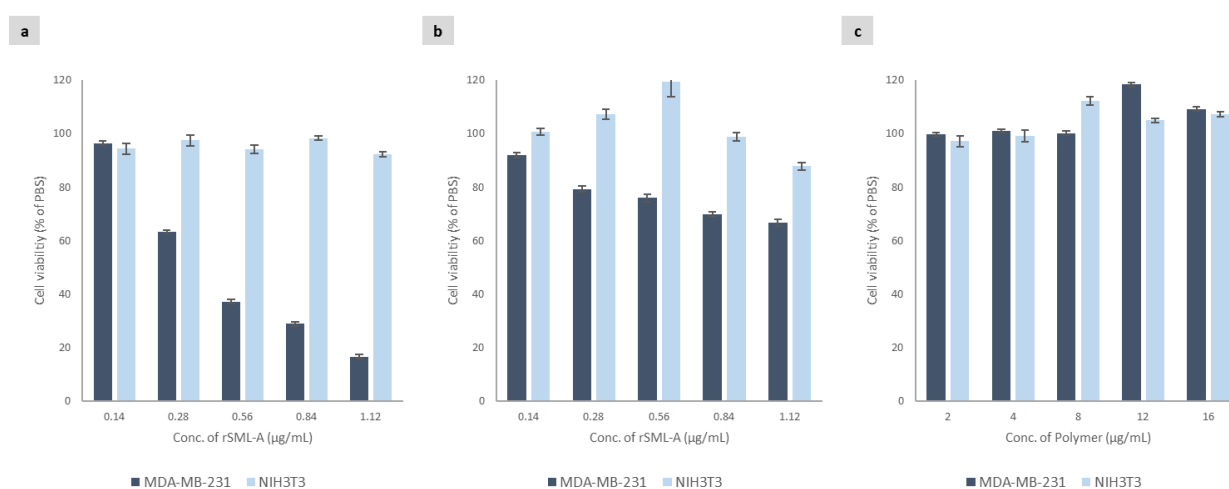


**Figure 2.24** | WST-8 cell viability assays of (a) **2-30B@A**, (b) **2-30B**, and (c) **2-29**, in MDA-MB-231 cells (dark blue) and NIH3T3 (light blue). The cells were incubated with substrates under normal growth condition, in presence of glucose and FBS for 70 hours. The cell viability percentages shown here were normalized to that of negative control, PBS (cell viability = 100%).

Based on the results shown in **Figure 2.24**, relatively good toxicity was achieved selectively against breast cancer cells, MDA-MB-231, under growth conditions upon treatment with the final conjugate, **2-30B@A**. This study further demonstrates the applicability of using cheap alternatives such as boronic acids as targeting ligands, instead of the very expensive antibodies. Endosomal escape was achieved with the aid of modified Aurein 1.2, and the low cell viability observed indicated that the protein, rSML-A, has been successfully delivered in its native form into the cytosol, in which it was able to fulfil its role as a ribosome-inactivating protein. To further substantiate this, lysosomal tracking assay was conducted to determine visually. **2-30B@A**, tagged



with rhodamine dye, was incubated with MDA-MB-231 for 12 hours. Thereafter, the old media was aspirated, and the seeded cells were washed with PBS thrice. The cells were then stained with LysoTracker Green according to protocol provided by the manufacturer, and they were washed with PBS again before staining with DAPI. Next, the cells were washed with PBS thrice and fixed with 4% paraformaldehyde according to previously described conditions. Finally, after washing the cells, the glass coverslip was gently removed from the culture plate and analysed by confocal microscopy. Another technique, z-stack, was used to capture different slices of the desired region along the z-axis. The compiled image generates a three-dimensional (3D) view of the region of interest (see Figure 2.25). The 3D view showed that majority of our final conjugate, **2-30B@A**, has successfully escaped from the lysosomes, and this image captured the early apoptotic stage of cell death.

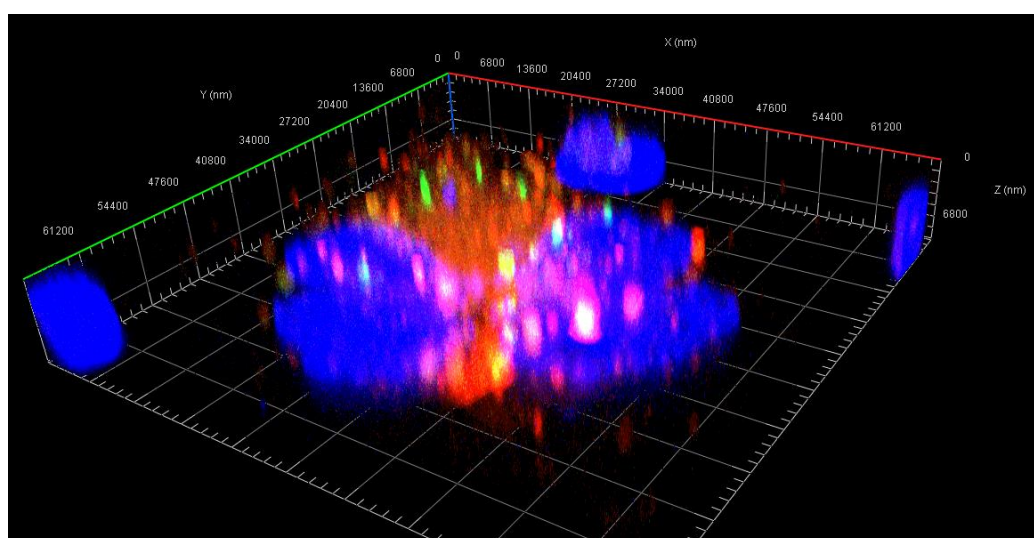


**Figure 2.25** | Compiled z-stack images depicts a three-dimensional view of MDA-MB-231 after 12 hours incubation with our final conjugate, **2-30B@A** (red) which most had successfully escaped from the endosomes before lysosomes (green) fusion. Blue color represents nuclei as stained by DAPI.



## 2.4 | Conclusion

In summary, the viability of this targeted system have been demonstrated through straightforward synthetic routes and uptake of the final conjugate (**2-30B@A**) into the sialic-acid overexpressed cells (MDA-MB-342) selectively against the control (NIH3T3), in which cytosolic delivery of rSML-A was achieved. Early designs and subsequent modifications have aided in fine-tuning of the delivery system into a viable one that allows the protein to be delivered in its native form. As such, it is able to unleash its potency upon escaping from the endosomes before lysosomes fusion, thereby killing the cancerous cells selectively. This delivery system was resisted by the normal cells, in which uptake of the conjugate was close to none. In addition, the carrier, **2-29**, has shown excellent biocompatibility, even in the breast cancer cells. In conclusion, this design of a combination of highly specific components was substantiated by promising biological activities observed in this study, and provides an excellent platform for future applications in protein delivery.

## 2.5 | Methods and Materials

### 2.5.1 | Materials

High MW glycol chitosan ( $M_w \geq 80$  kDa, DD  $\geq 85\%$ ), Sulforhodamine B acid chloride, cell proliferation reagent WST-1 solution (abbreviated as WST-1), diisopropylethylamine (DIPEA), 4-dimethylaminopyridine (DMAP) and all other chemicals used in synthesis were purchased from Merck (Darmstadt, Germany). 2,5-Dihydro-4-methyl-2,5-dioxo-3-furanpropanoic acid (CDM) was purchased from Tokyo Chemical Industry (Tokyo, Japan). 1-[Bis(dimethylamino)methylene]-1H-1,2,3-triazolo[4,5-b]pyridinium 3-oxid hexafluorophosphate (HATU), 3H-[1,2,3]-Triazolo[4,5-b]pyridin-3-ol (HOAt), and all amino acids used in synthesis were purchased from GL Biochem Ltd. (Shanghai, China). Sulfo-LC-SPDP, Rhodamine Green carboxylic acid succinimidyl ester (abbreviated as rhodamine green), LysoTracker Red DND-99 (abbreviated as LysoTracker Red), and LysoTracker Green DND-26 (abbreviated as LysoTracker Green) were purchased from Thermo Fisher Scientific Inc. (Waltham, USA). Cell counting kit-8 (also known as WST-8) was purchased from Dojindo Molecular Technologies, Inc. (Maryland, USA). Dialysis tubing was purchased from Spectra/Por (Singapore). Milli-Q water ( $18\text{ M}\Omega$ ) was prepared using a Milli-Q Synthesis System (Millipore, Bedford, MA, USA) for dialysis and experiments. Cell lines, MDA-MB-231 and NIH3T3, were obtained as gifts from our collaborator, Professor Yoon Ho Sup.

### 2.5.2 | Chemical Synthesis

#### **General Experimental Details**

All reactions were carried out in oven-dried glasswares and under ambient conditions, unless otherwise stated. Reactions were monitored by thin-layer chromatography (TLC) silica gel plates 60-F254 using UV light at 254 nm to visualise and  $\text{KMnO}_4$  as a staining agent, together with Liquid Chromatography Mass Spectrometer (LCMS) to monitor the change in molecular weights.

Solvents used were either purified according to standard procedures in literature or as purchased from Merck. Product purification was done by flash chromatography using silica gel 60 (0.010-0.063 mm), with reagent grade solvents and distilled technical grade solvents, unless otherwise stated. Nuclear magnetic resonance (NMR) spectra were recorded at 400MHz or 500MHz for  $^1\text{H}$  and 100MHz or 125MHz for  $^{13}\text{C}$ , using Bruker AVIII 400 spectrometer or Bruker AV 500 spectrometer. Chemical shifts in  $^1\text{H}$ -NMR were calibrated to either TMS residue peak (0 ppm) or trace chloroform peak (7.26 ppm) in  $\text{CDCl}_3$ , or trace methanol peak (3.31 ppm) in  $\text{MeOD-d}_4$ . Chemical shifts ( $\delta$ ) are reported in ppm and the coupling constants (J) are given in Hz. The following abbreviations are used to classify the multiplicity: s = singlet, d = doublet, t = triplet, m = multiplet or unresolved, brs = broad signal.  $^1\text{H}$  NMR for substrates were recorded below for reference. In addition,  $^{13}\text{C}$  NMR were given for newly prepared small molecules.

Monotosylation of tetraethylene glycol (TEG) and  $\text{PEG}_{1000}$  was carried out in a similar manner following protocol reported by Daniel *et al.*<sup>53</sup>  $\text{S}_{\text{N}}2$  reactions to formation of azido compounds was also carried out in a similar manner following method reported by Cubberley and Iverson.<sup>54</sup> Protection and deprotection of alcohols were done according to methods reported in ref. 55. Esterification reactions were done in a similar manner as peptide coupling protocols reported by Kahne *et al.*<sup>56</sup> Click reaction between azido and alkyne was done in a similar manner reported by Wang and Hu *et al.*<sup>57</sup> Deprotection of pinacol esters were done in a similar manner as reported by Matsubara *et al.*<sup>58</sup> Potassium thioacetate  $\text{S}_{\text{N}}2$  reaction was carried out in a similar manner reported by Gee *et al.*<sup>59</sup> Protection and subsequent deprotection of chitosan was done following protocols similar to those reported by Ifuku *et al.* and Gagnon *et al.*<sup>60-61</sup> Tosylation reaction on C6 hydroxyl of chitosan was carried out in a similar manner as reported by Chen *et al.*<sup>62</sup> Calculations for reactions involving polymer were based on repeating monosaccharide units.

### **Initial Design: Synthesis of Targeting Ligands**

**Synthesis of tetraethylene glycol monotosylate, TEG-Ts, (2-1):** Tetraethylene glycol (10.0 g, 0.693 mol) and sodium hydroxide (3.09 g, 0.104 mol) were dissolved in THF/ $\text{H}_2\text{O}$  (110 mL, v/v

= 10:1) at 0 °C. *p*-Toluenesulfonyl chloride (9.82 g, 0.693 mol), dissolved in THF (10 mL), was added dropwise to the mixture. The mixture was warmed to room temperature and stirred for 5 hours. The solvent was then removed *in vacuo*, followed by DCM/water extraction. The combined organic layers were dried over sodium sulfate and the solvent was removed under reduced pressure. TEG-OTs was purified using flash column chromatography on silica gel chromatography with acetone:DCM (v/v =1:5) as the eluent to give TEG-Ts (**2-1**) as a clear colorless oil (13.8 g, 57%). <sup>1</sup>H NMR (400 MHz, CDCl<sub>3</sub>) δ: 7.71 (2H, d, J = 7.2 Hz), 7.27 (2H, d, J = 7.2 Hz), 4.08 (2H, m), 3.56 (14H, m), 2.84 (1H, brs), 2.36 (3H, s).

**Synthesis of 1-Azido-3,6,9-trioxaundecane-11-ol, TEG-N<sub>3</sub>, (2-2):** TEG-Ts (5.00 g, 0.144 mol) and sodium azide (1.87 g, 28.7 mmol) were dissolved in acetonitrile and heated at reflux for 18 hours. Acetonitrile was then removed *in vacuo*, and DCM/H<sub>2</sub>O extraction was carried out. The combined organic layers were dried over sodium sulfate and the solvent removed under reduced pressure, giving TEG-N<sub>3</sub> (**2-2**) as colorless oil (2.45 g, 78%). <sup>1</sup>H NMR (400 MHz, CDCl<sub>3</sub>) δ: 3.63 (14H, m), 3.34 (2H, t, J = 4.8 Hz), 2.83 (1H, brs).

**Synthesis of *tert*-Butyldimethylsilyl tetraethylene glycol *p*-tosyl diether, TBDMS-TEG-TS, (2-3):** TEG-OTs (2.00 g, 5.74 mmol) and triethylamine (0.88 mL, 6.31 mmol) were added into DCM (16 mL), under nitrogen atmosphere. *tert*-Butyldimethylsilyl chloride (0.950 g, 6.31 mmol) was then dissolved in DCM (2 mL) and subsequently added dropwise at room temperature. DMAP (69.6 mg, 0.57 mmol), dissolved in DCM (2 mL), was then added to the reaction mixture, and stirred overnight. The solvent was removed *in vacuo* and water (20 mL) was added and subsequently extracted with EtOAc twice, and washed with 20 mL of acidic water twice, and once with brine. The organic layer was dried over sodium sulfate, and the solvent was removed *in vacuo* to give TBDMS-TEG-TS (**2-3**) as a clear pale yellow oil (2.52 g, 95%). <sup>1</sup>H NMR (500 MHz, CDCl<sub>3</sub>) δ: 7.6 (2H, d, J = 7.2 Hz), 7.2 (2H, d, J = 7.2 Hz), 4.01 (2H, m), 3.47 (14H, m), 2.24 (3H, s), 0.71 (9H, s), -0.12 (6H, s).

**Synthesis of TBDMS-OEG-N<sub>3</sub>, (2-4)** Sodium hydride (36.0 mg, 1.51 mmol) was added portion-wise to DMF (3 mL) at 0 °C under inert atmosphere. TBDMS-TEG-OTS (0.300 g, 1.37 mmol) was added to the mixture, followed by dropwise addition of TEG-N<sub>3</sub> (0.633 g, 1.37 mmol). The reaction mixture was allowed to warm to room temperature and stirred overnight. 20 mL of water was added, and the mixture was extracted with chloroform. The combined organic layers were washed with brine, dried over sodium sulfate, and concentrated *in vacuo*. TBDMS-OEG-N<sub>3</sub> (**2-4**) was obtained as a pure yellow oil (0.244 g, 35%) by flash chromatography using EtOAc:DCM (1:9 to 3:7) as the eluent. <sup>1</sup>H NMR (400 MHz, CDCl<sub>3</sub>) δ: 3.71 (2H, m), 3.60 (26H, m), 3.50 (2H, m), 3.34 (2H, m), 0.85 (9H, s), 0.01 (6H, s). <sup>13</sup>C NMR (100 MHz, CDCl<sub>3</sub>) δ: 72.61, 70.68, 70.65, 70.63, 70.6, 70.54, 69.99, 62.67, 50.64, 29.63, 25.90, 18.31.

**Synthesis of OEG-N<sub>3</sub>, (2-5):** TBDMS-OEG-N<sub>3</sub> (0.244 g, 0.480 mmol) was dissolved in 3 mL THF at 0 °C and TBAF (1.4 mL, 1.44 mmol) was added dropwise under nitrogen atmosphere, and the reaction mixture was stirred overnight. Thereafter, the reaction mixture was transferred into a falcon tube, and activated sulfonic acid resins and calcium carbonate were added, following that of a reported procedure by Kaburagi and Kishi.<sup>63</sup> The mixture was stirred at room temperature for an hour and filtered. The filtrate was collected and concentrated *in vacuo* to give **2-5** as a clear yellow oil (0.178 g, 95%). <sup>1</sup>H NMR (500 MHz, CDCl<sub>3</sub>) δ: 3.56 (29H, m), 3.32 (3H, m). <sup>13</sup>C NMR (100 MHz, CDCl<sub>3</sub>) δ: 72.51, 70.62, 70.58, 70.55, 70.48, 70.24, 68.96, 61.65, 50.30.

**Synthesis of CDM-OEG-N<sub>3</sub>, (2-6):** CDM (62.4 g, 0.339 mmol), HATU (129 mg, 0.339 mmol), and HOAt (46.1 mg, 0.339 mmol) were dissolved in DMF (3 mL) at 0 °C. OEG-N<sub>3</sub> (89.4 g, 0.226 mmol) was added to the mixture followed by dropwise addition of *N,N*-diisopropylethylamine (0.06 mL, 0.339 mmol). The mixture was left to stir for 30 min at 0 °C before warming up to room temperature, and further stirred overnight. DMF was then removed *in vacuo* and CDM-OEG-N<sub>3</sub> was purified using flash column chromatography on silica gel using EtOAc:DCM (1:9 to 1:3) to give **2-6** as a clear yellow oil (0.25 g, 20%). <sup>1</sup>H NMR (400 MHz, CDCl<sub>3</sub>) δ: 4.23 (2H, m), 3.66

(28H, m), 3.39 (2H, m), 2.74 (4H, m), 2.12 (3H, s).  $^{13}\text{C}$  NMR (100 MHz,  $\text{CDCl}_3$ )  $\delta$ : 173.46, 165.96, 165.80, 142.52, 142.01, 77.21, 71.04, 53.31, 9.53.

**Synthesis of CDM-OEG-BE, (2-7):** CDM-OEG- $\text{N}_3$  (204 mg, 0.364 mmol), 4-ethynylphenyl boronic acid pinacolato ester (83.0 mg, 0.364 mmol) and copper (I) iodide (3.47 mg, 18.2  $\mu\text{mol}$ ) were added to DCM (3 mL). *N,N*-Diisopropylethylamine (0.19 mL, 1.09 mmol) was then added, and the mixture was left to stir at room temperature for 3 hours. Dichloromethane was removed under reduced pressure and CDM-OEG-BE was purified using flash column chromatography on silica gel with EtOAc:acetone (v/v = 1:0 to 7:1) as the eluent to give yellow oil (0.119 g, 40 %).  $^1\text{H}$  NMR (400 MHz,  $\text{CDCl}_3$ )  $\delta$ : 8.05 (1H, s), 7.86 (4H, brs), 4.60 (2H, m), 4.22 (2H, m), 3.92 (2H, m), 3.65 (26H, m), 2.73 (4H, m), 2.12 (3H, s), 1.36 (12H, s).  $^{13}\text{C}$  NMR (100 MHz,  $\text{CDCl}_3$ )  $\delta$ : 171.63, 165.85, 165.57, 147.35, 142.21, 142.18, 135.24, 133.33, 124.77, 121.57, 83.82, 72.46, 70.50, 70.39, 70.31, 69.44, 68.87, 63.01, 50.29, 30.97, 24.86, 19.83, 9.69.

**Synthesis of CDM-OEG-BA, which is abbreviated as BA0, (2-8):** CDM-OEG-triazole-BE (100 mg, 0.127 mmol) was dissolved in acetone (2.5 mL). ammonium acetate (48.9 mg, 0.635 mmol), dissolved in deionised water (0.5 mL), was added, followed by sodium periodate (136 mg, 0.635 mmol). The mixture was allowed to stir at room temperature until completion, as monitored by LCMS. The mass of CDM-OEG-BA was observed  $[\text{M}+\text{Na}]^{+*} = 729.84$ . The compound is purified by flash chromatography on silica gel with DCM:acetone (v/v = 1:1) as the eluent to give a pale yellow oil (89.8 mg, quantitative).  $^1\text{H}$  NMR (400 MHz,  $\text{CDCl}_3$ )  $\delta$ : 7.89 (1H, s), 7.66 (2H, d,  $J = 7.8$  Hz), 6.88 (2H, d,  $J = 7.8$  Hz), 4.56 (2H, m), 4.18 (2H, m), 3.88 (2H, m), 3.59 (26H, m), 2.65 (4H, m), 2.08 (3H, s).  $^{13}\text{C}$  NMR (100 MHz,  $\text{CDCl}_3$ )  $\delta$ : 171.67, 165.85, 165.57, 147.65, 142.35, 142.20, 137.88, 134.40, 127.45, 121.35, 115.99, 77.29, 72.41, 70.40, 69.46, 69.38, 68.90, 64.05, 61.97, 50.36, 30.99, 30.76, 19.85, 9.64.

**Synthesis of PEG-OTs, (2-12):** PEG<sub>1000</sub> (5.90 g, 0.572 mol) and sodium hydroxide (0.343 g, 0.858 mol) were dissolved in 110 mL THF/ $\text{H}_2\text{O}$  (v/v = 10:1) at 0 °C. *p*-Toluenesulfonyl chloride (1.09 g, 0.572 mmol), dissolved in THF (1 mL), was added dropwise to the mixture. The mixture

was warmed to room temperature and stirred for 5 hours. The solvents were then removed under reduced pressure. The product was then purified by silica gel chromatography using methanol/dichloromethane (v/v, 1:25) as the eluent. PEG<sub>1000</sub>-OTs was obtained as colorless oil (3.52 g, 46 %). <sup>1</sup>H NMR (400 MHz, CDCl<sub>3</sub>) δ: 7.73 (2H, d), 7.29 (2H, d), 4.09 (2H, m), 3.62-3.45 (88H, m), 2.87 (1H, brs), 2.35 (3H, s).

**Synthesis of PEG-N<sub>3</sub>, (2-13):** PEG-OTs (0.965 g, 1.00 mmol) and sodium azide (0.195 g, 3.00 mmol) were charged to a round bottom flask. Anhydrous acetonitrile (10 mL) was added under nitrogen atmosphere, and the reaction mixture was stirred under reflux for 12 hours. ACN was then removed under reduced pressure, and the residue was then dissolved in chloroform (10 mL). Unreacted sodium azide was removed by celite filtration. The crude product was used directly without further purification.

**Synthesis of CDM-PEG-N<sub>3</sub>, (2-14):** CDM (0.393 g, 1.50 mmol), HATU (0.569 g, 1.50 mmol), and HOAt (0.203 g, 1.50 mmol) were dissolved in 13 mL DMF at 0 °C. PEG-N<sub>3</sub> (~1 mmol) was added to the mixture followed by dropwise addition of *N,N*-diisopropylethylamine (0.26 mL, 1.50 mmol). The mixture was left to stir for 30 min at 0 °C before warming up to room temperature, and further stirred overnight. DMF was then removed *in vacuo* and the crude oil was used without further purification.

**Synthesis of CDM-PEG-BE, (2-15):** Crude **2-14** (~1 mmol), 4-ethynylphenyl boronic acid pinacolato ester (228 mg, 1.00 mmol) and copper (I) iodide (9.52 mg, 50.0 μmol) were added to 4 mL DCM/THF (v/v = 3:1). *N,N*-Diisopropylethylamine (0.35 mL, 2.00 mmol) was then added, and the mixture was left to stir at room temperature for 3 hours. Dichloromethane was removed under reduced pressure and the crude product was used directly in the next step.

**Synthesis of CDM-PEG-BA, which is abbreviated as BA1, (2-16):** **2-15** (~1 mmol) was dissolved in acetone (5 mL). Ammonium acetate (0.385 g, 5.00 mmol), dissolved in deionised water (1 mL), was added, followed by sodium periodate (1.07 g, 5.00 mmol). The mixture was allowed to stir at room temperature for 24 hours. Thereafter, the solvents were removed under

reduced pressure till concentrated, which was then transferred into a dialysis tubing with 1 kDa MWCO, and dialysed for three days. The sample was concentrated under reduced pressure and subsequently lyophilised to give **2-16** (0.252 mg, 21% yield over 4 steps) as off white solids.  $^1\text{H}$  NMR (400 MHz,  $\text{CDCl}_3$ )  $\delta$ : 8.04 (1H, s), 7.71 (2H, d), 7.55 (2H, d), 4.55 (2H, t), 4.16 (2H, t), 3.89 (2H, t), 3.61-3.54 (~88H, m), 2.68 (4H, m), 2.10 (3H, s).  $^{13}\text{C}$  NMR (100 MHz,  $\text{CDCl}_3$ )  $\delta$ : 171.66, 165.86, 165.56, 146.58, 142.30, 142.19, 137.87, 134.19, 127.48, 121.34, 115.97, 77.28, 72.42, 70.43, 69.44, 69.35, 68.89, 64.03, 61.87, 59.50, 50.40, 30.98, 30.76, 19.84, 9.65.

### **Initial Design: Assembling of GC-BA-SPDP/rSML-A**

GC-BA-SPDP/rSML-A is assembled in a stepwise manner, starting with the amide formation between the targeting ligand and glycol chitosan under basic conditions, followed by addition of sulfo-LC-SPDP linker, and finally, conjugation of rSML-A. Reaction with sulfo-LC-SPDP linker was carried out according to protocol reported by manufacturer.<sup>64</sup> Calculations are based on repeating monosaccharide units on the polymer.

**Synthesis of GC-BA0 (2-9):** Glycol chitosan (50.0 mg, 0.282 mmol) was first suspended in DMSO (10 mL) together with the targeting ligand, BA0 (86.3 mg, 0.122 mmol). Next, DMAP was added (14.9 mg, 0.122 mmol). The mixture was then stirred at 50 °C for 24 hours. Thereafter, the mixture was dialysed with deionised water (2 L), and the water was changed every 6-8 hours for 3 days. Water was then removed *in vacuo*, and lyophilised. 23 mg of pale yellow film was obtained.

**Synthesis of GC-BA0-SPDP (2-10):** **2-9** (15.0 mg, 17.0  $\mu\text{mol}$ ) was first dispersed in 15 mL DMSO/PBS (pH 7.0). Sulfo-LC-SPDP (4.0 mg, 7.58  $\mu\text{mol}$ ) was added into the mixture and the resultant mixture was stirred for 24 hours at room temperature. Thereafter, the mixture was dialysed with deionised water (2 L), and the water was changed every 6-8 hours for 3 days. Water was then removed *in vacuo*, and lyophilised. 4.2 mg of pale yellow film was obtained.

**Synthesis of GC-BA0-SPDP/rSML-A (2-11):** rSML-A was first treated with TCEP at 4 °C in PBS for an hour and filtered by 3 kDa membrane with centrifugation condition set at 10,000 X g



for 10 minutes at 4 °C, prior to conjugation. The protein concentrate was collected and added to the PBS mixture, consisting of GC-BA0-SPDP, in 3 different mass ratios (polymer/rSML-A = 5:1, 20:1, 40:1) for 18 hours at 4 °C. Thereafter, the mixture was purified by ultrafiltration with 30 kDa membrane and centrifuged at 10,000 X g for 8 minutes at 4 °C. The concentrated was resuspended with PBS, and the process was repeated twice to obtain GC-BA0-SPDP/rSML-A.

**Synthesis of GC-BA1 (2-17):** Glycol chitosan (50.0 mg, 0.282 mmol) was first suspended in DMSO (10 mL) together with the targeting ligand, BA0 (167 mg, 0.122 mmol). Next, DMAP was added (14.9 mg, 0.122 mmol). The mixture was then stirred at 50 °C for 24 hours. Thereafter, the mixture was dialyse with deionised water (2 L), and the water was changed every 6-8 hours for 3 days. Water was then removed *in vacuo*, and lyophilised. 51 mg of pale yellow film was obtained.

**Synthesis of GC-BA1-SPDP (2-18):** 2-9 (30.0 mg, 19.4 µmol) was first dispersed in 30 mL DMSO/PBS (pH 7.0). Sulfo-LC-SPDP (4.50 mg, 8.53 µmol) was added into the mixture and the resultant mixture was stirred for 24 hours at room temperature. Thereafter, the mixture was dialyse with deionised water (2 L), and the water was changed every 6-8 hours for 3 days. Water was then removed *in vacuo*, and sample was lyophilised. 6.9 mg of pale yellow film was obtained.

**Synthesis of GC-BA1-SPDP/rSML-A (2-19):** rSML-A was first treated with TCEP at 4 °C in PBS for an hour and filtered by 3 kDa membrane with centrifugation condition set at 10,000 X g for 10 minutes at 4 °C, prior to conjugation. The protein concentrate was collected and added to the PBS mixture, consisting of GC-BA0-SPDP, in polymer/rSML-A ratio 40:1 for 18 hours at 4 °C. Thereafter, the mixture was purified by ultrafiltration with 30 kDa membrane and centrifuged at 10,000 X g for 8 minutes at 4 °C. The concentrated was resuspended with PBS, and the process was repeated twice to obtain GC-BA0-SPDP/rSML-A.

#### **New Model: Synthesis of Acid-Labile Disulfide Linker and Protected Targeting Ligand**

**Synthesis of -PEG<sub>1000</sub>-BE, which is abbreviated as BE (2-20):** 4-Ethynylphenylboronic acid pinacol ester (0.096 g, 0.422 mmol), PEG<sub>1000</sub>-N<sub>3</sub> (0.500 g, 0.422 mmol) and copper (I) iodide (4.02

mg, 0.0211 mmol) were charged to a round bottom flask containing DCM (2 mL). DIPEA (73.0  $\mu$ L, 0.422 mmol) and acetic acid (2.4  $\mu$ L, 0.042 mmol) was added dropwise, and the reaction mixture was stirred for 2 hours. The compound was then purified by dialysis with dialysis tubing (500 Da MWCO), and subsequently lyophilised. Off-white powders are obtained (0.553 g, 92%).

**Synthesis of TEG-SAc (2-21):** TEG-SAc was synthesized in grams scale using previously reported method with slight modification. To a stirred solution of tetraethylene glycol monotosylate (4.50 g, 12.9 mmol) in acetone (130 mL), potassium thioacetate (3.69 g, 32.3 mmol) and sodium iodide (0.194 g, 1.29 mmol) were added. The mixture was heated at 60 °C and stirred overnight. The solids were removed by celite filtration, and the filtrate was concentrated before loading on to the flash column. Upon purification by silica gel chromatography using acetone/dichloromethane (v/v, 1:4), TEG-SAc was obtained as colorless oil (2.74 g, 84%).

**Synthesis of TEG-SSPy (2-22):** TEG-SSPy was prepared according to a reported method. Dipyrldyl disulfide (0.960 g, 4.36 mmol) was charge to a round bottom flask containing compound **2** (1.0 g, 3.96 mmol) in methanol (40 mL), followed by portion-wise addition of sodium methoxide (0.321 g, 5.95 mmol). The resultant mixture was stirred for 2 hours. Methanol was removed by *in vacuo* evaporation, and the chloroform was added to dissolve the organic compounds. The solids precipitated were removed by celite filtration, and the filtrate was concentrated before loading on to the flash column. Upon purification by silica gel chromatography using acetone/chloroform (v/v, 1:4), TEG-SSPy was obtained as colorless oil (0.755 g, 60%).

**Synthesis of CDM-TEG-SSPy, which is abbreviated as SSPy (2-23):** CDM (0.208 g, 1.13 mmol), HATU (0.536 g, 1.41 mmol) and HOAt (0.192 g, 1.41 mmol) were charged to a round bottom flask containing anhydrous DCM (10 mL) under nitrogen atmosphere. DIPEA (0.245 mL, 1.41 mmol) and TEG-SSPy (0.300 g, 0.94 mmol) were then added, and the resultant mixture was stirred for 12 hours. After removing DCM under reduced pressure, the product was purified by silica gel chromatography with acetone/chloroform (v/v, 1:4) as the eluent. CDM-TEG-SSPy (SSPy) was obtained as colorless oil (0.312 g, 69%).

### **New Model: Solid-Phase Peptide Synthesis of modified Aurein 1.2**

Modified Aurein 1.2 was synthesized manually in 0.2 mmol scale under standard Fmoc-protocols on Sieber amide resin loaded in a reaction vessel for manual peptide synthesis. The Sieber amide resins (0.358 g, 0.2 mmol), was soaked in DMF for 30 minutes before activation with 20% piperidine/DMF for an hour. The solvents were flushed out and washed thrice with DMF. Sequential assembly of Fmoc-protected amino acids were achieved by pre-activation of Fmoc-(amino acid)-OH with HATU (1.1 equiv.), HOAt (1.1 equiv.) and DIPEA (2 equiv.) for 10 minutes in DMF prior to addition to the reaction vessel. After the attachment of the first amino acid, capping reagent (DMF/DIPEA/Ac<sub>2</sub>O, v/v = 8:1:1) was added for 30 minutes, and subsequently flushed out and washed thrice with DMF. Fmoc deprotection was achieved with 10 minutes of soaking with 20% piperidine/DMF twice. Thereafter, the resins were washed thrice with DMF before the introduction of the preactivated amino acid to couple. Boc-Gly-OH was added as the final monomer, as the Boc protecting group can be during cleavage of peptide from the resins under acidic conditions. Mild cleavage condition is 0.5% TFA in DCM for 30 minutes, while strong cleavage condition (which will cleave off all acid-labile protecting groups) is TFA/TIPS/H<sub>2</sub>O, v/v = 95:2.5:2.5 for an hour. Triisopropylsilane (TIPS) in this case acts as scavengers. The peptides were dried, crystallized and purified by reverse-phase C18 HPLC.

### **New Model: Assembling of BA-GC-SSPy, BA-GC-SS/rSML-A and BA-GC-SS/rSML-A@Aurein**

**Synthesis of polymer GC-NPhth (2-24):** Glycol chitosan 1 (1.0 g, 4.87 mmol) was dissolved in 100 mL mixture of AcOH/H<sub>2</sub>O (v/v, 1:9). Phthalic anhydride (3.61 g, 24.4 mmol) was then added and the solution was stirred at 120 °C for 24 hours before cooling down to room temperature. The solvent was removed under reduced pressure and residue washed with ethanol and diethyl ether to give GC-NPhth as an off white solid (1.02 g, 63 %).

**Synthesis of TsO-GC-NPhth (2-25):** GC-NPhth (0.500 g, 1.49 mmol), DMAP (35.0 mg, 0.289 mmol) and triethylamine (0.60 mL, 4.47 mmol) were charged to a round bottom flask containing

anhydrous DMF (23 mL) under nitrogen atmosphere. Tosyl chloride (0.425 g, 2.23 mmol) was dissolved in DMF (2 mL) and added dropwise, and the resultant mixture was stirred overnight. DMF and triethylamine was removed under reduced pressure, and the residue was washed with acetone, water and methanol over Buchner filtration. TsO-GC-NPhth was obtained as an off white solid (0.434 g, 60%).

**Synthesis of BE-GC-NPhth (2-26):** BE (0.145 g, 0.102 mmol) and TsO-GC-NPhth (0.05 g, 0.102 mmol) were charged in a round bottom flask containing anhydrous DMF and put under nitrogen atmosphere. It was cooled to 0 °C before portion-wise addition of sodium hydride (0.006 g, 0.153 mmol). The resultant mixture was stirred at room temperature overnight and quenched with MeOH. The solvents were removed under reduced pressure, and the residue was resuspended in water. The suspension was then separated by a 10 kDa membrane during centrifugation at 5,000 X g for 10 minutes. Water was added to the concentrate and centrifuged again. The process was repeated for three times. Thereafter, water was removed *in vacuo* to give **2-26** as a pale-yellow residue (54.5 mg, 32%).

**Synthesis of BA-GC-NPhth (2-27):** BE-GC-NPhth (0.050 g, 0. mmol) and sodium periodate (0.035 g, 0.165 mmol) were charged to a round bottom flask containing 0.3 mL DMF/water (v/v, 19:1). 1N hydrochloric acid (0.02 mL, 0.020 mmol) was added to the mixture, and the resultant mixture was stirred for 12 hours. The reaction mixture was then quenched with water (3 mL), and the solvents were removed under reduced pressure, and the residue was resuspended in water. The suspension was then separated by a 10 kDa membrane during centrifugation at 5,000 X g for 10 minutes. Water was added to the concentrate and centrifuged again. The process was repeated for three times. Thereafter, water was removed *in vacuo* to yield **2-27** as a pale-yellow solid (51.5 mg, 94%).

**Synthesis of BA-GC-NH<sub>2</sub> (2-28):** Hydrazine (3.77 mL, 0.121 mmol) was added to a round bottom flask containing BA-GC-NPhth (0.02 g, 0.0121 mmol) in methanol (2 mL). The resultant mixture was stirred for 12 hours. Methanol and unreacted hydrazine under reduced pressure. Diethyl ether

was added to precipitate out the polymer, which was collected by Buchner filtration. The residue collected was pale yellow, which is **2-28** (18 mg, 97%).

**Synthesis of BA-GC-SSPy (2-29):** BA-GC-NH<sub>2</sub> (6 mg, 3.92 μmol), DMAP (0.192 g, 1.57 μmol), DIPEA (0.8 μL, 4.71 μmol) was charged to a round bottom flask containing DMF (2 mL). CDM-TEG-SSPy (0.95 mg, 1.96 μmol) in DMF (0.95 mL). The reaction mixture was stirred at room temperature for 24 hours. Thereafter, the solvents were removed under reduced pressure and the residue was dispersed in water for dialysis. Dialysis tubing (14 kDa MWCO) was used, and the product was dialysed for three days, and subsequently lyophilised. **2-29** is obtained as off-white powder (20 mg, 16 %).

**Synthesis of BA-GC-SS/rSML-A (2-30):** 4 mg/mL rSML-A (50 μL, 6.95 nmol) was first incubated with 1 mM DTT (34.8 μL, 34.8 nmol) in PBS (315 μL) for an hour at 4 °C before ultrafiltration using 10 kDa membrane with the centrifugation condition set at 10,000 X g for 5 minutes at 4 °C. The protein concentrate was collected, split into two, and added to the PBS mixture, consisting of BA-GC-SSPy, in respective ratios (**A**: 89.9 μg, 3.48 nmol; **B**: 120 μg, 3.48 nmol) for 24 hours at 4 °C. Thereafter, the mixture was purified by ultrafiltration with 50 kDa membrane and centrifuged at 10,000 X g for 5 minutes at 4 °C. The concentrated was resuspended with PBS, and the process was repeated twice to obtain BA-GC-SS/rSML-A.

**Synthesis of BA-GC-SS/rSML-A@Aurein (2-30B@A):** Modified Aurein 1.2 (1 mg, 0.632 μmol) was first dissolved in 50 μL DMSO/PBS (v/v = 1:9). Aurein mixture (1.38 μL, 17.4 nmol) was then added to **2-30B** (1.74 nmol) in PBS (48.5 μL) and incubated for 24 hours at 4 °C. Thereafter, the mixture was purified by ultrafiltration with 50 kDa membrane and centrifuged at 10,000 X g for 5 minutes at 4 °C. The concentrated was resuspended with PBS, and the process was repeated twice to obtain **2-30B@A**.

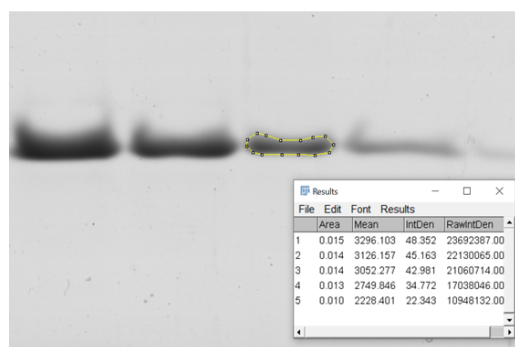
### 2.5.3 | Expression and Purification of rSML-A from *E. coli*

Recombinant protein, rSML-A was expressed and purified in accordance to the protocol developed by our collaborator, Nyugen.<sup>27</sup> An schematic illustration of the general procedure was shown in **Scheme 2.6**. Purification was done with Ni<sup>2+</sup>-NTA column due to presence of SUMO-tag in the protein which has high affinity towards Ni<sup>2+</sup>. First two rounds of washing were carried out with a buffer solution that contains 20 mM imidazole while flush out solution contains 0.5 M imidazole. The protein with the SUMO-tag was then incubated with SUMO protease to cleave off the SUMO-tag. The mixture was then purified by Ni<sup>2+</sup>-NTA column again, and the flow through was concentrated via ultrafiltration. The concentrate was then purified in FPLC (see **Figure 2.15**).

### 2.5.4 | SDS-Polyacrylamide Gel Electrophoresis (SDS-PAGE) Analysis of rSML-A

SDS-PAGE analysis was carried out to access the purity of the protein sample. Since rSML-A is approximately 29 kDa, a 12% separating gel was selected. 5x loading buffer (10 mL) was prepared with the following compositions: 2 mL of 1.5 M Tris-Cl (pH6.8), 0.5 mL of 1% bromophenol blue, 5 mL glycerol, 1 g of SDS, without the addition of 2.5 mL DTT solution. The mixture prepared were aliquoted in 10 tubes, with each tube comprising of 750 µL. 250 µL of DTT solution was then added to a tube prior to use and kept in -20 °C after usage for up to 2-3 weeks. If the analysis requires the absence of reducing agent, then 250 µL of DTT solution was replaced with DI water. The loading dye was then added to the samples, and the mixture was heat at 90 °C for 20 minutes. Precision Plus Protein unstained or all-blue standards (Bio-Rad, CA) was also loaded together in another well of the same gel, which acts as a reference for estimating protein size after staining. Gel electrophoresis was run at 60-80 V for the stacking gel portion, and 80-100 V for the running gel portion, till the loading dye reaches near the end of the gel. The gel was then stained with Coomassie staining solution for 30, followed by destaining for another 30 minutes with destaining solution, and overnight in water till the gel became clear. Gel images were captured by GS-800 Calibrated Densitometer by Bio-Rad.

For a specific study that required a plot of mean intensity against amount of protein, Fiji ImageJ was used to compute the mean intensity values. **Figure 2.26** (top left.) below showed how the values were obtained by outlining the gel bands. Upon obtaining the values for mean intensities of different amount of rSML-A, a graph was plotted in **Figure 2.18**. The mean intensities of sample bands were recorded too and subtracted from the background signals. ‘x’ values (amount of protein) were then calculated.



*Gel - Concentration series*

Amount of rSML-A (µg)	Area	Mean	IntDen	RawIntDen	Mean intensity (-BG)
5	0.015	3296.103	48.352	23692387	2703.3826
4	0.014	3126.157	45.163	22130065	2533.4366
3	0.014	3052.277	42.981	21060714	2459.5566
2	0.013	2749.846	34.772	17038046	2157.1256
1	0.01	2228.401	22.343	10948132	1635.6806
0.5	0.009	1522.618	13.498	6614254	929.8976
0.2	0.007	854.697	6.382	3127338	261.9766

Background (BG)				
Entry No.	Area	Mean	IntDen	RawIntDen
1	0.022	571.825	12.361	6056771
2	0.022	600.222	12.975	6357552
3	0.022	603.916	13.054	6396677
4	0.022	589.592	12.745	6244959
5	0.022	598.047	12.928	6334517
Average =		592.7204		

*Reaction crude between 2-30 with rSML-A to for, 2-30A and 2-30B*

		Area	Mean	IntDen	RawIntDen	Mean intensity (-BG)	x value (amount of unreacted rSML-A) in µg
Bottom	A	0.01	2136.845	22.306	10929963	1068.4962	0.532894329
	B	0.01	2013.838	20.882	10232310	945.4892	0.45168877
Top	A	0.01	2318.224	24.039	11778897	1249.8752	0.680010915
	B	0.01	2127.048	22.056	10807530	1058.6992	0.525923263

Background (BG)				
Entry No.	Area	Mean	IntDen	RawIntDen
1	0.022	1075.981	23.557	11543127
2	0.022	993.95	21.761	10663097
3	0.022	1099.181	24.065	11792019
4	0.022	1046.968	22.922	11231878
5	0.022	1125.664	24.645	12076122
Average =		1068.3488		

*After washing twice with PBS*

	Area	Mean	IntDen	RawIntDen	Mean intensity (-BG)	x value (amount of unreacted rSML-A) in µg
A	0.021	1314.615	27.932	13686460	305.0638	0.190989437
B	0.021	1317.461	27.992	13716085	307.9098	0.191721412

Background (BG)				
Entry No.	Area	Mean	IntDen	RawIntDen
1	0.022	1028.741	22.17	10863504
2	0.022	1088.951	23.468	11499322
3	0.022	943.61	20.336	9964526
4	0.022	1013.805	21.849	10705783
5	0.022	972.649	20.962	10271176
Average =		1009.5512		

**Figure 2.26** | Image of how the mean intensity values were obtained using Fiji ImageJ (top, left), and values recorded (Area, Mean, IntDen, RawIntDen) are shown in tables above. Mean intensity is obtained by subtracting the mean values from the average of the gel background.

## 2.5.5 | *In Vitro* Biological Assays

### Cell Culture

MDA-MB-231 and NIH3T3 cells were cultured in at 37 °C in a humidified chamber with 5% CO<sub>2</sub>. They were grown and maintained in Dulbecco’s Modified Eagle Medium (DMEM) (Gibco, high glucose with L-glutamine) supplemented with 10% (v/v) fetal bovine serum (FBS), 100 U/mL

streptomycin, 100 µg/mL penicillin. The cells were passaged with 0.025% trypsin-EDTA for cell detachment every 3-4 days upon their growing to a confluency of approximately 80%. New cells were thawed and cultured for two weeks prior to use.

### **Annexin V/ Propidium Iodide (PI) Assay**

MDA-MB-231 cells were seeded in 24-well plates at a density of  $8 \times 10^5$  cells per well 18 hours before experiment. Cells were incubated with GC-BA0-SPDP/rSML-A conjugate at different polymer/rSML-A weight ratios (5:1, 20:1, 40:1), the polymer alone GC-BA0-SPDP, and two negative controls, PBS and rSML-A for 12 hours at 37 °C with 5% CO<sub>2</sub>. Thereafter, the cells were gently washed with PBS, and trypsin was added, making sure that they are not over-trypsinised (by visualization using light microscope). The trypsin was then quenched by addition of media (1 mL) and transferred to respective eppendorf tubes and centrifuged at 0.4 rcf for 5 minutes to pellet down the cells and remove the supernatant. The cells were then resuspended in ice-cold PBS (1 mL) and pelleted down again by centrifugation. The cells were resuspended in annexin-binding buffer (1x), and the samples were diluted to  $1 \times 10^6$  cells per 0.1 mL of buffer. Annexin V (5 µL) and PI (1 µL, 100 µL/mL) were added to each 100 µL of cell suspension and incubated for 15 minutes. Thereafter, 400 µL 1x Annexin V binding buffer was added to each tube, and the samples were kept on ice. Flow cytometry analysis was carried out using BD LSRFortessa X-20.

### **Cytotoxicity Assay**

Cells were seeded in transparent 96-well plate at a density of  $1 \times 10^4$  cells per well 18 hours (in triplicates) before experiment. Old media were discarded, and 70 µL of new media (depending on the requirement of the experiment to be run) were added to each well. Stock solutions of different concentrations of the substrates to be tested were prepared beforehand, with the difference being balanced out by PBS (final volume of 8 µL per well), and DMEM was added to the stock (22 µL per well). As such 30 µL of substrate/media mixtures can be added to each well using the multichannel micropipette (30 µL - 300 µL). The substrates were incubated with the cells in accordance to the duration required (usually 70 to 72 hours) at 37 °C in the incubator. Thereafter,



the media were aspirated and 110  $\mu$ L of normal grown media mixed with WST-1 or WST-8 (100  $\mu$ L of media + 10  $\mu$ L of WST-1 or WST-8) were added to each well using the multichannel pipette and incubated for an hour at 37 °C in the incubator in dark. Absorbance of the water-soluble formazan dye would then be quantified by Tecan Infinite 2—PRO microplate spectrometer at absorbance wavelength of 450 nm, and reference wavelength at 600 nm. The higher the amount of formazan dye detected indicates higher metabolic activity of the cells (more cells are alive). Cell viability of each concentrations were tabulated and normalized as a percentage against the negative PBS control (cell viability = 100%).

### **Confocal Microscopy**

The substrates to be imaged were first tagged with rhodamine or rhodamine green, depending on the conditions of the experiment. The reactions were carried out in accordance to the protocol described by the manufacturer. Thereafter, excess fluorophores were removed by ultrafiltration with MWCO 10 kDa (for rSML-A alone) or 50 kDa (for the rest of the substrates). The cells were seeded on glass coverslips in a 24-well plate at a density of  $1 \times 10^5$  cells per well. Each well was treated with different substrates (with a final rSML-A concentration at 0.8  $\mu$ g/mL in each well), and incubated for either 4 hours, or 6 hours, or 12 hours, depending on the condition of the experiments. Thereafter, the media were aspirated and washed thrice with PBS. The cells were stained with DAPI for better visualization purpose at (1:1000 dilution) and incubated at room temperature for an hour. Thereafter, the samples were fixed with 4% paraformaldehyde for 30 minutes prior to washing with PBS for three times, and the glass coverslips were then gently removed from the wells and placed on top of the glass slides, with a drop of PBS/glycerol mixture in between. Staining with LysoTracker Red DND-99 and LysoTracker Green DND 26 were carried out prior to DAPI staining, according to the protocol provided by the manufacturer. Cell images were acquired with a confocal laser scanning microscope Zeiss LSM 800, and the excitation wavelength used were 488 nm (for Rhodamine Green or LysoTracker Green DND 26 samples), 568 nm (for Rhodamine B or LysoTracker Red DND 99 samples), and 305 nm for DAPI.

## 2.6 | References

1. Siegel, R.L; Miller, K.D.; Jemal, A. Cancer Statistics, 2018. *CA-Cancer J. Clin.* **2018**, 68, 7-30.
2. Ministry of Health Singapore, Principal Causes of Death. <https://www.moh.gov.sg/resources-statistics/singapore-health-facts/principal-causes-of-death> (accessed Aug. 15, 2019).
3. Mura, S.; Nicolas, J.; Couvreur, P., Stimuli-Responsive Nanocarriers for Drug Delivery. *Nat. Mater.* **2013**, 12, 991-1003.
4. Matsumura, Y.; Maeda, H., A New Concept for Macromolecular Therapeutics in Cancer Chemotherapy: Mechanism of Tumoritropic Accumulation of Proteins and the Antitumor Agent Smancs. *Cancer Res.* **1986**, 46, 6387-6392.
5. Carmeliet, P.; Jain, R.K., Angiogenesis in Cancer and Other Diseases. *Nature.* **2000**, 407, 249-257.
6. Østergaard, L.; Tietze, A.; Nielsen, T.; Drasbek, K.R.; Mouridsen, K.; Jespersen, S.N.; Horsman, M.R., The relationship Between Tumor Blood Flow, Angiogenesis, Tumor Hypoxia, and Aerobic Glycolysis. *Cancer Res.* **2013**, 73, 5618-5624.
7. Balendiran, G.K.; Dabur, R.; Fraser, D., The Role of Glutathione in Cancer. *Cell Biochem. Funct.* **2004**, 22, 343-352.
8. Wang, J.; Tao, X.; Zhang, Y.; Wei, D.; Ren, Y., Reversion of Multidrug Resistance by Tumor Targeted Delivery of Antisense Oligodeoxynucleotides in Hydroxypropyl-Chitosan Nanoparticles. *Biomaterials* **2010**, 31, 4426-4433.
9. Wang, S.; Yin, D.; Wang, W.; Shen, X.; Zhu, J.-J.; Chen, H.-Y.; Liu, Z., Targeting and Imaging of Cancer Cells via Monosaccharide-Imprinted Fluorescent Nanoparticles. *Sci. Rep.* **2016**, 6, 22757-22768.
10. Mocellin, S.; Rossi, C.R.; Pilati, P.; Nitti, D., Tumor Necrosis Factor, Cancer and Anticancer Therapy. *Cytokine Growth F. Rev.* **2005**, 16, 35-53.

11. Scott, A.M.; Wolchok, J.D.; Old, L.J., Antibody Therapy of Cancer. *Nat. Rev. Cancer* **2012**, *12*, 278-287.
12. Mitragotri, S.; Burk, P.A.; Langer, R., Overcoming the Challenges in Administering Biopharmaceuticals: Formulation and Delivery Strategies. *Nat. Rev. Drug Discov.* **2014**, *13*, 655-672.
13. He, C.; Tang, Z.; Tian, H.; Chen, X., Co-Delivery of Chemotherapeutics and Proteins for Synergistic Therapy. *Adv. Drug Delivery Rev.* **2016**, *98*, 64-76.
14. Gu, Z.; Biswas, A.; Zhao, M.; Tang, Y., Tailoring Nanocarriers for intracellular protein delivery. *Chem. Soc. Rev.* **2011**, *40*, 3638-3655.
15. Leader, B.; Baca, Q.J.; Golan, D.E., Protein Therapeutics: A Summary and Pharmacological Classification. *Nat. Rev Drug Discov.* **2008**, *7*, 21-39.
16. de Virgilio, M., Lombardi, A., Caliandro, R.; Fabbrini, M. S., Ribosome-Inactivating Proteins: from Plant Defense to Tumor Attack., *Toxins* **2010**, *2*, 2699-2737.
17. Zeng, M.; Zheng, M.; Lu, D.; Wang, J.; Jiang, W.; Sha, O., Anti-Tumor Activities and Apoptotic Mechanism of Ribosome-Inactivating Proteins. *Chin. J. Cancer* **2015**, *34*, 325-334.
18. Krauspenhaar, R.; Eschenburg, S.; Perbandt, M.; Kornilov, V.; Konareva, N.; Mikailova, I.; Stoeva, S.; Wacker, R.; Maier, T.; Singh, T.; Mikhailov, A.; Voelter, W.; Betzel, C., Crystal Structure of Mistletoe Lectin I from *Viscum album*. *Biochem. Biophys. Res. Commun.* **1999**, *257*, 418-424.
19. Bantel, H.; Engels, I. H.; Voelter, W.; Schulze-Osthoff, K.; Wesselborg, S., Mistletoe Lectin Activates Caspase-8/FLICE Independently of Death Receptor Signaling and Enhances Anticancer Drug-induced Apoptosis. *Cancer Res.* **1999**, *59*, 2083-2090.
20. Beztsinna, N.; de Matos, M.B.C.; Walther, J.; Heyder, C.; Hildebrandt, E.; Leneweit, G.; Mastrobattista, E.; Kok, R.J., Quantitative Analysis of Receptor Mediated Uptake and Pro-Apoptotic Activity of Mistletoe Lectin-1 by High Content Imaging. *Sci. Rep.* **2018**, *8*, 2768-2777.

21. Vervecken, W.; Kleff, S.; Pfüller, U. Büssing, A., Induction of Apoptosis by Mistletoe Lectin I and its Subunits. No Evidence for Cytotoxic Effects Caused by Isolated A- and B-Chains. *Int. J. Biochem. Cell Biol.* **2000**, *32*, 317-326.
22. Liu, B.; Bian, H.J.; Bao, J.K., Plant Lectins: Potential Antineoplastic Drugs from Bench to Clinic. *Cancer Lett.* **2010**, *287*, 1-12.
23. Endo, Y.; Chan, Y.; Lin, A.; Tsurugi, K.; Wool, I.G., The Cytotoxins Alpha-Sarcin and Ricin Retain Their Specificity when Tested on a Synthetic Oligoribonucleotide (35-mer) that Mimics a Region of 28 S Ribosomal Ribonucleic Acid. *J. Biol. Chem.* **1988**, *263*, 7917-7920.
24. Yang, P.; Jiang, Y.; Pan, Y.; Ding, X.; Rhea, P.; Ding, J.; Hawke, D. H.; Felsher, D.; Narla, G.; Lu, Z.; Lee, R. T., Mistletoe Extract Fraxini Inhibits the Proliferation of Liver Cancer by Down-Regulating c-Myc Expression. *Sci. Rep.* **2019**, *9*, 6428-6439.
25. Krejsa, C.; Rpgge, M.; Sadee, W., Protein Therapeutics: New Applications for Pharmacogenetics. *Nat. Rev. Drug Discov.* **2006**, *5*, 507-552.
26. Pavlou, A.K.; Reichert, J.M., Recombinant Protein Therapeutics - Success Rates, Market Trends and Values to 2010 *Nat. Biotechnol.* **2004**, *22*, 1513-1519.
27. Nyguen, Q.T., Biochemical and Structural Characterization of a Type 2 Ribosome-Inactivating Protein from *Viscum ovalifolium*, PhD Dissertation, Nanyang Technological University, Singapore, 2016.
28. Narang, A.S.; Mahato, R.I. Therapeutic Potential of Targeted Drug Delivery. In *Targeted Delivery of Small and Macromolecular Drugs*; Narang, A. S., Mahato, R. I., Ed.; CRC Press: Florida, United States, 2010; pp 1-10.
29. Postupalenko, V.; Desplancq, D.; Orlov, I.; Arntz, Y.; Spehner, D.; Mely, Y.; Klaholz, B.P.; Schultz, P.; Weiss, E.; Zuber, G., Protein Delivery System Containing a Nickel-Immobilized Polymer for Multimerization of Affinity-Purified His-Tagged Proteins Enhances Cytosolic Transfer. *Angew. Chem., Int. Ed.* **2015**, *54*, 10583-10586.
30. Peer, D.; Karp, J. M.; Hong, S.; Farokhzad, O. C.; Margalit, R.; Lancer, R., Nanocarriers as an Emerging Platform for Cancer Therapy. *Nat. Nanotechnol.* **2007**, *2*, 751-760.

31. Fu, A.; Tang, R.; Hardie, J.; Farkas, M. E.; Rotello, V. M., Promises and Pitfalls of Intracellular Delivery of Proteins. *Bioconjugate Chem.* **2014**, *25*, 1602-1608.
32. Ma., S.-F.; Nishikawa, M.; Katsumi, H.; Yamashita, H.; Hashida, M., Cationic Charge-Dependent Hepatic Delivery of Amidated Serum Albumin *J. Control. Release* **2005**, *102*, 583-594.
33. Lee, H.J.; Pardridge, W.M., Monoclonal Antibody Radiopharmaceuticals: Cationization, Pegylation, Radiometal Chelation, Pharmacokinetics, and Tumor Imaging. *Bioconjugate Chem.* **2003**, *14*, 546-553.
34. Khan, M.; Ong, Z.Y.; Wiradharma, N.; Attia, A. B.E.; Yang, Y.-Y., Advanced Materials for Co - Delivery of Drugs and Genes in Cancer Therapy. *Adv. Healthcare Mater.* **2012**, *1*, 373-392.
35. Yin, H.; Kauffman, K.J.; Anderson, D.G., Delivery Technologies for Genome Editing. *Nat. Rev. Drug Discov.* **2017**, *16*, 387-399.
36. Abuchowski, A.; van Es, T.; Palczuk, N.C., Alteration of Immunological Properties of Bovine Serum Albumin by Covalent Attachment of Polyethylene Glycol. *J. Biol. Chem.* **1977**, *252*, 3578-3581.
37. Abuchowski, A.; McCoy, J.R.; Palczuk, N.C.; van Es, T.; Davis, F. F., Effect of Covalent Attachment of Polyethylene Glycol on Immunogenicity and Circulating Life of Bovine Liver Catalase. *J. Biol. Chem.* **1997**, *252*, 3582-3586.
38. Kataoka, K.; Harada, A.; Nagasaki, Y., Block Copolymer Micelles for Drug delivery: design, characterization and biological significance *Adv. Drug Delivery Rev.* **2001**, *47*, 113-131.
39. Caliceti, P.; Veronese, F.M., Pharmacokinetic and Biodistribution Properties of Poly(ethylene glycol)-Protein Conjugates. *Adv. Drug Deliv. Rev.* **2003**, *55*, 1261-1277.
40. Ekladios, I.; Colson, Y. L.; Grinstaff, M. W., Polymer–Drug Conjugate Therapeutics: Advances, Insights and Prospects. *Nat. Rev. Drug Discov.* **2019**, *18*, 273-294.
41. Hakomori, S., Tumor Malignancy Defined by Aberrant Glycosylation and Sphingo(glyco)lipid Metabolism. *Cancer Res.* **1996**, *56*, 5309-5318.

42. Dube, D.H.; Bertozzi, C.R., Glycans in Cancer and Inflammation--Potential for Therapeutics and Diagnostics. *Nat. Rev. Drug Discov.* **2005**, *4*, 477-488.
43. Kannagi, R.; Izawa, M.; Koike, T.; Miyazaki, K.; Kimura, N., Carbohydrate-Mediated Cell Adhesion in Cancer Metastasis and Angiogenesis. *Cancer Sci.* **2004**, *95*, 377-384.
44. Deshayes, S.; Cabral, H.; Ishii, T.; Miura, Y.; Kobayashi, S.; Yamashita, T.; Matsumoto, A.; Miyahara, Y.; Nishiyama, N.; Kataoka, K., Phenylboronic Acid-Installed Polymeric Micelles for Targeting Sialylated Epitopes in Solid Tumors. *J. Am. Chem. Soc.* **2013**, *135*, 15501-15507.
45. Levonis, S.M.; Kiefel, M.J.; Houston, T.A., Boronolactin with Divergent Fluorescent Response Specific for Free Sialic Acid. *Chem. Commun.* **2009**, *17*, 2278-2280.
46. Teichert, J.F.; Mazunin, D.; Bode, J.W., Chemical Sensing of Polyols with Shapeshifting Boronic Acids as a Self-Contained Sensor Array. *J. Am. Chem. Soc.* **2013**, *135*, 11314-11321.
47. Rozema, D.B.; Lewis, D.L.; Wakefield, D.H.; Wong, S.H.; Klein, J.J.; Roesch, P.L.; Bertin, S.L.; Reppen, T.W.; Chu, Q.; Blokhin, A.V.; Hagstrom, J.E.; Wolff, J.A., Dynamic PolyConjugates for Targeted *In Vivo* Delivery of siRNA to Hepatocytes. *Proc. Natl. Acad. Sci. U.S.A.* **2007**, *104*, 12982-12987.
48. Saito, G.; Swanson, J.A.; Lee, K.D., Drug Delivery Strategy Utilizing Conjugation via Reversible Disulfide Linkages: Role and Site of Cellular Reducing Activities. *Adv. Drug Deliv. Rev.* **2003**, *55*, 199-215.
49. Gamcsik, M.P.; Kasibhatla, M.S.; Teeter, S.D.; Colvin, O.M., Glutathione Levels in Human Tumors. *Biomarkers* **2012**, *17*, 671-691.
50. Saha, B.; Saikia, J.; Das, G., Correlating Enzyme Density, Conformation and Activity on Nanoparticle Surfaces in Highly Functional Bio-Nanocomposites. *Analyst* **2015**, *140*, 532-542.
51. Dynamic Biosensors, List of Protein Hydrodynamic Diameters DH. <https://www.dynamic-biosensors.com/project/list-of-protein-hydrodynamic-diameters/> (accessed 20 Aug 2019).

52. Liu, M.; Tao, Y.; Shu, Y.; LaRochelle, J. R.; Steinauer, A.; Thompson, D.; Schepartz, A.; Cheng, Z.-Y.; Liu, D. R., Discovery and Characterization of a Peptide that Enhances Endosomal Escape of Delivered Proteins *In Vitro* and *In Vivo*. *J. Am. Chem. Soc.* **2015**, *137*, 14084-14093.
53. Pan, H.; Grow, M. E.; Wilson, O.; Daniel, M.-C., A New Poly(propylene imine) Dendron as Potential Convenient Building-Block in the Construction of Multifunctional Systems. *Tetrahedron* **2013**, *69*, 2799-2806.
54. Cubberley, M.S.; Iverson, B.L., <sup>1</sup>H NMR Investigation of Solvent Effects in Aromatic Stacking Interactions. *J. Am. Chem. Soc.* **2001**, *123*, 7560-7563.
55. Wuts, P.G.M. Greene's Protective Groups in Organic Synthesis; John Wiley & Sons, Inc.: New Jersey, 2014.
56. Zhang, Y.; Fechter, E.J.; Wang, T.-S.A.; Barrett, D.; Walker, S.; Kahne, D.E., Synthesis of Heptaprenyl-Lipid IV to Analyze Peptidoglycan Glycosyltransferases. *J. Am. Chem. Soc.* **2007**, *129*, 3080-3081.
57. Shao, C.; Wang, X.; Zhang, Q.; Luo, S.; Zhao, J.; Hu, Y., Acid-Base Jointly Promoted Copper(I)-Catalyzed Azide-Alkyne Cycloaddition. *J. Org. Chem.* **2011**, *76*, 6832-6836.
58. Matsubara, R.; Koide, M.; Shin, Y.-S.; Shimada, T.; Hayashi, M., A Concise Synthesis of Asymmetrically 4,5-Disubstituted 9,9-Dimethyl-9*H*-Xanthenes. *Synthesis*, **2015**, *47*, 187-192.
59. Wang, X.; Hu, Y.-Z.; Chen, A.; Wu, Y.; Aggeler, R.; Low, Q.; Kang, H. C.; Gee, K. R., Water-Soluble Poly(2,7-dibenzosilole) as an Ultra-Bright Fluorescent Label for Antibody-Based Flow Cytometry. *Chem. Commun.* **2016**, *52*, 4022-4024.
60. Ifuku, S.; Miwa, T.; Morimoto, M.; Saimoto, H., Preparation of Highly Chemoselective *N*-Phthaloyl Chitosan in Aqueous Media. *Green Chem.* **2011**, *13*, 1499-1502.
61. Binette, A.; Gagnon, J., Regioselective Silylation of *N*-Phthaloylchitosan with TBDMS and TBDPS Groups. *Biomacromolecules* **2007**, *8*, 1812-1815.

62. Chen, Y.; Ye, Y.; Wang, L.; Guo, Y.; Tan, H., Synthesis of Chitosan C6-Substituted Cyclodextrin Derivatives with Yosyl-Chitin as the Intermediate Precursor. *J. Appl. Polym. Sci.* **2012**, *125*, E378-E383.
63. Kuburagi, Y.; Kishi, Y., Operationally Simple and Efficient Workup Procedure for TBAF-Mediated Desilylation: Application to Halichondrin Synthesis. *Org. Lett.* **2007**, *9*, 723-726.
64. Thermo Fisher Scientific Inc., Instructions: SPDP Cross linkers. [http://tools.thermofisher.com/content/sfs/manuals/MAN0011212\\_SPDP\\_CrsLnk\\_UG.pdf](http://tools.thermofisher.com/content/sfs/manuals/MAN0011212_SPDP_CrsLnk_UG.pdf) (accessed 30 Aug 2019).



## **Chapter 3 | A Facile Synthetic Approach to PGO Derivatives Using Chitosan Scaffolds and Evaluation of the Resultant Modifications**

### **Abstract**

The development of antibiotic resistance is an inevitable outcome of using antibiotics to combat bacterial infections, possibly due to a narrow selection of drugs available with limited range of mechanisms, making it difficult to combat the rise of antibiotic-resistant bacteria (ARB). Hence, it is important to invest more resources in discovery of new antibiotics with new mechanism of actions, rather than in improvement of conventional targets. In order to achieve this, in-depth understanding of the biology and mechanisms behind the mode of action of antibiotics and ARB are essential. Particularly, the biosynthetic pathway of peptidoglycan (PG) in the bacterial cell wall garnered a lot of interest since the formation of this three-dimensional network occurs mostly in the periplasmic space, thus making it more susceptible to interferences, in which antibiotics such as penicillin and vancomycin takes advantage of. Interestingly, the main formation of PG network is consistent between different bacterial strains and regardless of their gram distinction. This makes it a very intriguing target for further exploration and better understanding of the biology, bioimaging purposes, as well as mechanistic studies of the development of resistant strains. However, access to PG substrates were restricted, especially for the analysis of the peptidoglycan glycosyltransferase (PGT) domain in penicillin binding protein (PBP) due to limitations experienced in producing a library of PGOs for SAR studies. Our group came up with the unconventional method of accessing these PGOs by ‘top-down’ approach which utilise a chitosan scaffold. Uptake and recognition of the PGOs substrate by the enzymes in the biological studies, such as lysozyme degradation and incorporation of our PGO into the bacterial cell wall demonstrated the practicability of this approach. Furthermore, the feasibility of this approached was tested by synthesis of two other PGO derivatives that were not reported before to the best of my knowledge.

## 3.1 | Introduction

### 3.1.1 | General Overview of Antibiotics and Antibiotic Resistance

Antibiotics are a subcategory of antimicrobial drugs designed to be highly active against bacteria. They are either bactericidal or bacteriostatic (slow or inhibit growth). Several classes of antibiotics (see **Figure 3.1**) have been developed over the decades with various mode of actions.<sup>1-2</sup> For instance, beta-lactams such as more commonly seen penicillin and amoxicillin, are bactericidal to most of the Gram-positive (G+ve) bacteria by preventing the amino acid chains in the cell wall to crosslink.<sup>3</sup> This causes the weakening of cell wall and inability to maintain required osmotic gradient, which ultimately leads to cell lysis and cell death. Aminoglycosides, such as kanamycin and streptomycin, on the other hand are effective against most of the Gram-negative bacteria (G-ve), in which they bind to 30S ribosome, thereby disrupting and inhibiting protein synthesis necessary for growth and survival.<sup>4</sup>

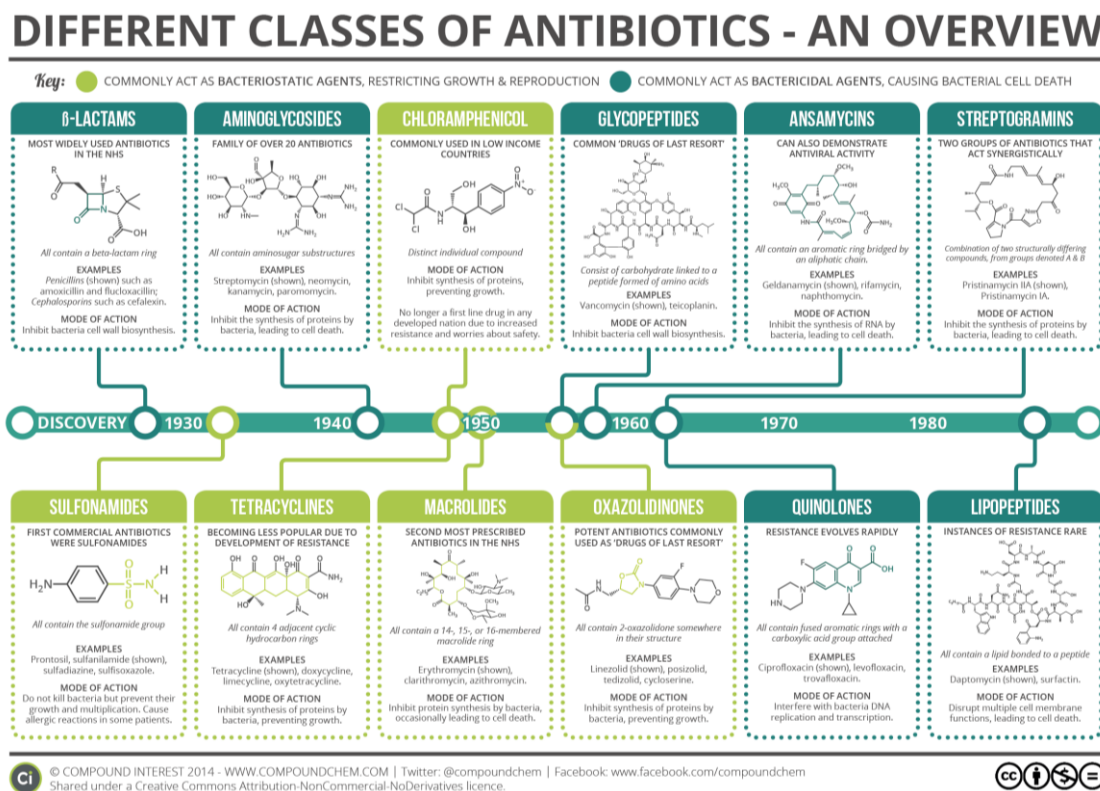


**Figure 3.1** | A general schematic illustration on some of the different classes of antibiotics available till 2003. Image adapted from ref. 2.

From 2000 to 2015, 32 new drugs were launched to counter bacterial infections (see **Figure 3.2a** for more details).<sup>1</sup> Of which, two of them are combinations of new drugs used in synergy with existing antibiotics. Out of these new drugs, only six of them belong to new classes (see **Figure 3.2b**) which target G+ve bacteria with the exception of Avibactam (active against G-ve bacteria).

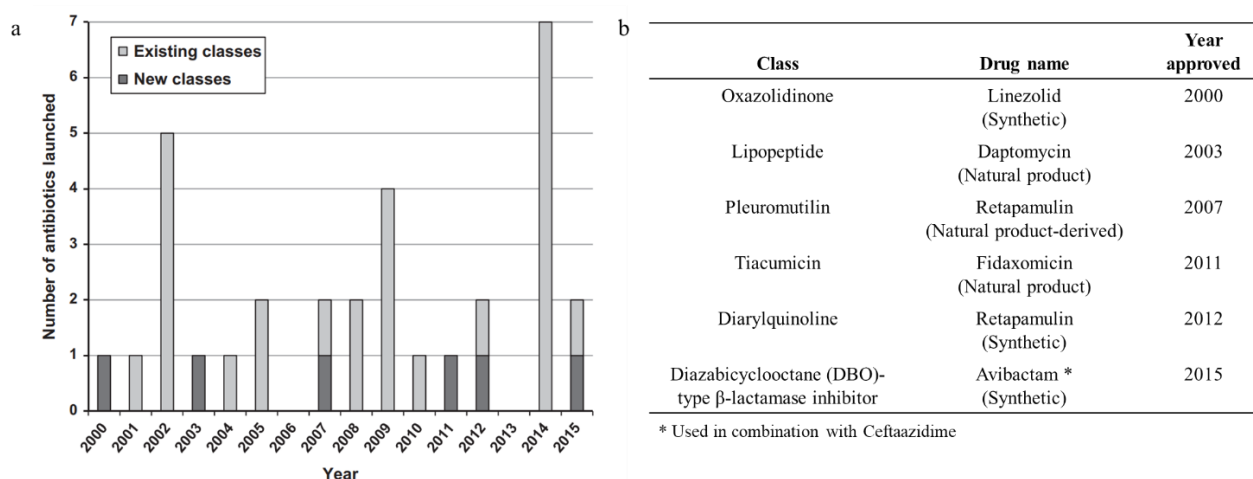


**Figure 3.2 | (a)** Statistic of new antibiotic approvals from 2000 to 2015. A total of 32 new antibiotic drugs were launched, with two of them used in combinations with existing antibiotics. Reprinted with permission from ref. 1. Copyright (2019), Springer Nature. **(b)** A list of new first-in-class antibiotics launched from 2000 to 2015.

One of the reasons for the constant need for discovery of new antibiotics is to combat bacterial infections that have developed resistance to known antibiotics, shortly after their approvals.<sup>5</sup> For instance, in the case of new classes of antibiotics, such as lipopeptide (daptomycin) and oxazolidinone (linezolid), which were introduced in 2000 and 2003 respectively, cases of bacteria developing resistance to them were reported in 2001 and 2005 respectively.<sup>5</sup> This development of antibiotic resistance to bacteria strains that were once effective are known as secondary resistance. In contrast, primary resistance stem from inherent resistance in some bacterial types or strains to certain antibiotics. Secondary resistance can be developed through mutations in chromosomal genes, with the outcome of modifying certain biosynthetic pathways, altering of target sites, or simply inactivating the antibiotics.<sup>6-7</sup> Certain bacteria are able to develop efflux pumps as some sort of defensive mechanism to avoid the action of antibiotics by expelling them. These genetic

mutations can be spread through horizontal gene transfer. In addition, bacterial population as a whole is able to exhibit heteroresistance, in which one or more subpopulations exhibit much greater levels of antibiotic resistance as compared to the majority.<sup>8</sup> This poses a great clinical concern as these subpopulations are difficult to detect and often result in inaccurate prescription such as higher dosage or longer antibiotic exposure, which may lead to failure in treatment and enhances the development of secondary resistance. The situation is worsened with the aid of globalisation, facilitating the spread of antibiotic resistant bacteria (ARB) and their antibiotic resistance gene (ARG) on a global scale.

Although it is more commonly known as antimicrobial resistance (AMR), WHO stated that this term should be only applicable in the context whereby bacteria become antibiotic-resistant.<sup>9</sup>  
<sup>10</sup> Over the years, AMR has been becoming a huge world health problem mainly due to abuse of antimicrobial drugs thereby accelerating the rate of resistance development, together with increasing interconnectivity of the world which facilitate in spreading of the resistant strains. It was predicted in 2016 that annual global death toll will grow to 10 million by 2050, according to a review commissioned by the government from United Kingdom with AMR data released by the British government.<sup>5,11</sup> Based on a report released by The World Bank in 2017, AMR will cost us economically, which may be as severe as during the time of financial crisis experienced in 2008-2009.<sup>12</sup> They estimated that the global GDP will drop by approximately 1.1 to 3.8 percent by 2050 as a result of AMR, with the lower income countries being affected the most.

The development of antibiotic resistance is an inevitable outcome of using antibiotics to combat bacterial infections. A narrow selection of drugs available, with limited range of mechanisms, will be difficult in combating the rise of ARB.<sup>13</sup> Hence, it is important to invest more resources in discovery of new antibiotics with new mechanism of actions, rather than in improvement of conventional targets. In order to achieve this, it is necessary to understand the biology and mechanisms behind the mode of action of antibiotics and ARB.

### 3.1.2 | Peptidoglycan (PG) in Gram-Positive (G+ve) and Gram-Negative (G-ve) Bacteria

It has been widely adapted to classify most bacteria into two main categories, Gram-positive (G+ve) and Gram-negative (G-ve), according to a staining method developed by Hans Christian Gram.<sup>14-15</sup> It is often used in preliminary morphologic identification of bacteria, since it is fast and relatively inexpensive. Briefly, the bacteria are first treated with crystal violet solution for half a minute, followed by Gram's iodine solution (comprising of iodine and potassium iodide) for another minute, before decolorising with ethanol or acetone and subsequent addition of safranin solution as a counterstain. If purple-violet color is retained, the bacteria are classified as Gram-positive, whereas if the color of the counterstain (i.e. pink due to safranin presence) is observed, then the bacteria is classified as Gram-negative.

The outcome observed is due to the morphological difference between them, in which G-ve cells have much thinner peptidoglycan (PG) layer as compared to G+ve cells (see Figure 3.3). Crystal violet-iodine complexes formed are easily washed away from the thin PG layer (~5 nm) when outer membrane of G-ve bacteria was disrupted during the treatment with ethanol or acetone. Whereas the crystal complexes are trapped in the thick, multi-layered of PG (20-50 nm) in G+ve bacteria remains even during the same treatment process.

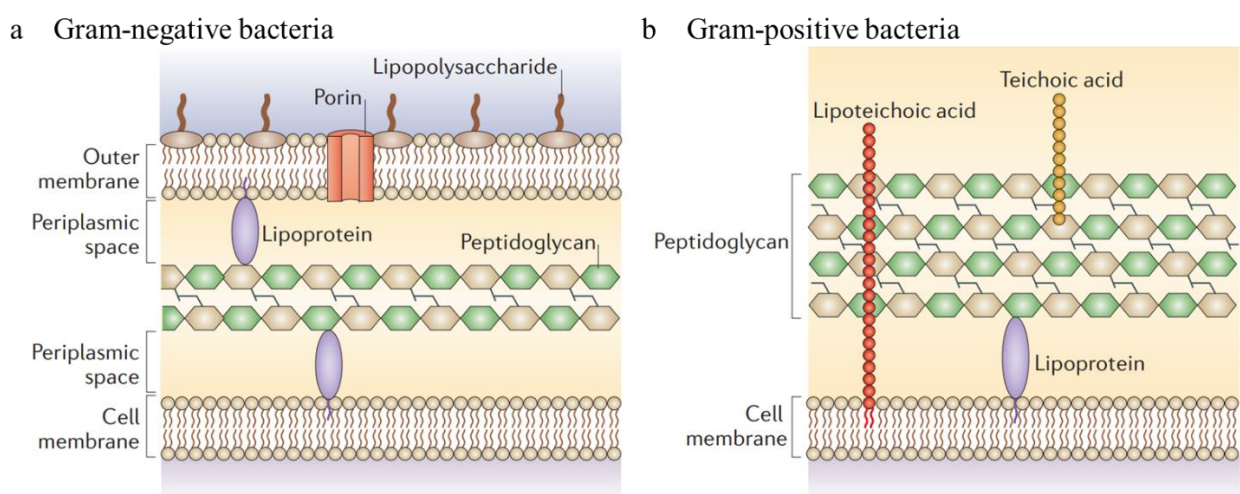
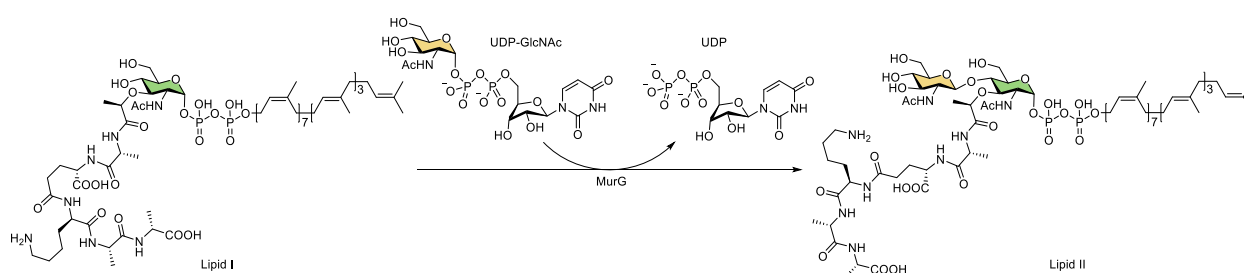


**Figure 3.3** | A schematic illustration of the structure of cell wall in (a) Gram-negative bacteria and (b) Gram-positive bacteria. Reprinted with permission from ref. 16. Copyright (2019), Springer Nature.

Peptidoglycan consists of repeating units of *N*-acetylglucosamine (GlcNAc or NAG) linked to *N*-acetylmuramic acid (MurNAc or NAM) in an alternating manner by  $\beta$ -(1,4)-glycosidic linkages, with the latter coupled to a pentapeptide at C3 hydroxyl group. Cross-linking between the pentapeptide on different NAG-NAM chains give rise to the three-dimensional net-like mesh structure that aid in regulating osmotic pressure and serves as a platform for carbohydrates, lipids and proteins to embed in. It is worthy to note that different bacteria strains have different compositions in the make-up of the pentapeptide.<sup>17</sup> Biosynthesis of PG starts in the cytosol, where NAG is first converted into NAM followed by addition of a lipid pyrophosphate on the anomeric position, at the cytoplasmic membrane, to form Lipid I.<sup>18</sup> Thereafter, glycosylation between NAG and NAM formed Lipid II with the aid of the enzyme, glycosyltransferase MurG, which helps to transfer NAG from UDP-NAG (see **Scheme 3.1**). The newly formed Lipid II is then flipped onto the other side of the cell membrane, into the periplasmic space.<sup>19</sup> Subsequent PG elongation occurs via addition of the NAG-NAM disaccharide unit with the help of peptidoglycan glycosyltransferases (PGTs), while the transpeptidase (TPs) are responsible for the crosslinking of the peptide chains once the PG polysaccharide has reached a certain length.<sup>20</sup> Both of the domains, PGT and TP, can be found in class A penicillin-binding proteins (aPBPs), while PGT is absent in class B-penicillin binding proteins (bPBPs).<sup>21</sup>



**Scheme 3.1** | Synthetic scheme illustrating the biosynthesis of Lipid II from Lipid I which occur at the cytoplasmic membrane. The sugar ring color coded in green is NAM, while the other that is color coded in yellow is NAG.

Since the formation of this three-dimensional network occurs mostly in the periplasmic space, it is susceptible to interferences, in which antibiotics such as penicillin and vancomycin takes advantage of. Interestingly, the main formation of PG network is consistent between different

bacterial strains and regardless of their gram distinction. This makes it a very intriguing target for further exploration and better understanding of the biology, bioimaging purposes, as well as mechanistic studies of the development of resistant strains.

### 3.1.3 | Reported Studies with PG Substrates and the Challenges Faced During the Journey

As mentioned, PGTs and TPs are two types of very important enzymes that helps in forming the mesh-like structure of PG, which not only helps to protect the bacteria organelles and provide mechanical support against osmotic pressure, it also helps to decrease the bacteria's susceptibility to antibiotics. The mechanistic studies behind TPs are relatively practical to explore with the use amino acids and short peptide chains as substrates.<sup>22-26</sup> In order to better understand the mechanism behind the polymerisation of NAG-NAM polysaccharides of the PG, many different types of PBPs have been successfully isolated and characterised. However, the substrates for PGTs' structure-activity relationship (SAR) studies are much harder to obtain, due to synthetic challenges faced as well as structural modifications of Lipid II and peptidoglycan oligosaccharides (PGOs).

In 2001, Schwartz *et al.* reported the total synthesis of Lipid II, which comprises of 11 steps with an overall yield of approximately 1%, excluding the synthesis of the protected tetrapeptide, H- $\gamma$ -D-Glu(OTMSE)-L-Lys(TEOC)-D-Ala-D-Ala(OTMSE), starting from an expensive NAM precursor.<sup>27</sup> They have noted that the yields obtained are comparable to chemoenzymatic routes in milligram quantities, and that scaling up would be difficult for both. A few months after, VanNieuwenhze *et al.* too reported a total synthesis of Lipid II using an alternative route, making use of mild reaction conditions, especially since the diphosphate linkage present is chemically sensitive.<sup>28</sup>

During the same year, Kahne and Walker *et al.* reported the synthesis of Lipid by chemoenzymatic method with chemically synthesized Lipid I and an enzyme, glycosyltransferase MurG.<sup>29</sup> They went on to synthesize different analogues of Lipid II (with different types of alkenyl

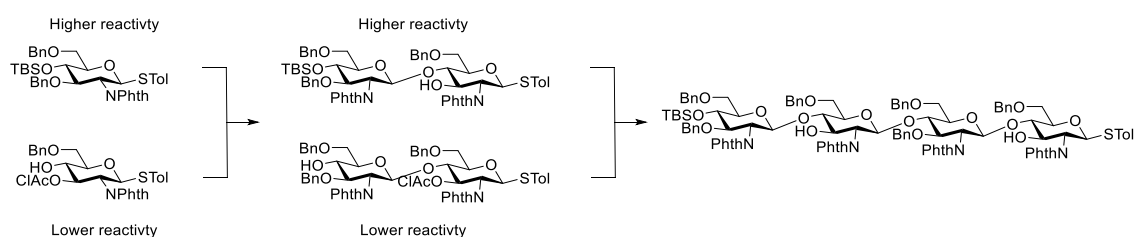
lipids) using the same methodology, and during SAR studies with PGTs, they observed that these analogues showed comparable activities.

In a similar study by Wong *et al.* in 2003, they too synthesized Lipid II and its analogues via chemoenzymatic route.<sup>30</sup> In their study, they compared the MurG activities of natural Lipid I and various Lipid I modifications at the lipid tail, which include different lengths of linear saturated alkyl chains, a shorter natural lipid tail, and one with a nitrophenyl group. They observed that the linear alkyl chains with 12-14 carbons have better interactions with MurG as compared to the natural Lipid I. They also observed that modified Lipid I with nitrophenyl tail showed good activity, thereby suggesting that the lipid's role is simply to provide hydrophobic interactions with MurG in the enzymatic synthesis of Lipid II. A few years later, they reported another study on the effect of different pentapeptide compositions in Lipid II and their binding with PBP's transglycosylase (TGase; also known as PGTs) domain.<sup>31</sup> As per previous study, they obtained Lipid II derivatives using chemoenzymatic route. They found out that the D-lactate group and methyl group in L-alanine in Lipid II are crucial for binding to TGase, whereas the two D-alanine at the end and  $\epsilon$ -NH<sub>2</sub> group in L-lysine did not play a major role in affecting the binding affinity. They also reported the first enzymatic one-pot synthesis of Lipid II from an unprotected glucosamine in 2014, with an overall yield of approximately 70%.<sup>32</sup> They have also successfully synthesized analogues of Lipid II with various alkenyl lipid tails that bare some similarities to the natural tail.

Although it is feasible to obtain Lipid II via chemoenzymatic and enzymatic method, it has been noted that there are difficulties in obtaining controlled length of PGOs using enzymatic route.<sup>31,33</sup> In 2004, Mobashery *et al.* first reported the synthesis of Lipid IV fragment with a study of different approaches, utilising 4 different glycosyl acceptors and donors synthesized from glucosamine.<sup>34</sup> Walker and Kahne *et al.* then reported the total synthesis of Lipid IV, using a slightly different approach. In their approach, they made use three different monomeric thioglycosides as their building blocks to form two different disaccharides, in which they will then couple to form the tetrasaccharide backbone of Lipid IV.<sup>33</sup> The thiophenol group in glycosyl donor



is first oxidised into sulfoxide before glycosylation. Wong *et al.* next came up with another approach of convergent synthesis of Lipid IV in 2011.<sup>35</sup> They designed two different monosaccharides with different reactivity, such that after the formation of disaccharide, they are able to couple them together by tuning the reactivity of the respective disaccharides (see **Scheme 3.2**). The largest PGO substrate obtained currently is Lipid VIII is also by chemical synthetic method, in which Fmoc was utilised as a protecting group for milder deprotection condition to free up the hydroxyl in the glycosyl acceptor for glycosylation.<sup>36</sup>



**Scheme 3.2** | General synthetic route of the tetrasaccharide core in Lipid IV by Wong et al.<sup>35</sup>

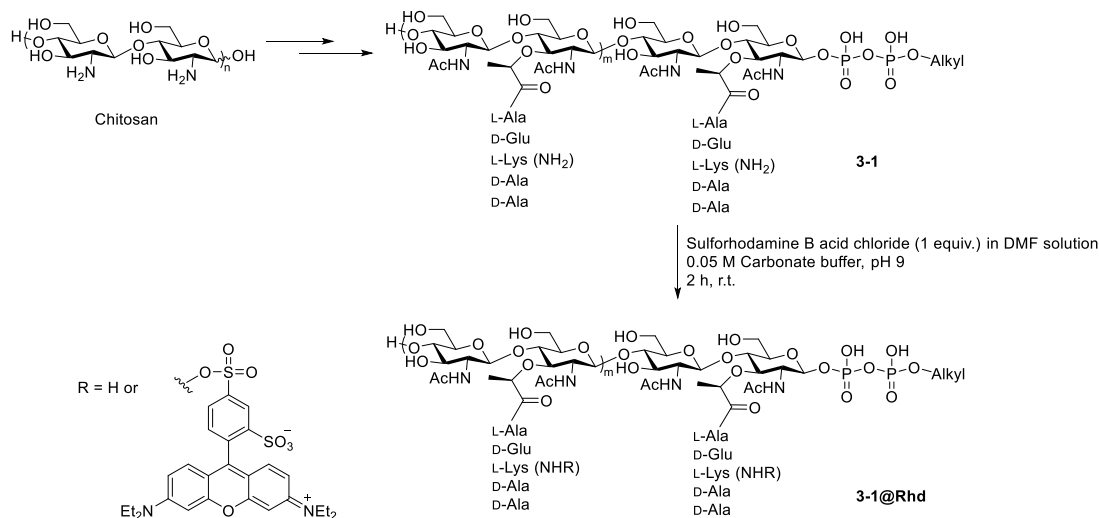
### 3.2 | Proposed Study and Rationale

The development of antibiotic resistance is an inevitable outcome of using antibiotics to combat bacterial infections, and the rising trend of antibiotic resistant bacteria observed is becoming a global health problem. There are several mechanisms in which the antibiotic works against, and of which, the one that targets bacterial cell wall biosynthesis is appealing since majority of the process occur outside of the cell membrane (inner cell membrane in the case of Gram-negative bacteria), which are relatively easier to access as compared to those that targets within the bacteria's inner membrane. Thus, antibiotics such as beta-lactams (i.e. penicillin, amoxicillin, methicillin, etc) and vancomycin, are one of the most successful broad-spectrum drugs to treat bacterial infections. As discussed earlier, one of the most important protein responsible for peptidoglycan (PG) synthesis, a major component of the cell wall, is penicillin binding protein (PBP). Of which some possess PGT and TP domains, while some only have TP domains. There are many reports on studies regarding TP, but a small amount for PGT, which mainly due to difficulties in accessing PG substrates and derivatives.

Although several chemoenzymatic methods reported posed easier access to short PGO substrates such as Lipid II, there are limitations in obtaining controlled length of PGO substrates that have sugar cores larger than a disaccharide. In such cases, one would need to resort back to chemical synthesis, with specifically designed monomeric units in their highly attuned synthetic scheme, comprising of various protecting groups manipulations for the different hydroxyl groups and amino group present. In addition, careful consideration has to be taken into design of the synthesis and monomeric units, including the chemoselectivities and regioselectivities of each group.

In order to combat this issue, our group has designed a 'top-down' approach from a sugar polymer, as opposed to the conventional 'bottom-up' approaches described previously. This would allow us to obtain PGOs in a practical manner as this approach enable us to evade many necessary steps in glycosylation such as synthesis of specific glycosides, deprotection of glycosyl acceptors

and activation of glycosyl donors. Part of the work described herein are done in collaboration with Mr. He Jingxi, in which he came up with and optimised the synthetic design of PGO from chitosan and has successfully obtained the PGO substrate (see **Scheme 3.3**). Detailed synthetic scheme, as well as synthesis protocols of this PGO substrate, will not be described herein (synthetic methods developed by our group are not published yet due to patent filing in progress). In the design of PGO-like substrate, an alkyl tail, tetradecanyl group, is used instead of the natural lipid tail as a study conducted by Wong *et al.* showed that the former has a better binding affinity to MurG.<sup>30</sup>



**Scheme 3.3** | A schematic illustration of our ‘top-down’ approach to PGO derivative (**3-1**) which starts from a chitosan polymer. **3-1** was stained with rhodamine to give **3-1@Rhd**, in which each molecule of **3-1** is tagged with at most 1 molecule of rhodamine on the amino group on L-lysine.

In this study, we aim to study the interaction between PGO **3-1** and an enzyme, lysozyme, and conduct bacterial cell wall labelling studies with **3-1@Rhd**, which is a rhodamine labelled **3-1**, to better understand the mechanism of uptake. Different bacterial strains will be used, and a brief SAR study between different intermediates will be conducted. Thereafter, we propose to demonstrate the feasibility of this methodology developed by our group to obtain other PGO derivatives, in which the position of the pentapeptide differs, which can be used for further biological studies to better understand the interaction of PGO with the enzyme.

### 3.3 | Results and Discussions

#### 3.3.1 | MALDI-TOF MS Analysis and Enzymatic Degradation Assay

Upon obtaining the PGO-like substrate (**3-1**), together with NMR analysis, we proceed on to determine the molecular weight of the final compound. Attempts have been made to obtain the mass of **3-1** using MALDI-TOF MS analysis (see appendix A for more details). After several tries with different conditions (stated in **Tables A1.1** and **A1.2** in Appendix I), although the mass-to-charge ( $m/z$ ) ratio of **3-1** was not able to be characterised, the mass of singly charged chitosan starting material (purchased from Carbosynth Ltd. which states that the MW is less than 3 kDa) had been obtained successfully. From there, the number of repeating monosaccharide units was calculated, and it was determined that there are approximately ten repeating units.

Thereafter, in order to determine the sugar composition, **3-1** was subjected to enzymatic degradation assay by lysozyme, for LC-MS analysis in our preliminary study. Lysozyme are known to bind to tetrasaccharides, or longer motifs, in peptidoglycan and cleaves the glycosidic linkages in the middle. After 24 hours incubation with lysozyme (40% wt) at 37 °C, the mixture was extracted with DCM, and 10  $\mu$ L of the organic layer was dissolved in MeOH (1 mL) for LC-MS analysis (see **Figure 3.4**). In the next trial, lower weight percentage of lysozyme (10% wt) was tested and treated to the mixture at 40 °C. Both the organic layer and crude mixture were analysed by LC-MS (see **Figure 3.5**).

The metabolites that matches to the  $m/z$  signals detected are shown in the inserts of both figures. It is observed that majority of the peaks correspond to the NAM-NAG fragment (with pentapeptide) seen in Lipid II. Encouraged by the preliminary results, a higher resolution analysis by LC-ESI-TOF MS analysis was carried out. The result obtained showed the presence of NAM-NAG unit with pentapeptide and phospholipid (see **Figure 3.6**). From these results, our ‘top-down’ approach is able to generate an alternating NAG-NAM core pattern, as seen in PGs, instead of NAG-NAG or NAM-NAM fragments.

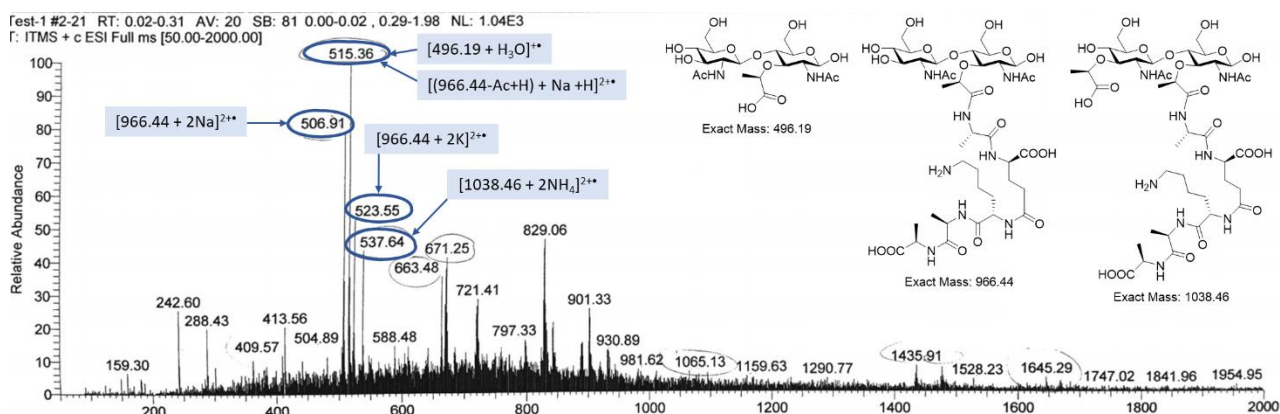


**Figure 3.4** | LC-MS spectrum of the organic layer from lysozyme (40% wt) degradation assay. The metabolites that matches with the m/z signals are shown in the insert.

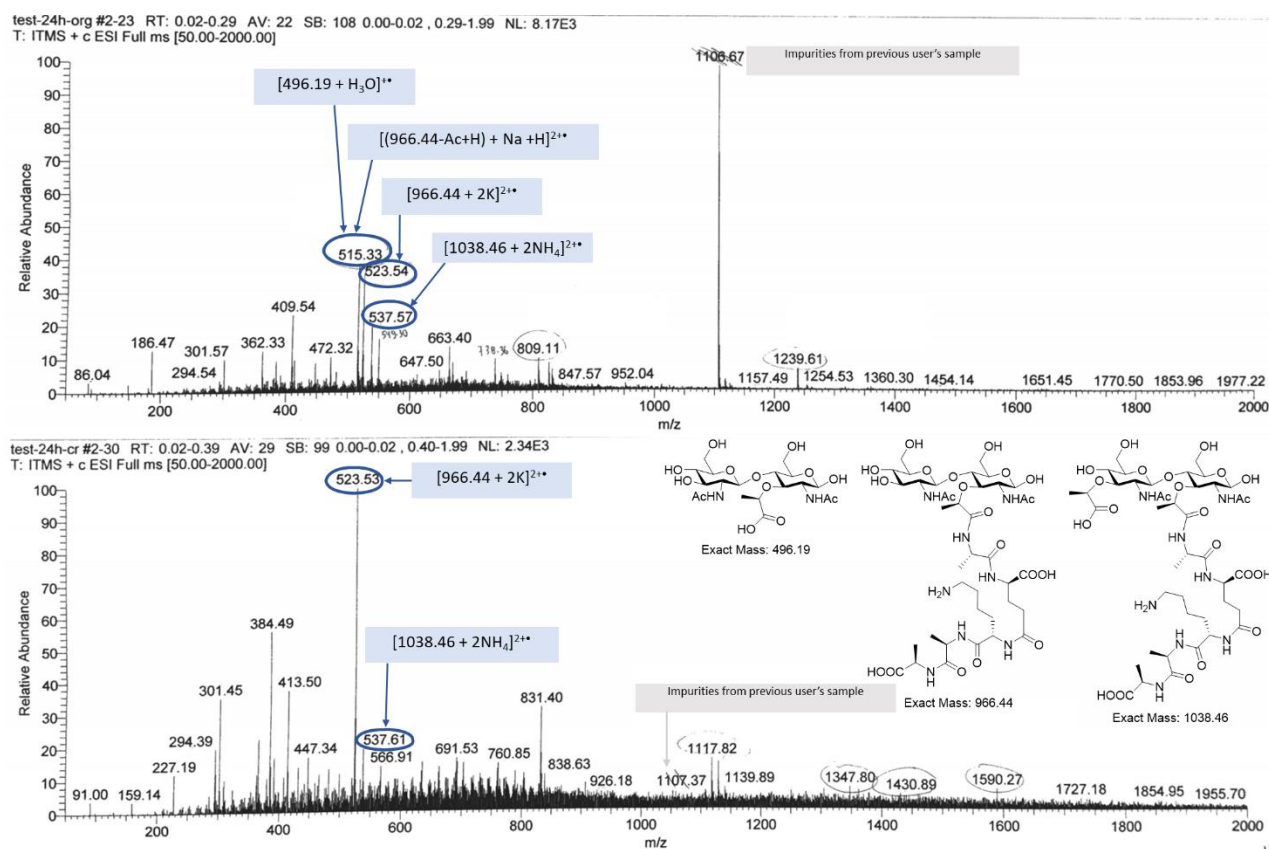


**Figure 3.5** | LC-MS spectra of the organic layer (top) and crude (bottom) lysozyme (10% wt) degradation assay. The metabolites that matches with the m/z signals are shown in the insert.

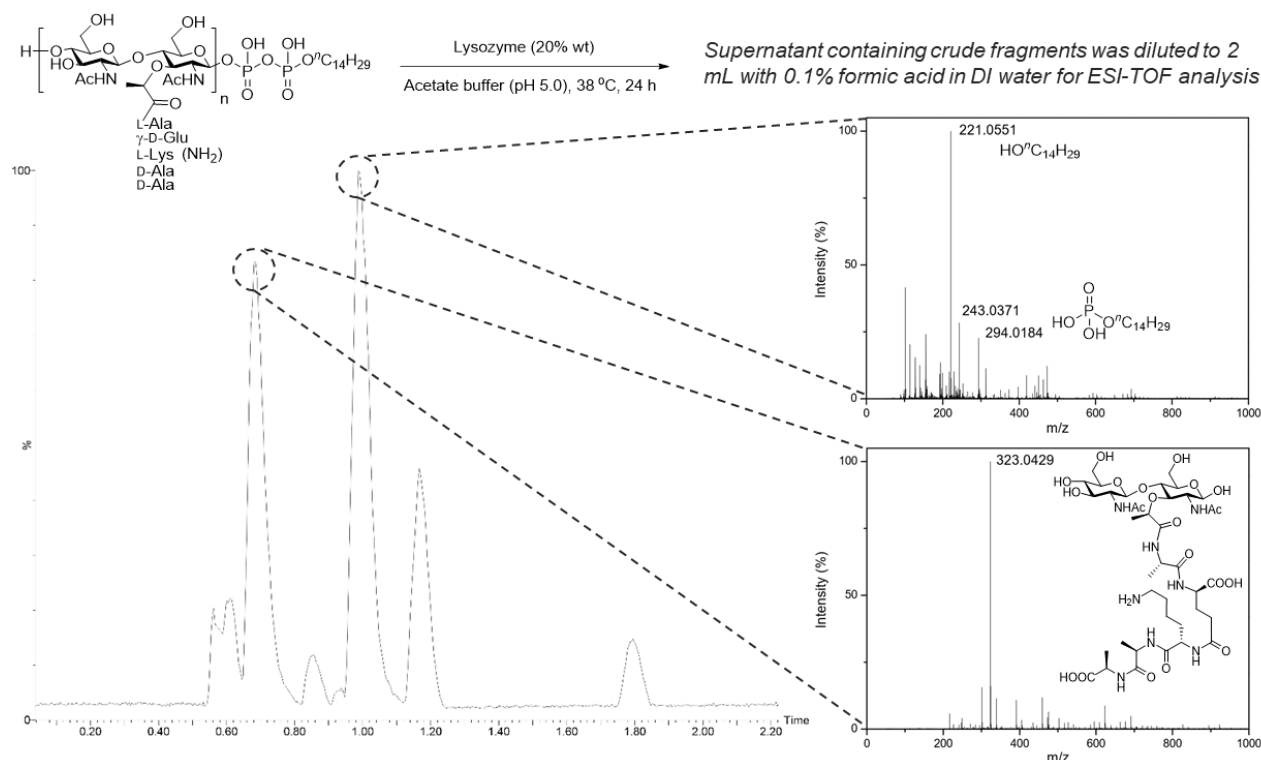


**Figure 3.6** | Schematic illustration of lysozyme degradation (top) and the LC-ESI-TOF MS result obtained from lysozyme (20% wt) degradation assay (bottom). Two major resultant peaks at  $t = 0.69$  min and  $t = 0.99$  min correspond to the NAG-NAM fragment and the phospholipid respectively. The remaining peaks were from metabolites from the enzyme and the buffer used in the lysozyme degradation assay.

### 3.3.2 | Bacterial Cell Wall Labelling Mechanistic Studies with Our PGO.

For bacteria cell wall labelling studies, **3-1** was subjected to further reaction with sulforhodamine B acid chloride to obtain rhodamine tagged substrate (**3-1@Rhd**) for further biological studies (see **Scheme 3.3**). Rhodamine was chosen as its fluorescence emission wavelength is compatible with stimulated emission depletion (STED) technique for super-resolution microscopy studies. STED microscopy has the advantage of enhancing the spatial resolution (lateral point spread function) to less than 200 nm, as compared to confocal microscopy which is greater than 200 nm due to diffraction limit according to Rayleigh criterion. STED is able to capture and generate images of reasonably high resolution in a much shorter time as compared to other super-resolution techniques such as stochastic optical reconstruction microscopy (STORM) and photoactivated localisation microscopy (PALM). The comparison of confocal

microscopic image, STED microscopic image, and processed STED confocal image are shown in **Figure 3.7**. Although the fluorescence intensity observed in STED microscopic images are significantly weaker than the confocal microscopic images, the clarity of the former are much better than the latter, especially in the case of imaging bacteria since they are much smaller compared to mammalian cells.

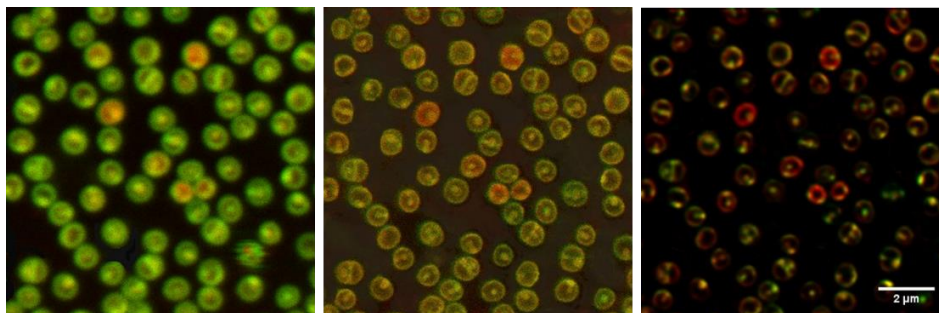


**Figure 3.7** | Confocal microscopic image (left), STED confocal microscopic image (middle), and processed STED confocal image (right) of MRSA-BAA40 incubated with **3-1@Rhd** (red) and cell surface staining dye, FM 1-43fx. Scale bar = 2  $\mu\text{m}$ .

6 bacteria strains were chosen for the study, of which 4 of them are Gram-positive (G+ve) and the other 2 are Gram-negative (G-ve). They are methicillin-resistant *Staphylococcus aureus* (MRSA BAA40 and MRSA USA300), vancomycin-resistant *Enterococcus faecalis* (V583), *Pseudomonas aeruginosa* (PA01), *Escherichia coli* (K12) and *Bacillus subtilis* (6633). The first four are clinical-relevant strains that represent multi-drug resistant (MDR) bacteria, while the last two are commonly used in model study. Media rich in nutrients such as MHB and BHI were used to better resemble real-life environment and the PGO substrate, **3-1@Rhd**, was incubated at varying concentration and durations, with the optimal condition being an hour-long incubation with 100  $\mu\text{g/mL}$  of **3-1@Rhd**. Cell surface staining dye, FM 1-43fx, was used in addition as an indicator of the location of the bacterial surface.

The fluorescence signal from **3-1@Rhd** (red) colocalized well with that of FM 1-43fx (green) in all of the strains tested, implying the successful incorporation of the PGO into the bacterial cell wall (see **Figure 3.8** for G+ve bacteria and **Figure 3.9** for G-ve bacteria). This is a useful indication that the enzyme is able to recognize our PGO substrate, **3-1@Rhd**. This also demonstrated that

the synthesized PGO substrate is able to act as a potential platform for bioimaging. Furthermore, the activity seen in the 6 chosen strains implied a broad spectrum of bacteria which can utilize our substrate to build their cell wall despite the difference in their PG compositions. This tolerance to structural variations could be particularly helpful during our fight against bacterial resistance from mutation in cell wall.

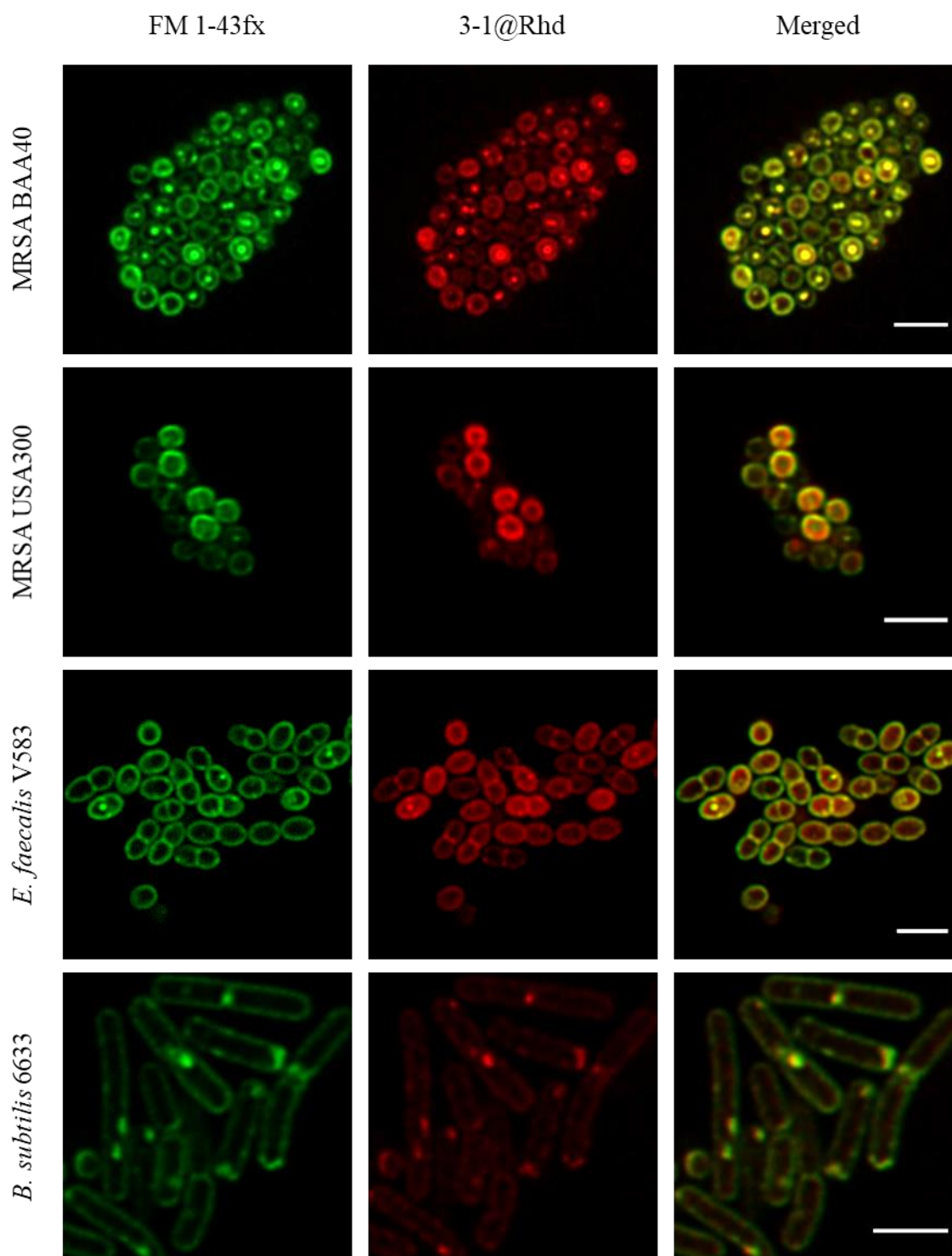


**Figure 3.8** | STED microscopy studies of G<sup>+</sup>ve bacteria, where green = FM 1-43fx, red = 3-1@Rhd, yellow = region of colocalization of two fluorophores. Scale bar = 2  $\mu$ m.



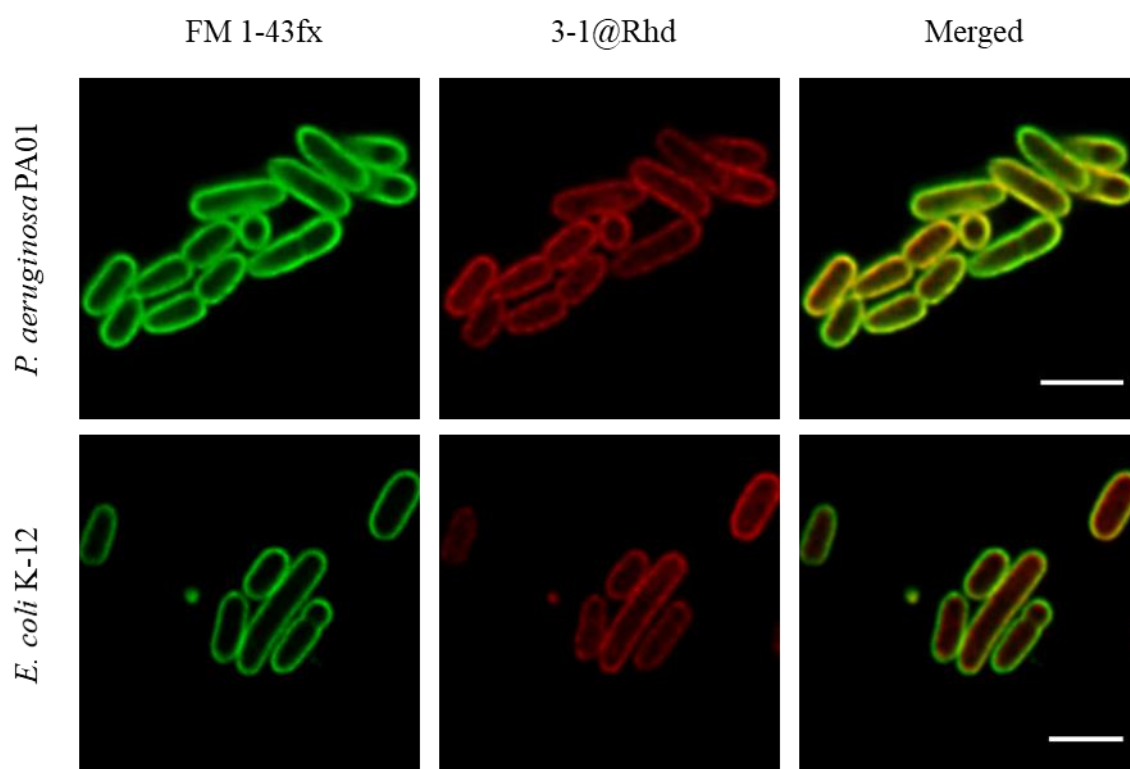


**Figure 3.9** | STED microscopy studies of G-ve bacteria, where green = FM 1-43fx, red = **3-1@Rhd**, yellow = region of colocalization of two fluorophores. Scale bar = 2  $\mu$ m.

Thereafter, higher magnification was sought for determination of a more precise location of the synthesized PGO substrate using STED microscopy. Magnification was further increased for *S. aureus* and *E. faecalis*, both of which had thick cell wall and good uptake of the substrate, based on the images captured previously in **Figures 3.8** and **3.9**. It was noticed that the signal from rhodamine (**3-1@Rhd**) resided at an inner part of bacteria cell compared to the staining dye (FM 1-43fx) which was adsorbed directly onto the bacteria cell surface (see **Figure 3.10**). Incomplete colocalization indicated that the substrate (**3-1@Rhd**) was not physically adsorbed on to the exterior of bacterial cells, which was in the case of FM 1-43fx. This strongly supported our hypothesis that the substrates were incorporated into the bacteria cell wall.

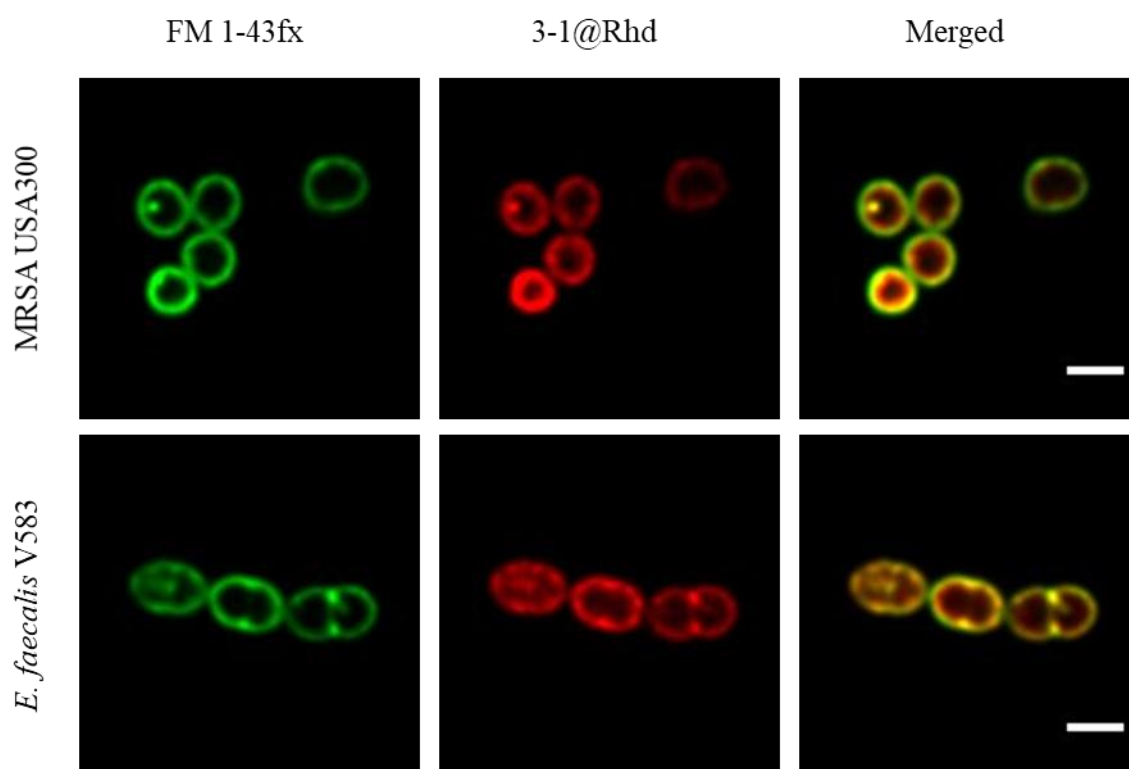


**Figure 3.10** | Magnified STED microscopic images of *S. aureus* and *E. faecalis*, where green = FM 1-43fx, red = **3-1@Rhd**, yellow = region of colocalization of two fluorophores. Scale bar = 1  $\mu$ m.

It was interesting to note that there was a variation in fluorescence intensity observed across different bacteria strains. Hence, the fluorescence signals were quantified, following a method reported by Burgess *et al.*<sup>37-38</sup> In a study conducted by Pires *et al.*, they observed that D-amino acids as labelling agents has less efficacy against G-ve strains, hypothetically due to inherent structural variation across strains.<sup>24</sup> Further description on the quantification method can be found in section 3.5.4. In general, intensity of fluorescence signals obtained in STED microscopy are significantly lower than that obtained in confocal microscopy, due to the working mechanism of STED. The relative intensity for G+ve bacteria, methicillin-resistant *S. aureus* (MRSA-BAA40 and MRSA-USA300) and *E. faecalis* (V583) were amongst the highest as compared to the other three (see **Figure 3.11**). It was intriguing at first sight that the signal intensity of *B. subtilis* (6633), a G+ve bacteria, was much lower than that of G-ve bacteria. We hypothesized that it could be a result of main difference in amino acids composition in the bacteria strains respective PGs that resulted in this phenomenon observed. The second amino acid in the pendant peptide in PG existed

as D-isoglutamate form for most G-ve bacteria species, while it is present in the D-isoglutamine form for most G+ve bacteria species.<sup>17</sup> Most G-ve bacteria has their third amino acid as *meso*-A<sub>2</sub>pm in the PG structure, while it is L-Lys in the case of most G+ve bacteria, except for *B. subtilis* which is amidated *meso*-A<sub>2</sub>pm (see **Figure 3.11** insert for chemical structures of these three amino acids). The structure of the third amino acid in *B. subtilis* resembles more to that of G-ve species, as compared to G+ve species.

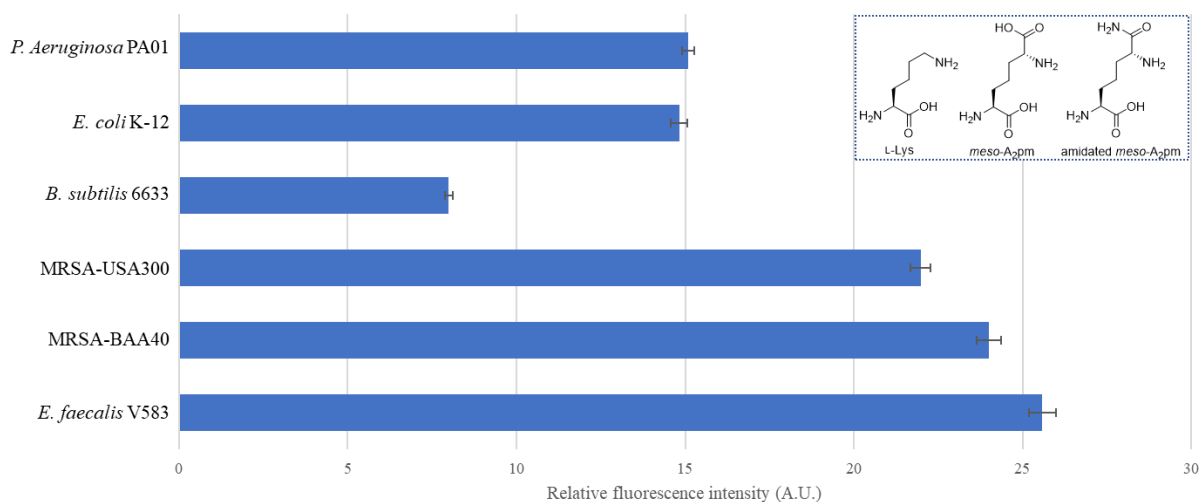
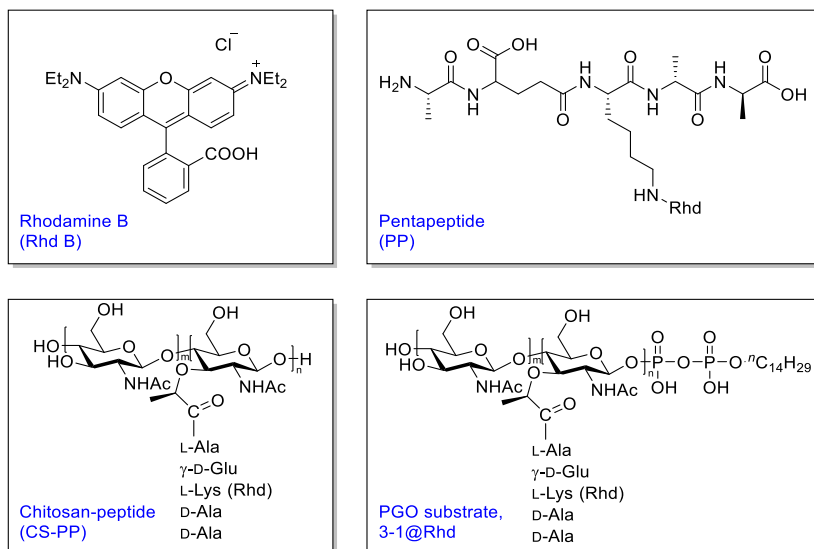


**Figure 3.11** | Relative fluorescence intensity on bacterial surface after treatment in **3-1@Rhd**. A total of at least a hundred bacteria cells from each strain were used for calculation, and the average **3-1@Rhd** fluorescence signal per cell was measured for comparison. Chemical structures of the different third amino acids found in natural PGs of these 6 strains are shown in insert.

A brief structure-activity relationship (SAR) study was conducted, to determine the minimal core structure required for glycosyltransferases recognition. Intermediary substrates (chitosan-peptide and peptide alone, which are abbreviated as CS-PP and PP respectively) were synthesized and characterised by Mr. He Jingxi, and subsequently subjected to labelling with sulforhodamine B acid chloride. *E. faecalis* was then treated with these rhodamine-labelled substrates and rhodamine B (see **Scheme 3.4** for the substrates in the study). Thereafter, intensity of the fluorescence signals was quantified as per previous experiment, and the total intensity was normalized by the area of fluorescence (see **Figure 3.12**).



**Scheme 3.4** | Schematic illustration of rhodamine-labelled substrates for brief SAR study on *E. faecalis*.

Among the different substrates tested, *E. faecalis* treated with **3-1@Rhd-B** showed the highest relative fluorescence intensity, as compared to the others. This result obtained is consistent with a study reported by Wong *et al.* whom demonstrated that the oligosaccharide backbone and pentapeptide chains in PGOs are necessary for effective binding to active site of PGT.<sup>39</sup> The great difference in intensity observed further validates our hypothesis that the PGO substrate, **3-1@Rhd**, has been taken up by the bacteria and incorporated as part of its cell wall, and not as a result of physical accumulation.

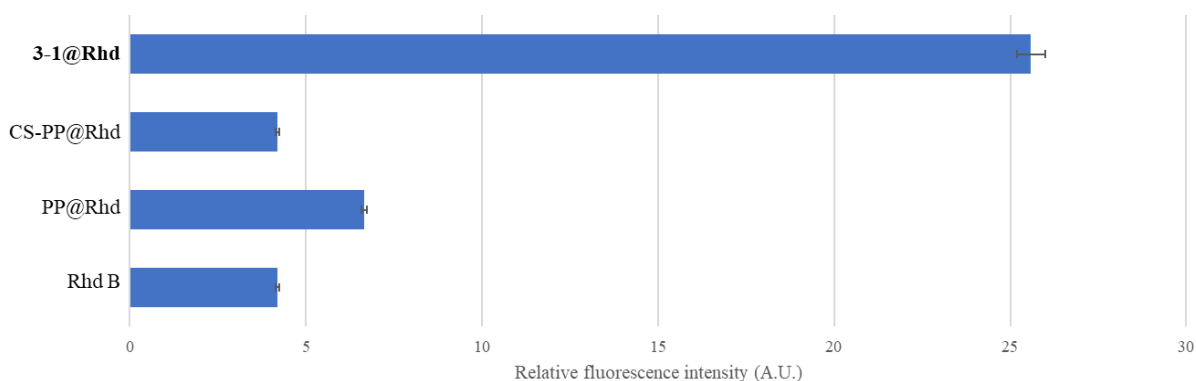


**Figure 3.12** | Relative fluorescence intensity on *E. faecalis* surface after treatment with **3-1@Rhd**, CS-PP@Rhd, PP@Rhd and rhodamine alone (Rhd). A total of at least a hundred bacteria cells from each strain were used for calculation, and the average rhodamine fluorescence signal per cell was measured for comparison.

### 3.3.3 | Facile and Practical Synthesis of PGO-Derivatives

Following the success in the *in vitro* studies conducted, which demonstrated that PGO substrate synthesized by our ‘top-down’ approach resembles the natural PGO in which enzymes are able to recognize and interact. Moreover, this ‘top-down’ approach serves as an excellent platform for obtaining different PGO-derivatives for further studies in a practical manner.

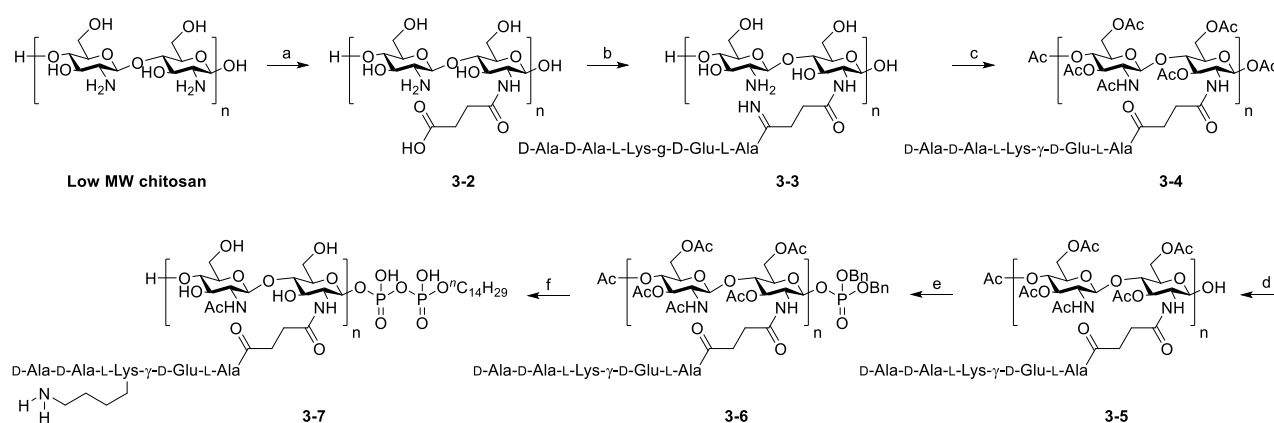
Over the years, several studies have been done in an effort to better understand the mechanism behind PGT interactions with PGOs, which is one of the core domains in PBPs for further PG network in the bacteria cell wall. As mentioned previously, oligosaccharide backbone and pentapeptide in PGOs are essential for binding to PGT. In natural PGO, the pentapeptide was attached at the third hydroxyl position in NAG. As to the best of our knowledge, there are no studies done on the synthesis, as well as the effect of different position of pentapeptide covalently linked to the sugar backbone on PGT. One of the main plausible reason could be due to high difficulty in accessing such derivatives using the conventional ‘bottom-up’ approach, in which an even wider library of glycosides and subsequent glycosylation routes have to be carefully designed and optimised.

Hence, using our synthetic methodologies in ‘top-down’ approach, we are able to design and obtain the desired PGO **3-1** in 13 steps (excluding peptide synthesis). In addition, PGO derivatives are able to be obtained in a feasible manner, in which the pentapeptides are attached on the C2 amino group (see **Scheme 3.5**) and on the C6 hydroxyl group (see **Scheme 3.6**).

PGO-derivative, **3-7**, was obtained using the same very low MW chitosan as in our *in vitro* studies described previously. Succinic anhydride was first added to the chitosan in half an equivalence in a protection-less reaction since primary amine is much more reactive than hydroxyl groups, the former will react at a much faster rate and thereafter, forming a very stable amide bond and pushing the reaction forward thermodynamically. The reason for adding half an equivalence of succinic anhydride is to mimic the alternating pattern of the PG repeating motif. The product obtained was subjected to coupling with peptide using the conventional HATU/HOAt method.

Pentapeptide's side chains' protecting groups and terminals were capped in Fmoc for amino groups, and benzyl or methyl ester for carboxylic acid groups. This is so that a single step in global deprotection using LiOH can be achieved at the end. Next, all of the free hydroxyl groups present were first protected with acetyl before covalent linkage of the pentapeptide moiety. Upon acetylation, the solubility of **3-5** in organic solvents such as dichloromethane (DCM) was improved greatly. Partial cleavage frees the anomeric hydroxyl group, which can then react with dibenzyl *N,N*-diisopropylphosphoramidite to form **3-6**. Hydrogenation reaction releases the benzyl protecting group from the phosphate, and a second lipid-linked monophosphate can be linked to it, to give the crude PGO-derivative. It was then purified by dialysis, filtration, and lyophilisation to yield the pure final product, **3-7**, as beige-colored powder.

Pentapeptide attachment on the C-2 amino group.

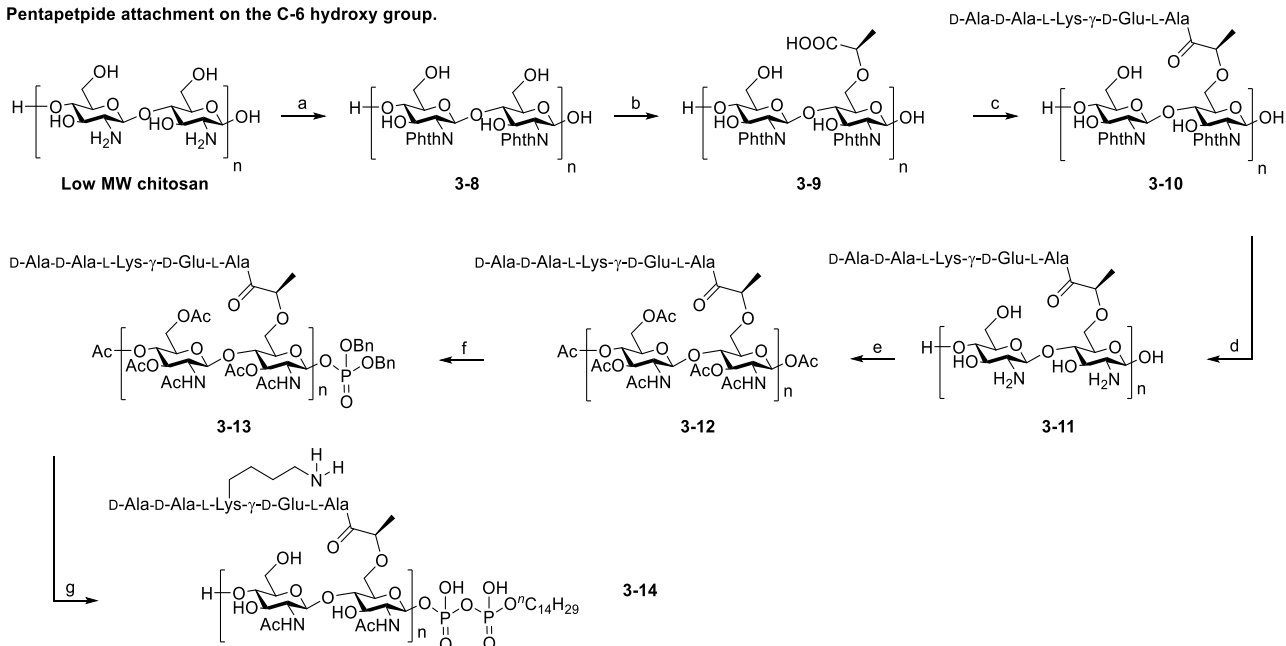


**Scheme 3.5** | Synthesis of modified PGOs with peptide attachment on the C2 amino group, **3-7**. Reactions and conditions: a, succinic anhydride (0.5 equiv.), DMF; b,  $H_2NR$  (peptide) (1 equiv.), HATU, HOAt, DIPEA, DMF; c, acetic anhydride (5 equiv.), pyridine; d,  $MeNH_2$ , MeOH; e, 1. 1H-tetrazole, dibenzyl *N,N*-diisopropylphosphoramidite (2 equiv.), 2. tert-butyl hydroperoxide, DCM; f, 1.  $H_2$ , Pd/C, MeOH, 2.  $nC_{14}H_{29}OPO(OH)_2$  (2 equiv.), DMF, 3. LiOH, MeOH/ $H_2O$  (v/v, 1:1).

In the case of obtaining PGO-derivative, **3-14**, very low MW chitosan was first subjected to phthaloyl protection in order to mask the reactivity of the primary amino group present in chitosan. Next, 2-bromopropanoate was introduced at C6 using  $S_N2$  chemistry, in which half the equivalence of 2-bromopropanoate was used. Next, pentapeptide (same as the one used in **Scheme 3.5**) was

coupled with the carboxylic acid group with the use of coupling reagents, HATU. Next, phthaloyl protecting group was removed upon treatment with hydrazine. Global acetylation was carried out first, and anomeric hydroxyl was then freed for reacting with *N,N*-diisopropylphosphoramidite to yield **3-13**. The final step was carried out under same conditions as in **Scheme 3.5**. Crude **3-14** obtained was first dialysed, then filtered, and finally lyophilised for better storage. Pure **3-14** was obtained as beige-colored power as well.

**Pentapeptide attachment on the C-6 hydroxy group.**



**Scheme 3.6** | Synthesis of modified PGOs with peptide attachment on the C6 hydroxyl group, **3-14**. Reactions and conditions: a, phthalic anhydride (3 equiv.), AcOH/H<sub>2</sub>O; b, NaH, 2-bromopropanoate (0.5 equiv.), DMF; c, H<sub>2</sub>NR (peptide) (1 equiv.), HATU, HOAt, DIPEA, DMF; d, hydrazine, AcOH, MeOH; e, acetic anhydride (5 equiv.), pyridine; f, 1. MeNH<sub>2</sub>, 2. 1H-tetrazole, dibenzyl *N,N*-diisopropylphosphoramidite (2 equiv.), 3. tert-butyl hydroperoxide, DCM; g, 1. H<sub>2</sub>, Pd/C, MeOH, 2. *n*-C<sub>14</sub>H<sub>29</sub>OPO(OH)<sub>2</sub> (2 equiv.), DMF, 3. LiOH, MeOH/H<sub>2</sub>O (v/v, 1:1).

### 3.4 | Conclusion

PGO substrate, **3-1**, obtained using our group's 'top-down' approach, have been demonstrated that it could be incorporated into the cell walls of different bacteria strains after a series of studies conducted. Brief SAR study conducted revealed that rhodamine-labelled PGO substrate (**3-1@Rhd**) was incorporated while intermediary substrates were not. Difference in uptake was observed, as quantified by their average intensities of the fluorescence signals across different bacteria strains as well as different intermediary substrates within in the same strain, in which plausible explanations to both phenomena have been provided. The initial lysozyme degradation assays showed that the PGO substrate's (**3-1**) metabolites resembles that of the natural peptidoglycans. The feasibility of this approach was then tested when I ventured on to synthesize PGO-derivatives **3-7** and **3-14**, that were, to the best of my knowledge, not reported before. This 'top-down' methodology in obtaining PGO and PGO-derivatives are highly convenient, and thus provides a versatile platform for future mechanistic studies on bacterial cell wall biosynthesis, as well as a great tool in combating antibiotic resistance and bioimaging applications.



## 3.5 | Methods and Materials

### 3.5.1 | Materials

Very low MW Chitosan ( $\leq 3$  kDa, DD > 85%) was purchased from Carbosynth Ltd. (Berkshire, UK). 1-[Bis(dimethylamino)methylene]-1H-1,2,3-triazolo[4,5-b]pyridinium 3-oxid hexafluorophosphate (HATU), 3H-[1,2,3]-Triazolo[4,5-b]pyridin-3-ol (HOAt) and all amino acids used in synthesis were purchased from GL Biochem Ltd. (Shanghai, China). Sulforhodamine B acid chloride, Lysozyme (from egg white) and all other chemicals used in synthesis were purchased from Sigma-Aldrich Co. LLC. (St. Louis, USA). Membrane-staining dye FM 1-43fx was purchased from Thermo Fisher Scientific Inc. (Waltham, USA). Bacterial strains (*Escherichia coli* K12 ATCC8739, *Pseudomonas aeruginosa* PA01 ATCC27853, *Staphylococcus aureus* ATCCBAA-40 and USA300 ATCC29213, *Enterococcus faecalis* V583 ATCC700802, and *Bacillus subtilis* ATCC6633) were purchased from the American Type Culture Collection (Manassas, USA) and stored at  $-80^{\circ}\text{C}$ . Mueller-Hinton26 broth (MHB, Difco), brain heart infusion broth (BHI, Difco) and trypticase soy broth (TSB, Difco) were purchased from Beckton, Dickinson and company (Franklin Lakes, USA). Dialysis tubing was purchased from Spectra/Por (Singapore). Milli-Q water (18 M $\Omega$ ) was prepared using a Milli-Q Synthesis System (Millipore, Bedford, MA, USA) for dialysis and experiments. Protected pentapeptide (Boc-L-Ala-D-*iso*-Glu(OBn)-L-Lys(Fmoc)-D-Ala-D-Ala-OMe) and tetradecyl monophosphate linker were obtained as gifts from Dr. Lin Yichao and Mr He Jingxi from our group.

### 3.5.2 | Lysozyme Degradation Assay

In general, 2 mg of PGO substrate (**3-1**) was dissolved in 0.2 mL 10 mM acetate buffer, pH 5.0. Lysozyme (LC-MS trial 1: 40% wt, LC-MS trial 2: 10% wt, and LC-ESI-TOF MS trial: 20% wt) was added, and the resultant mixture was vortex briefly, before incubating for 24 hours (at  $37^{\circ}\text{C}$  for trial 1,  $40^{\circ}\text{C}$  for trial 2, and  $38^{\circ}\text{C}$  for ESI-TOF trial). The enzyme was pelleted by

centrifugation at 1,500 X g for 5 minutes, and the supernatant was separated. In trials 1 and 2, part of the supernatant was subjected to DCM extraction, and 10 µL of the organic layers were dissolved in MeOH (1 mL) and sent for LC-MS analysis. In the case of LC-ESI-TOF-MS, the supernatant containing crude metabolites were diluted to 2 mL with 0.1% formic acid in deionized water.

### 3.5.3 | Labelling of Bacterial Cell Walls with 3-1@Rhd and STED Microscopy

Overnight broth cultures were grown in 4 mL fresh culture broth in 1:100 dilution, such that the bacteria are able to enter the logarithmic growth phase after 4 hours of incubation at 37 °C in a shaking incubator (set at 225 rpm). The bacteria cells were then collected by centrifugation at 1,500 X g for 5 minutes and resuspended in respective culture media (MRSA is grown in TSB, *B. subtilis* and *E. faecalis* are grown in BHI, while *P. aeruginosa* and *E. coli* are grown in MHB) at a concentration of  $10^8$  CFU ml<sup>-1</sup> and incubated with 100 µg/mL of 3-1@Rhd for 1 hour in absence of light at 37 °C with agitation (225 rpm). The bacteria were collected by centrifugation at 1,500 X g for 5 minutes, resuspended in PBS, and the process was repeated thrice to wash off excess substrates that were not taken up by the cells.

The bacteria cells were then incubated with cell staining dye FM 1-43fx according to the protocol by the manufacturer at a final concentration of 5 µg/mL for 5 minutes. The bacteria were collected again by centrifugation at 3,000 X g for 5 minutes, and the process was repeated three times to wash off excess staining dye. Thereafter, the bacteria pellets were treated with a fixative solution of 4% paraformaldehyde in PBS (pH = 7.0) for 30 minutes at 37 °C in a shaking incubator (225 rpm). The bacteria were then collected by centrifugation at 3,000 X g for 5 minutes, and the process was repeated three times to fully wash off excess paraformaldehyde.

The concentrated bacteria solutions were then applied on to a sterile glass bottom collagen coated dish (MatTek Corporation), and glycerol was added as a thickening agent to minimize cell suspensions from floating around. STED super resolution microscopy was performed on a Leica

TCS SP8 STED-3X microscope (Leica Microsystems, Wetzlar, Germany) at SingHealth Advanced Biomaging Core. 479 nm and 556 nm lasers were used for fluorescence excitation, while 660 nm STED laser was used for depletion. In order to achieve maximum lateral resolution, all images were acquired in 2D STED mode. Further image processing required deconvolution, which was done using Huygens Professional software (Scientific Volume Imaging, Hilversum, Netherlands). Fiji ImageJ was utilized for further image processing and quantification of the intensity of the fluorescence signals.

In the case of brief SAR study, 100 µg/mL of different substrates (see **Scheme 3.4**) were incubated with *E. faecalis*, following the same method as described above.

#### **3.5.4 | Quantifying Intensity of Fluorescence Signals**

Quantification of the intensity of fluorescence signals were computed and calculated according to the procedure reported by Burgess *et al.*<sup>37-38</sup> The laser power and STED power (660 nm) were kept constant throughout the experiments for acquisition of the images for calculation purposes. Excitation wavelength of the red channel (for exciting rhodamine) was set at 570 nm and the emission photons collected from 580 nm to 620 nm, so as to minimize crosstalk. Only cells that were in focus were taken into account for calculation. The channels of the raw STED images (not processed by deconvolution) obtained were split, and only the intensities from red channel were read and computed. The area with fluorescence on each bacterial surface was drawn (see **Figure 3.13**) and the total intensity was normalized by the number of pixels found in the area (mean). A total of hundred or more cells per bacterial strain were tabulated and computed to obtain the average relative intensity for comparison. The values recorded and subsequently calculated are shown in Appendix III.

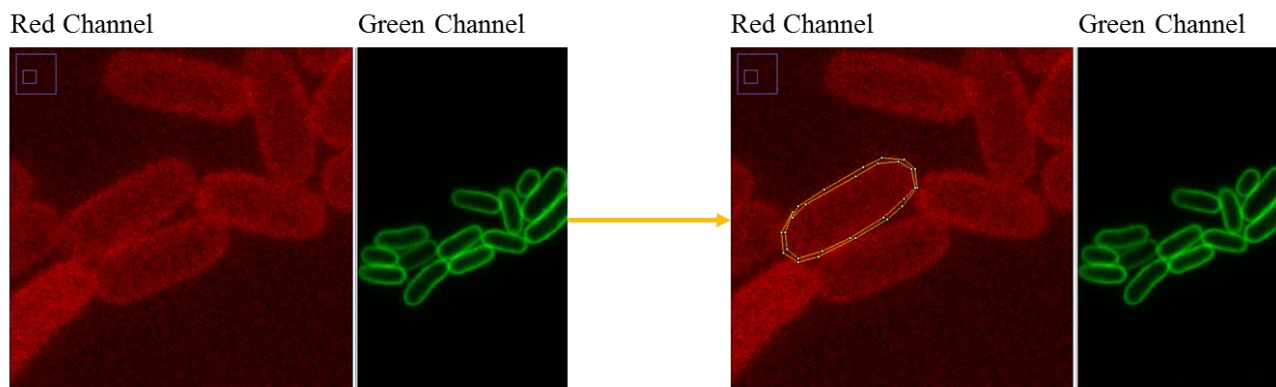


**Figure 3.13** | Schematic illustration on the quantification of fluorescence intensity using Fiji ImageJ, in which the raw STED microscopic image was used, and the channels were first split before any quantifications in the red channel.

### 3.5.5 | Chemical Synthesis of PGO Derivatives

#### General Experimental Details

All reactions were carried out in oven-dried glasswares and under nitrogen atmosphere, unless otherwise stated. Reactions were monitored by thin-layer chromatography (TLC) silica gel plates 60-F254 using UV light at 254 nm to visualise and  $\text{KMO}_4$  as a staining agent, together with Liquid Chromatography Mass Spectrometer (LCMS) to monitor the change in molecular weights. Solvents used were either purified according to standard procedures in literature or as purchased from Merck. Product purification was done by flash chromatography using silica gel 60 (0.010-0.063 mm), with reagent grade solvents and distilled technical grade solvents, unless otherwise stated. Final polymeric substrates were purified by dialysis using dialysis tubing cellulose membrane (1 kDa MWCO) for 3 days.

Chitosan reaction with succinic anhydride was carried out in accordance to reported protocol by Yan *et al.* with slight modification.<sup>40</sup> Chitosan protection was carried out according to protocol reported by Ifuku *et al.*<sup>41</sup> Reactions involving peptide coupling, and key steps in synthesis of Lipid II such as attachment of the pyrophosphate lipid tail and deprotection, were carried out following reported protocols by Kahne *et al.* and Wong *et al.*, with slight modification.<sup>24,30-31</sup> Calculations were based on repeating monosaccharide units on the oligomers.

### **PGO Modified with Pentapeptide at C2 position (PP@C2/PGO)**

**Synthesis of (3-2):** Chitosan (3.00 g, 18.6 mmol) was dissolved in DMF (60 mL). Succinic anhydride (0.931 g, 9.30 mmol) was added portion-wise with stirring, and the resultant mixture was stirred at 60 °C for 24 hours. Thereafter, upon cooling, pH of the mixture was tuned to 5.0 by careful addition of NaOH (5% wt) solution. Precipitates formed were collected by Buchner filtration and washed with NaOH (5% wt) solution, ethanol and diethyl ether to give **3-2** (3.57 g, 91%) as an off-white solid.

**Synthesis of (3-3):** Boc deprotection of pentapeptide Boc-L-Ala-D-*iso*-Glu(OBn)-L-Lys(Fmoc)-D-Ala-D-Ala-OMe was carried out prior to coupling reaction. Boc-protected pentapeptide (156 mg, 0.171 mmol) was first dissolved in MeOH/DCM (2 mL, v/v = 1:1), and 4.0 M HCl in dioxane (0.9 mL) was added dropwise to the mixture at room temperature. Reaction was monitored by TLC, till Boc-protected pentapeptide was consumed. The solvent was removed under reduced pressure and the crude H-L-Ala-D-*iso*-Glu(OBn)-L-Lys(Fmoc)-D-Ala-D-Ala-OMe was then dissolved in DMF (5 mL) and used without further purification. **3-2** (72.2 mg, 0.342 mmol), HATU (97.5 mg, 0.257 mmol), HOAt (34.8 mg, 0.257 mmol) and DIPEA (66.3 mg, 0.513 mmol) were added to a round bottom flask containing DMF (20 mL) and stirred at room temperature. H-L-Ala-D-*iso*-Glu(OBn)-L-Lys(Fmoc)-D-Ala-D-Ala-OMe (0.171 mmol) in DMF was then added to the reaction mixture and left to stir overnight. The solvents are then removed under pressure, and the crude mixture was carried on to the next step without further purification.

**Synthesis of (3-4):** **3-3** (0.342 mmol) and pyridine (4 mL) was charge to a round bottom flask at 0 °C. Acetic anhydride (174 mg, 1.71 mmol) was added dropwise with stirring. The resultant mixture was warmed to room temperature and stirred for 24 hours. Thereafter, the solvent was removed under reduced pressure, and the residue was dissolved in dichloromethane (DCM), and extracted twice with saturated ammonium chloride solution followed by water. DCM was then removed *in vacuo* to give **3-4** (0.199 g, 84%) as brown solids

**Synthesis of (3-5):** **3-4** (199 mg, 0.288 mmol) was dissolved in MeOH (5 mL) and cooled to 0 °C. 2.0 M methylamine in THF (0.22 mL, 0.432 mmol) was added dropwise to the mixture. The resultant mixture was then warmed up to room temperature and stirred overnight. The solvent was then removed *in vacuo* and the crude mixture was used without further purification.

**Synthesis of (3-6):** DCM (15 mL) was added to dissolve the dried residue of **3-5**, and the mixture was allowed to cool to 0 °C. 1*H*-tetrazole (0.13 mL, 0.058 mmol) and dibenzyl *N,N*-diisopropylphosphoramidite (0.05 mL, 0.043 mmol) was then added, and the resulting mixture was slowly allowed to warm to room temperature, and left to stir for 5 hours, before cooling to -50 °C. Then *tert*-butyl hydroperoxide (70%, 0.5 mL) was added and the mixture was left to stir overnight. The volatiles were then removed under reduced pressure, and the residue was washed with saturated ammonium chloride solution, followed by saturated sodium bicarbonate solution, and finally water to give **3-5** as a yellow oil which was used directly in the next step without further purification.

**Synthesis of (3-7):** Tetradecyl monophosphate (102 mg, 0.345 mmol) was dissolved in DMF/THF (20 mL, v/v = 1:1). CDI (280 mg, 1.73 mmol) was then added to the mixture, and the resultant mixture was stirred at room temperature for 2 hours, before quenching with methanol (1 mL). The mixture was left to stir for another hour at room temperature, to yield activated tetradecyl phosphoroimidazolidate (C<sub>14</sub>PI<sub>m</sub>). Crude **3-5** was dissolved in methanol (20 mL), and Pd on activated charcoal (8 mg) was added, and the suspension mixture was stirred under hydrogen atmosphere at room temperature overnight. The suspension mixture was then filtered through a pad of celite, and the solvent was removed under reduced pressure, and thereafter, resuspending in DMF (and transferred to the round bottom flask containing 0.087 mmol of activated tetradecyl phosphoroimidazolidate (C<sub>14</sub>PI<sub>m</sub>). Next, 0.45 M tetrazole in ACN (0.19 mL, 0.087 mmol) was added to the reaction mixture, and the resultant mixture was stirred at room temperature overnight. The solvents were removed *in vacuo*, and the residue was re-dispersed in MeOH/water (15 mL, v/v = 1:1), and 1 M LiOH in water (0.58 mL) was added, and the reaction mixture was stirred for

3 hours before dialysis and lyophilisation to give the final product, **3-7** (10 mg, 7% overall yield) as a beige-colored powder.

### **PGO Modified with Pentapeptide at C6 position (PP@C6/PGO)**

**Synthesis of (3-8):** Chitosan (1.00 g, 6.21 mmol) was dissolved in AcOH/water (50 mL, v/v = 1:9) mixture, and phthalic acid (2.76 g, 18.6 mmol) was added portion-wise. The reaction mixture was stirred at 120 °C for 24 hours. Thereafter, the mixture was cooled to room temperature and the solvent was removed under reduced pressure. The residue was then washed with ethanol and diethyl ether to give **3-8** (1.448 g, 80%) as an off-white solid.

**Synthesis of (3-9):** **3-8** (600 mg, 2.06 mmol) was first dissolved in DMF (90 mL) and cooled to 0 °C. Sodium hydride (412 mg, 8.24 mmol) was added portion-wise, followed by dropwise addition of (*S*)-(-)-2-Bromopropionic acid (158 mg, 1.03 mmol). The reaction mixture was then allowed to warm to room temperature and stirred for 24 hours, before quenching with methanol. The solvents were removed under reduced pressure, and the residue was washed with water and ethanol to give **3-9** (0.37 g, 55 %) as yellow solid.

**Synthesis of (3-10):** Attachment of peptide onto the polymer was carried out as described in the synthesis of **3-3**. Boc deprotection of pentapeptide Boc-L-Ala-D-*iso*-Glu(OBn)-L-Lys(Fmoc)-D-Ala-D-Ala-OMe was carried out prior to coupling reaction. Boc-protected pentapeptide (250 mg, 0.273 mmol) was first dissolved in MeOH/DCM (2 mL, v/v = 1:1), and 4.0 M HCl in dioxane (1.37 mL) was added dropwise to the mixture at room temperature. Reaction was monitored by TLC, till Boc-protected pentapeptide was consumed. The solvent was removed under reduced pressure and the crude H-L-Ala-D-*iso*-Glu(OBn)-L-Lys(Fmoc)-D-Ala-D-Ala-OMe was then dissolved in DMF (5 mL) and used without further purification. **3-9** (179 mg, 0.546 mmol), HATU (156 mg, 0.410 mmol), HOAt (55.0 mg, 0.410 mmol) and DIPEA (106 mg, 0.820 mmol) were added to a round bottom flask containing DMF (25 mL) and stirred at room temperature. H-L-Ala-D-*iso*-Glu(OBn)-L-Lys(Fmoc)-D-Ala-D-Ala-OMe (0.273 mmol) in DMF was then added to the

reaction mixture and left to stir overnight. The solvents are then removed under pressure, and the crude mixture was carried on to the next step without further purification.

**Synthesis of (3-11):** **3-10** (~0.546 mmol) was dissolved in methanol (15 mL), followed by addition of acetic acid (0.10 mL, 1.73 mmol) and hydrazine (0.05 mL, 1.73 mmol). The mixture was stirred at room temperature for 24 hours before the removal of solvents under reduced pressure. The crude product was used directly in the next step without further purification.

**Synthesis of (3-12):** **3-11** (~0.546 mmol) and pyridine (4 mL) was charge to a round bottom flask at 0 °C. Acetic anhydride (278 mg, 2.73 mmol) was added dropwise with stirring. The resultant mixture was warmed to room temperature and stirred for 24 hours. Thereafter, the solvent was removed under reduced pressure, and the residue was dissolved in dichloromethane (DCM), and extracted twice with saturated ammonium chloride solution followed by water. DCM was then removed *in vacuo* to give **3-12** (0.593 g, 77% over three steps) as brown solids.

**Synthesis of (3-13):** **3-12** (593 mg, 0.0423 mmol) was dissolved in MeOH (5 mL) and cooled to 0 °C. 2.0 M methylamine in THF (0.13 mL, 0.259 mmol) was added dropwise to the mixture. The resultant mixture was then warmed up to room temperature and stirred overnight. The solvent was then removed *in vacuo* and the crude mixture was used without further purification. DCM (15 mL) was added to dissolve the dried residue obtained, and the mixture was cooled to 0 °C. 1*H*-tetrazole (0.38 mL, 0.173 mmol) and dibenzyl *N,N*-diisopropylphosphoramidite (0.14 mL, 0.130 mmol) was then added, and the resulting mixture was slowly allowed to warm to room temperature, and left to stir for 5 hours, before cooling to -50 °C. Then *tert*-butyl hydroperoxide (70%, 1 mL) was added and the mixture was left to stir overnight. The volatiles were then removed under reduced pressure, and the residue was washed with saturated ammonium chloride solution, followed by saturated sodium bicarbonate solution, and finally water to give **3-13** as a yellow oil which was used directly in the next step without further purification.

**Synthesis of (3-14):** Crude **3-13** was dissolved in methanol (20 mL), and Pd on activated charcoal (8 mg) was added, and the suspension mixture was stirred under hydrogen atmosphere at room



temperature overnight. The suspension mixture was then filtered through a pad of celite, and the solvent was removed under reduced pressure. Activated tetradecyl phosphoroimidazolidate ( $C_{14}PI_m$ ) crude was obtained in the synthesis of **3-7**. The residue was resuspended in DMF (2.5 mL) and transferred to the round bottom flask containing 0.258 mmol activated tetradecyl phosphoroimidazolidate ( $C_{14}PI_m$ ). Next, 0.45 M tetrazole in ACN (0.57 mL, 0.258 mmol) was added to the reaction mixture, and the resultant mixture was stirred at room temperature overnight. The solvents were removed *in vacuo*, and the residue was re-dispersed in MeOH/water (25 mL, v/v = 1:1), and 1 M LiOH in water (0.86 mL) was added, and the reaction mixture was stirred for 3 hours before dialysis and lyophilisation to give the final product, **3-14** (20.6 mg, 5% overall yield) as a beige-colored powder.

### 3.6 | References

1. Butler, M.S.; Blaskovich, M.A.T.; Cooper, M.A., Antibiotics in the Clinical Pipeline at the End of 2015. *J. Antibiot.* **2017**, *70*, 3-24.
2. Compound Interest, A Brief Overview of Classes of Antibiotics. <https://www.compoundchem.com/2014/09/08/antibiotics/> (accessed Aug 30, 2019).
3. Yocum, R.R.; Rasmussen, J.R.; Strominger, J.L., The Mechanism of Action of Penicillin. *J. Biol. Chem.* **1980**, *255*, 3977-3996.
4. Mingeot-Leclercq, M.-P.; Glupczynski, Y.; Tulkens, P.M., Aminoglycosides: Activity and Resistance. *Antimicrob. Agents Chemother.* **1999**, *43*, 727-737.
5. Kupferschmidt, K., Resistance fighters. *Science* **2016**, *352*, 758-761.
6. Blair, J.M.A.; Webber, M.A.; Baylay, A.J.; Ogbolu, D.O.; Piddock, L.J.V., Molecular Mechanisms of Antibiotic Resistance. *Nat. Rev. Microbiol.* **2014**, *13*, 42-51.
7. Nicolaou, K.C.; Rigol, S., A Brief History of Antibiotics and Select Advances in Their Synthesis. *J. Antibiot.* **2018**, *71*, 153-184.
8. Andersson, D.I.; Nicoloff, H.; Hjort, K., Mechanisms and Clinical Relevance of Bacterial Heteroresistance. *Nat. Rev. Microbiol.* **2019**, *17*, 479-496.
9. World Health Organisation, Antibiotic Resistance. <https://www.who.int/news-room/fact-sheets/detail/antibiotic-resistance> (accessed Aug 30, 2019).
10. Hernando-Amado, S.; Coque, T.M.; Baquero, F.; Martínez, J.L., Defining and Combating Antibiotic Resistance from One Health and Global Health Perspectives. *Nat. Microbiol.* **2019**, *4*, 1432-1442.
11. O'Neill, J., Tackling Drug-Resistant Infections Globally: Final Report and Recommendations. [https://amr-review.org/sites/default/files/160518\\_Final%20paper\\_with%20cover.pdf](https://amr-review.org/sites/default/files/160518_Final%20paper_with%20cover.pdf) (accessed Aug 30, 2019).

12. The World Bank, Drug-Resistant Infections: A Threat to Our Economic Future. <https://www.worldbank.org/en/topic/health/publication/drug-resistant-infections-a-threat-to-our-economic-future> (accessed Aug 30, 2019).
13. Brown, E.D.; Wright, G.D., Antibacterial Drug Discovery in the Resistance Era. *Nature* **2016**, *529*, 336-242.
14. Gram, H.C., Ueber Die Isolirte Färbung Der Schizomyceten In Schnitt-und Trockenpräparate. *Fortschritte Med.* **1884**, *2*, 185-189.
15. Colco, R., Gram Staining. *Curr. Protoc. Microbiol.* **2006**, *00*, A.3C.1-A.3C.2.
16. Brown, L.; Wolf, J.M.; Prados-Rosales, R.; Casadevall, A., Through the Wall: Extracellular Vesicles in Gram-Positive Bacteria, Mycobacteria and Fungi. *Nat. Rev. Microbiol.* **2015**, *13*, 620-630.
17. Vollmer, W.; Blanot, D.; de Pedro, M.A., Peptidoglycan Structure and Architecture. *FEMS Microbiol. Rev.* **2008**, *32*, 149-167.
18. Huang, L.-Y.; Huang, S.-H.; Chang, Y.-C.; Cheng, W.-C.; Cheng, T.-J. R.; Wong, C.-H., Enzymatic Synthesis of Lipid II and Analogues. *Angew. Chem. Int. Ed.* **2014**, *53*, 8060-8065,
19. Sham, L.T.; Butler, E.K.; Lebar, M.D.; Kahne, D.; Bernhardt, T.G.; Ruiz, N. Bacterial Cell Wall. MurJ is the Flippase of Lipid-Linked Precursors for Peptidoglycan Biogenesis. *Science* **2014**, *345*, 220-222.
20. Typas, A.; Banzhaf, M.; Gross, C.A.; Vollmer, W., From the Regulation of Peptidoglycan Synthesis to Bacterial Growth and Morphology. *Nat. Rev. Microbiol.* **2012**, *10*, 123-136.
21. Greene, N.G.; Fumeaux, C.; Bernhardt, T.G., Conserved Mechanism of Cell-Wall Synthase Regulation Revealed by the Identification of a new PBP Activator in *Pseudomonas Aeruginosa*. *Proc. Natl Acad. Sci. U.S.A.* **2018**, *115*, 3150-3155.
22. Lam, H.; Oh, D.-C.; Cava, F.; Takacs, C.N.; Clardy, J.; de Pedro, M.A.; Waldor, M.K., D-Amino Acids Govern Stationary Phase Cell Wall Remodeling in Bacteria. *Science* **2009**, *325*, 1552-155.

23. Lupoli, T.J.; Tsukamoto, H.; Doud, E.H.; Wang, T.-S.A.; Walker, S.; Kahne, D., Transpeptidase-Mediated Incorporation of D-Amino Acids into Bacterial Peptidoglycan. *J. Am. Chem. Soc.* **2011**, *133*, 10748-10751.
24. Pidgeon, S.E.; Fura, J.M.; Leon, W.; Birabaharan, M.; Vezenov, D.; Pires, M.M., Metabolic Profiling of Bacteria by Unnatural C-terminated D-Amino Acids. *Angew. Chem. Int. Ed.* **2015**, *54*, 6158-6162.
25. van Heijenoort, Y.; Gómez, M.; Derrien, M.; Ayala, J.; van Heijenoort, J., Membrane Intermediates in the Peptidoglycan Metabolism of *Escherichia Coli*: Possible Roles of PBP 1b and PBP 3. *J. Bacteriol.* **1992**, *174*, 3549-3557.
26. Lebar, M.D.; May, J.M.; Meeske, A.J.; Leiman, S.A.; Lupoli, T.J.; Tsukamoto, H.; Losick, R.; Rudner, D.Z.; Walker, S.; Kahne, D., Reconstitution of Peptidoglycan Cross-Linking Leads to Improved Fluorescent Probes of Cell Wall Synthesis. *J. Am. Chem. Soc.* **2014**, *136*, 10874-10877.
27. Schwartz, B.; Markwalder, J.A.; Wang, Y., Lipid II: Total Synthesis of the Bacterial Cell Wall Precursor and Utilization as a Substrate for Glycosyltransfer and Transpeptidation by Penicillin Binding Protein (PBP) 1b of *Escherichia Coli*. *J. Am. Chem. Soc.* **2001**, *123*, 11638-11643.
28. VanNieuwenhze, M.S.; Mauldin, S.C.; Zia-Ebrahimi, M.; Winger, B.E.; Hornback, W.J.; Saha, S.L.; Aikins, J.A.; Blaszcak, L.C., The First Total Synthesis of Lipid II: The Final Monomeric Intermediate in Bacterial Cell Wall Biosynthesis. *J. Am. Chem. Soc.* **2002**, *124*, 3656-3660.
29. Ye, X.-Y.; Lo, M.-C.; Brunner, L.; Walker, D.; Kahne, D.; Walker, S., Better Substrates for Bacterial Transglycosylases. *J. Am. Chem. Soc.* **2001**, *123*, 3155-3156.
30. Liu, H.; Ritter, T.K.; Sadamoto, R.; Sears, P.S.; Wu, M.; Wong, C.-H., Acceptor Specificity and Inhibition of the Bacterial Cell-Wall Glycosyltransferase MurG. *ChemBioChem* **2003**, *4*, 603-609.

31. Shih, H.-W.; Chang, Y.-F.; Li, W.-J.; Meng, F.-C.; Huang, C.-Y.; Ma, C.; Cheng, T.-J. R.; Wong, C.-H.; Cheng, W.-C., Effect of the Peptide Moiety of Lipid II on Bacterial Transglycosylase. *Angew. Chem. Int. Ed.* **2012**, *51*, 10123-10126.
32. Huang, L.-Y.; Huang, S.-H.; Chang, Y.-C.; Cheng, W.-C.; Cheng, T.-J. R.; Wong, C.-H., Enzymatic Synthesis of Lipid II and Analogues. *Angew. Chem. Int. Ed.* **2014**, *53*, 8060-8065.
33. Zhang, Y.; Fechter, E.J.; Wang, T.-S.A.; Barrett, D.; Walker, S.; Kahne, D.E., Synthesis of Heptaprenyl–Lipid IV to Analyze Peptidoglycan Glycosyltransferases. *J. Am. Chem. Soc.* **2007**, *129*, 3080-3081.
34. Hessek, D.; Lee, M.; Morio, K.-i.; Mobashery, S., Synthesis of a Fragment of Bacterial Cell Wall. *J. Org. Chem.* **2004**, *69*, 2137-2146.
35. Shih, H.-W.; Chen, K.-T.; Cheng, T.-J. R.; Wong, C.-H.; Cheng, W.-C., A New Synthetic Approach Toward Bacterial Transglycosylase Substrates, Lipid II and Lipid IV. *Org. Lett.* **2011**, *13*, 4600-4603.
36. Wang, N.; Hasegawa, H.; Huang, C.-y.; Fukase, K.; Fujimoto, Y., Synthesis of Peptidoglycan Fragments from *Enterococcus Faecalis* with Fmoc-Strategy for Glycan Elongation. *Chem. Asian J.* **2017**, *12*, 27-30.
37. Burgess, A.; Vigneron, S.; Brioudes, E.; Labbé, J.-C.; Lorca, T.; Castro, A., Loss of Human Greatwall Results in G2 Arrest and Multiple Mitotic Defects Due to Deregulation of the Cyclin B-Cdc2/PP2A Balance. *Proc. Natl. Acad. Sci. USA* **2010**, *107*, 12564-12569.
38. McCloy, R.A.; Rogers, S.; Caldon, C.E.; Lorca, T.; Castro, A.; Burgess, A., Partial Inhibition of Cdk1 in G2 Phase Overrides the SAC and Decouples Mitotic Events. *Cell Cycle* **2014**, *13*, 1400-1412.
39. Huang, C.-Y.; Shih, H.-W.; Lin, L.-Y.; Tien, Y.-W.; Cheng, T.-J. R.; Cheng, W.-C.; Wong, C.-H.; Ma, C., Crystal Structure of *Staphylococcus aureus* Transglycosylase in Complex with a Lipid II Analog and Elucidation of Peptidoglycan Synthesis Mechanism. *Proc. Natl. Acad. Sci. USA* **2012**, *109*, 6496-6501.

40. Yan, C.; Cheng, D.; Gu, J.; Hu, H.; Zhao, Z.; Qiao M., Preparation of *N*-Succinyl-Chitosan and Their Physical-Chemical Properties as a Novel Excipient. *Chem. Pharm. Bull.* **2006**, *126*, 789-793.
41. Ifuku, S.; Miwa, T.; Morimoto, M.; Saimoto, H., Preparation of Highly Chemoselective *N*-Phthaloyl Chitosan in Aqueous Media. *Green Chem.* **2011**, *13*, 1499-1502.

## Chapter 4 | Conclusion and Future Directions

### 4.1 | Conclusion

In conclusion, the key parameters of chitosan as well as its pharmaceutical and biomedical applications that were relevant to the content of this thesis have been described and discussed in the first chapter. Of which, its ability as a delivery agent, as well as its inherent antimicrobial properties caught our attention.

In the second chapter, a viable delivery system for the delivery of a biomacromolecule had been designed, in which the system has high specificity towards breast cancer cells, MDA-MB-231. That is due to overexpression of sialic acids on the surface of the breast cancer cells as compared to the negative control (NIH3T3). Presence of targeting ligand acts as a ‘key’ in which by targeting the ‘lock’ the whole system is then able to enter the desired cells. A disulfide motif was added in the design, which links the protein, rSML-A to the chitosan delivery agent. This will act as a second barrier in preventing the release of the bioactive proteins in its native form when the required conditions are not met. As such, in this study, the viability of this targeted system had been demonstrated through straightforward synthetic routes and uptake of the final conjugate (**2-30B@A**) into the sialic-acid overexpressed cells (MDA-MB-342) selectively against the control (NIH3T3), in which cytosolic delivery of rSML-A was achieved. Obtaining a good delivery system at first go is almost not possible, and many trials and errors were required to fine-tune the delivery system into a viable one.

The ability of the final conjugate, **2-30B@A**, in escaping the endosome before lysosomes fusion had been demonstrated, thereby killing the cancerous cells when the cargo safely reached the cytosol. In addition, the carrier, **2-29**, has shown excellent biocompatibility, even in the breast cancer cells. Thus, this design of a combination of highly specific components was substantiated by promising biological activities observed in this study and provides an excellent platform for future applications in protein delivery.

Chitosan is a very interesting biopolymer, which exhibits a plethora of inherent pharmaceutical properties, as well as its adaptability in undergoing different kinds of modifications. Interestingly enough, its parent polymer, chitin greatly resembles the peptidoglycan (PG) core structure of the sugar component. However, chitin is not as versatile as chitosan in undergoing modifications, and hence we have decided to utilise it in our attempt of obtaining peptidoglycan oligosaccharides (PGOs) substrates.

Over the past decades, there is a spike interest of studying the biosynthesis of bacterial cell wall, namely which it is one of the key sites in which well-established antibiotics such as penicillin and vancomycin targets. Another reason is that majority of the formation of this three-dimensional mesh-like network, that gives bacterial its stability as well as protection against osmotic pressure, occurs mainly in the periplasmic space, which is not within the bacteria's membrane (inner membrane for G-ve bacteria). Hence such drugs are able to avoid one of the most commonly occurred defensive mechanism adopted by the bacteria is the introduction of efflux pumps to pump out whatever antibiotics that managed to enter beyond the inner membrane. Although targeting the cell wall biosynthetic pathway seems like a gold-mine, but progress have been limited due to high difficulties in obtaining a library of PGOs derivatives for SAR studies of PGT domains in PBPs.

To combat this, an unconventional 'top-down' approach of obtaining PGO substrates have been developed in our group. The PGO obtained via this methodology greatly resembles the natural PGs, such that bacteria's enzymes are able to recognize them and incorporate our substrates into their cell wall. An analysis of the metabolites obtained from lysozyme degradation of the PGO showed presence of NAM-NAG(+pentapeptide) instead of other combination such as NAM-NAM or NAG-NAG. In addition, the cell wall labelling ability of the synthesized PGO substrate was tested against different bacteria strains. Although all strains were able to uptake the PGO, but upon closer inspection, there was a difference in the amount of PGO substrate being take up by the bacteria. Moreover, a brief SAR study was also conducted between PGO, chitosan-peptide and pentapeptide, and it was observed that only PGO were significantly uptake by the bacteria, while



the other two were not as effective. Thereafter, the practicability of our approach was demonstrated in an attempt to obtain PGO derivatives that were not reported before to the best of our knowledge.

## 4.2 | Future Directions

### 4.2.1 | Turning Our Delivery System into a Nanotheranostic System

In recent years, nanotheranostic – a combination of therapy and diagnostic in the nano system – has been emerging as a powerful tool in combating against diseases.<sup>1,2</sup> Since we have achieved active targeting of delivering our biomacromolecular therapeutic agent, rSML-A, our next goal is to turn this delivery system into a theranostic system that allows us to study biological processes such as cellular uptake, as well as intracellular trafficking in real time using live confocal microscopic imaging. From here, we can trace the distribution and also demonstrate ligand-receptor interaction. Furthermore, adding an imaging handle makes studying the biological processes in preclinical and clinical stages possible and more convenient.

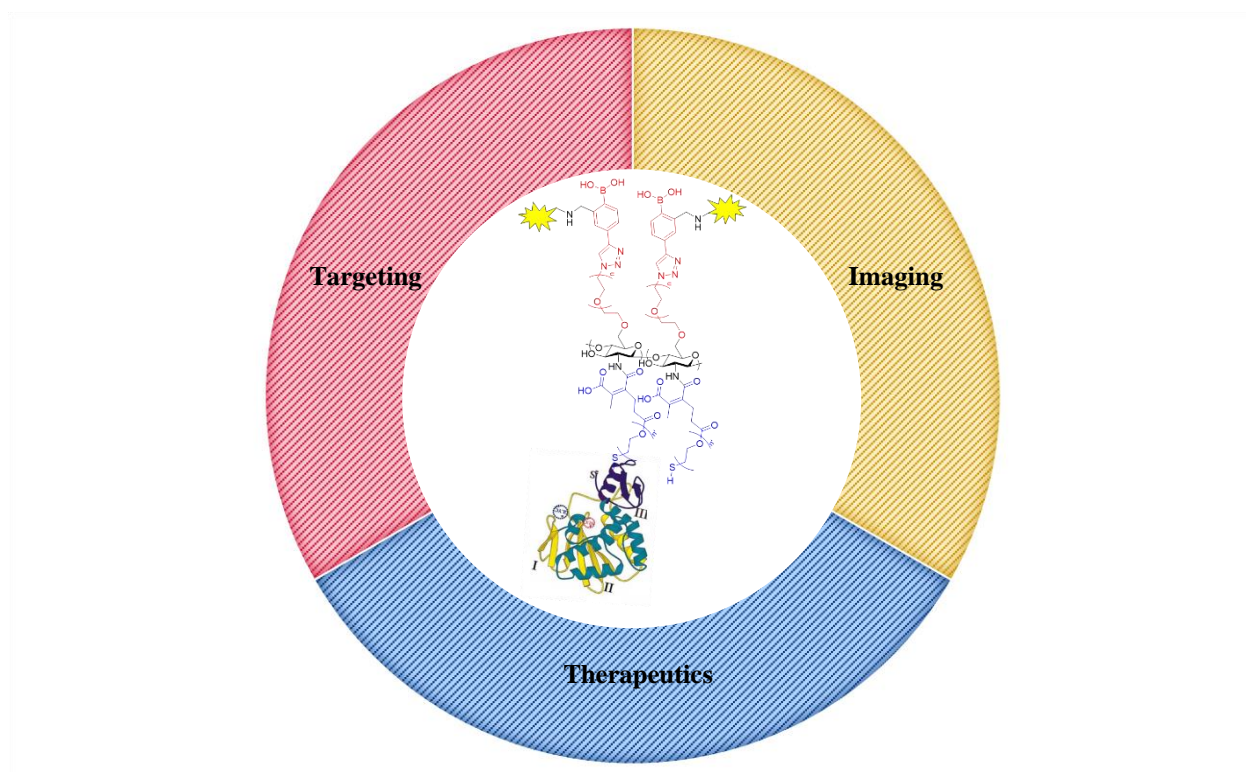
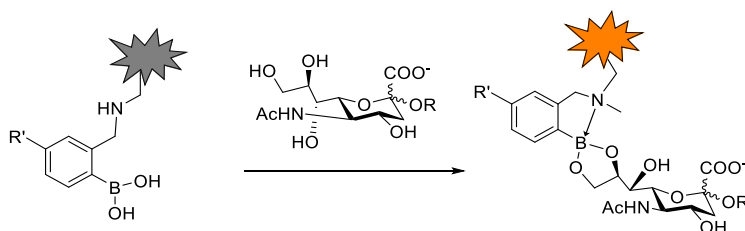


**Figure 4.1** | Schematic diagram showing the three key components of a nanotheranostic system, which comprises of an active targeting moiety, a therapeutic agent to be delivered, as well as an imaging handle for diagnostic purposes.

Hence, by making use of boron's inherent properties, adding a tailored fluorescence tag to our system will result in a drastic change in fluorescence intensity will be observed upon binding (see **Scheme 4.1**). Before binding to the sialic acid, the fluorophore's fluorescence will be quenched by photoinduced electron transfer (PET) via the nitrogen's lone pair of electrons.<sup>3</sup> Upon binding to the cis-diol of the sialic acid of the antigen (Lewis<sup>a</sup>, Lewis<sup>x</sup>, etc), the formation of the boron ester adduct increases the electron deficiency of the boron's p-orbital,<sup>4</sup> hence, the nitrogen atom will be able to donate its lone pair of electrons into it. Thus, this donation will result in its inability to quench the fluorescence by PET, and we can observe the fluorescence signal as well as trace it as it internalizes into the cell.



**Scheme 4.1** | Schematic diagram showing how fluorescence can be observed upon binding to sialic acid due to inability of the nitrogen's lone pair of electrons to quench the fluorescence by PET.

#### 4.2.2 | A Customizable Targeted Delivery System

The true versatility of the design of our delivery system, **2-30B@A**, is that both the targeting ligand and cargo can be customised according to the needs required, in which the latter will be discussed in the next section (**4.2.3**). In our delivery system, the boronic acid targeting moiety (4-ethynylphenylboronic acid) is attached to the azide end of the PEG spacer via click chemistry. As such, a wider variety of targeting ligands can be synthesized and attached to the delivery system to target respective receptors for different bioapplications. It would be a straight-forward synthesis to include an alkyne moiety for click reaction. In the case that the targeting ligand is less stable to withstand multiple types of reactions, one could attach a strained octyne to the targeting moiety such that the metal-free click reaction can be carried out under relatively mild conditions at the final step.

Carbohydrates are good choices as targeting ligands since the glycoproteins on the surfaces of different cell types are unique and responses to specific types of sugars. Our group has previously reported the use of galactose (Gal) as an efficient targeting moiety which is highly recognised by asialoglycoprotein receptor (ASGPR) on HepG2, a human hepatic carcinoma, as well as aiding the system in internalising into the cells.<sup>5</sup> ASGPR are often found in highest amount on the cells of hepatic region, and HepG2 has a density much higher density of ASGPR as compared to healthy hepatic cells, with density reaching greater than 76,000 receptors per cell.<sup>6-7</sup> Mannose, on the other hand, is recognised by mannose receptor expressed on the surfaces of dendritic cells and macrophages, in which, the receptor is involved in regulating our innate immunity.<sup>8</sup>

Short-chain peptides, such as RGD (arginine-glycine-aspartic acid) peptides have often been used as targeting moieties as well. RGD was found to be highly selectively towards  $\alpha_v\beta_3$ ,  $\alpha_v\beta_1$ , and  $\alpha_5\beta_1$  integrins, in which overexpression were observed in angiogenic epithelial cells.<sup>9-12</sup> Further studies demonstrated that the anti-tumor efficacy of cyclic RGD peptides much higher than their linear analogues.<sup>13</sup>

#### **4.2.3 | Delivery of A Wide-Variety of Biomacromolecules**

Recombinant techniques for protein expression have been a game-changing invention that allows facile access to complex structures found in nature, in which many have displayed intriguing biological and/or therapeutic effects. Desired DNA vector can be constructed on commercially available expression vector using specific PCR (polymerase chain reaction) machines. Additional codes for cysteine can be included at the terminal (for proteins that does not have terminal cysteine available for binding onto our delivery system), and subsequently transcribe and translate into the desired therapeutic proteins of interest.

Studies have shown that Concanavalin A (ConA) and Polygonatum cyrtonema lectin (PCL) can result in autophagy after internalisation into the cancer cells or binding onto sugar-containing receptors on the surfaces.<sup>14-15</sup> In addition, studies have also shown that in the case of A375 cells

(melanoma) and HepG2 cells (hepatocellular carcinoma), internalisation of ConA can result in the potential collapse of mitochondrial membrane, thereby releasing cytochrome c and causing caspase activation, which will then trigger mitochondria-mediated apoptosis.<sup>16-17</sup> Therefore, it would be interesting to further study and establish the mechanism using live-imaging to track the whole process.

Another popular approach for anticancer treatment is through the use of immunotherapy. Passive immunotherapies are able to induce and enhance anti-tumor effects through the delivery of monoclonal antibodies and cytokines. It is more general and convenient compared to active immunotherapy, in which the patient's immune system is being directed to target the cancer cells (personalized treatment).

Cytokines are a class of small proteins (5-20 kDa) that are capable of modulating the activity of the immune system. In addition, cytokine-based products typically do not exhibit a direct toxicity to clearance-related organs and to the bone marrow, thus making them ideally suited for synergistic therapy with conventional anticancer cytotoxic agents. Of particular interest is interleukin-13 (IL13), which is mainly produced by activated T helper (Th) 2 cells, and it has been proposed that induction of an apoptotic pathway in cancer cells is made possible by direct IL13-mediated cell killing.<sup>18</sup> A study conducted by Hess and Neri demonstrated this activity via recombinant antibody-mediated delivery of interleukin-13 to syngeneic murine tumours.<sup>19</sup>

#### **4.2.4 | Investigation of the Mechanisms of Bacterial Cell Wall Biosynthesis**

With regards to PGs (peptidoglycans), several studies have been conducted on the effect of different amino acids or peptides, and the effect of different lipid tail structure on the activity of glycosyltransferase. In a study by Wong *et al.*, they demonstrated that the oligosaccharide backbone and pentapeptide chains in PGOs are necessary for effective binding to active site of PGT (peptidoglycan glycosyltransferase).<sup>20</sup> It would be interesting to study the bare minimum requirements of PGO for enzymatic binding as well upon obtaining other derivatives. To the best of our knowledge, there are no reports on the effect of different the different position of the

pentapeptide positions on the NAM-NAG backbone on the activity of PGTs. Hence this unconventional ‘top-down’ approach has opened up the accessibility of PGO derivatives, in which can help us to better understand the bacteria intrinsic mechanism, and this can ultimately provide a crucial pillar in combating against the rising trend of ARB.

### 4.3 | References

1. Mohapatra, S. S.; Ranjan, S.; Dasgupta, N.; Raghvendra, K. M.; Thomas, S. Applications of Targeted Nano Drugs and Delivery Systems; Elsevier Inc.: Amsterdam, 2019.
2. Azevedo, H. S.; de Silva, R. M. P. Self-Assembling Biomaterials; Woodhead Publishing: Cambridge, 2018.
3. Gao, S.; Wang, W.; Wang, B., Building Fluorescent Sensors for Carbohydrates Using Template-Directed Polymerizations. *Bioorg. Chem.* **2001**, 29, 308-320.
4. Wu, X.; Li, Z.; Chen, X.-X.; Fossey, J. S.; James, T. D.; Jiang, Y.-B., Selective Sensing of Saccharides using Simple Boronic Acids and Their Aggregates. *Chem. Soc. Rev.* **2013**, 42, 8032-8048.
5. Wu, X.; Tan, Y. J.; Toh, H. T.; Nguyen, L. H.; Kho, S. H.; Chew, S. Y.; Yoon, H. S.; Liu, X.-W. Stimuli-Responsive Multifunctional Glyconanoparticle Platforms for Targeted Drug Delivery and Cancer Cell Imaging. *Chem. Sci.* **2017**, 8, 3980-3988.
6. D'Souza, A. A.; Devarajan, P. V. J. Asialoglycoprotein Receptor Mediated Hepatocyte Targeting - Strategies and Applications. *Control. Release* **2015**, 203, 126-139.
7. Li, Y.; Huang, G.; Diakur, J.; Wiebe, L. I. Targeted Delivery of Macromolecular Drugs: Asialoglycoprotein Receptor (ASGPR) Expression by Selected Hepatoma Cell Lines Used in Antiviral Drug Development. *Curr. Drug Deliv.* **2008**, 5, 299-302.
8. Gazi, U.; Martinez-Pomares, L. Influence of the Mannose Receptor in Host Immune Responses. *Immunobiology* **2009**, 214, 554-561.
9. Eliceiri, B. P.; Cheresh, D. A. The Role of  $\alpha_v$  Integrins During Angiogenesis: Insights into Potential Mechanisms of Action and Clinical Development *J. Clin. Invest.* **1999**, 103, 1227.
10. Brooks, P. C.; Stromblad, S.; Sanders, L. C.; von Schalscha, T. L.; Aimes, R. T.; Stetler-Stevenson, W. G.; Quigley, J. P.; Cheresh, D. A. Localization of Matrix Metalloproteinase MMP-2 to the Surface of Invasive Cells by Interaction with Integrin  $\alpha_v\beta_3$ . *Cell* **1996**, 85, 683-693.

11. Zeng, Z.-Z.; Yao, H.; Staszewski, E. D.; Rockwood, K. F.; Markwart, S. M.; Fay, K. S.; Spalding, A. C.; Livant, D. L.  $\alpha_5\beta_1$  Integrin Ligand PHSRN Induces Invasion and  $\alpha_5$  mRNA in Endothelial Cells to Stimulate Angiogenesis. *Transl. Oncol.* **2009**, *2*, 8-20.
12. Jha, A. K.; Thrap, K. M.; Browne, S.; Ye, J.; Stahl, A.; Yeghiazarians, Y.; Healy, K. E. Matrix Metalloproteinase-13 Mediated Degradation of Hyaluronic Acid-based Matrices Orchestrates Stem Cell Engraftment through Vascular Integration. *Biomaterials* **2016**, *89*, 136-147.
13. Colombo, G.; Curnis, F.; De Mori, G. M. S.; Gasparri, A.; Longoni, C.; Sacchi, A.; Longhi, R.; Corti, A. Structure-Activity Relationships of Linear and Cyclic Peptides Containing the NGR Tumor-homing Motif. *J. Biol. Chem.* **2002**, *277*, 47891-47897.
14. Lei, H. Y.; Chang, C. P. Induction of Autophagy by Concanavalin A and Its Application in Anti-Tumor Therapy. *Autophagy* **2007**, *3*, 402-404.
15. Liu, B.; Cheng, Y.; Zhang, B.; Bian, H. J.; Bao, J. K. Polygonatum Cyrtonema Lectin Induces Apoptosis and Autophagy in Human Melanoma A375 Cells Through a Mitochondria-Mediated ROS-p38-p53 pathway. *Cancer Lett.* **2009**, *275*, 54-60.
16. Liu, B.; Li, C. Y.; Bian, H. J.; Min, M. W.; Chen, L. F.; Bao, J. K. Antiproliferative Activity and Apoptosis-Inducing Mechanism of Concanavalin A on Human Melanoma A375 cells. *Arch. Biochem. Biophys.* **2009**, *482*, 1-6.
17. Liu, Z. Y.; Li, X. F.; Ding, X. P.; Yang, Y. In Silico and Experimental Studies of Concanavalin A: Insights into Its Antiproliferative Activity and Apoptotic Mechanism. *Appl. Biochem. Biotechnol.* **2010**, *162*, 134-145.
18. Hsi, L. C.; Kundu, S.; Palomo, J.; Xu, B.; Ficco, R.; Vogelbaum, M. A.; Cathcart, M. K. Silencing IL-13R $\alpha_2$  Promotes Glioblastoma Cell Death via Endogenous Signaling. *Mol. Cancer Ther.* **2011**, *10*, 1149-1160.
19. Hess, C.; Neri, D. The Antibody-Mediated Targeted Delivery of Interleukin-13 to Syngeneic Murine Tumors Mediates a Potent Anticancer Activity. *Cancer Immunol. Immunother.* **2015**, *64*, 635-644.

20. Huang, C.-Y.; Shih, H.-W.; Lin, L.-Y.; Tien, Y.-W.; Cheng, T.-J. R.; Cheng, W.-C.; Wong, C.-H.; Ma, C., Crystal Structure of *Staphylococcus aureus* Transglycosylase in Complex with a Lipid II Analog and Elucidation of Peptidoglycan Synthesis Mechanism. *Proc. Natl. Acad. Sci. USA* **2012**, *109*, 6496-6501.



## APPENDIX I – MALDI-TOF MS Analysis

### A1.1 | Brief Introduction

MALDI-TOF MS stands for matrix-assisted laser desorption/ionization time-of-flight mass spectroscopy.<sup>1</sup> MS is an analytical technique that measures the mass to charge ( $m/z$ ) ratio of the ionised compound.<sup>2</sup> MALDI is a “soft” method of ionising samples in solid state, which is capable of generating singly charge ions, and is usually preferable for ionising samples of large molecular weight (MW).<sup>2-3</sup> In comparison to another “soft” ionisation method, electron spray ionisation (ESI) ionises samples in solution phase, and it tends to produce ions with multiple charges.<sup>4</sup> Another advantage of MALDI-TOF MS is that it has rapid turnover time with a very high accuracy.<sup>1</sup> The crucial step in this analysis is the sample preparation method, and there are several key parameters that need to be considered, such as matrices in which the samples will co-crystallise, deposition methods on the MALDI plate, and whether additives such as cationising agents and derivatising agents are needed.

### A1.2 | MALDI Results and Discussion

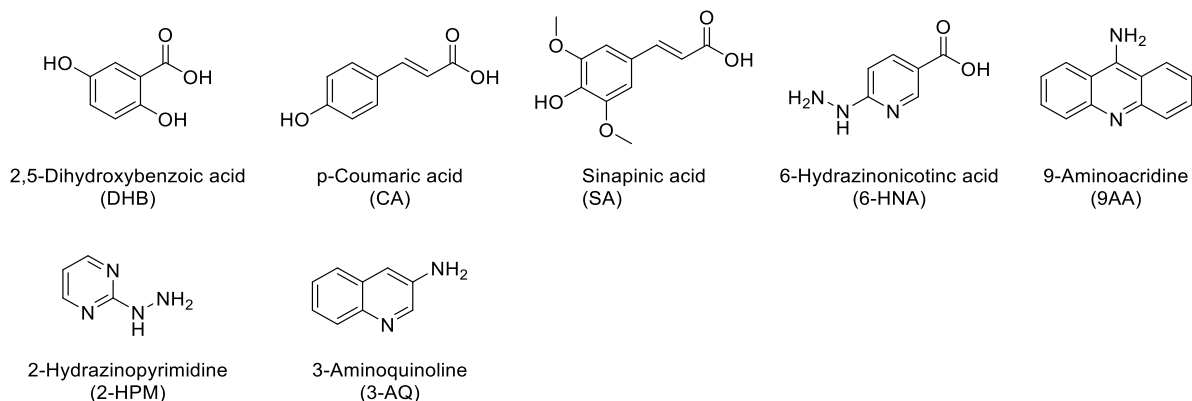
Due to several advantages posed by MALDI, we attempted to use this method to determine the molecular weights of the chitosan starting materials used in this thesis (< 3 kDa chitosan from Carbosynth and high MW glycol chitosan from Sigma Aldrich), PGO substrate obtained in chapter 3, and different pullulan standards (6.2 kDa, 45 kDa and 119 kDa) as standards for calibration. The conditions tried are listed in **Tables A1.1** and **A1.2**.

Initial trials started with a few commonly used matrices for biopolymers, such as sinapinic acid (SA) and 2,5-dihydroxybenzoic acid (DHB).<sup>5-6</sup> Non-volatile solvents are often avoided as they have to be evaporated for crystallisation to occur. Polar solvents with low boiling point such as deionised water ( $H_2O$ ), acetone, methanol (MeOH), ethanol (EtOH), acetonitrile (ACN) or a mixture of these are preferred for both dissolving matrices and samples. Cationizing agents were

also used to help in ionising the samples for better detection purposes.<sup>7-9</sup> A few commonly used depositions methods such as dried droplet method (DD) and thin-layer method (TL) were utilised in the experiments. Other matrices such as 9-aminoacridine (9-AA) and 6-hydrazinonicotinic acid (6-HNA) were also experimented.<sup>10-11</sup>

However, the attempts were not successful, with only noise signals observed in the background. Another study conducted by Xiong *et al.*, showed that second crystallisation with ethanol (will be abbreviated as 2nd-Co. in the tables), instead of the matrix, greatly enhanced crystal formation.<sup>12</sup> 3-Aminoquinoline (3-AQ) can act as both the matrix and derivatising agent for oligosaccharides samples in MALDI-MS analysis, as it reacts with the reducing ends of glycans.<sup>13,16-17</sup> Tanaka *et al.* reported the use of 3-AQ in combination with *p*-coumaric acid (CA) instead of  $\alpha$ -cyano-4-hydroxycinnamic acid (CHCA) as it more hydrophilic and thus has higher affinity for hydrophilic compounds such as unprotected glycans.<sup>13</sup> Also, they observed that by using ammonium dihydrogen phosphate (ADP) solution as the solvent for dissolving both 3-AQ and CA, sensitivity was improved by 10-fold. Another agent that caught our attention is 2-hydrazinopyrimidine (2-HPM), which can act as a co-matrix and derivative agent, as reported in a study by Wang *et al.* in 2016.<sup>14</sup> The hydrazine group is attached to C2 of the pyrimidine ring, which is in-between two high electron-withdrawing imine-like nitrogen atoms. As a result, hydrazine's reactivity is increased greatly, and thus enabling it to react with the reducing ends of the glycans more easily. In addition, they observed that the presence of pyrimidine ring greatly enhances MALDI-MS signal of the sample. Novotny *et al.* reported another method of derivatising, known as permethylation, in which they are able to obtain relatively good signal-to-noise ratios for sugars.<sup>13,18</sup>

Hence, we proceeded with experimenting different conditions reported, as well as a few combinations of the reported methods, and the results are shown in **Tables A1.3, A1.4 and A1.5**. Signal-to-noise (S/N) ratios were recorded for reference, while MALDI-TOF-MS spectra obtained are shown in **Figures A1.1, A1.2 and A1.3**.



**Scheme A1.1** | Schematic illustrations of the chemical structures of the matrices (top row) as well as derivatising agent (bottom row) mentioned.

Matrix compounds	Matrix concentration	Matrix solvent	Solvents used for samples	Additives	Matrix (vol.) : Sample (vol.) : Additives (vol.)	Methods of deposition	Adapted from ref.	Entry No.
Sinapinic acid (SA) <sup>§</sup>	Saturated *	(0.1% TFA in H <sub>2</sub> O)/ACN, v/v = 7:3	ACN, H <sub>2</sub> O	-	1:1:0	DD, TL	5	a
	Saturated *	EtOH	ACN, H <sub>2</sub> O	-	1:1:0	DD, TL	5	b
9-aminoacridine (9AA) <sup>#</sup>	15 mg/mL	Acetone	ACN, H <sub>2</sub> O	-	1:1:0	DD, TL	10	n
6-Hydrazinonicotinic acid (6-HNA)	2 mg/mL	2% HAC in MeOH	ACN, H <sub>2</sub> O	-	1:1:0	DD, TL	11	o
p-Coumaric acid (CA) (Recrystallised from reagent grade)	1 mg/mL	2 mM ADP solution (dissolved in H <sub>2</sub> O/ACN, v/v = 1:1)	ACN, H <sub>2</sub> O	Derivatising solution A	2:1:1	DD, 2nd-Co	12-14	t
	50 mg/mL	2 mM ADP solution (dissolved in H <sub>2</sub> O/ACN, v/v = 1:1)	ACN, H <sub>2</sub> O	Derivatising solution B	2:1:1	DD, 2nd-Co	12-14	aa
	50 mg/mL	2 mM ADP solution (dissolved in H <sub>2</sub> O/ACN, v/v = 1:1)	ACN, H <sub>2</sub> O	Derivatising solution C	2:1:1	DD, 2nd-Co	12-14	ab
	50 mg/mL	2 mM ADP solution (dissolved in H <sub>2</sub> O/ACN, v/v = 1:1)	ACN, H <sub>2</sub> O	Derivatising solution D	2:1:1	DD, 2nd-Co	12-14	ac
	100 mg/mL	2 mM ADP solution (dissolved in H <sub>2</sub> O/ACN, v/v = 1:1)	ACN, H <sub>2</sub> O	Derivatising solution B	2:1:1	DD, 2nd-Co	12-14	ad
	100 mg/mL	2 mM ADP solution (dissolved in H <sub>2</sub> O/ACN, v/v = 1:1)	ACN, H <sub>2</sub> O	Derivatising solution C	2:1:1	DD, 2nd-Co	12-14	ae
	100 mg/mL	2 mM ADP solution (dissolved in H <sub>2</sub> O/ACN, v/v = 1:1)	ACN, H <sub>2</sub> O	Derivatising solution D	2:1:1	DD, 2nd-Co	12-14	af

**Table A1.1** | List of conditions tried, part 1. Derivatising solution A comprises of 2 mg of 3-AQ dissolved in 1 mL of 2 mM ADP solution. Derivatising solution B is a mixture of 4 mg/mL 2-HPM solution and 4 mM ADP solution (v/v = 1:1), such that upon mixing, the final concentrations of 2-HPM and ADP are halved. Derivatising solution C is a mixture of 10 mg/mL 2-HPM solution and 4 mM ADP solution (v/v = 1:1). Derivatising solution D is a mixture of 20 mg/mL 2-HPM solution and 4 mM ADP solution (v/v = 1:1). ADP solution is a mixture of ADP dissolved in H<sub>2</sub>O/ACN (v/v = 1:1), and 2-HPM solution is a mixture of 2-HPM dissolved in MeOH/AcOH (v/v = 9:1). <sup>§</sup> Matrix was purchased and used without further purification. <sup>#</sup> MALDI-TOF-MS analysis was carried out in negative mode. \* Matrix was added till saturation point, in which the solid particles were settled at the bottom and the supernatant was remove for usage.

Matrix compounds	Matrix concentration	Matrix solvent	Solvents used for samples	Additives	Matrix (vol.) : Sample (vol.) : Additives (vol.)	Methods of deposition	Adapted from ref.	Entry No.
2,5-Dihydroxybenzoic acid (DHB) <sup>\$</sup>	20 mg/mL	(0.1% TFA in H <sub>2</sub> O)/ACN, v/v = 7:3	ACN, H <sub>2</sub> O	-	1:1:0	DD	5	c
	10 mg/mL	(0.1% TFA in H <sub>2</sub> O)/ACN, v/v = 7:3	ACN, H <sub>2</sub> O	-	1:1:0	DD	5	d
	10 mg/mL	H <sub>2</sub> O/EtOH, v/v = 9:1	ACN, H <sub>2</sub> O	-	1:1:0	DD	6	e
	Saturated *	H <sub>2</sub> O/EtOH, v/v = 9:1	ACN, H <sub>2</sub> O	-	1:1:0	DD	6	f
	15.4 mg/mL	H <sub>2</sub> O	ACN, H <sub>2</sub> O	NaI (1 mM in H <sub>2</sub> O)	1:1:5	DD	7-8	j
	15.4 mg/mL	H <sub>2</sub> O	ACN, H <sub>2</sub> O	AgOTf (10 mg/mL in MeOH/DCM, v/v = 1:3)	1:1:5	DD	7, 9	k
	Saturated *	(0.1% TFA in H <sub>2</sub> O)/ACN, v/v = 1:1	ACN, H <sub>2</sub> O	NaI (1 mM in H <sub>2</sub> O)	1:1:5	DD, TL	6-8	l
	Saturated *	(0.1% TFA in H <sub>2</sub> O)/ACN, v/v = 1:1	ACN, H <sub>2</sub> O	AgOTf (10 mg/mL in MeOH/DCM, v/v = 1:3)	1:1:5	DD, TL	6-7, 9	m
	Saturated *	H <sub>2</sub> O/ACN, v/v = 1:1	ACN, H <sub>2</sub> O	Derivatising solution C	2:1:1	DD	13-14	p
2,5-Dihydroxybenzoic acid (DHB) (Recrystallised from reagent grade)	Saturated *	H <sub>2</sub> O/ACN, v/v = 1:1	ACN, H <sub>2</sub> O	Derivatising solution D	2:1:1	DD	13-14	q
	Saturated *	(0.1% TFA in H <sub>2</sub> O)/ACN, v/v = 1:1	ACN, H <sub>2</sub> O	-	1:1:0	DD, TL	-	g
	Saturated *	(0.1% TFA in H <sub>2</sub> O)/ACN, v/v = 3:7	ACN, H <sub>2</sub> O	-	1:1:0	DD, TL	-	h
	Saturated *	(0.1% TFA in H <sub>2</sub> O)/ACN, v/v = 7:3	ACN, H <sub>2</sub> O	-	1:1:0	DD, TL	-	i
	Saturated *	H <sub>2</sub> O/ACN, v/v = 1:1	ACN, H <sub>2</sub> O	Derivatising solution C	2:1:1	DD	13-14	r
	Saturated *	H <sub>2</sub> O/ACN, v/v = 1:1	ACN, H <sub>2</sub> O	Derivatising solution D	2:1:1	DD	13-14	s
	50 mg/mL	H <sub>2</sub> O/ACN, v/v = 1:1	ACN, H <sub>2</sub> O	Derivatising solution B	2:1:1	DD, 2nd-Co	12-14	u
	50 mg/mL	H <sub>2</sub> O/ACN, v/v = 1:1	ACN, H <sub>2</sub> O	Derivatising solution C	2:1:1	DD, 2nd-Co	12-14	v
	50 mg/mL	H <sub>2</sub> O/ACN, v/v = 1:1	ACN, H <sub>2</sub> O	Derivatising solution D	2:1:1	DD, 2nd-Co	12-14	w
	100 mg/mL	H <sub>2</sub> O/ACN, v/v = 1:1	ACN, H <sub>2</sub> O	Derivatising solution B	2:1:1	DD, 2nd-Co	12-14	x
	100 mg/mL	H <sub>2</sub> O/ACN, v/v = 1:1	ACN, H <sub>2</sub> O	Derivatising solution C	2:1:1	DD, 2nd-Co	12-14	y
	100 mg/mL	H <sub>2</sub> O/ACN, v/v = 1:1	ACN, H <sub>2</sub> O	Derivatising solution D	2:1:1	DD, 2nd-Co	12-14	z
	25 mg/mL	H <sub>2</sub> O/ACN, v/v = 1:1	ACN, H <sub>2</sub> O	MeI	2:1:1	DD, 2nd-Co	12-15	ag
	25 mg/mL	H <sub>2</sub> O/ACN, v/v = 1:1	ACN, H <sub>2</sub> O	MeI + NaOAc	2:1:1	DD, 2nd-Co	12-15	ah
	25 mg/mL	H <sub>2</sub> O/ACN, v/v = 1:1	ACN, H <sub>2</sub> O	Derivatising solution D + MeI	2:1:1	DD, 2nd-Co	12-15	ai
	25 mg/mL	H <sub>2</sub> O/ACN, v/v = 1:1	ACN, H <sub>2</sub> O	Derivatising solution D + MeI + NaOAc	2:1:1	DD, 2nd-Co	12-15	aj
	50 mg/mL	H <sub>2</sub> O/ACN, v/v = 1:1	ACN, H <sub>2</sub> O	MeI	2:1:1	DD, 2nd-Co	12-15	ak
	50 mg/mL	H <sub>2</sub> O/ACN, v/v = 1:1	ACN, H <sub>2</sub> O	MeI + NaOAc	2:1:1	DD, 2nd-Co	12-15	al
	50 mg/mL	H <sub>2</sub> O/ACN, v/v = 1:1	ACN, H <sub>2</sub> O	Derivatising solution D + MeI	2:1:1	DD, 2nd-Co	12-15	am
	50 mg/mL	H <sub>2</sub> O/ACN, v/v = 1:1	ACN, H <sub>2</sub> O	Derivatising solution D + MeI + NaOAc	2:1:1	DD, 2nd-Co	12-15	an
	100 mg/mL	H <sub>2</sub> O/ACN, v/v = 1:1	ACN, H <sub>2</sub> O	MeI	2:1:1	DD	13-15	ao
	100 mg/mL	H <sub>2</sub> O/ACN, v/v = 1:1	ACN, H <sub>2</sub> O	MeI + NaOAc	2:1:1	DD	13-15	ap
	100 mg/mL	H <sub>2</sub> O/ACN, v/v = 1:1	ACN, H <sub>2</sub> O	Derivatising solution D + MeI	2:1:1	DD	13-15	aq
	100 mg/mL	H <sub>2</sub> O/ACN, v/v = 1:1	ACN, H <sub>2</sub> O	Derivatising solution D + MeI + NaOAc	2:1:1	DD	13-15	ar

**Table A1.2** | List of conditions tried, part 2. Derivatising solutions B, C and D were the same as described in Table A.1. <sup>\$</sup> Matrix was purchased and used without further purification. \* Matrix was added till saturation point, in which the solid particles were settled at the bottom and the supernatant was remove for usage.

Entry No.	Pullulan standard, 6.2 kDa		Chitosan, < 3 kDa (Carbosynth)		PGO final substrate		Pullulan standard, 45 kDa		Pullulan standard, 119 kDa		Glycol Chitosan (Sigma Aldrich)	
	DD	TL	DD	TL	DD	TL	DD	TL	DD	TL	DD	TL
a	X	X	X	X	X	X	X	X	X	X	X	X
b	X	X	X	X	X	X	X	X	X	X	X	X
c	X	N.D.	X	N.D.	X	N.D.	X	N.D.	X	N.D.	X	N.D.
d	X	N.D.	X	N.D.	X	N.D.	X	N.D.	X	N.D.	X	N.D.
e	X	N.D.	X	N.D.	X	N.D.	X	N.D.	X	N.D.	X	N.D.
f	X	N.D.	X	N.D.	X	N.D.	X	N.D.	X	N.D.	X	N.D.
g	X	N.D.	X	N.D.	X	N.D.	X	N.D.	X	N.D.	X	N.D.
h	X	N.D.	X	N.D.	X	N.D.	X	N.D.	X	N.D.	X	N.D.
i	X	N.D.	X	N.D.	X	N.D.	X	N.D.	X	N.D.	X	N.D.
j	X	N.D.	X	N.D.	X	N.D.	X	N.D.	X	N.D.	X	N.D.
k	X	N.D.	X	N.D.	X	N.D.	X	N.D.	X	N.D.	X	N.D.
l	X	X	X	X	X	X	X	X	X	X	X	X
m	X	X	X	X	X	X	X	X	X	X	X	X
n	X	X	X	X	X	X	X	X	X	X	X	X
o	X	X	X	X	X	X	X	X	X	X	X	X
p	X	N.D.	X	N.D.	X	N.D.	X	N.D.	X	N.D.	X	N.D.
q	S/N = 7	N.D.	X	N.D.	X	N.D.	X	N.D.	X	N.D.	X	N.D.
r	S/N = 23	N.D.	X	N.D.	X	N.D.	X	N.D.	X	N.D.	X	N.D.
s	S/N = 25	N.D.	X	N.D.	X	N.D.	X	N.D.	X	N.D.	X	N.D.

**Table A1.3** | Results obtained from MALDI-TOF-MS analysis of entries **a** to **s**, were ‘X’ = only noise observed, ‘S/N’ = signal to noise ratio, and ‘N.D.’ = not determined.

Entry No.	Pullulan standard, 6.2 kDa		Chitosan, < 3 kDa (Carbosynth)		PGO final substrate		Pullulan standard, 45 kDa		Pullulan standard, 119 kDa		Glycol Chitosan (Sigma Aldrich)	
	DD	2nd-Co	DD	2nd-Co	DD	2nd-Co	DD	2nd-Co	DD	2nd-Co	DD	2nd-Co
<b>t</b>	- heat	X	X	S/N = 1	S/N = 2	X	X	X	X	X	X	X
	+ heat	X	X	X	X	X	X	X	X	X	X	X
<b>u</b>	- heat	X	S/N = 12	X	X	X	X	X	X	X	X	X
	+ heat	S/N = 8	S/N = 4	X	X	X	X	X	X	X	X	X
<b>v</b>	- heat	S/N = 23	S/N = 7	X	X	X	X	X	X	X	X	X
	+ heat	S/N = 21	S/N = 13	X	X	X	X	X	X	X	X	X
<b>w</b>	- heat	S/N = 25	S/N = 15	X	S/N = 9	X	X	X	X	X	X	X
	+ heat	S/N = 21	S/N = 13	S/N = 1-2	S/N = 7	X	X	X	X	X	X	X
<b>x</b>	- heat	S/N = 7-11	S/N = 11-12	S/N = 4	X	X	X	X	X	X	X	X
	+ heat	S/N = 11-12	S/N = 7-10	S/N = 5	S/N = 1-2	X	X	X	X	X	X	X
<b>y</b>	- heat	S/N = 4-9	S/N = 3-5	S/N = 4	S/N = 4	X	X	X	X	X	X	X
	+ heat	S/N = 8-13	S/N = 7-14	X	X	X	X	X	X	X	X	X
<b>z</b>	- heat	S/N = 9	S/N = 9-12	S/N = 8	S/N = 1-2	X	X	X	X	X	X	X
	+ heat	S/N = 12	S/N = 11	S/N = 7-8	S/N = 6	X	X	X	X	X	X	X
<b>aa</b>	- heat	X	X	X	X	X	X	X	X	X	X	X
	+ heat	X	X	X	X	X	X	X	X	X	X	X
<b>ab</b>	- heat	X	X	X	X	X	X	X	X	X	X	X
	+ heat	X	X	X	X	X	X	X	X	X	X	X
<b>ac</b>	- heat	X	X	X	X	X	X	X	X	X	X	X
	+ heat	X	X	X	X	X	X	X	X	X	X	X
<b>ad</b>	- heat	X	X	X	X	X	X	X	X	X	X	X
	+ heat	X	S/N = 1-2	X	X	X	X	X	X	X	X	X
<b>ae</b>	- heat	X	X	X	X	X	X	X	X	X	X	X
	+ heat	X	X	X	X	X	X	X	X	X	X	X
<b>af</b>	- heat	X	X	X	X	X	X	X	X	X	X	X
	+ heat	X	X	X	X	X	X	X	X	X	X	X

**Table A1.4** | Results obtained from MALDI-TOF-MS analysis of entries **t** to **af**, were ‘X’ = only noise observed, ‘S/N’ = signal to noise ratio, and ‘N.D.’ = not determined.

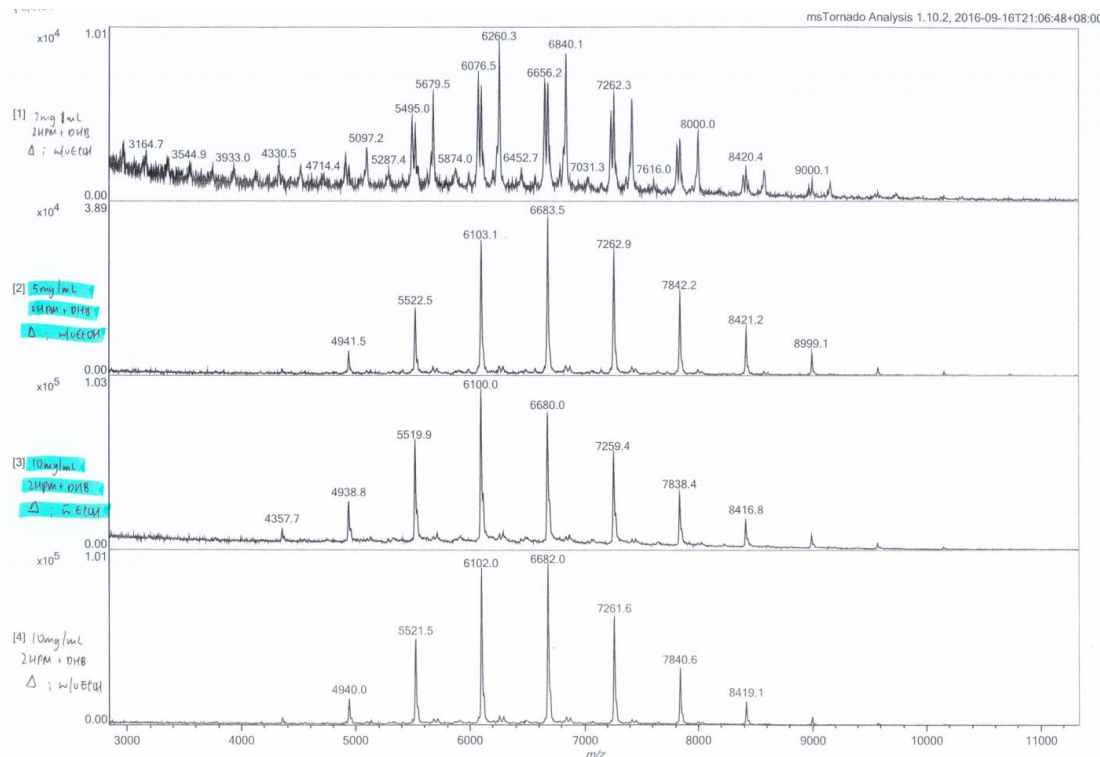


**Figure A1.1** | Image scan of selected MALDI-TOF-MS spectra of the pullulan standard (6.2 kDa), for entries **u** (DD, +heat), **v** (DD, +heat), **w** (2nd-Co., +heat), **w** (DD, +heat).

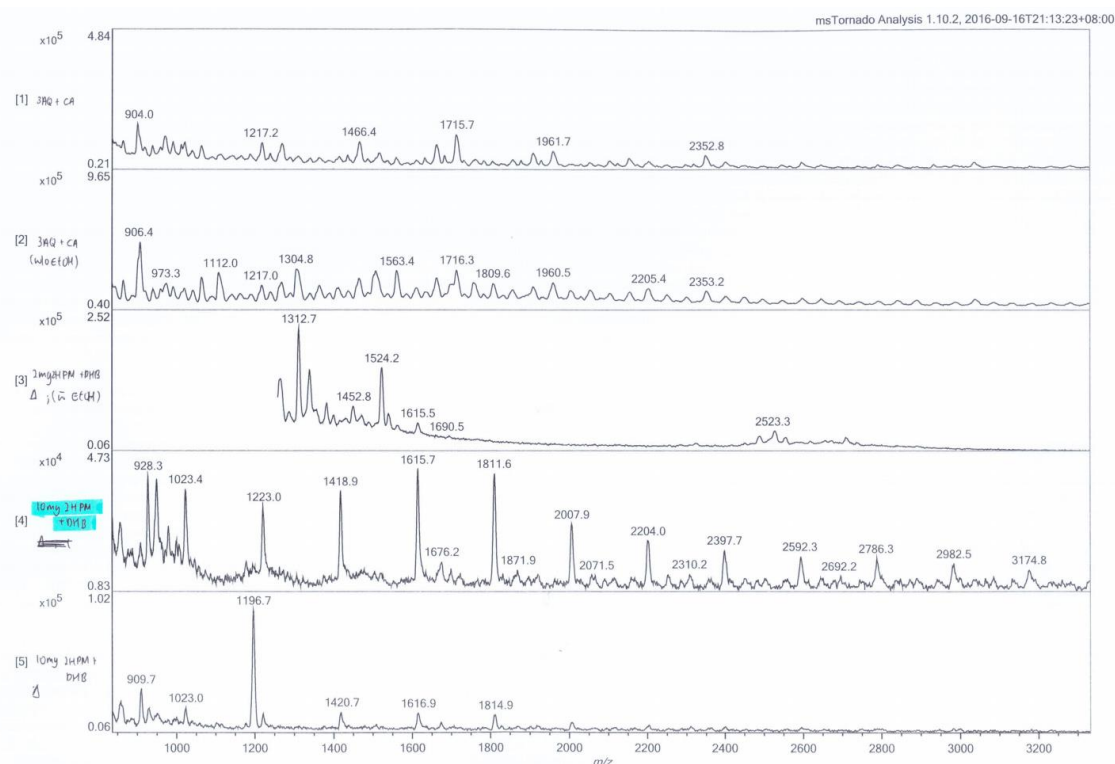


**Figure A1.2** | Image scan of selected MALDI-TOF-MS spectra of the chitosan (< 3 kDa, Carbosynth), for entries **t** (2nd-Co., -heat), **t** (DD, -heat), **u** (2nd-Co., +heat), **z** (DD, -heat), **w** (2nd-Co., +heat).

Entry No.		Pullulan standard, 6.2 kDa	Chitosan, < 3 kDa (Carbosynth)		PGO final substrate		Pullulan standard, 45 kDa	Pullulan standard, 119 kDa	Glycol Chitosan (Sigma Aldrich)
		DD	DD	2nd-Co	DD	2nd-Co	DD	DD	DD
ag	- heat	S/N = 1-2	S/N = 13-17	N.D.	X	N.D.	X	X	X
	+ heat	N.D.	N.D.	S/N = 11-16	N.D.	X	N.D.	N.D.	N.D.
ah	- heat	S/N = 10	S/N = 14-17	N.D.	X	N.D.	X	X	X
	+ heat	N.D.	N.D.	S/N = 17-21	N.D.	X	N.D.	N.D.	N.D.
ai	- heat	X	X	N.D.	X	N.D.	X	X	X
	+ heat	N.D.	N.D.	X	N.D.	X	N.D.	N.D.	N.D.
aj	- heat	X	X	N.D.	X	N.D.	X	X	X
	+ heat	N.D.	N.D.	X	N.D.	N.D.	N.D.	N.D.	N.D.
ak	- heat	S/N = 1-2	N.D.	S/N = 16	N.D.	N.D.	N.D.	N.D.	N.D.
	+ heat	N.D.	N.D.	N.D.	N.D.	N.D.	N.D.	N.D.	N.D.
al	- heat	S/N = 7-8	N.D.	S/N = 13	N.D.	N.D.	N.D.	N.D.	N.D.
	+ heat	N.D.	N.D.	N.D.	N.D.	N.D.	N.D.	N.D.	N.D.
am	- heat	X	N.D.	X	N.D.	N.D.	N.D.	N.D.	N.D.
	+ heat	N.D.	N.D.	N.D.	N.D.	N.D.	N.D.	N.D.	N.D.
an	- heat	X	N.D.	X	N.D.	N.D.	N.D.	N.D.	N.D.
	+ heat	N.D.	N.D.	N.D.	N.D.	N.D.	N.D.	N.D.	N.D.
ao	- heat	N.D.	S/N = 1-2	N.D.	N.D.	N.D.	X	X	X
	+ heat	N.D.	N.D.	N.D.	N.D.	X	N.D.	N.D.	N.D.
ap	- heat	N.D.	X	N.D.	N.D.	N.D.	X	X	X
	+ heat	N.D.	N.D.	N.D.	N.D.	X	N.D.	N.D.	N.D.
aq	- heat	N.D.	X	N.D.	N.D.	N.D.	X	X	X
	+ heat	N.D.	N.D.	N.D.	N.D.	X	N.D.	N.D.	N.D.
ar	- heat	N.D.	X	N.D.	N.D.	N.D.	X	X	X
	+ heat	N.D.	N.D.	N.D.	N.D.	X	N.D.	N.D.	N.D.

**Table A1.5** | Results obtained from MALDI-TOF-MS analysis of entries **ag** to **ar**, were ‘X’ = only noise observed, ‘S/N’ = signal to noise ratio, and ‘N.D.’ = not determined.

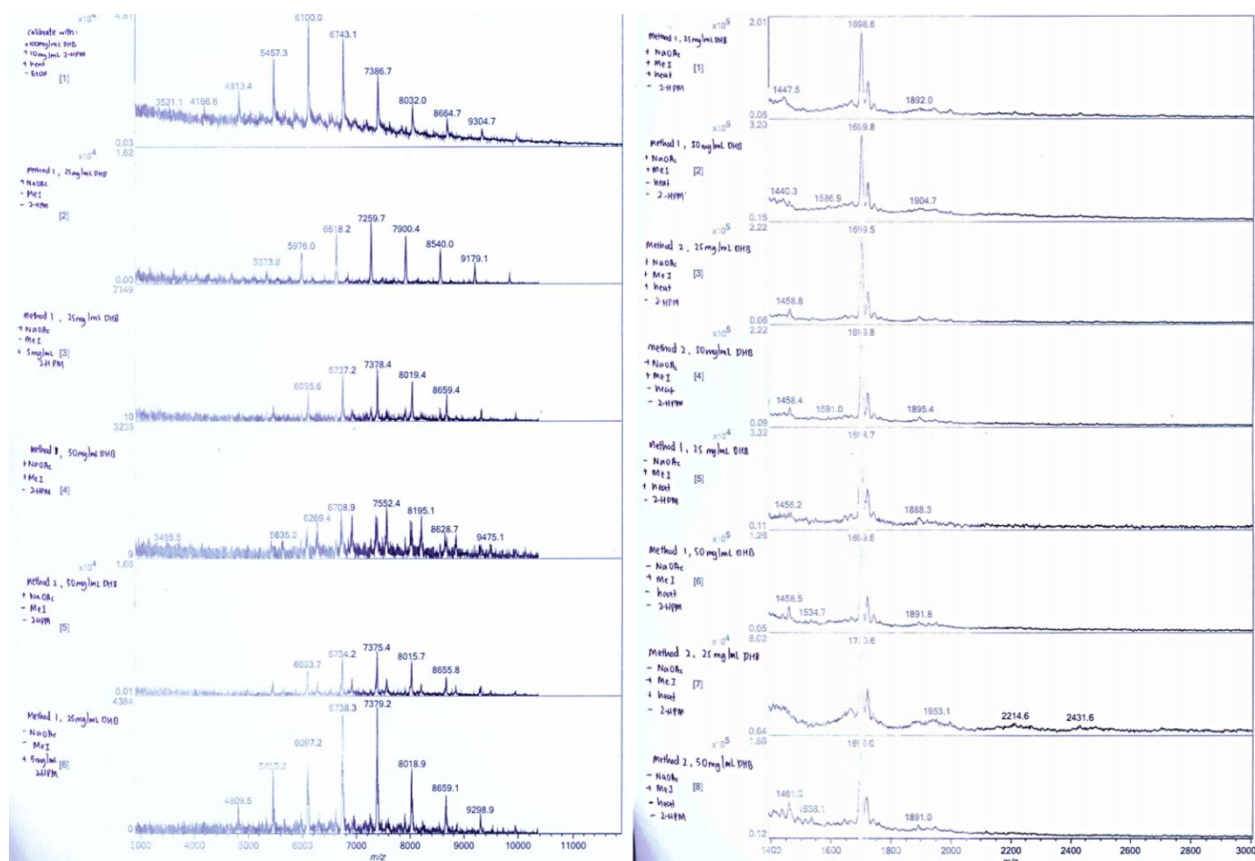


**Figure A1.3** | Successful MS spectrums pullulan 6.2 kDa (left) chitosan purchased from Carbosynth (right) obtained from different conditions.

### A.3 | Summary and Conclusion

In summary, for chitosan starting material used in chapter 3, the MW peak detected was 1615.7 kDa (see **Figure A1.4** below), which roughly corresponds to 10 repeating units of glucosamine (exact mass = 161.06 Da). Samples first derivatised with 2-HPM works best together with utilising 25 mg/mL of recrystallised DHB as matrix using dried deposition method followed by second co-crystallisation with ethanol. Another condition that works too is to derivatise the reducing end of chitosan with 2-HPM and using 50 mg/mL of recrystallised DHB as matrix, using the dried deposition method.

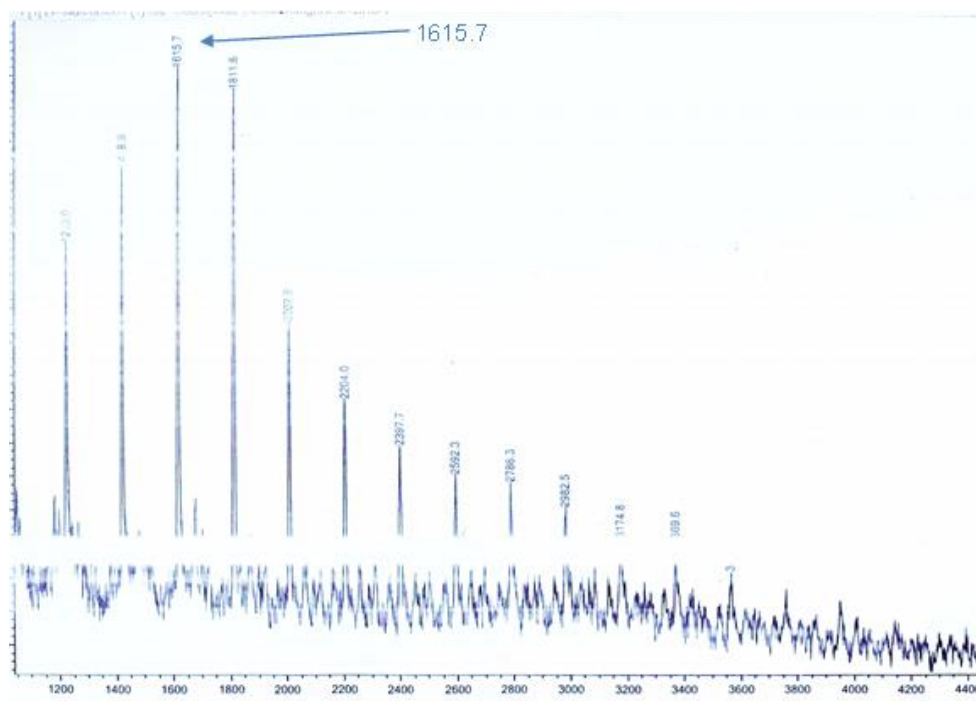


**Figure A1.4** | MALDI-TOF-MS spectrum depicting a distribution of different MW of chitosan, with the peak height corresponding to 1615.7 kDa.

As for Pullulan standard (6.2 kDa), derivative agent such as 2-HPM or permethylation does not affect the outcome as much. Dried droplet method with DHB matrix (25 mg/mL to 100 mg/mL) gives better S/N ratios. Adding cationizing agent such as NaOAc prior to deposition does not seem to have a significant impact on the S/N ratio.



## A.4 | References

1. Clark, A. E.; Kaleta, E. J.; Arora, A.; Wolk, D. M., Matrix-Assisted Laser Desorption Ionization–Time of Flight Mass Spectrometry: a Fundamental Shift in the Routine Practice of Clinical Microbiology. *Clin. Microbiol. Rev.* **2013**, *26*, 547-603.
2. El-Aneed, A.; Cohen, A.; Banoub, J., Mass Spectrometry, Review of the Basics: Electrospray, MALDI, and Commonly Used Mass Analyzers. *Appl. Spectrosc. Rev.* **2009**, *44*, 210-230.
3. Hillenkamp, F.; Karas, M.; Beavis, R. C.; Chait, B. T., Matrix-Assisted Laser Desorption/Ionization Mass Spectrometry of Biopolymers. *Anal. Chem.* **1991**, *63*, 1193A-1203A.
4. Kebarle, P., A Brief Overview of the Present Status of the Mechanisms Involved in Electrospray Mass Spectrometry. *J. Mass Spectrom.* **2000**, *35*, 804-817.
5. Bruker, Instruction for Use: Bruker Guide to MALDI Sample Preparation. [https://www.bruker.com/fileadmin/user\\_upload/8-PDF-Docs/Separations\\_MassSpectrometry/InstructionForUse/8702557\\_IFU\\_Bruker\\_Guide\\_MALDI\\_Sample\\_Preparation\\_Revision\\_E.pdf](https://www.bruker.com/fileadmin/user_upload/8-PDF-Docs/Separations_MassSpectrometry/InstructionForUse/8702557_IFU_Bruker_Guide_MALDI_Sample_Preparation_Revision_E.pdf) (accessed September 15, 2019).
6. Strupat, K.; Karas, M.; Hillenkamp, F., 2,5-Dihydroxybenzoic Acid: A New Matrix for Laser Desorption-Ionization Mass Spectrometry. *Int. J. Mass Spectrom. Ion Processes* **1991**, *111*, 89-102.
7. Choi, S.-S.; Lee, H.M., Analysis of Mixture of Maltoogligoses Using MALDI-TOFMS: Influence of Cationizing Agent Types. *Bull. Korean Chem. Soc.* **2009**, *30*, 2806-2808.
8. Watanabe, T.; Kawasaki, H.; Kimoto, T.; Arakawa, R., Halohydration of Epoxy Resins Using Sodium Halides as Cationizing Agents in MALDI-MS and DIOS-MS. *J. Mass Spectrom.* **2008**, *43*, 1664-1672.
9. Shao, Y.; Yin, H.; Wang, X.-M.; Han, S.-Y.; Yan, X.; Xu, J.; He, J.; Ni, P.; Zhang, W.-B., Mixed [2 : 6] Hetero-Arm Star Polymers Based on Janus POSS with Precisely Defined Arm Distribution. *Polym. Chem.* **2016**, *7*, 2381-2388.

10. Vermillion-Salsbury, R.L.; Hercules, D.M., 9-Aminoacridine as a Matrix for Negative Mode Matrix-Assisted Laser Desorption/Ionization. *Rapid Commun. Mass Spectrom.* **2002**, *16*, 1575-1581.
11. Jiao, J.; Zhang, Y.; Yang, P.; Lu, H., Hydrazinonicotinic Acid as a Novel Matrix for Highly Sensitive and Selective MALDI-MS Analysis of Oligosaccharides. *Analyst* **2015**, *140*, 156-161.
12. Zhao, Z.-w.; Xiong, L.; Wang, Z.-P.; Xin, B.; Hu, W.-H.; Xiong, S.-X., Analysis of Chitosan by Matrix-assisted Laser Desorption/Ionization Time-of-Flight Mass Spectrometry. *Chinese J. Anal. Chem.* **2007**, *35*, 1025-1028.
13. Fukuyama, Y.; Funakoshi, N.; Takeyama, K.; Hioki, Y.; Nishikaze, T.; Kaneshiro, K.; Kawabata, S.-i.; Iwamoto, S.; Tanaka, K., 3-Aminoquinoline/p-Coumaric Acid as a MALDI Matrix for Glycopeptides, Carbohydrates, and Phosphopeptides. *Anal. Chem.* **2014**, *86*, 1937-1942.
14. Jiang, K.; Aloor, A.; Qu, J.; Xiao, C.; Wu, Z.; Ma, C.; Zhang, L.; Wang, G.P., Rapid and Sensitive MALDI MS Analysis of Oligosaccharides by Using 2-Hydrazinopyrimidine as a Derivative Reagent and Co-Matrix. *Anal. Bioanal. Chem.* **2017**, *409*, 421-429.
15. Alley, W. R.; Mann, B. F.; Novotny, M. V., High-Sensitivity Analytical Approaches for the Structural Characterization of Glycoproteins. *Chem. Rev.* **2013**, *113*, 2668-2732.
16. Rohmer, M.; Meyer, B.; Mank, M.; Stahl, B.; Bahr, U.; Karas, M., 3-Aminoquinoline Acting as Matrix and Derivatizing Agent for MALDI MS Analysis of Oligosaccharides. *Anal. Chem.* **2010**, *82*, 3719-3726.
17. Kaneshiro, K.; Fukuyama, Y.; Iwamoto, S.; Sekiya, S.; Tanaka, K., Highly Sensitive MALDI Analyses of Glycans by a New Aminoquinoline-Labeling Method using 3-Aminoquinoline/ $\alpha$ -Cyano-4-Hydroxycinnamic Acid Liquid Matrix. *Anal. Chem.* **2011**, *83*, 3663-3667.
18. Kang, P.; Mechref, Y.; Novotny, M. V., High-Throughput Solid-Phase Permethylolation of Glycans Prior to Mass Spectrometry *Rapid Commun. Mass Spectrom.* **2008**, *22*, 721-734.

## AII.1 | NMR Spectra

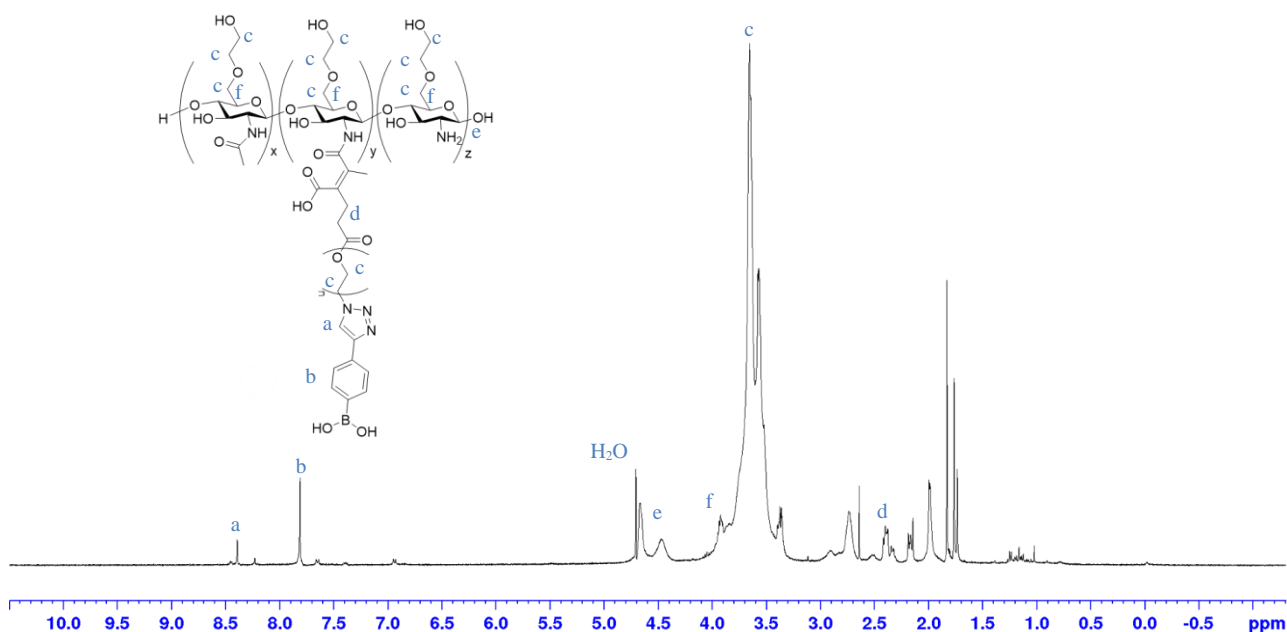


**Figure A2.1** |  $^1\text{H}$  NMR spectrum of **2-9** in  $\text{D}_2\text{O}$  (water-suppressed).

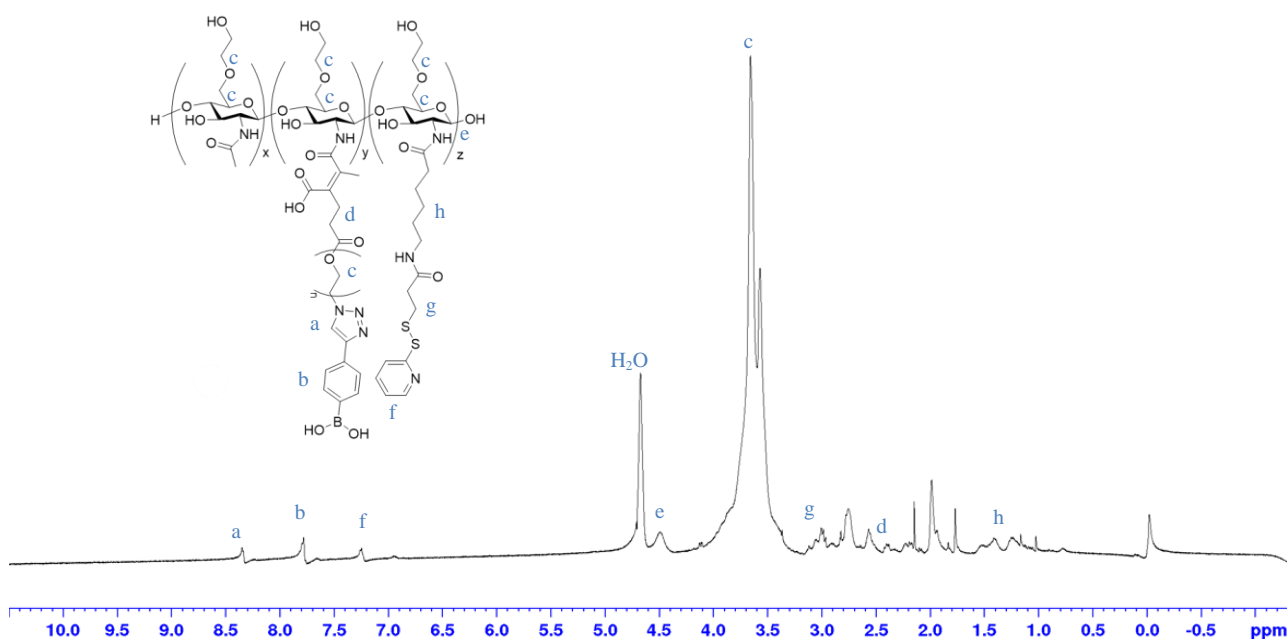


**Figure A2.2** |  $^1\text{H}$  NMR spectrum of **2-10** in  $\text{D}_2\text{O}$  (water-suppressed).

The appearance of the peaks at regions 7.3, 3.0, and 1.5-1.0 signified the presence of LC-SPDP chain in the polymer.

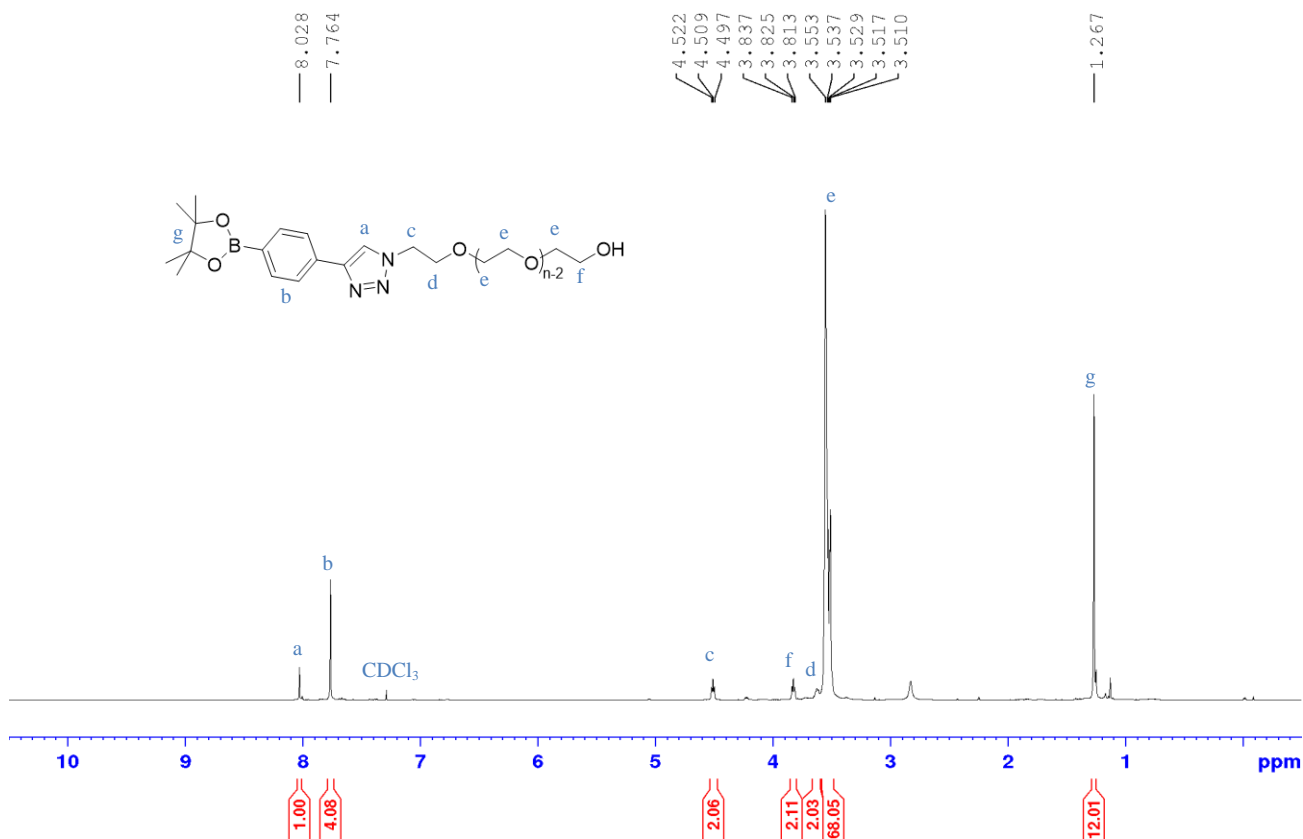


**Figure A2.3** | <sup>1</sup>H NMR spectrum of **2-20** in CDCl<sub>3</sub> (400 MHz).

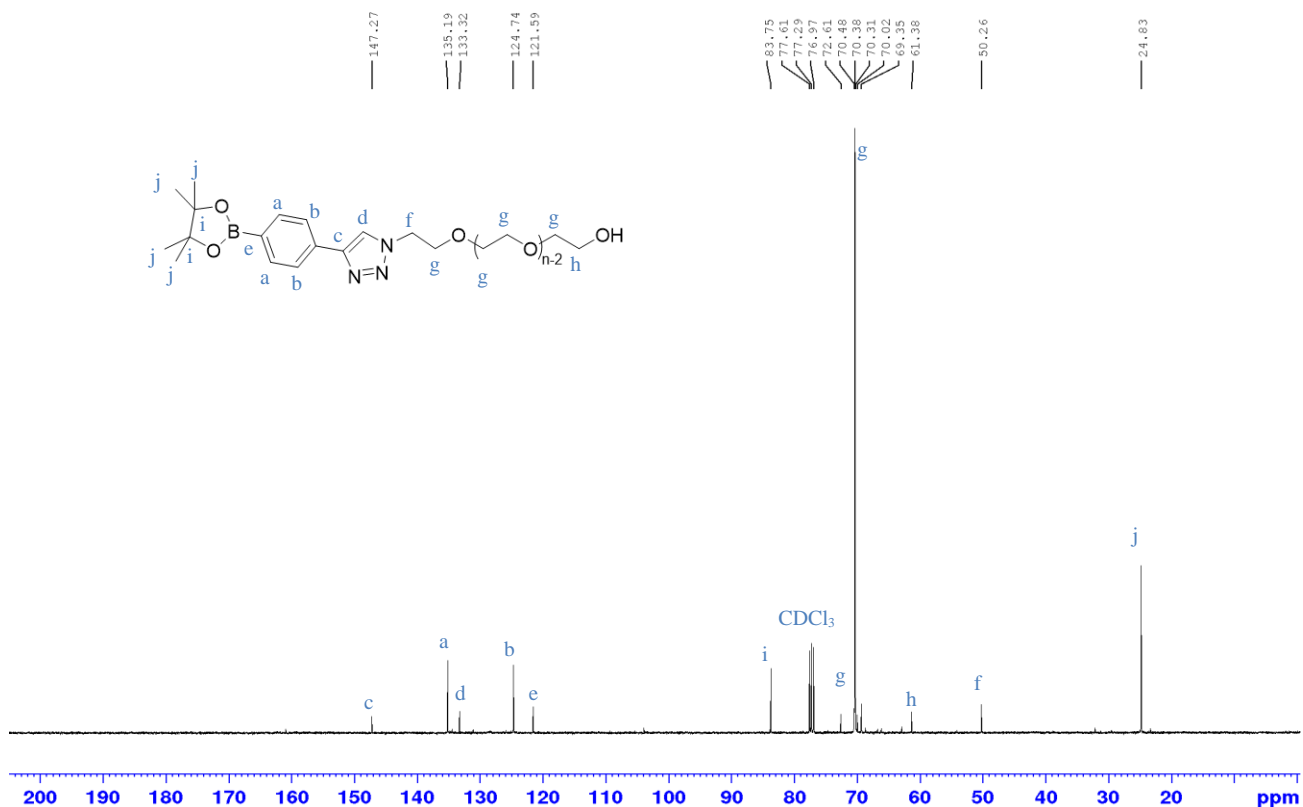


**Figure A2.4** | <sup>13</sup>C NMR spectrum of **2-20** in CDCl<sub>3</sub> (101 MHz)

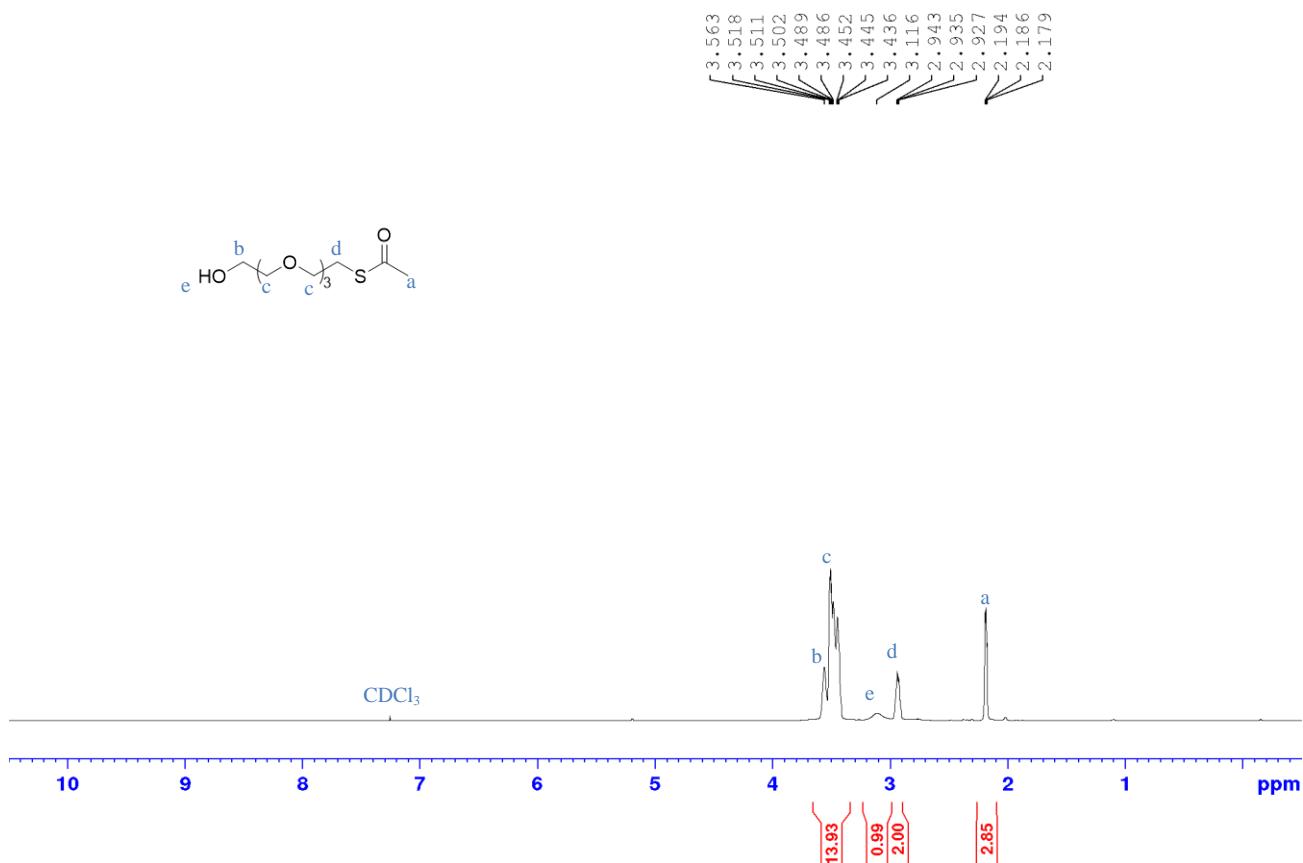


**Figure A2.5** | <sup>1</sup>H NMR spectrum of **2-21** in CDCl<sub>3</sub> (400 MHz). Reaction was successful as confirmed by the appearance of acetyl peak at 2.2 ppm.

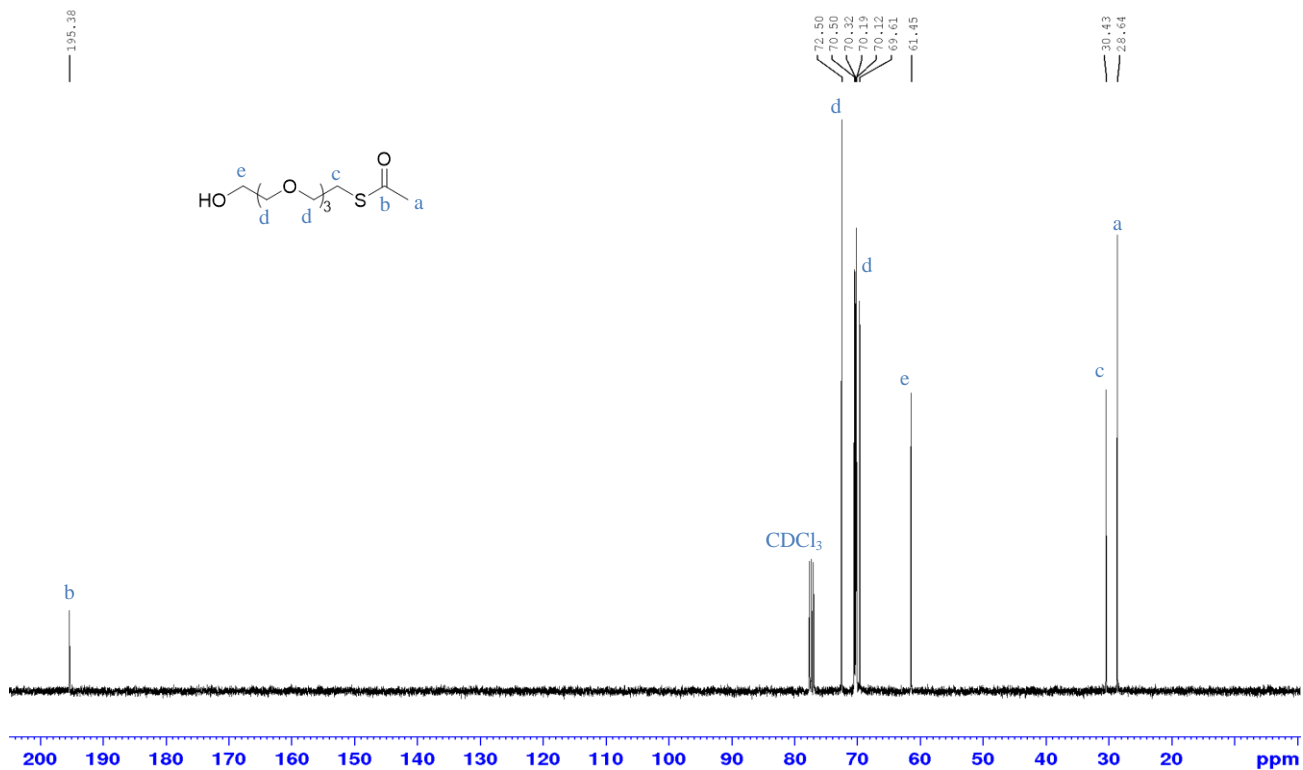


**Figure A2.6** | <sup>13</sup>C NMR spectrum of **2-21** in CDCl<sub>3</sub> (101 MHz).

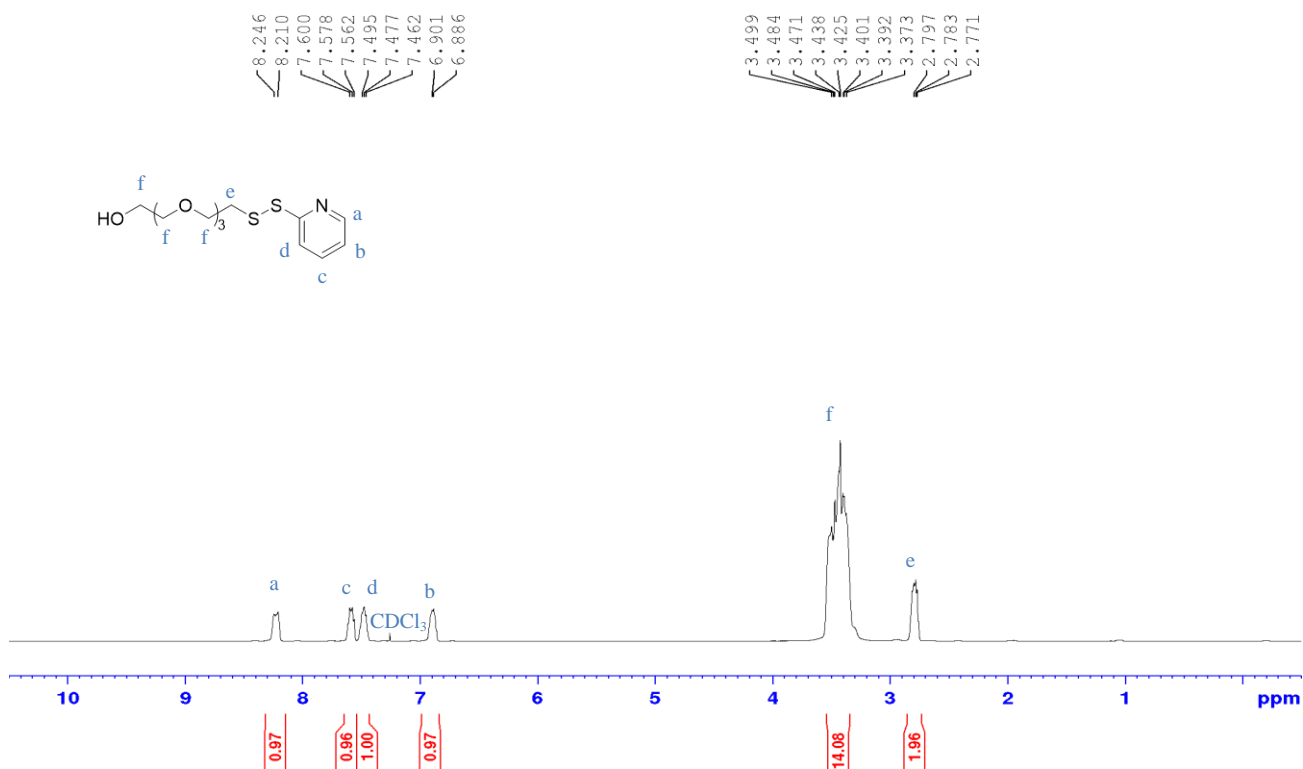


**Figure A2.7** | <sup>1</sup>H NMR spectrum of **2-22** in CDCl<sub>3</sub> (400 MHz). Formation of disulfide bridge was successful as can be seen by disappearance of acetyl peak at 2.2 ppm and appearance of aromatic peaks at region 8.4–6.6 ppm.

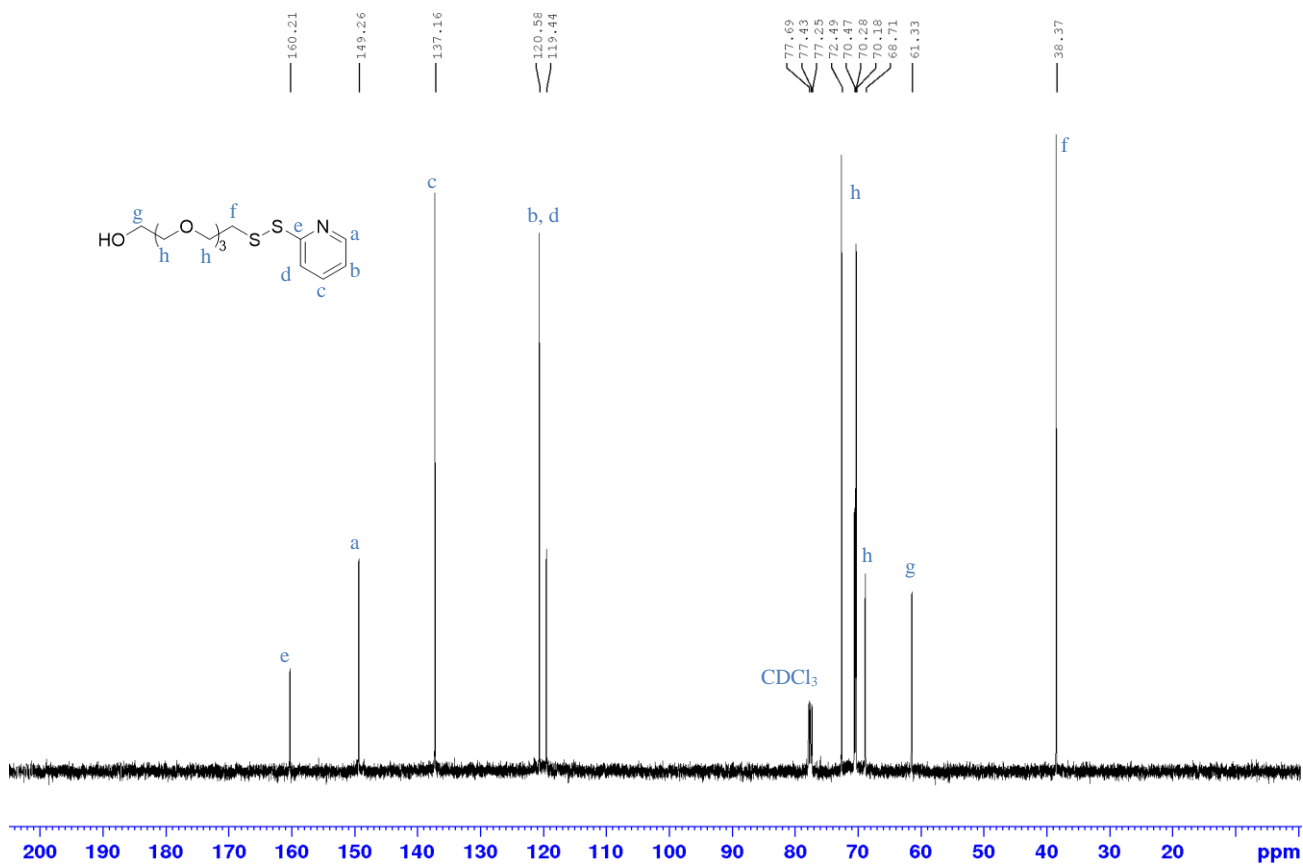


**Figure A2.8** | <sup>13</sup>C NMR spectrum of **2-22** in CDCl<sub>3</sub> (101 MHz).

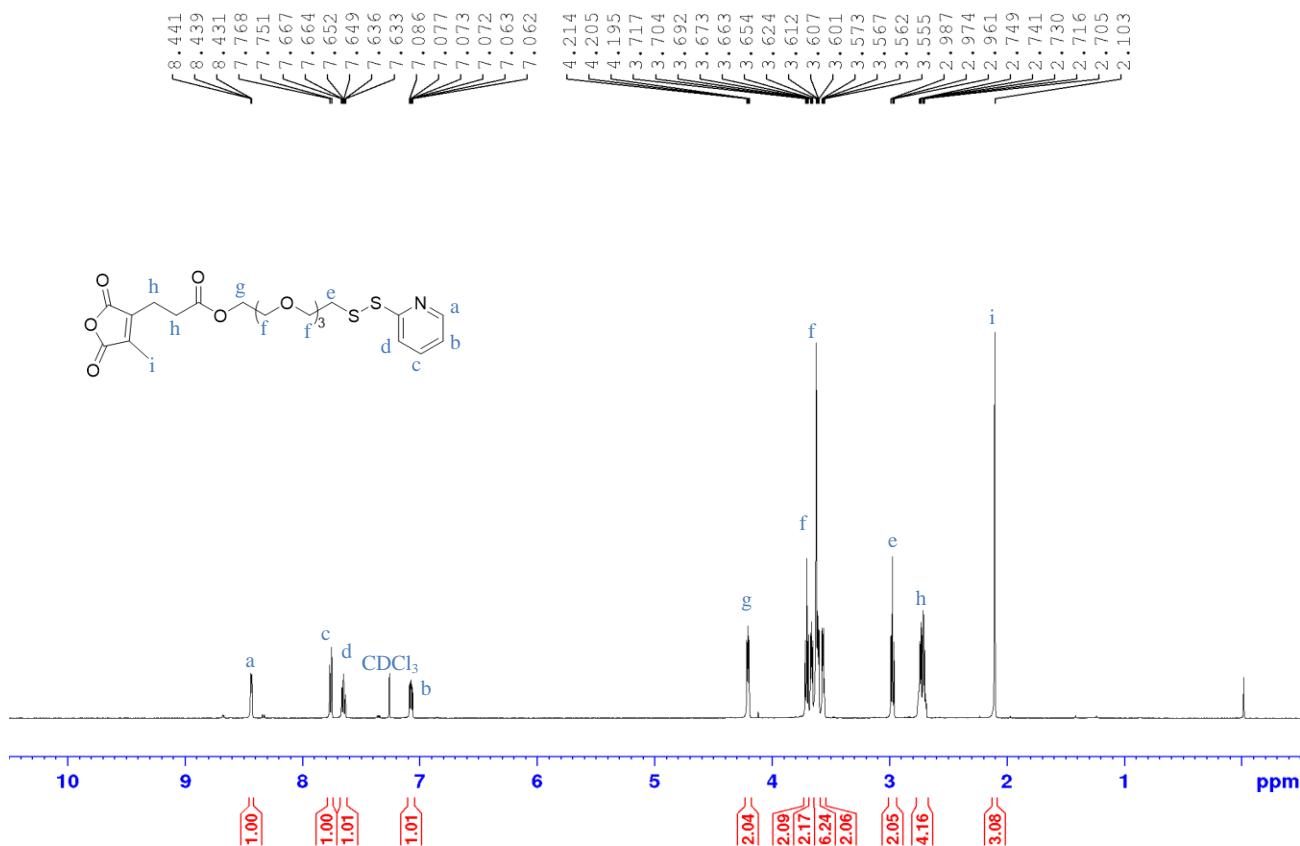


**Figure A2.9** | <sup>1</sup>H NMR spectrum of **2-23** in CDCl<sub>3</sub> (400 MHz). Esterification reaction was successful as can be seen by downfield movement of protons peak from 3.5 to 4.2 ppm. Appearance of peaks at 2.6 ppm and 2.1 ppm corresponds to ethyl groups and acetyl groups in CDM.

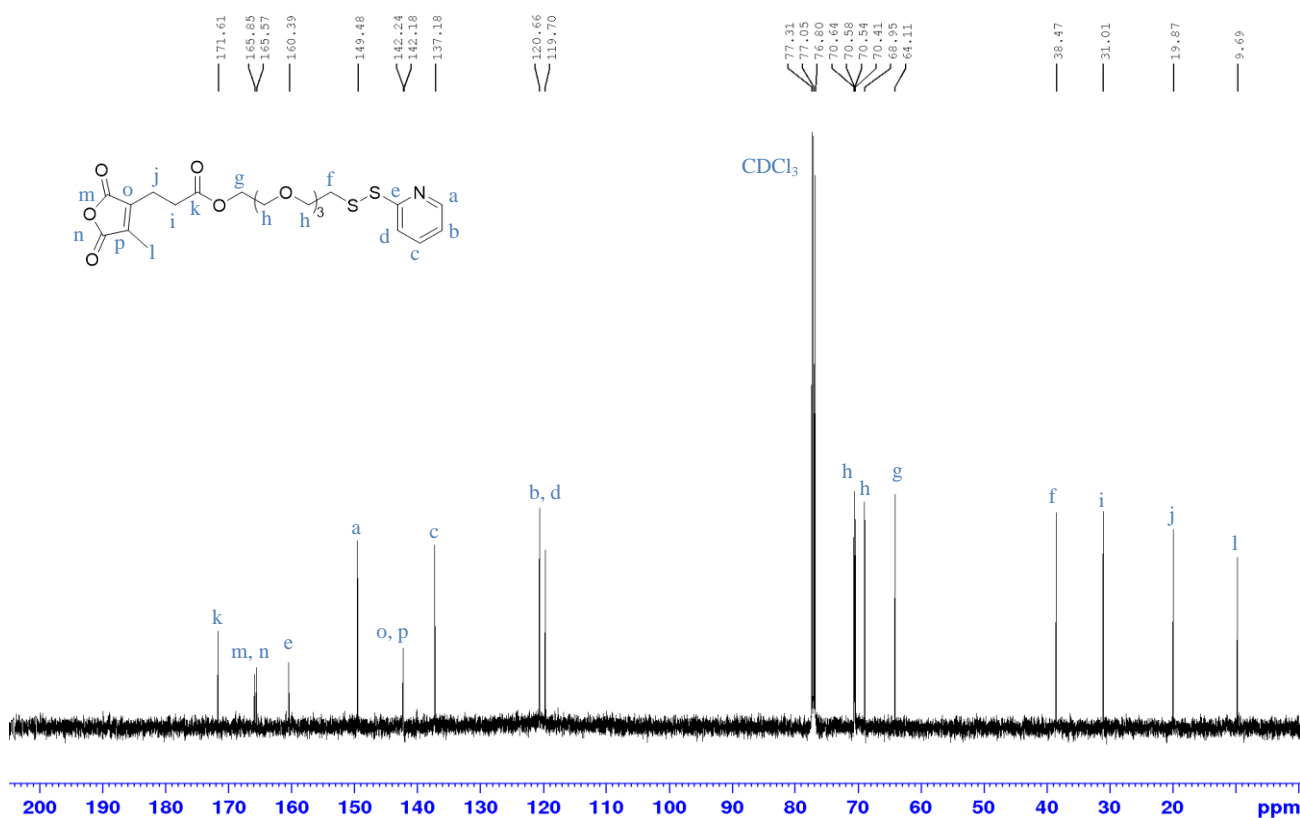


**Figure A2.10** | <sup>13</sup>C NMR spectrum of **2-23** in CDCl<sub>3</sub> (101 MHz).

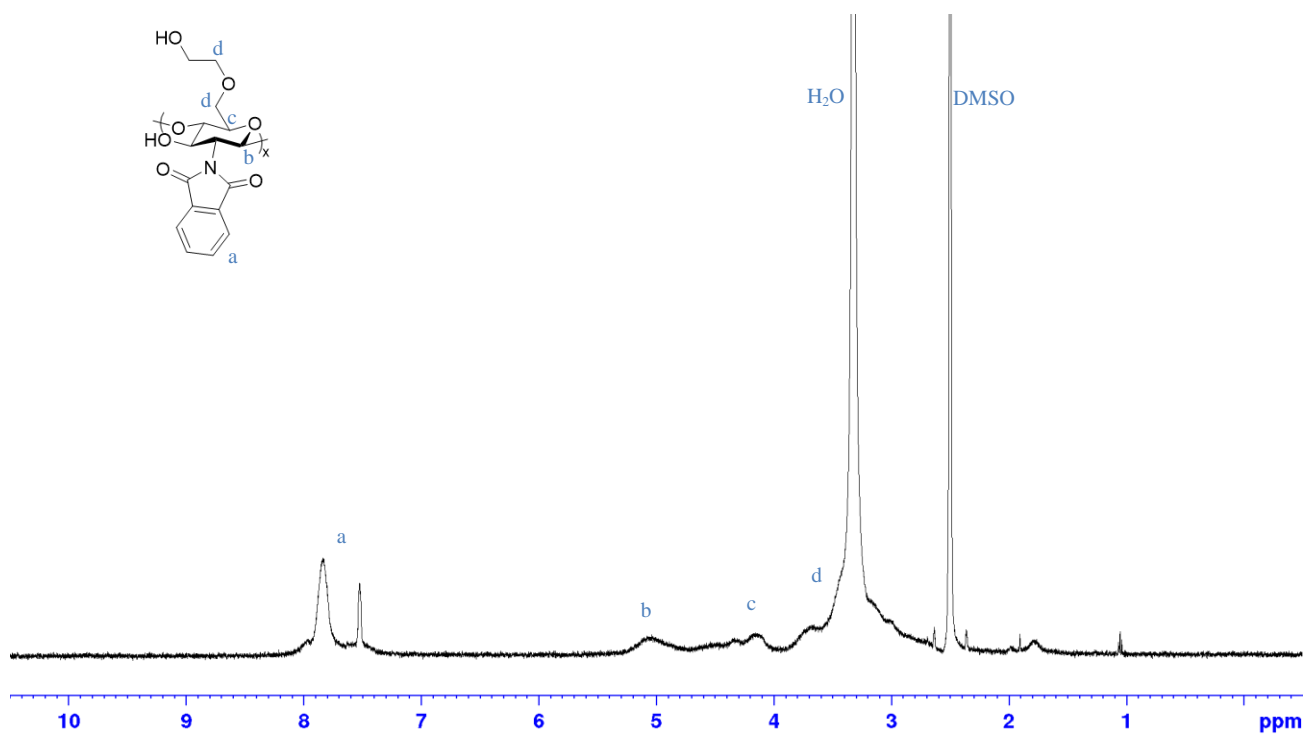


**Figure A2.11** | <sup>1</sup>H NMR spectrum of **2-24** in DMSO-d<sub>6</sub> (400 MHz).

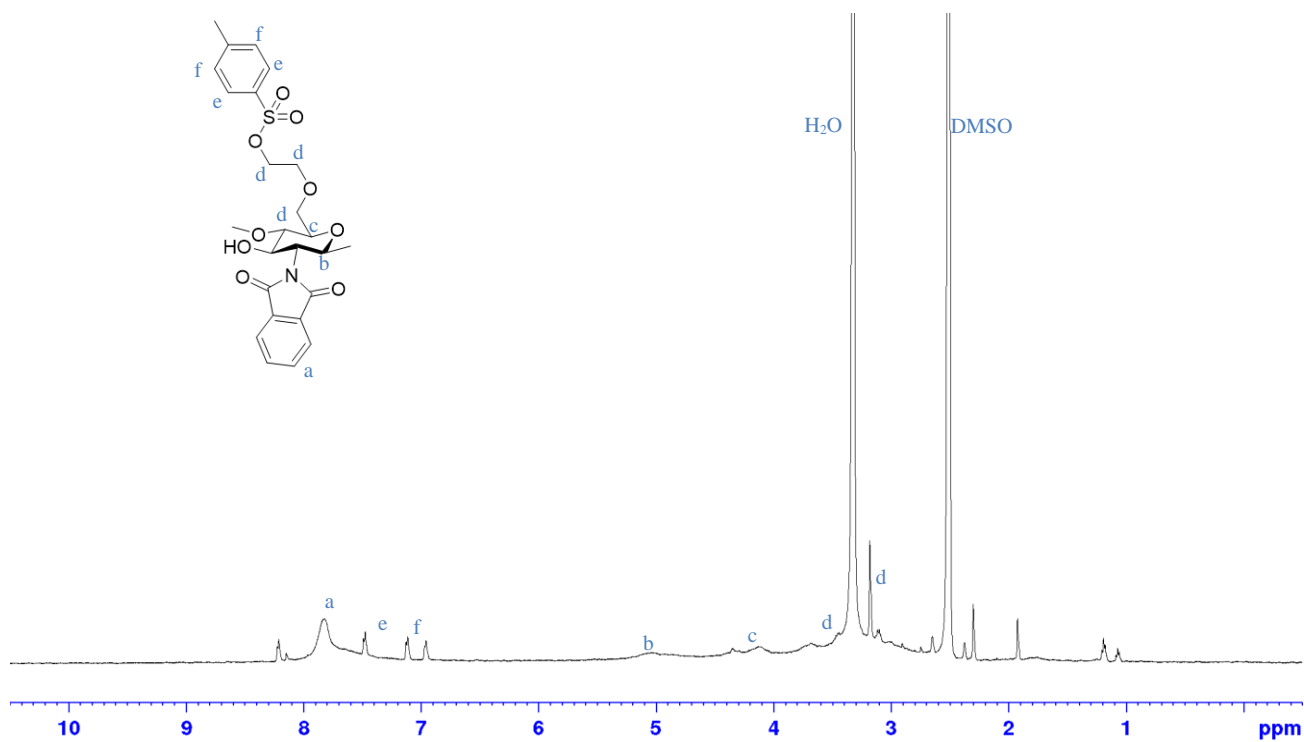


**Figure A2.12** | <sup>1</sup>H NMR spectrum of **2-25** in DMSO-d<sub>6</sub> (500 MHz).



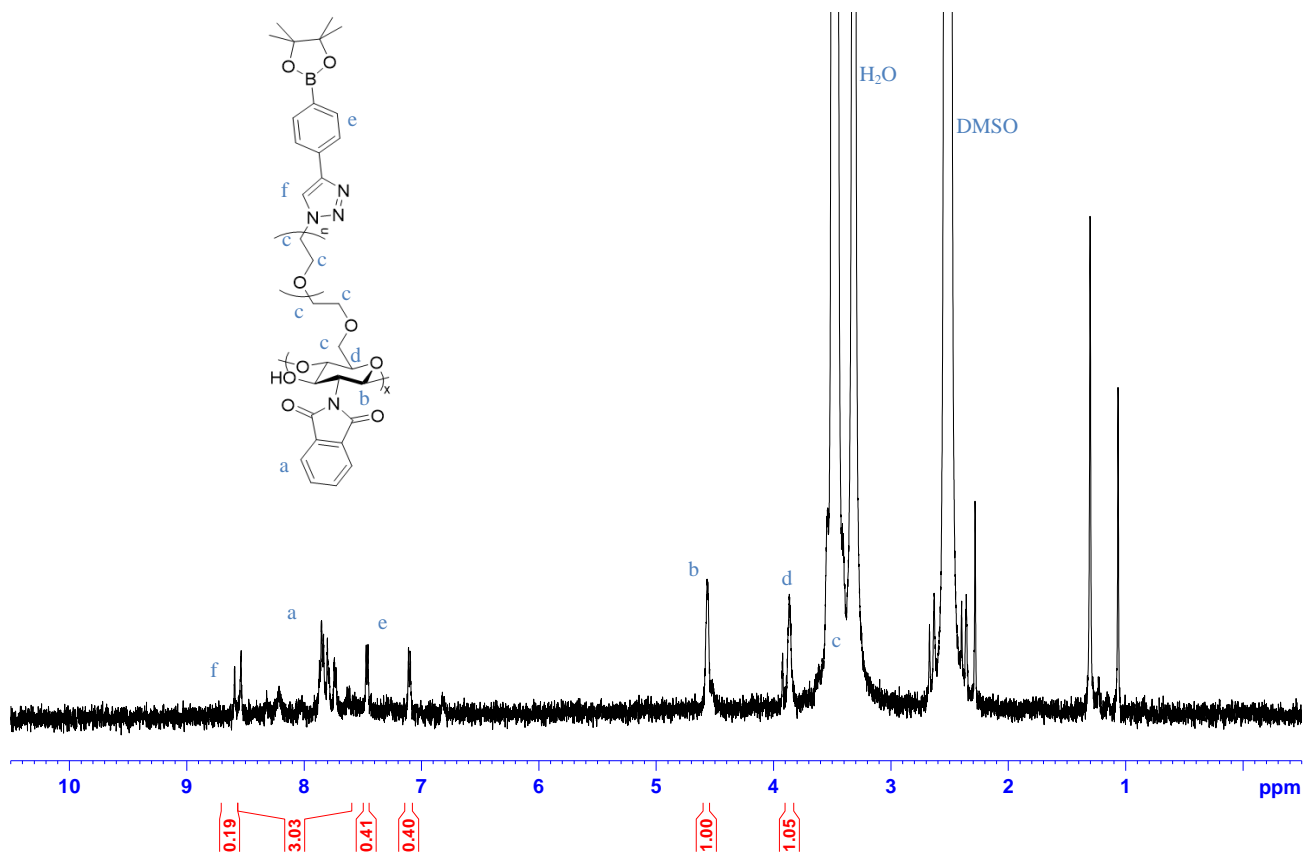


**Figure A2.11** | <sup>1</sup>H NMR spectrum of **2-26** in DMSO-d<sub>6</sub> (500 MHz).

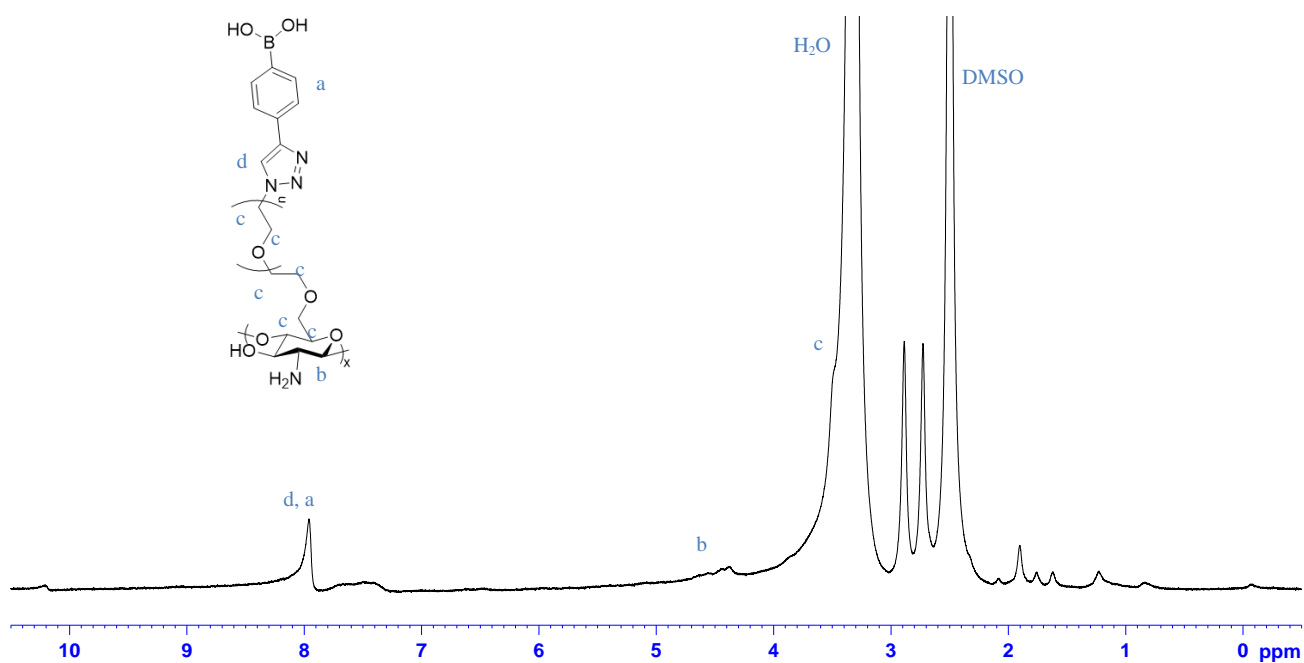


**Figure A2.13** | <sup>1</sup>H NMR spectrum of **2-28** in DMSO-d<sub>6</sub> (400 MHz).

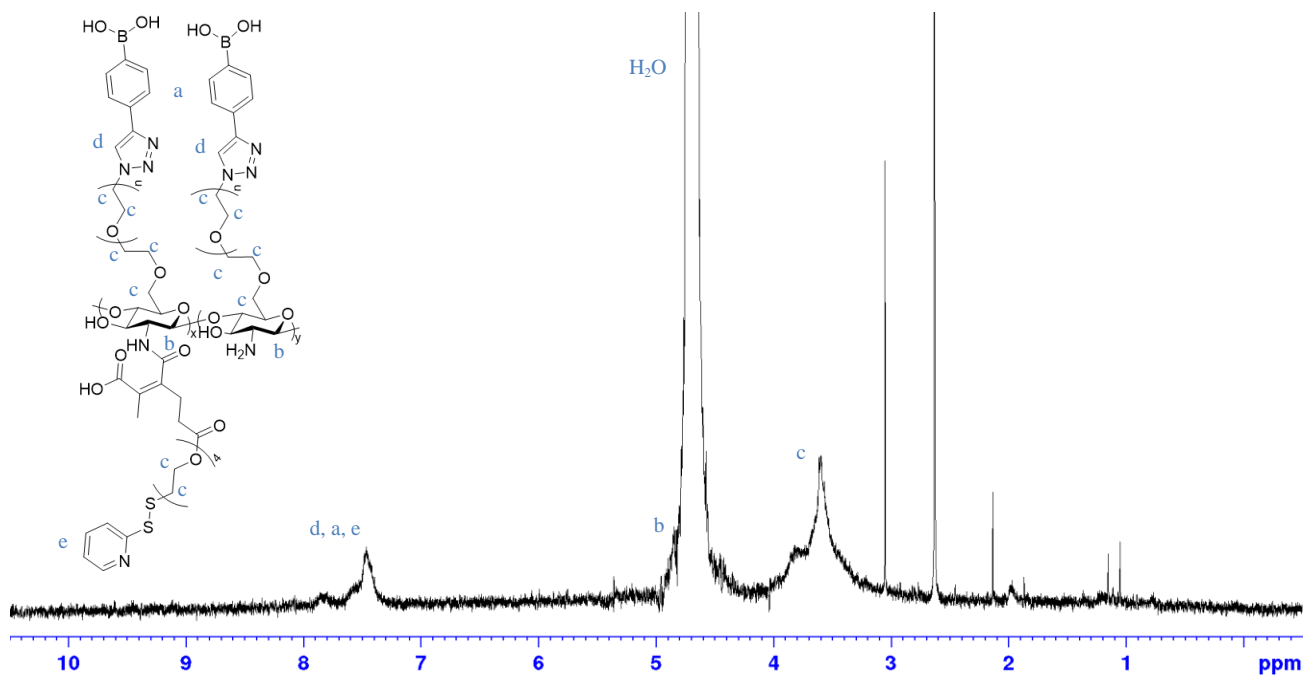


**Figure A2.14** |  $^1\text{H}$  NMR spectrum of **2-29** in  $\text{D}_2\text{O}$  (500 MHz).

## AII.2 | Zeta Potential and Dynamic Light Scattering (DLS) Measurement of **2-30**

**Zeta Potential:**

	Zeta Potential (mV)	Temperature ( $^{\circ}\text{C}$ )
1	-7.67	25.1
2	-1.98	25.0
3	-4.48	25.0
Mean	-4.71	25.0
Std. Dev.	2.85	0.1

**DLS:**

	Z-Average (nm)	PDI
1	117.9	0.396
2	145.3	0.286
3	134.8	0.331
Mean	132.7	0.338
Std. Dev.	13.82	0.055

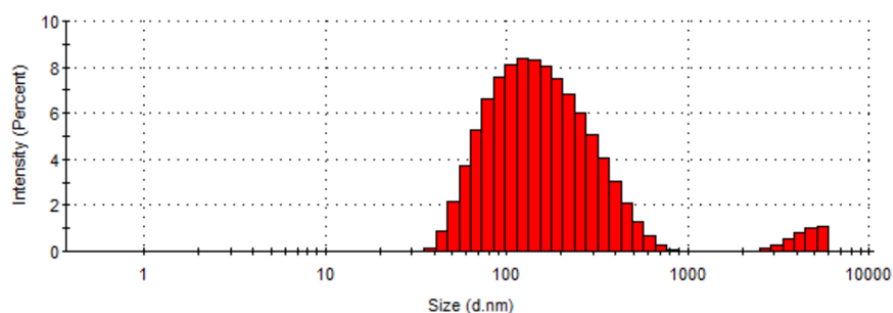


**Figure A2.15** | Zeta potential and size distribution of 19.5 nM of **2-30** (0.56  $\mu\text{g/mL}$  of rSML-A) were carried out in PBS using Malvern zetasizer (Malvern Instruments Ltd, Malvern, UK).

### AII.3 | Preliminary Confirmation Study of Formation of Maleamate Linkage Via IR Spectroscopy

A shorter chain of targeting ligand 1, with a tetraethylene glycol spacer, was first used in our preliminary study. The formation of maleamate bond was confirmed during our preliminary studies via IR spectroscopy, in addition to NMR analysis. An azide peak can be observed at 2101  $\text{cm}^{-1}$  in the IR spectrum, for the compound CDM-TEG- $\text{N}_3$  (see **Figure A2.16**). After reacting with glycol chitosan according to **Scheme A2.1**, IR spectrum of the product was recorded (see **Figure A2.17**) after purification by dialysis.

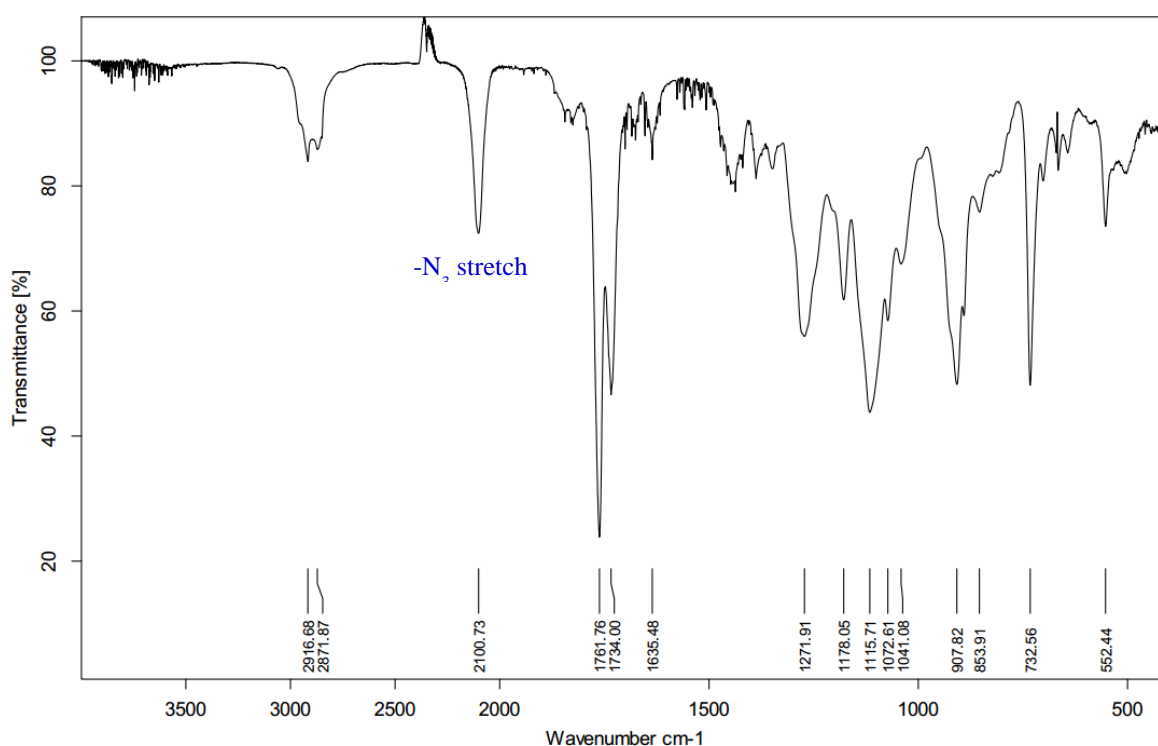
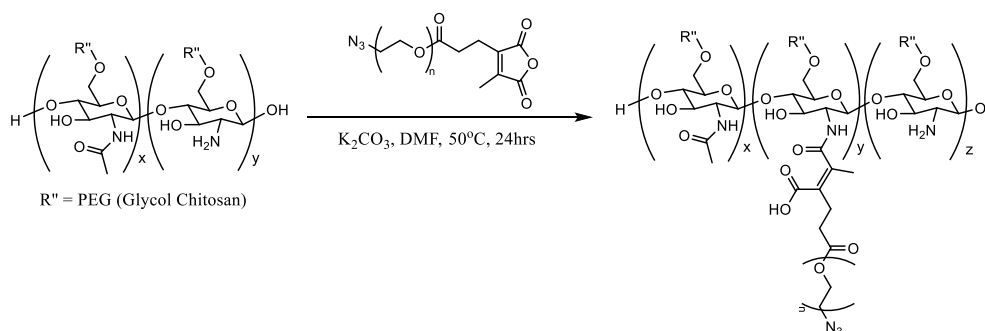


**Figure A2.16** | IR spectrum of CDM-TEG- $\text{N}_3$ .



**Scheme A2.1** | Amide formation between glycol chitosan (GC) and modified linker, CDM-TEG- $\text{N}_3$ .

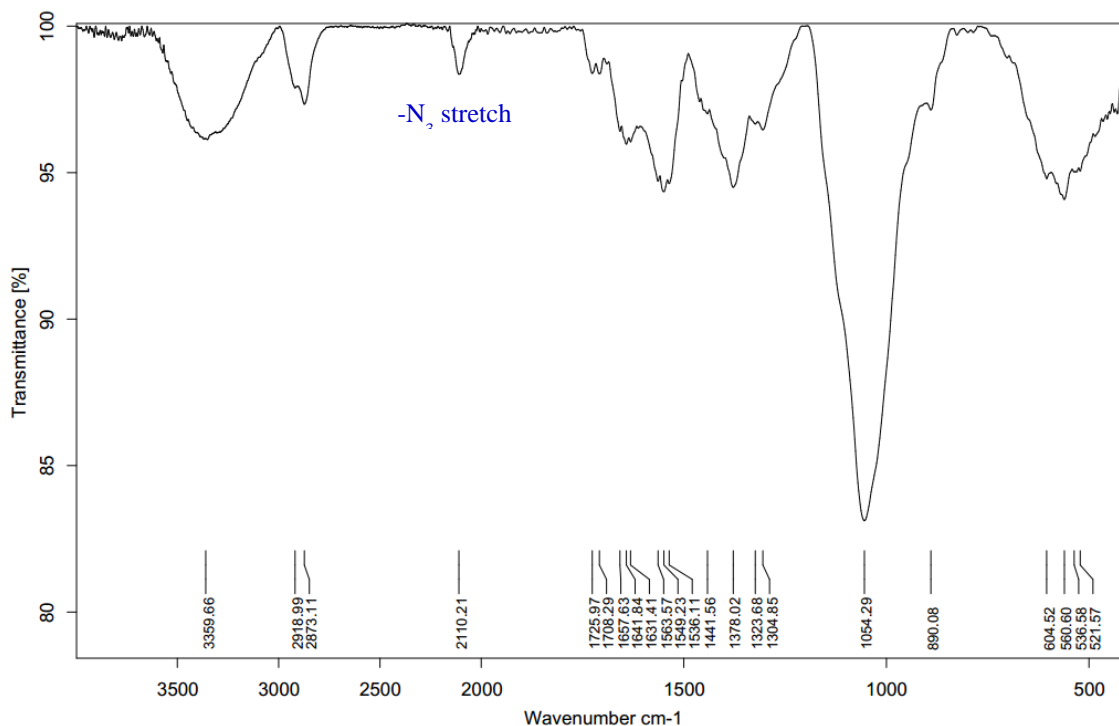
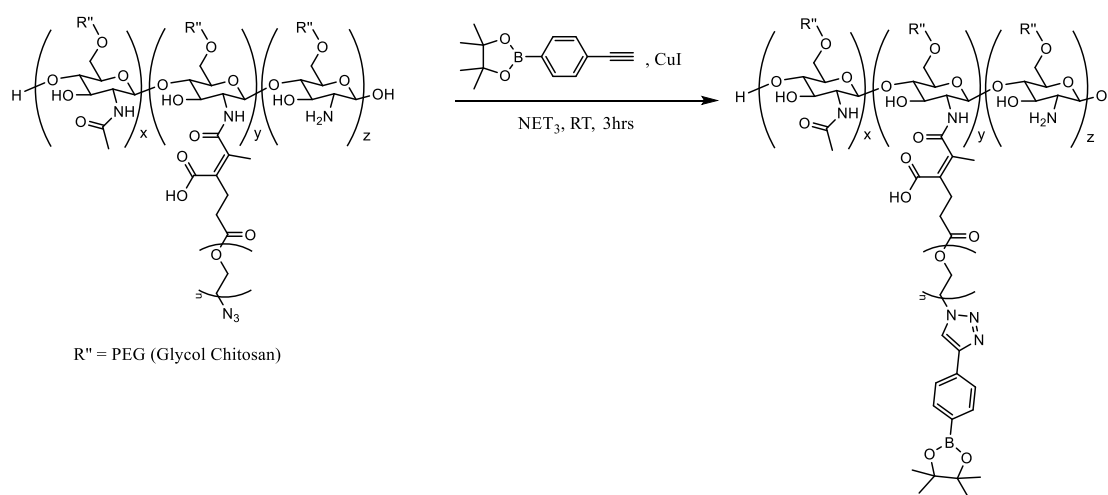


**Figure A2.17** | IR spectrum of GC-(CDM-TEG-N<sub>3</sub>).

After obtaining the azide-modified glycol chitosan, it was further subjected to click reaction with 4-ethynylphenylboronic acid pinacolato ester (see **Scheme A2.2**), which is the moiety responsible for targeting the cancer cells. Thereafter, the product (GC-BE) was purified by dialysis according to procedure described in Chapter 2.



**Scheme A2.2** | Subsequent click reaction between GC-(CDM-TEG-N<sub>3</sub>) and the targeting moiety, 4-ethynylphenylboronic acid pinacolato ester, to obtain the product, GC-BE.

IR spectrum of GC-BE was recorded (see **Figure A2.18**) and compared against the IR spectrum of GC-BA (see **Figure A2.19**) which was obtained according to the original synthetic route. Both

spectra showed similar absence of the azide stretch at  $2110\text{ cm}^{-1}$ , which signifies that both the click reaction, as well as the amide formation reaction was successful.

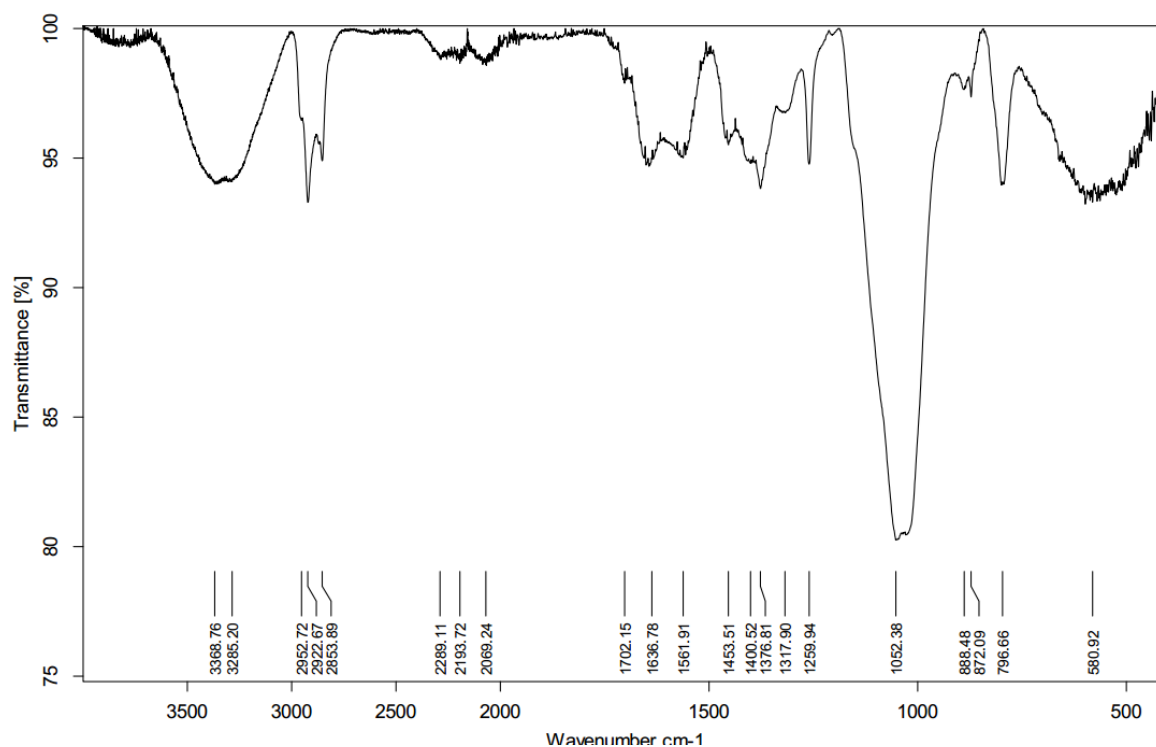


**Figure A2.18** | IR spectrum of GC-BE obtained from click reaction described in Scheme A2.2.

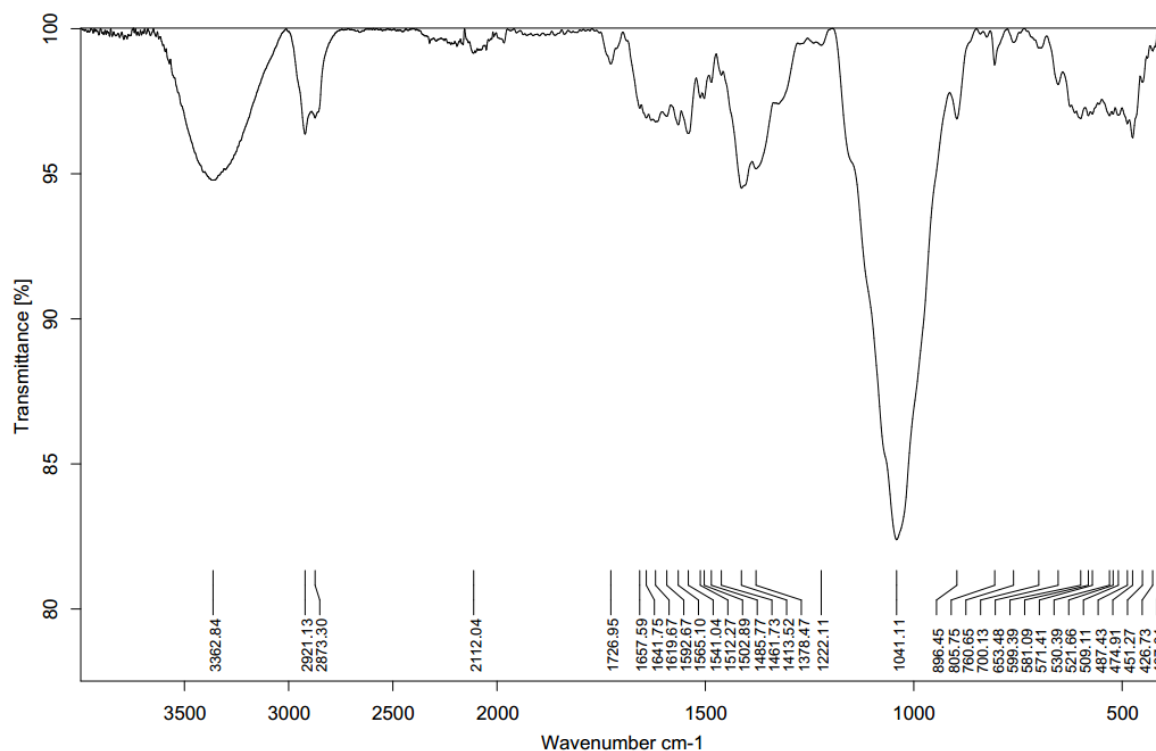


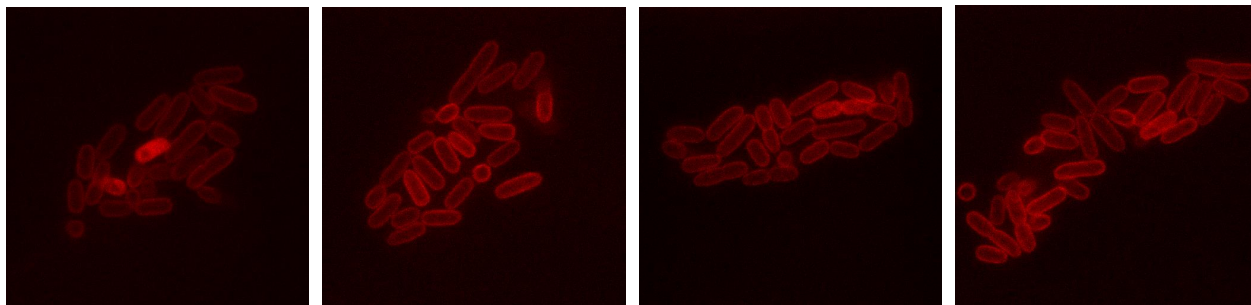
**Figure A2.19** | IR spectrum of GC-BA obtained from amide formation between GC and targeting ligand, CDM-TEG-BA.

## APPENDIX III – Supplementary Data for Chapter 3

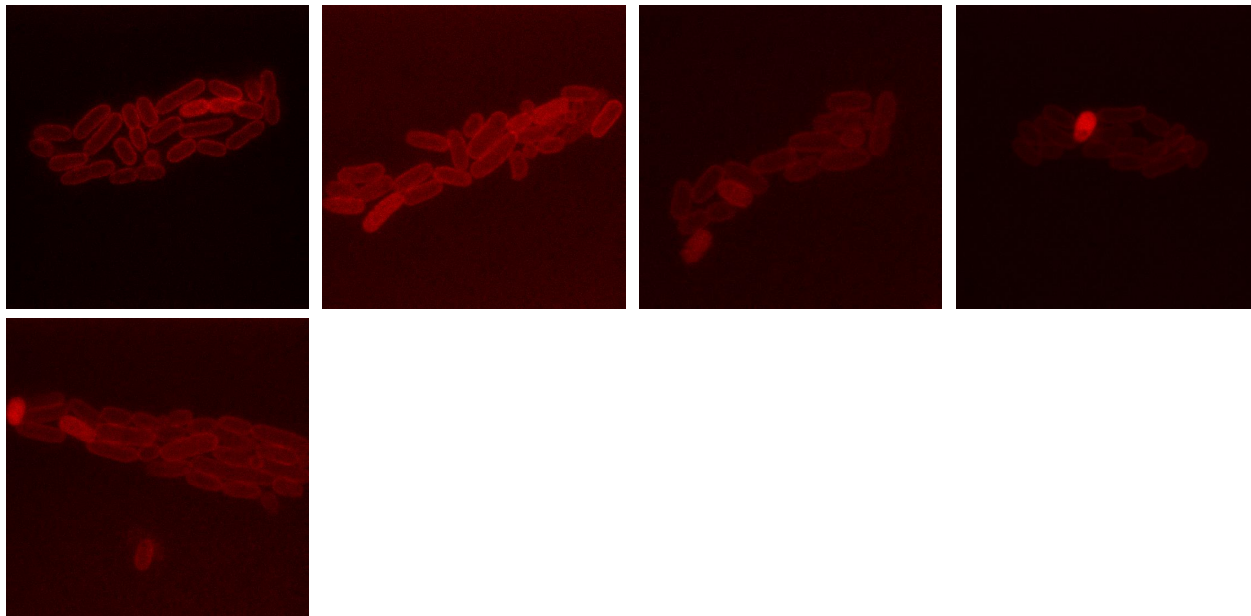
### AIII.1 | Fluorescence Intensity Calculation

The images used for fluorescence intensity calculation in chapter 3 are listed below:

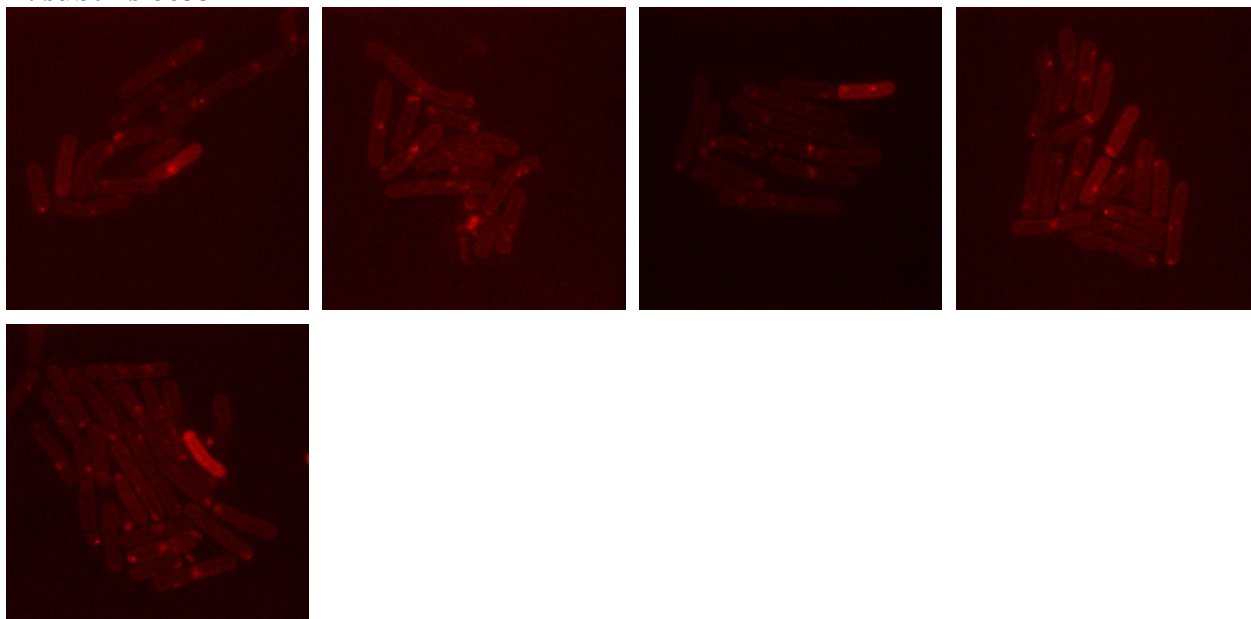
#### PA01



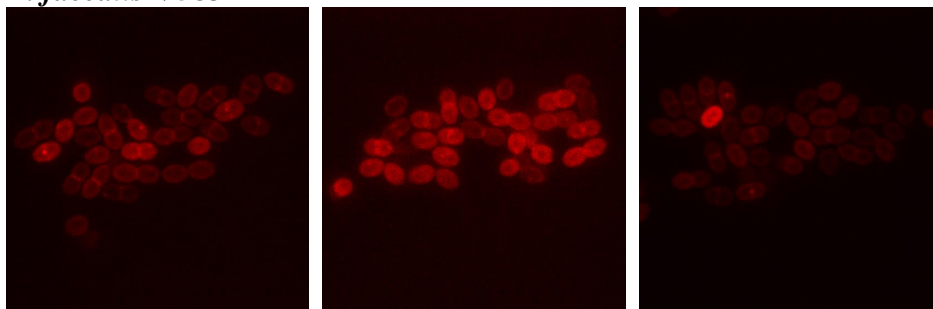
#### *E. coli* K12



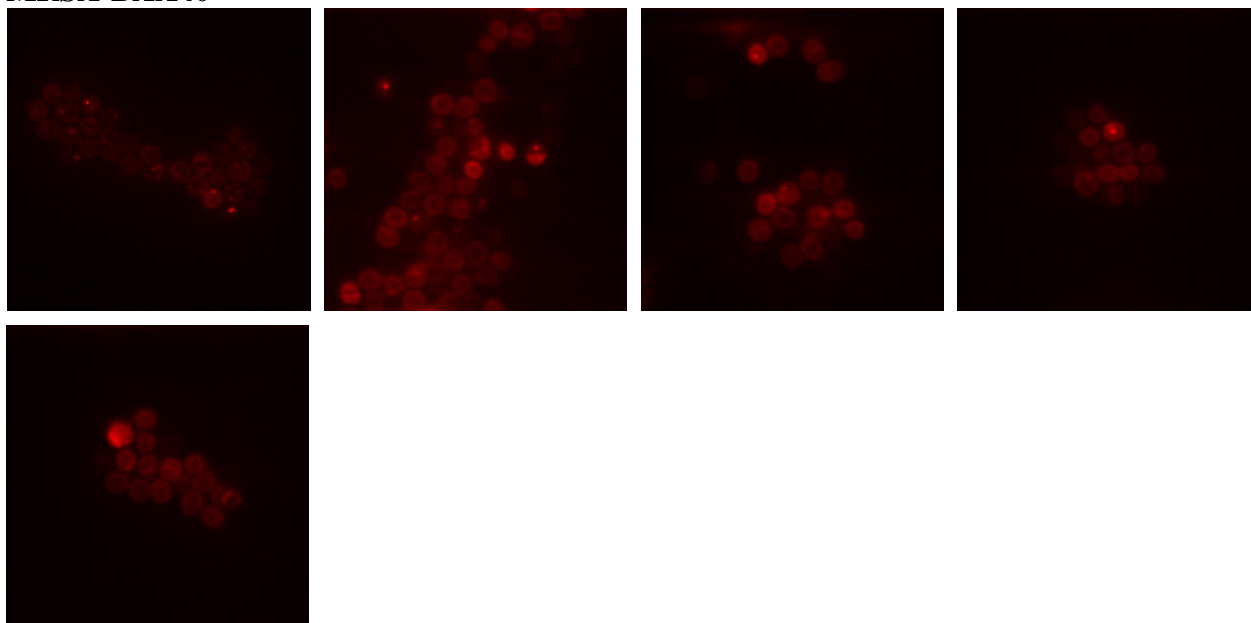
#### *B. subtilis* 6633



***E. faecalis* V583**



**MRSA-BAA40**



**MRSA-USA300**

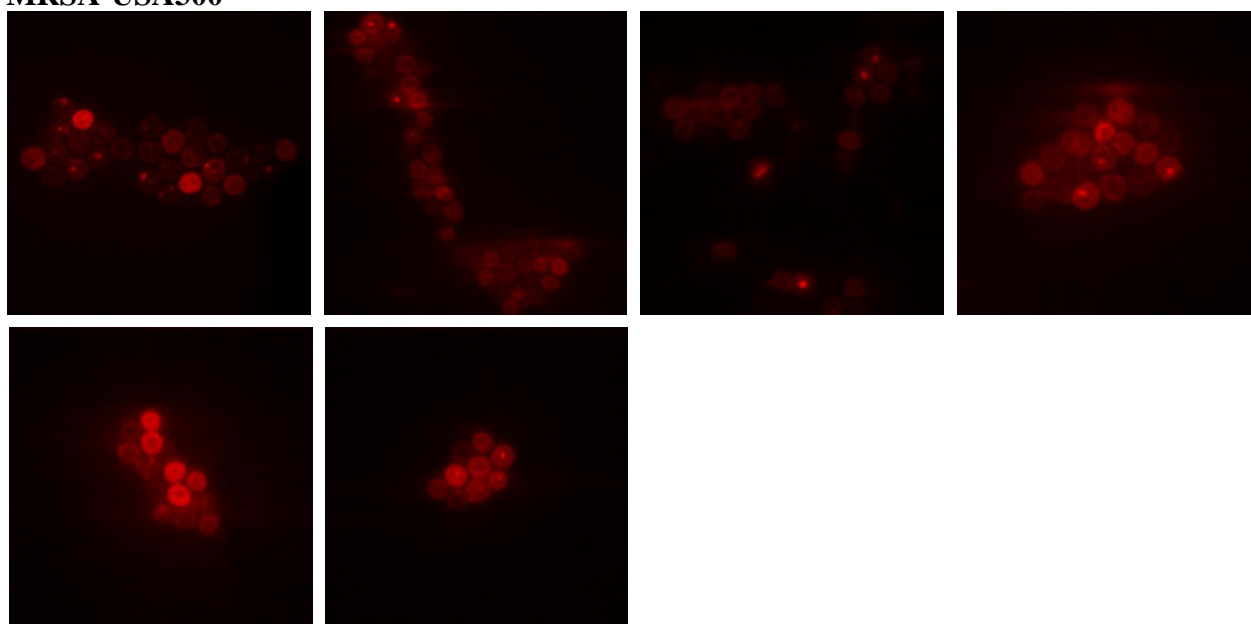


Table used for computation is shown as follows:

***Pseudomonas aeruginosa***

<i>PA01</i>		Red Channel			
Series01		Area	Mean	IntDen	RawIntDen
Cell	1	0.1	17.618	1.758	2537
	2	0.207	17.759	3.68	5310
	3	0.203	20.034	4.068	5870
	4	0.215	15.823	3.399	4905
	5	0.247	23.298	5.748	8294
	6	0.104	31.387	3.263	4708
	7	0.204	18.337	3.736	5391
	8	0.211	20.489	4.331	6249
	9	0.108	22.481	2.43	3507
	10	0.109	17.57	1.924	2776
	11	0.101	24.644	2.493	3598
	12	0.111	18.594	2.062	2975
	13	0.216	37.01	8.002	11547
	14	0.259	19.021	4.93	7114
	15	0.261	19.78	5.168	7457
	16	0.26	20.237	5.259	7589
	17	0.198	16.839	3.326	4799
	18	0.291	20.343	5.921	8544
	19	0.1	18.278	1.824	2632
	20	0.179	18.236	3.261	4705
	21	0.169	18.697	3.161	4562
	22	0.264	15.302	4.04	5830
	23	0.268	21.398	5.739	8281
Avg (-background):		14.63372609			
Std Dev:		4.917777026			
Std Error:		1.025427395			
BG	1	0.115	5.446	0.626	904
	2	0.15	6.088	0.911	1315
	3	0.15	5.958	0.892	1287
	4	0.15	5.875	0.879	1269
	5	0.15	5.764	0.863	1245
	6	0.15	6.144	0.92	1327
	7	0.15	6.736	1.008	1455
	8	0.15	5.472	0.819	1182
	9	0.15	6.491	0.972	1402
	10	0.15	5.417	0.811	1170
Avg:		5.9391			

<i>PA01</i>		Red Channel			
Series02		Area	Mean	IntDen	RawIntDen
Cell	1	0.175	17.793	3.11	3861
	2	0.228	16.76	3.82	4743
	3	0.198	17.467	3.461	4297
	4	0.255	16.237	4.146	5147
	5	0.23	20.561	4.72	5860
	6	0.242	24.711	5.991	7438
	7	0.228	14.314	3.263	4051
	8	0.176	19.128	3.359	4170
	9	0.231	23.118	5.344	6635
	10	0.215	20.449	4.398	5460
	11	0.193	18.803	3.62	4494
	12	0.147	26.098	3.847	4776
	13	0.201	26.333	5.282	6557
	14	0.203	19.175	3.892	4832
	15	0.165	25.776	4.256	5284
	16	0.437	15.994	6.996	8685
	17	0.255	15.64	3.994	4958
	18	0.238	14.24	3.395	4215
	19	0.159	23.645	3.752	4658
	20	0.264	19.009	5.022	6235
	21	0.222	22.764	5.061	6283
	22	0.238	16.537	3.943	4895
	23	0.263	21.483	5.659	7025
Avg (-background):		15.7658087			
Std Dev:		3.801236171			
Std Error:		0.792612533			
BG	1	0.184	4.259	0.782	971
	2	0.184	4.158	0.764	948
	3	0.184	4.224	0.776	963
	4	0.184	3.833	0.704	874
	5	0.184	4.096	0.752	934
	6	0.184	3.706	0.681	845
	7	0.184	3.75	0.689	855
	8	0.184	3.895	0.715	888
	9	0.184	4.368	0.802	996
	10	0.184	4.329	0.795	987
Avg:		4.0618			

<i>PA01</i>		Red Channel			
Series03		Area	Mean	IntDen	RawIntDen
Cell	1	0.234	13.341	3.116	3869
	2	0.202	12.554	2.538	3151
	3	0.244	16.089	3.927	4875
	4	0.284	15.127	4.301	5340
	5	0.303	17.019	5.154	6399

<i>PA01</i>		Red Channel			
Series04		Area	Mean	IntDen	RawIntDen
Cell	1	0.21	17.18	3.612	4484
	2	0.304	16.889	5.142	6384
	3	0.219	16.757	3.671	4558
	4	0.221	16.011	3.534	4387
	5	0.241	16.803	4.047	5024



	6	0.241	17	4.094	5083	
	7	0.266	20.185	5.365	6661	
	8	0.183	17.916	3.276	4067	
	9	0.184	14.43	2.65	3290	
	10	0.174	14.685	2.555	3172	
	11	0.138	17.409	2.398	2977	
	12	0.22	17.597	3.87	4804	
	13	0.214	18.729	4.013	4982	
	14	0.286	18.563	5.308	6590	
	15	0.177	24.923	4.417	5483	
	16	0.291	16.277	4.733	5876	
	17	0.208	18.229	3.788	4703	
	18	0.215	15.569	3.348	4157	
	19	0.268	14.694	3.941	4893	
	20	0.18	20.359	3.657	4540	
	21	0.205	22.392	4.599	5710	
	22	0.16	18	2.885	3582	
	23	0.172	15.014	2.588	3213	
	24	0.171	13.778	2.353	2921	
	Avg (-background):		14.65429167			
	Std Dev:		2.905052009			
	Std Error:		0.592991258			
	BG	1	0.155	2.651	0.41	509
		2	0.155	2.812	0.435	540
3		0.155	2.516	0.389	483	
4		0.155	1.917	0.296	368	
5		0.155	2.609	0.404	501	
6		0.155	2.365	0.366	454	
7		0.155	1.958	0.303	376	
8		0.155	2.448	0.379	470	
9		0.155	2.25	0.348	432	
10		0.155	2.714	0.42	521	
Avg:		2.424				

	6	0.258	17.328	4.467	5545	
	7	0.239	20.502	4.905	6089	
	8	0.221	23.026	5.082	6309	
	9	0.259	20.131	5.205	6462	
	10	0.241	18.97	4.569	5672	
	11	0.226	14.256	3.227	4006	
	12	0.126	21.75	2.733	3393	
	13	0.255	14.633	3.725	4624	
	14	0.257	12.856	3.303	4101	
	15	0.244	15.31	3.737	4639	
	16	0.184	15.576	2.873	3567	
	17	0.214	19.733	4.228	5249	
	18	0.158	22.209	3.506	4353	
	19	0.271	21.507	5.838	7248	
	20	0.198	17.089	3.386	4204	
	21	0.277	23.608	6.541	8121	
	22	0.143	21.921	3.143	3902	
	23	0.18	20.987	3.787	4701	
	24	0.207	21.381	4.426	5495	
	25	0.121	14.053	1.698	2108	
	26	0.168	14.76	2.473	3070	
	27	0.11	17.577	1.94	2408	
	28	0.166	19.223	3.19	3960	
	29	0.178	20.113	3.58	4445	
	30	0.184	19.332	3.566	4427	
	Avg (-background):		15.23216667			
	Std Dev:		2.970623231			
	Std Error:		0.542359118			
	BG	1	0.143	2.74	0.391	485
		2	0.143	3.056	0.436	541
3		0.143	3.531	0.503	625	
4		0.143	3.209	0.458	568	
5		0.143	3.215	0.458	569	
6		0.143	3.395	0.484	601	
7		0.143	3.316	0.473	587	
8		0.143	2.944	0.42	521	
9		0.143	2.825	0.403	500	
10		0.143	3.271	0.466	579	
Avg:		3.1502				

### *Escherichia coli*

<i>E. coli</i> K12		Red Channel			
Series01		Area	Mean	IntDen	RawIntDen
Cell	1	0.25	23.108	5.781	8342
	2	0.103	28.311	2.904	4190
	3	0.244	25.435	6.204	8953
	4	0.201	25.569	5.139	7415
	5	0.286	24.421	6.99	10086
	6	0.225	23.96	5.396	7787
<i>E. coli</i> K12		Red Channel			
Series02		Area	Mean	IntDen	RawIntDen
Cell	1	0.283	21.721	6.141	8862
	2	0.207	22.505	4.663	6729
	3	0.247	24.272	5.988	8641
	4	0.243	23.66	5.739	8281
	5	0.285	24.998	7.12	10274
	6	0.241	24.71	5.959	8599

	7	0.255	23.965	6.111	8819
	8	0.207	25.768	5.321	7679
	9	0.24	23.087	5.536	7988
	10	0.257	26.949	6.929	9998
	11	0.22	26.16	5.765	8319
	12	0.143	24.869	3.55	5123
	13	0.256	27.293	6.979	10071
	14	0.201	46.862	9.418	13590
	15	0.175	44.866	7.866	11351
	16	0.185	28.869	5.342	7708
	17	0.209	27.056	5.662	8171
	18	0.103	31.642	3.245	4683
	19	0.244	28.727	7.008	10112
	20	0.236	23.094	5.441	7852
	21	0.091	21.076	1.913	2761
	22	0.27	20.139	5.429	7834
	23	0.26	21.984	5.713	8244
Avg (-background):		16.77838696			
Std Dev:		6.511262508			
Std Error:		1.357692087			
BG	1	0.906	9.528	8.636	12462
	2	0.906	10.346	9.378	13533
	3	0.906	10.338	9.371	13522
	4	0.906	10.718	9.715	14019
	5	0.906	10.489	9.507	13719
	6	0.906	10.056	9.115	13153
	7	0.906	10.037	9.098	13129
	8	0.906	10.644	9.649	13923
	9	0.906	10.161	9.21	13290
	10	0.906	10.86	9.844	14205
Avg:		10.3177			
	7	0.259	25.083	6.501	9381
	8	0.236	25.188	5.935	8564
	9	0.249	20.953	5.227	7543
	10	0.225	24.731	5.553	8013
	11	0.168	23.44	3.947	5696
	12	0.291	28.076	8.172	11792
	13	0.304	26.872	8.157	11770
	14	0.162	21.607	3.504	5056
	15	0.095	25.029	2.376	3429
	16	0.169	25.779	4.359	6290
	17	0.238	26.933	6.421	9265
	18	0.148	30.582	4.514	6514
	19	0.104	23.12	2.403	3468
	20	0.231	28.018	6.466	9330
	21	0.213	24.655	5.245	7569
	22	0.252	21.333	5.367	7744
	23	0.245	27.59	6.768	9767
Avg (-background):		14.20218261			
Std Dev:		2.435198311			
Std Error:		0.507773949			
BG	1	0.291	11.631	3.385	4885
	2	0.291	10.895	3.171	4576
	3	0.291	9.94	2.893	4175
	4	0.291	10.529	3.064	4422
	5	0.291	10.286	2.994	4320
	6	0.291	10.764	3.133	4521
	7	0.291	10.5	3.056	4410
	8	0.291	10.593	3.083	4449
	9	0.291	10.586	3.081	4446
	10	0.291	10.452	3.042	4390
Avg:		10.6176			

<i>E. coli</i> K12		Red Channel			
Series03		Area	Mean	IntDen	RawIntDen
Cell	1	0.25	25.895	6.478	9348
	2	0.214	23.793	5.095	7352
	3	0.169	24.082	4.072	5876
	4	0.126	29.571	3.73	5382
	5	0.272	26.407	7.192	10378
	6	0.253	26.753	6.767	9765
	7	0.258	28.199	7.269	10490
	8	0.216	25.763	5.57	8038
	9	0.22	25.899	5.707	8236
	10	0.235	26.785	6.292	9080
	11	0.195	31.655	6.164	8895
	12	0.179	24.209	4.328	6246
	13	0.245	26.89	6.597	9519
	14	0.2	23.436	4.694	6773
	15	0.192	25.56	4.906	7080
<i>E. coli</i> K12		Red Channel			
Series04		Area	Mean	IntDen	RawIntDen
Cell	1	0.213	23.642	5.03	7258
	2	0.193	25.273	4.869	7026
	3	0.15	26.602	3.982	5746
	4	0.252	27.755	7.001	10103
	5	0.199	28.296	5.628	8121
	6	0.252	54.959	13.825	19950
	7	0.21	27.554	5.786	8349
	8	0.227	27.341	6.215	8968
	9	0.262	29.235	7.658	11051
	10	0.172	25.419	4.369	6304
	11	0.188	26.812	5.035	7266
	12	0.239	24.435	5.842	8430
	13	0.191	24.58	4.701	6784
	14	0.191	29.855	5.71	8240
	15	0.281	26.202	7.354	10612

	16	0.222	26.75	5.932	8560
Avg (-background):			12.9667375		
Std Dev:			2.14288679		
Std Error:			0.535721698		
BG	1	0.292	13.176	3.844	5547
	2	0.292	13.102	3.823	5516
	3	0.292	13.622	3.974	5735
	4	0.292	13.822	4.033	5819
	5	0.292	14.107	4.116	5939
	6	0.292	12.9	3.764	5431
	7	0.292	13.031	3.802	5486
	8	0.292	13.249	3.866	5578
	9	0.292	13.43	3.918	5654
	10	0.292	13.423	3.916	5651
Avg:			13.3862		

	16	0.108	32.455	3.509	5063
	17	0.157	25.257	3.956	5708
Avg (-background):			17.16754118		
Std Dev:			7.152348718		
Std Error:			1.734699367		
BG	1	0.277	11.14	3.088	4456
	2	0.277	11.307	3.134	4523
	3	0.277	11.812	3.274	4725
	4	0.277	11.273	3.125	4509
	5	0.277	11.322	3.139	4529
	6	0.277	11.39	3.157	4556
	7	0.277	11.367	3.151	4547
	8	0.277	11.393	3.158	4557
	9	0.277	11.758	3.259	4703
	10	0.277	11.252	3.119	4501
Avg:			11.4014		

<i>E. coli</i> K12		Red Channel			
Series05		Area	Mean	IntDen	RawIntDen
Cell	1	0.216	31.788	6.873	9918
	2	0.229	25.109	5.759	8311
	3	0.261	23.691	6.173	8908
	4	0.243	23.889	5.811	8385
	5	0.23	35.084	8.072	11648
	6	0.213	22.623	4.829	6968
	7	0.168	25.252	4.235	6111
	8	0.164	24.92	4.093	5906
	9	0.306	30.893	9.441	13624
	10	0.277	28.018	7.747	11179
	11	0.139	27.463	3.825	5520
	12	0.168	26.453	4.455	6428
	13	0.294	28.854	8.478	12234
	14	0.164	25.844	4.245	6125
	15	0.109	24.49	2.665	3845
	16	0.157	27.132	4.268	6159
	17	0.201	26.121	5.249	7575
	18	0.161	27.515	4.443	6411
	19	0.35	26.794	9.377	13531
	20	0.175	26.818	4.702	6785
	21	0.202	24.712	5.001	7216
	22	0.091	20.364	1.863	2688
	23	0.158	25.009	3.951	5702
	24	0.233	29.622	6.897	9953
	25	0.087	24.736	2.143	3092
	26	0.335	26.377	8.829	12740
	27	0.169	26.287	4.445	6414
Avg (-background):		13.29215926			
Std Dev:		2.95911578			
Std Error:		0.569482097			

BG	1	0.265	11.527	3.06	4415
	2	0.265	13.337	3.54	5108
	3	0.265	13.358	3.545	5116
	4	0.265	14.713	3.905	5635
	5	0.265	13.389	3.554	5128
	6	0.265	14.616	3.879	5598
	7	0.265	13.984	3.712	5356
	8	0.265	11.911	3.161	4562
	9	0.265	12.433	3.3	4762
	10	0.265	12.943	3.435	4957
Avg:		13.2211			

### *Bacillus subtilis*

<i>B. subtilis</i> 6633		Red Channel			
Series01		Area	Mean	IntDen	RawIntDen
Cell	1	0.267	12.033	3.208	3983
	2	0.493	11.538	5.688	7061
	3	0.383	12.412	4.759	5908
	4	0.243	11.358	2.763	3430
	5	0.352	14.471	5.094	6324
	6	0.268	11.282	3.026	3757
	7	0.282	16.123	4.545	5643
	8	0.242	12.814	3.107	3857
	9	0.425	20.4	8.676	10771
	10	0.43	14.455	6.218	7719
	11	0.424	14.072	5.974	7416
	12	0.415	16.355	6.785	8423
	13	0.292	15.096	4.414	5480
	14	0.435	12.622	5.49	6816
Avg (-background):		7.091285714			
Std Dev:		2.522312681			
Std Error:		0.674116419			
BG	1	0.184	7.855	1.443	1791
	2	0.184	6.908	1.269	1575
	3	0.184	6.864	1.261	1565
	4	0.184	6.553	1.203	1494
	5	0.184	6.009	1.104	1370
	6	0.184	6.842	1.257	1560
	7	0.184	7.004	1.286	1597
	8	0.184	7.044	1.294	1606
	9	0.184	6.702	1.231	1528
	10	0.184	6.614	1.215	1508
Avg:		6.8395			

<i>B. subtilis</i> 6633		Red Channel			
Series02		Area	Mean	IntDen	RawIntDen
Cell	1	0.34	13.239	4.495	6487
	2	0.336	14.682	4.935	7121
	3	0.363	14.635	5.315	7669
	4	0.387	13.806	5.339	7704
	5	0.301	12.938	3.9	5628
	6	0.277	14.148	3.922	5659
	7	0.27	13.841	3.741	5398
	8	0.282	18.002	5.078	7327
	9	0.305	13.152	4.01	5787
	10	0.29	14.048	4.079	5886
	11	0.271	13.169	3.568	5149
	12	0.76	12.55	9.54	13767
	13	0.483	14.861	7.178	10358
	14	0.431	13.638	5.879	8483
	15	0.306	12.548	3.843	5546
Avg (-background):		9.938566667			
Std Dev:		1.339895351			
Std Error:		0.345959492			
BG	1	0.496	3.486	1.73	2496
	2	0.399	4.082	1.629	2351
	3	0.496	4.043	2.006	2895
	4	0.496	3.722	1.847	2665
	5	0.496	3.966	1.968	2840
	6	0.496	3.711	1.841	2657
	7	0.496	4.383	2.175	3138
	8	0.496	4.413	2.19	3160
	9	0.496	4.439	2.202	3178
	10	0.496	3.874	1.922	2774
Avg:		4.0119			

<i>B. subtilis</i> 6633		Red Channel			
Series03		Area	Mean	IntDen	RawIntDen
Cell	1	0.325	10.631	3.455	4986
	2	0.292	11.423	3.333	4809
	3	0.247	11.317	2.8	4040
	4	0.34	13.573	4.609	6651
	5	0.356	11.207	3.984	5749
	6	0.367	13.885	5.1	7359
	7	0.311	13.488	4.197	6056
	8	0.347	14.467	5.023	7248
	9	0.331	16.207	5.369	7747
	10	0.318	13.322	4.238	6115
	11	0.39	14.943	5.83	8413

<i>B. subtilis</i> 6633		Red Channel			
Series04		Area	Mean	IntDen	RawIntDen
Cell	1	0.371	11.35	4.208	6072
	2	0.36	10.398	3.747	5407
	3	0.358	12.198	4.362	6294
	4	0.34	11.996	4.082	5890
	5	0.346	15.006	5.189	7488
	6	0.362	13.125	4.748	6851
	7	0.444	13.752	6.099	8801
	8	0.405	15.259	6.175	8911
	9	0.696	11.228	7.812	11273
	10	0.615	11.717	7.202	10393
	11	0.322	14.049	4.527	6533

	12	0.394	15.023	5.924	8548	
	13	0.568	13.532	7.68	11083	
	14	0.325	12.141	3.946	5694	
	15	0.358	12.01	4.294	6197	
	16	0.339	12.951	4.389	6333	
	17	0.344	14.546	5	7215	
	18	0.352	20.398	7.181	10362	
Avg (-background):		8.160666667				
Std Dev:		2.278128489				
Std Error:		0.536960034				
BG	1	0.277	5.505	1.526	2202	
	2	0.277	5.555	1.54	2222	
	3	0.277	5.598	1.552	2239	
	4	0.139	5.285	0.732	1057	
	5	0.182	5.198	0.947	1367	
	6	0.08	5.207	0.419	604	
	7	0.277	5.218	1.446	2087	
	8	0.277	5.65	1.566	2260	
	9	0.277	5.695	1.579	2278	
	10	0.153	5.629	0.862	1244	
Avg:		5.454				
	12	0.369	15.146	5.595	8073	
	13	0.358	17.872	6.391	9222	
	14	0.359	17.11	6.142	8863	
	15	0.313	13.721	4.298	6202	
	16	0.408	14.217	5.803	8374	
	17	0.369	14.403	5.32	7677	
	18	0.312	12.738	3.972	5732	
	19	0.332	14.781	4.906	7080	
	20	0.383	14.043	5.372	7752	
	21	0.368	11.842	4.358	6288	
	22	0.311	12.038	3.746	5405	
	23	0.321	11.227	3.602	5198	
	24	0.321	14.205	4.558	6577	
	25	0.332	13.843	4.595	6631	
	Avg (-background):		7.91946			
	Std Dev:		1.846469832			
	Std Error:		0.369293966			
	BG	1	0.4	5.53	2.211	3191
		2	0.4	5.558	2.222	3207
		3	0.4	5.575	2.229	3217
		4	0.4	5.47	2.187	3156
		5	0.4	5.53	2.211	3191
		6	0.4	5.66	2.263	3266
		7	0.4	5.636	2.254	3252
		8	0.4	5.461	2.184	3151
9		0.4	5.65	2.259	3260	
10		0.4	5.641	2.256	3255	
Avg:		5.5711				

<i>B. subtilis</i> 6633			Red Channel		
Series05		Area	Mean	IntDen	RawIntDen
Cell	1	0.485	10.52	5.103	7364
	2	0.451	10.625	4.793	6917
	3	0.353	12.006	4.243	6123
	4	0.421	9.758	4.112	5933
	5	0.109	15.614	1.71	2467
	6	0.623	10.046	6.258	9031
	7	0.446	11.616	5.176	7469
	8	0.45	10.963	4.938	7126
	9	0.57	12.062	6.871	9915
	10	0.407	13.032	5.31	7663
	11	0.397	14.262	5.663	8172
	12	0.398	13.471	5.368	7746
	13	0.477	12.168	5.81	8384
	14	0.536	15.658	8.388	12104
	15	0.388	11.421	4.432	6396
	16	0.374	13.978	5.221	7534
	17	0.369	14.133	5.22	7533
	18	0.332	12.432	4.127	5955
	19	0.344	11.133	3.834	5533
	20	0.374	11.223	4.192	6049
	21	0.383	12.031	4.602	6641
	22	0.346	11.94	4.137	5970
	23	0.374	14.409	5.392	7781
	24	0.488	12.224	5.964	8606
	25	0.34	12.163	4.13	5960
	26	0.36	13.452	4.847	6995
	27	0.441	12.625	5.573	8042
	28	0.36	11.046	3.973	5733
	29	0.376	12.853	4.836	6979
	30	0.537	12.406	6.663	9615

	31	0.509	23.74	12.075	17425
	32	0.214	10.084	2.159	3116
	33	0.183	10.583	1.936	2794
Avg (-background):		7.444172727			
Std Dev:		2.507908258			
Std Error:		0.436570791			
BG	1	0.218	5.362	1.17	1689
	2	0.218	4.978	1.087	1568
	3	0.218	5.117	1.117	1612
	4	0.218	5.292	1.155	1667
	5	0.179	5.043	0.902	1301
	6	0.218	5.184	1.132	1633
	7	0.218	5.076	1.108	1599
	8	0.218	5.13	1.12	1616
	9	0.218	5.044	1.101	1589
	10	0.218	5.295	1.156	1668
Avg:		5.1521			

### *Enterococcus faecalis*

<i>E. faecalis</i> V583		Red Channel			
Series01		Area	Mean	IntDen	RawIntDen
Cell	1	0.311	28.245	8.789	12682
	2	0.268	52.106	13.974	20165
	3	0.156	45.653	7.118	10272
	4	0.113	48.73	5.504	7943
	5	0.193	37.627	7.275	10498
	6	0.199	27.537	5.477	7903
	7	0.19	36.369	6.906	9965
	8	0.203	31.597	6.416	9258
	9	0.258	37.016	9.568	13807
	10	0.119	28.715	3.423	4939
	11	0.277	23.609	6.528	9420
	12	0.204	39.241	7.995	11537
	13	0.29	39.038	11.335	16357
	14	0.19	27.894	5.297	7643
	15	0.177	47.762	8.473	12227
	16	0.305	56.468	17.218	24846
	17	0.178	32.008	5.701	8226
	18	0.171	31.486	5.389	7777
	19	0.185	30.165	5.581	8054
	20	0.179	49.838	8.945	12908
	21	0.105	28	2.949	4256
	22	0.142	36.439	5.177	7470
	23	0.281	26.569	7.475	10787
	24	0.161	27.082	4.354	6283
	25	0.151	29.202	4.412	6366
	26	0.195	34.408	6.724	9703
	27	0.278	29.741	8.265	11926
	28	0.221	31.614	6.989	10085
	29	0.245	46.824	11.454	16529
	30	0.261	28.215	7.352	10609
	31	0.264	34.625	9.142	13192
	32	0.266	26.557	7.067	10198
<i>E. faecalis</i> V583		Red Channel			
Series02		Area	Mean	IntDen	RawIntDen
Cell	1	0.104	34.413	3.577	5162
	2	0.192	32.657	6.269	9046
	3	0.182	30.825	5.618	8107
	4	0.123	33.864	4.154	5994
	5	0.125	39.667	4.948	7140
	6	0.223	22.22	4.958	7155
	7	0.142	18.888	2.683	3872
	8	0.249	30.287	7.535	10873
	9	0.203	29.898	6.071	8760
	10	0.157	27.379	4.307	6215
	11	0.149	25.307	3.771	5441
	12	0.211	34.397	7.27	10491
	13	0.203	37.075	7.528	10863
	14	0.125	35.21	4.416	6373
	15	0.13	30.75	4.006	5781
	16	0.155	24.567	3.814	5503
	17	0.15	23.189	3.487	5032
	18	0.144	23.091	3.328	4803
	19	0.125	34.95	4.36	6291
	20	0.139	33.194	4.624	6672
	21	0.131	20.873	2.734	3945
	22	0.143	35.246	5.056	7296
	23	0.151	39.904	6.028	8699
	24	0.108	31.981	3.457	4989
	25	0.102	21.898	2.231	3219
	26	0.119	37.07	4.393	6339
	27	0.15	30.281	4.554	6571
	28	0.257	36.779	9.456	13645
	29	0.184	19.545	3.603	5199
	30	0.172	17.395	2.99	4314
	31	0.164	27.161	4.442	6410
	32	0.269	33.75	9.075	13095

Avg (-background):			26.066875		
Std Dev:			8.75256418		
Std Error:			1.547249371		
BG	1	0.123	8.847	1.085	1566
	2	0.123	9.514	1.167	1684
	3	0.123	9.723	1.193	1721
	4	0.123	9.35	1.147	1655
	5	0.123	8.932	1.096	1581
	6	0.123	9.475	1.162	1677
	7	0.123	8.542	1.048	1512
	8	0.123	9.305	1.141	1647
	9	0.123	9.175	1.125	1624
	10	0.123	9.712	1.191	1719
Avg:		9.2575			

	33	0.17	38.398	6.546	9446
	34	0.166	34.658	5.764	8318
Avg (-background):			23.11712941		
Std Dev:			6.419002639		
Std Error:			1.100849871		
BG	1	0.218	7.359	1.606	2318
	2	0.218	7.238	1.58	2280
	3	0.218	6.721	1.467	2117
	4	0.218	6.781	1.48	2136
	5	0.218	7.349	1.604	2315
	6	0.218	8.273	1.806	2606
	7	0.218	7.679	1.676	2419
	8	0.218	6.159	1.344	1940
	9	0.218	6.949	1.517	2189
	10	0.218	6.311	1.378	1988
Avg:			7.0819		

<i>E. faecalis</i> V583		Red Channel			
Series03		Area	Mean	IntDen	RawIntDen
Cell	1	0.146	29.474	4.31	6219
	2	0.155	33.272	5.165	7453
	3	0.182	32.416	5.886	8493
	4	0.103	37.765	3.899	5627
	5	0.1	39.965	3.988	5755
	6	0.174	75.45	13.124	18938
	7	0.122	42.705	5.209	7516
	8	0.119	43.907	5.233	7552
	9	0.123	33.904	4.159	6001
	10	0.141	39.642	5.604	8087
	11	0.1	30.959	3.111	4489
	12	0.098	31.606	3.11	4488
	13	0.128	36.027	4.619	6665
	14	0.177	24.867	4.394	6341
	15	0.172	37.161	6.387	9216
	16	0.118	28.782	3.391	4893
	17	0.092	41.797	3.852	5559
	18	0.097	40.643	3.943	5690
	19	0.137	37.707	5.174	7466
	20	0.105	30.311	3.172	4577
	21	0.144	34.106	4.916	7094
	22	0.135	43.631	5.896	8508
	23	0.114	34.878	3.964	5720
	24	0.114	23.994	2.727	3935
	25	0.101	34.466	3.487	5032
	26	0.125	37.171	4.662	6728
	27	0.187	39.963	7.477	10790
	28	0.141	26.814	3.791	5470
	29	0.146	36.281	5.28	7619

	30	0.139	34.91	4.863	7017
	31	0.152	34.909	5.298	7645
	32	0.139	24.285	3.366	4857
	33	0.146	24.576	3.577	5161
	34	0.13	32.25	4.202	6063
	35	0.112	29.571	3.299	4761
	36	0.128	29.076	3.708	5350
	37	0.127	22.568	2.862	4130
	38	0.106	22.471	2.383	3438
	39	0.104	39.353	4.091	5903
Avg (-background):		27.35383846			
Std Dev:		8.988189762			
Std Error:		1.439262233			
BG	1	0.132	7.479	0.985	1421
	2	0.132	6.795	0.895	1291
	3	0.132	7.737	1.019	1470
	4	0.132	7.205	0.949	1369
	5	0.132	7.205	0.949	1369
	6	0.132	7.753	1.021	1473
	7	0.132	7.805	1.028	1483
	8	0.132	6.937	0.913	1318
	9	0.1	7.347	0.733	1058
	10	0.132	7.284	0.959	1384
Avg:		7.3547			

### *Staphylococcus aureus*

MRSA-BAA40		Red Channel			
Series01		Area	Mean	IntDen	RawIntDen
Cell	1	0.452	16.765	7.576	9405
	2	0.349	23.573	8.222	10207
	3	0.349	35.206	12.279	15244
	4	0.349	28.739	10.024	12444
	5	0.349	27.746	9.677	12014
	6	0.349	22.506	7.85	9745
	7	0.349	32.478	11.328	14063
	8	0.349	26.956	9.402	11672
	9	0.349	18.501	6.453	8011
	10	0.349	30.166	10.521	13062
	11	0.349	23.882	8.33	10341
	12	0.349	18.975	6.618	8216
	13	0.349	24.134	8.417	10450
	14	0.349	23.781	8.294	10297
	15	0.349	33.704	11.755	14594
	16	0.349	26.575	9.269	11507
	17	0.349	39.744	13.862	17209
	18	0.349	36.081	12.584	15623
	19	0.349	37.727	13.159	16336
	20	0.349	57.497	20.054	24896
	21	0.362	32.029	11.584	14381
	22	0.362	16.88	6.105	7579
	23	0.362	32.107	11.612	14416
	24	0.362	31.857	11.522	14304
	25	0.362	38.67	13.986	17363
	26	0.362	25.739	9.309	11557
	27	0.362	25.842	9.346	11603
	28	0.362	26.078	9.432	11709
MRSA-BAA40		Red Channel			
Series02		Area	Mean	IntDen	RawIntDen
Cell	1	0.115	22.933	2.648	5137
	2	0.211	22.954	4.84	9388
	3	0.106	22.834	2.413	4681
	4	0.081	21.108	1.708	3314
	5	0.132	23.191	3.061	5937
	6	0.171	25.885	4.417	8568
	7	0.125	28.124	3.509	6806
	8	0.126	21.657	2.735	5306
	9	0.101	27.658	2.795	5421
	10	0.125	24.252	3.026	5869
	11	0.206	37.902	7.796	15123
	12	0.084	36.871	3.098	6010
	13	0.174	31.855	5.551	10767
	14	0.115	24.621	2.843	5515
	15	0.123	37.017	4.542	8810
	16	0.113	24.068	2.73	5295
	17	0.087	22.13	1.928	3740
	18	0.117	21.894	2.551	4948
	19	0.104	21.289	2.206	4279
	20	0.126	28.739	3.63	7041
	21	0.164	29.028	4.759	9231
	22	0.119	24.9	2.952	5727
	23	0.113	25.918	2.926	5676
	24	0.123	20.854	2.569	4984
	25	0.123	22.454	2.755	5344
	26	0.11	19.315	2.121	4114
	27	0.116	23.929	2.776	5384
	28	0.18	32.157	5.802	11255



	29	0.362	15.43	5.581	6928
	30	0.362	19.027	6.881	8543
	31	0.421	36.201	15.251	18933
Avg (-background):		26.63205484			
Std Dev:		8.706465933			
Std Error:		1.563727443			
BG	1	0.421	1.677	0.706	877
	2	0.421	2.193	0.924	1147
	3	0.421	2.447	1.031	1280
	4	0.421	2.034	0.857	1064
	5	0.421	1.792	0.755	937
	6	0.421	1.57	0.661	821
	7	0.421	2.096	0.883	1096
	8	0.421	1.95	0.822	1020
	9	0.421	1.553	0.654	812
	10	0.421	1.721	0.725	900
Avg:		1.9033			
	29	0.119	31.515	3.753	7280
	30	0.1	30.263	3.027	5871
	31	0.137	26.272	3.589	6962
	32	0.114	22.611	2.576	4997
	33	0.148	32.618	4.843	9394
	Avg (-background):		21.58455758		
Std Dev:		5.028379082			
Std Error:		0.875328444			
BG	1	0.107	4.937	0.527	1022
	2	0.107	4.986	0.532	1032
	3	0.104	4.297	0.447	868
	4	0.107	4.213	0.45	872
	5	0.107	4.357	0.465	902
	6	0.107	4.961	0.529	1027
	7	0.107	4.836	0.516	1001
	8	0.107	4.7	0.502	973
	9	0.107	4.952	0.528	1025
	10	0.107	5.193	0.554	1075
Avg:		4.7432			

MRSA-BAA40			Red Channel		
Series03		Area	Mean	IntDen	RawIntDen
Cell	1	0.144	36.804	5.312	10305
	2	0.139	21.637	3.012	5842
	3	0.213	21.075	4.498	8725
	4	0.241	30.45	7.331	14220
	5	0.163	27.82	4.532	8791
	6	0.139	46.226	6.434	12481
	7	0.229	30.649	7.031	13639
	8	0.16	24.379	3.909	7582
	9	0.239	30.054	7.189	13945
	10	0.111	18.386	2.038	3953
	11	0.178	19.272	3.428	6649
	12	0.126	28.498	3.599	6982
	13	0.131	22.752	2.979	5779
	14	0.212	30.167	6.407	12429
	15	0.141	21.157	2.988	5797
	16	0.112	16.76	1.875	3637
Avg (-background):		23.108175			
Std Dev:		7.62787086			
Std Error:		1.906967715			
BG	1	0.123	3.416	0.419	813
	2	0.123	3.218	0.395	766
	3	0.123	3.324	0.408	791
	4	0.123	3.651	0.448	869
	5	0.123	4.008	0.492	954
	6	0.123	3.962	0.486	943
	7	0.123	3.399	0.417	809
	8	0.123	4.038	0.495	961
	9	0.123	2.748	0.337	654
	10	0.123	3.458	0.424	823
Avg:		3.5222			
MRSA-BAA40			Red Channel		
Series04		Area	Mean	IntDen	RawIntDen
Cell	1	0.103	25.575	2.637	5115
	2	0.123	29.444	3.628	7037
	3	0.116	39.582	4.591	8906
	4	0.127	30.502	3.884	7534
	5	0.131	40.193	5.263	10209
	6	0.113	25.836	2.93	5684
	7	0.112	18.064	2.03	8015
	8	0.128	32.189	4.132	5158
	9	0.105	25.409	2.659	9320
	10	0.124	38.672	4.805	5856
	11	0.129	23.424	3.019	9530
	12	0.156	31.452	4.913	3595
	13	0.107	17.367	1.853	5733
	14	0.13	22.75	2.955	3591
	15	0.12	15.478	1.851	3938
Avg (-background):		22.65013333			
Std Dev:		7.872994247			
Std Error:		2.032798373			
BG	1	0.123	5.412	0.664	1288
	2	0.123	5.13	0.629	1221
	3	0.123	5.525	0.678	1315
	4	0.123	5.601	0.687	1333
	5	0.123	4.866	0.597	1158
	6	0.123	4.298	0.527	1023
	7	0.123	4.483	0.55	1067
	8	0.123	4.975	0.61	1184
	9	0.123	5.143	0.631	1224
	10	0.123	5.357	0.657	1275
Avg:		5.079			

MRSA-BAA40			Red Channel		
Series05		Area	Mean	IntDen	RawIntDen
Cell	1	0.114	34.095	3.902	7569
	2	0.144	60.039	8.635	16751
	3	0.119	32.333	3.85	7469
	4	0.121	35.615	4.296	8334
	5	0.105	34.235	3.6	6984
	6	0.134	23.112	3.086	5986

	7	0.13	29.306	3.807	7385
	8	0.131	32.638	4.274	8290
	9	0.188	45	8.444	16380
	10	0.121	36.628	4.419	8571
	11	0.114	34.045	3.896	7558
	12	0.126	31.074	3.909	7582
	13	0.106	28.597	3.037	5891
	14	0.148	34.436	5.095	9883
Avg (-background):			26.40105714		
Std Dev:			8.661895073		
Std Error:			2.314988834		
BG	1	0.132	9.332	1.232	2389
	2	0.132	9.777	1.29	2503
	3	0.132	8.188	1.081	2096
	4	0.132	8.516	1.124	2180
	5	0.132	7.301	0.964	1869
	6	0.132	7.824	1.033	2003
	7	0.132	8.484	1.12	2172
	8	0.132	9.102	1.201	2330
	9	0.132	9.488	1.252	2429
	10	0.132	8.801	1.161	2253
Avg:			8.6813		

MRSA-USA300		Red Channel			
Series01		Area	Mean	IntDen	RawIntDen
Cell	1	0.188	23.433	4.398	5460
	2	0.171	26.208	4.475	5556
	3	0.155	20.663	3.212	3988
	4	0.28	29.107	8.136	10100
	5	0.242	24.697	5.968	7409
	6	0.248	21.448	5.321	6606
	7	0.268	35.559	9.538	11841
	8	0.293	20.044	5.877	7296
	9	0.138	23.088	3.18	3948
	10	0.151	17.481	2.633	3269
	11	0.242	18.127	4.38	5438
	12	0.249	16.32	4.062	5043
	13	0.262	27.557	7.214	8956
	14	0.227	23.674	5.378	6676
	15	0.159	22.409	3.574	4437
	16	0.179	19.396	3.468	4306
	17	0.19	16.775	3.189	3959
	18	0.331	21.275	7.043	8744
	19	0.377	43.235	16.299	20234
	20	0.212	19.084	4.043	5019
	21	0.319	28.321	9.034	11215
	22	0.183	15.868	2.901	3602
	23	0.136	17.746	2.416	2999
	24	0.173	26.484	4.587	5694
	25	0.191	16.245	3.101	3850
	26	0.163	19.01	3.093	3840
Avg (-background):			20.87866154		
Std Dev:			6.338790176		
Std Error:			1.243139031		
BG	1	0.35	2.558	0.894	1110
	2	0.35	1.544	0.54	670
	3	0.35	0.226	0.079	98
	4	0.35	0.15	0.052	65

MRSA-USA300		Red Channel			
Series02		Area	Mean	IntDen	RawIntDen
Cell	1	0.342	35.141	12.03	14935
	2	0.141	30.697	4.327	5372
	3	0.172	23.953	4.11	5102
	4	0.176	23.009	4.04	5016
	5	0.184	28.465	5.228	6490
	6	0.17	36.18	6.149	7634
	7	0.176	22.886	4.037	5012
	8	0.176	18.699	3.299	4095
	9	0.278	19.426	5.398	6702
	10	0.146	22.89	3.337	4143
	11	0.226	20.411	4.603	5715
	12	0.236	32.635	7.702	9562
	13	0.271	20.582	5.587	6936
	14	0.147	21.76	3.208	3982
	15	0.162	27.239	4.41	5475
	16	0.144	25.944	3.741	4644
	17	0.132	26.915	3.555	4414
	18	0.147	26.219	3.865	4798
	19	0.182	21.204	3.86	4792
	20	0.209	17.723	3.712	4608
	21	0.194	18.734	3.637	4515
	22	0.143	20.472	2.935	3644
	23	0.136	31.361	4.269	5300
	24	0.178	23.729	4.224	5244
	25	0.28	19.635	5.504	6833
	26	0.19	35.441	6.737	8364
	27	0.176	24.516	4.325	5369
	28	0.171	22.708	3.878	4814
Avg (-background):			22.63727143		
Std Dev:			5.408819752		
Std Error:			1.022170854		
BG	1	0.514	2.13	1.095	1359
	2	0.514	2.053	1.055	1310

	5	0.35	2.804	0.98	1217
	6	0.35	2.749	0.961	1193
	7	0.35	0.316	0.11	137
	8	0.35	2.926	1.023	1270
	9	0.35	2.878	1.006	1249
	10	0.35	3.237	1.132	1405
	Avg:		1.9388		
	3	0.514	2.082	1.07	1328
	4	0.514	2.649	1.361	1690
	5	0.514	2.741	1.409	1749
	6	0.514	2.188	1.124	1396
	7	0.514	2.375	1.22	1515
	8	0.514	2.335	1.2	1490
	9	0.514	1.994	1.025	1272
	10	0.514	2.571	1.321	1640
	Avg:		2.3118		

MRSA-USA300		Red Channel			
Series03		Area	Mean	IntDen	RawIntDen
Cell	1	0.122	27.349	3.348	4157
	2	0.124	22.273	2.763	3430
	3	0.118	27.212	3.2	3973
	4	0.101	24.392	2.456	3049
	5	0.13	31.441	4.077	5062
	6	0.113	23.443	2.644	3282
	7	0.111	23.63	2.627	3261
	8	0.1	22.887	2.286	2838
	9	0.121	17.78	2.148	2667
	10	0.104	22.465	2.334	2898
	11	0.118	21.644	2.545	3160
	12	0.133	22.103	2.938	3647
	13	0.121	20.427	2.468	3064
	14	0.114	19.475	2.212	2746
	15	0.116	24.5	2.842	3528
	16	0.109	24.711	2.687	3336
	17	0.128	27.264	3.492	4335
	18	0.118	20.075	2.377	2951
	19	0.108	20.022	2.161	2683
Avg (-background):		21.26998421			
Std Dev:		3.325245673			
Std Error:		0.762863676			
BG	1	0.11	1.838	0.201	250
	2	0.11	2.316	0.254	315
	3	0.11	1.706	0.187	232
	4	0.11	1.713	0.188	233
	5	0.11	2.096	0.23	285
	6	0.11	1.721	0.188	234
	7	0.11	2.243	0.246	305
	8	0.11	2.544	0.279	346
	9	0.11	2.279	0.25	310
	10	0.11	2.051	0.225	279
Avg:		2.0507			

MRSA-USA300		Red Channel			
Series04		Area	Mean	IntDen	RawIntDen
Cell	1	0.191	16.482	3.152	6115
	2	0.276	26.062	7.188	13943
	3	0.172	14.895	2.565	4975
	4	0.149	23.536	3.507	6802
	5	0.168	23.843	3.995	7749
	6	0.215	27.368	5.898	11440
	7	0.276	22.297	6.15	11929
	8	0.221	16.801	3.707	7191
	9	0.163	22.823	3.718	7212
	10	0.219	25.519	5.578	10820
	11	0.165	18.442	3.052	5920
	12	0.201	23.138	4.652	9024
Avg (-background):		19.78246667			
Std Dev:		4.106346902			
Std Error:		1.185400245			
BG	1	0.386	1.981	0.765	1484
	2	0.386	1.629	0.629	1220
	3	0.386	2.007	0.775	1503
	4	0.386	1.825	0.705	1367
	5	0.386	2.053	0.793	1538
	6	0.386	2.152	0.831	1612
	7	0.386	1.802	0.696	1350
	8	0.386	2.166	0.836	1622
	9	0.386	2.053	0.793	1538
	10	0.386	2.179	0.841	1632
Avg:		1.9847			

MRSA-USA300		Red Channel			
Series05		Area	Mean	IntDen	RawIntDen
Cell	1	0.219	38.856	8.493	16475
	2	0.211	19.443	4.099	7952
	3	0.203	23.567	4.775	9262
	4	0.216	39.095	8.445	16381
	5	0.196	38.969	7.654	14847
	6	0.176	31.692	5.571	10807
	7	0.199	41.391	8.236	15977
	8	0.192	21.614	4.156	8062

MRSA-USA300		Red Channel			
Series06		Area	Mean	IntDen	RawIntDen
Cell	1	0.156	23.139	3.614	7011
	2	0.125	25.634	3.211	6229
	3	0.206	25.325	5.222	10130
	4	0.168	28.485	4.787	9286
	5	0.195	34.639	6.768	13128
	6	0.152	19.2	2.92	5664
	7	0.125	17.407	2.181	4230
	8	0.125	16.819	2.107	4087

	9	0.224	20.278	4.547	8821	Avg (-background):			21.7166		
	10	0.234	19.725	4.616	8955	Std Dev:			6.051167184		
	11	0.175	20.558	3.593	6969	Std Error:			2.139410675		
Avg (-background):		26.70185455				BG	1	0.232	2.355	0.547	1062
Std Dev:		9.30949216					2	0.232	2.716	0.632	1225
Std Error:		2.806917498					3	0.232	1.659	0.386	748
BG	1	0.727	2.172	1.579	3062		4	0.232	2.82	0.656	1272
	2	0.727	1.825	1.326	2573		5	0.232	2.16	0.502	974
	3	0.727	2.323	1.688	3275		6	0.232	2.614	0.608	1179
	4	0.727	1.862	1.354	2626		7	0.232	1.437	0.334	648
	5	0.727	1.987	1.444	2802		8	0.232	2.106	0.49	950
	6	0.727	1.733	1.259	2443		9	0.232	1.539	0.358	694
	7	0.19	2.084	0.395	767		10	0.232	1.738	0.404	784
	8	0.727	1.733	1.26	2444	Avg:		2.1144			
	9	0.727	1.547	1.124	2181						
	10	0.716	2.25	1.61	3123						
Avg:			1.9516								

Overall values used for chart:

	MRSA-BAA40	MRSA-USA300	<i>E. faecalis</i> V583	<i>B. subtilis</i> 6633	<i>E. coli</i> Kf12	<i>P. aeruginosa</i> PA01
	26.63205484	20.87866154	26.066875	7.091285714	16.778387	14.63372609
	21.58455758	22.63727143	23.11712941	9.938566667	14.202183	15.7658087
	23.108175	21.26998421	27.35383846	8.160666667	12.966738	14.65429167
	22.65013333	19.78246667		7.91946	17.167541	15.23216667
	26.40105714	21.7166		7.444172727	13.292159	
		26.70185455				
Average	24.07519558	22.16447306	25.51261429	8.110830355	14.881402	15.07149828
No of cells	109	104	105	105	106	100
Std. Dev	7.654065019	5.960115982	8.286341025	2.316132294	4.8666858	3.652046134
Std. Error (±)	0.366563233	0.292218728	0.404332041	0.113015684	0.2363472	0.182602307

## AIII.2 | NMR Spectra

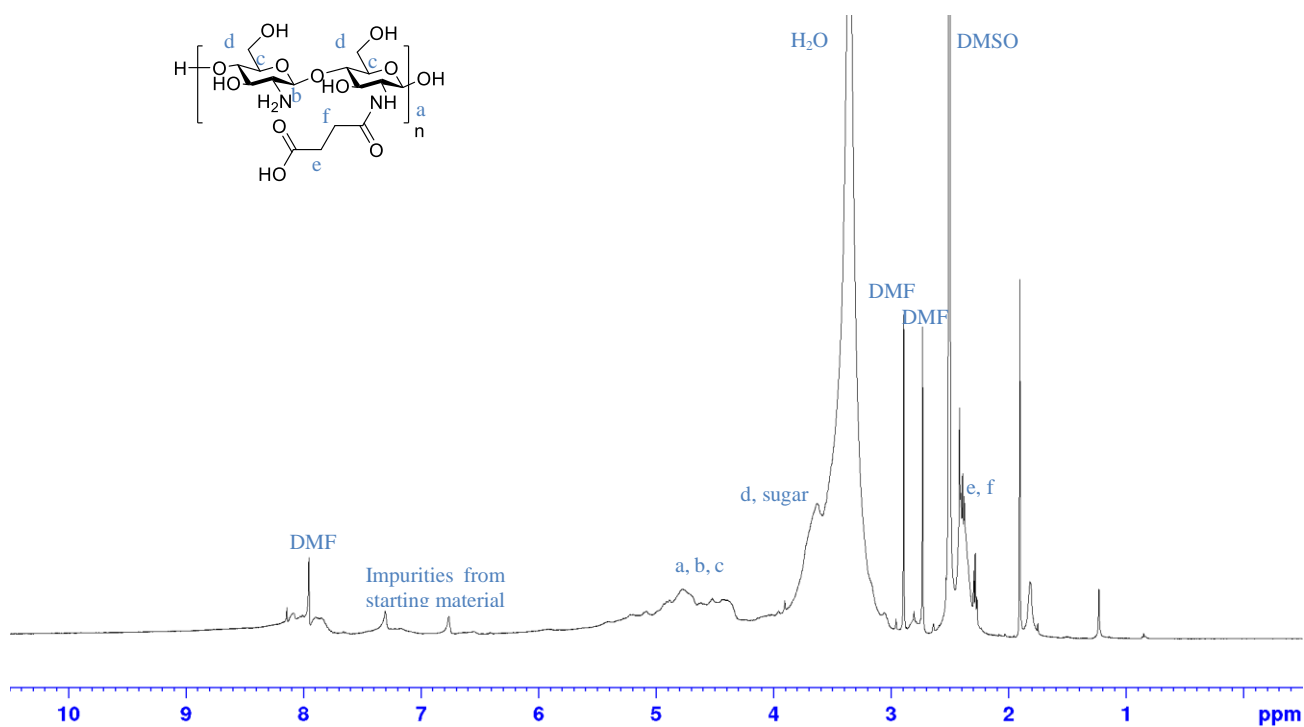


**Figure A3.1** |  $^1\text{H}$  NMR spectrum of **3-2** in  $\text{DMSO}-d_6$  (500 MHz).

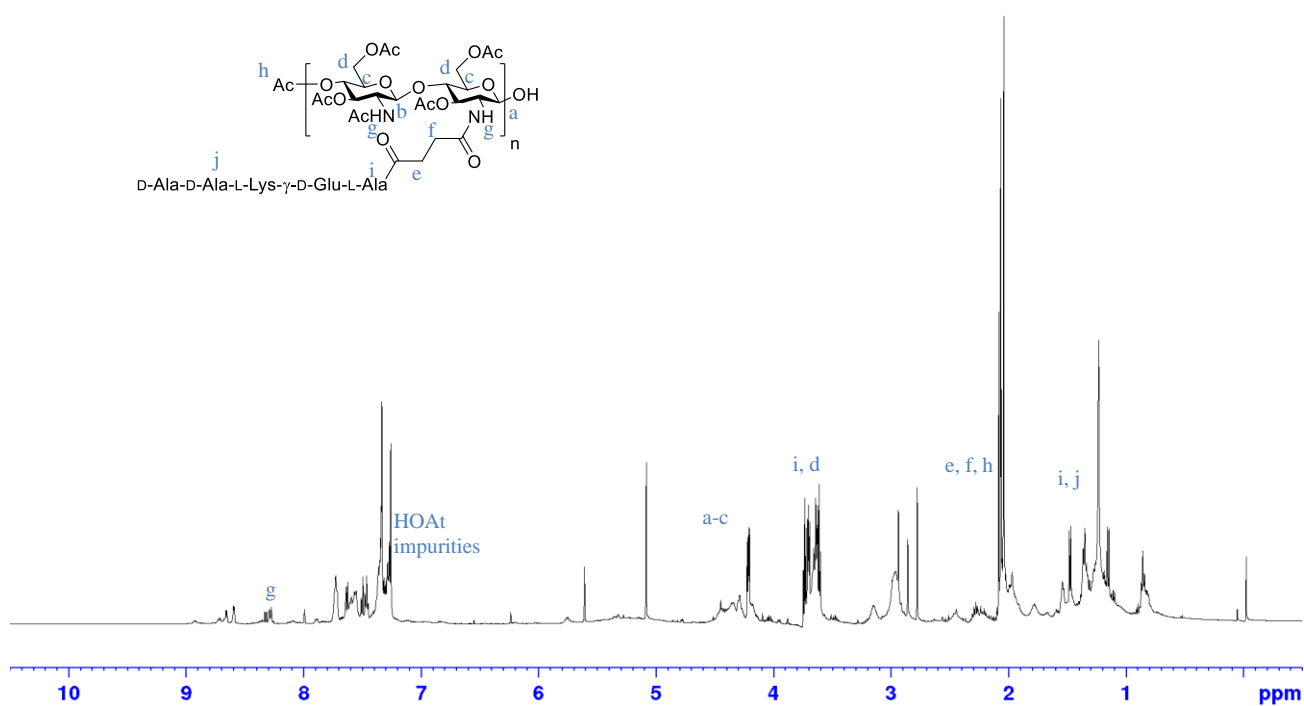


**Figure A3.2** |  $^1\text{H}$  NMR spectrum of **3-5** in  $\text{CDCl}_3$  (500 MHz)

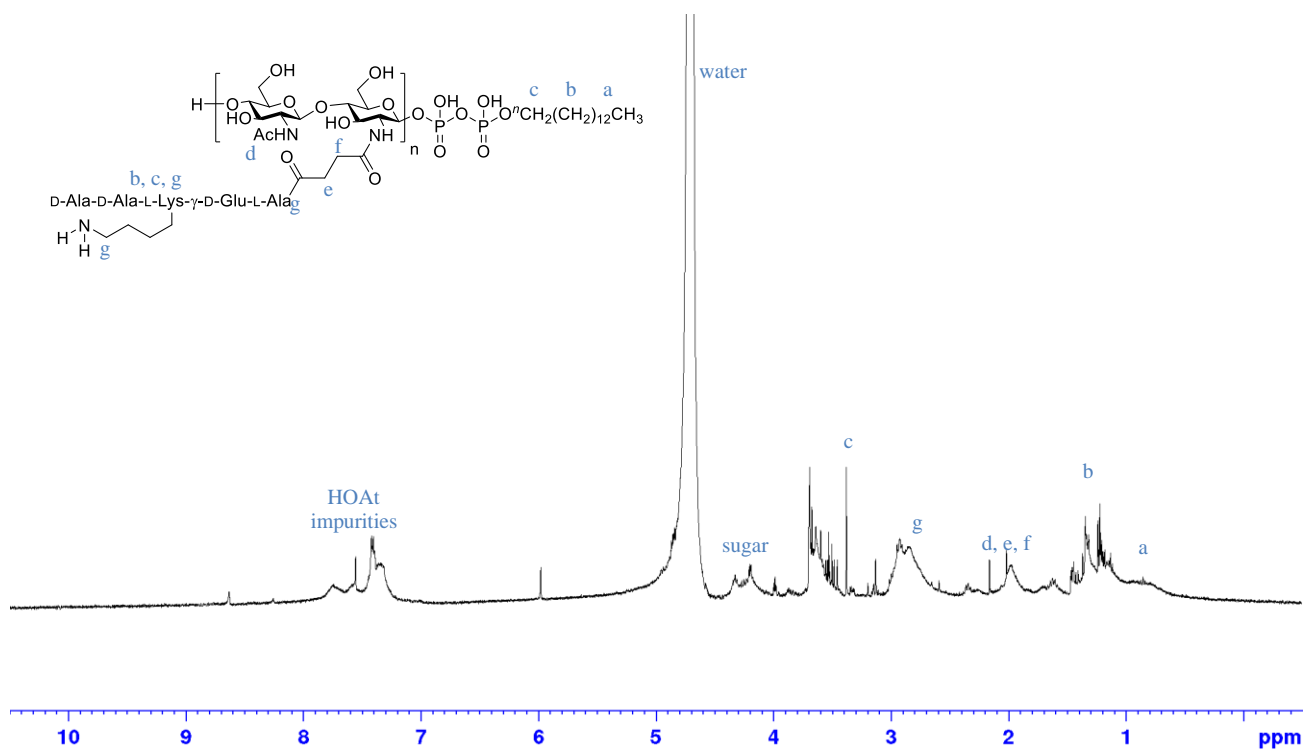


**Figure A3.3** |  $^1\text{H}$  NMR spectrum of **3-7** in  $\text{D}_2\text{O}$  (400 MHz).

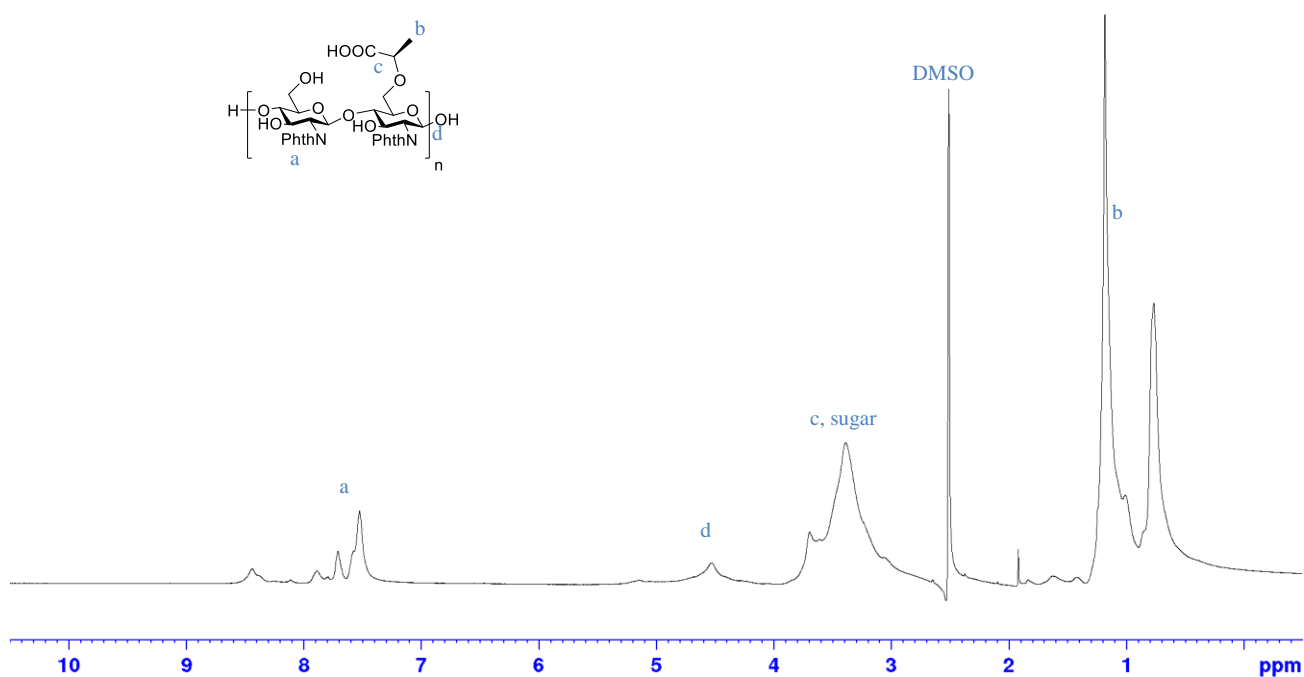


**Figure A3.4** |  $^1\text{H}$  NMR spectrum of **3-9** in  $\text{DMSO-d}_6$  (500 MHz)

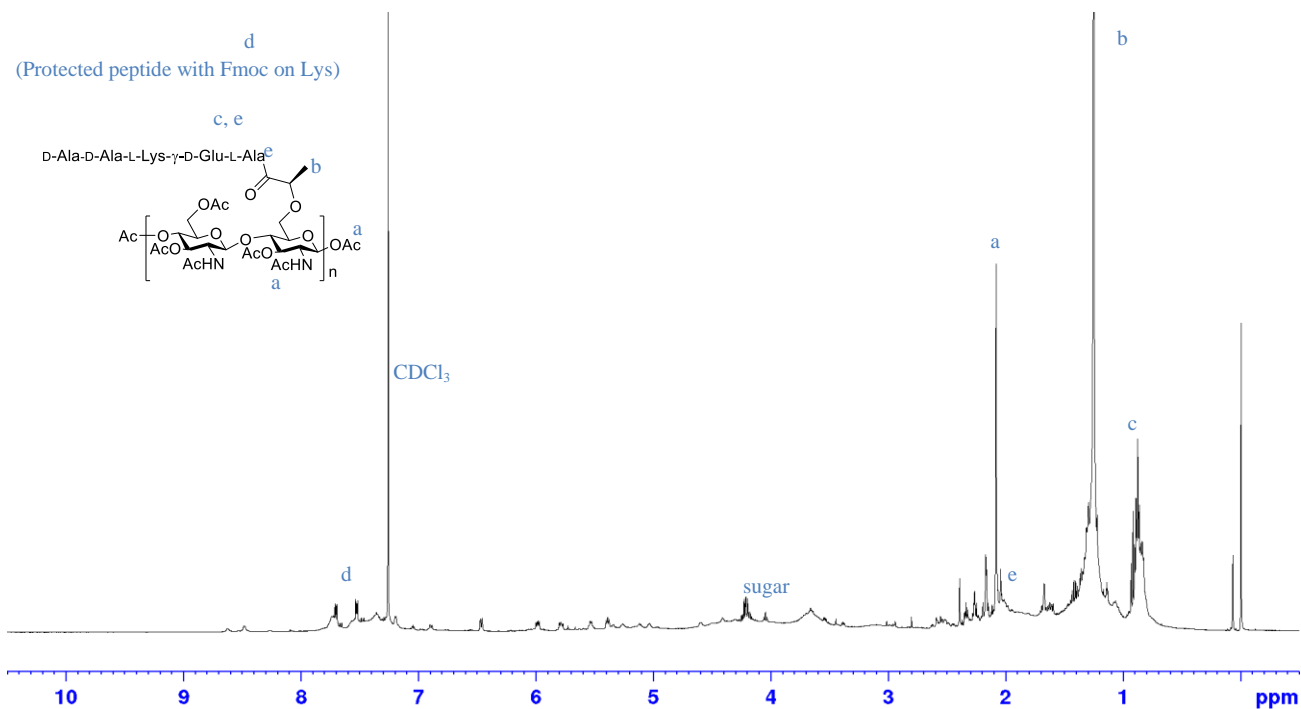


**Figure A3.5** |  $^1\text{H}$  NMR spectrum of **3-12** in CDCl<sub>3</sub> (500 MHz).

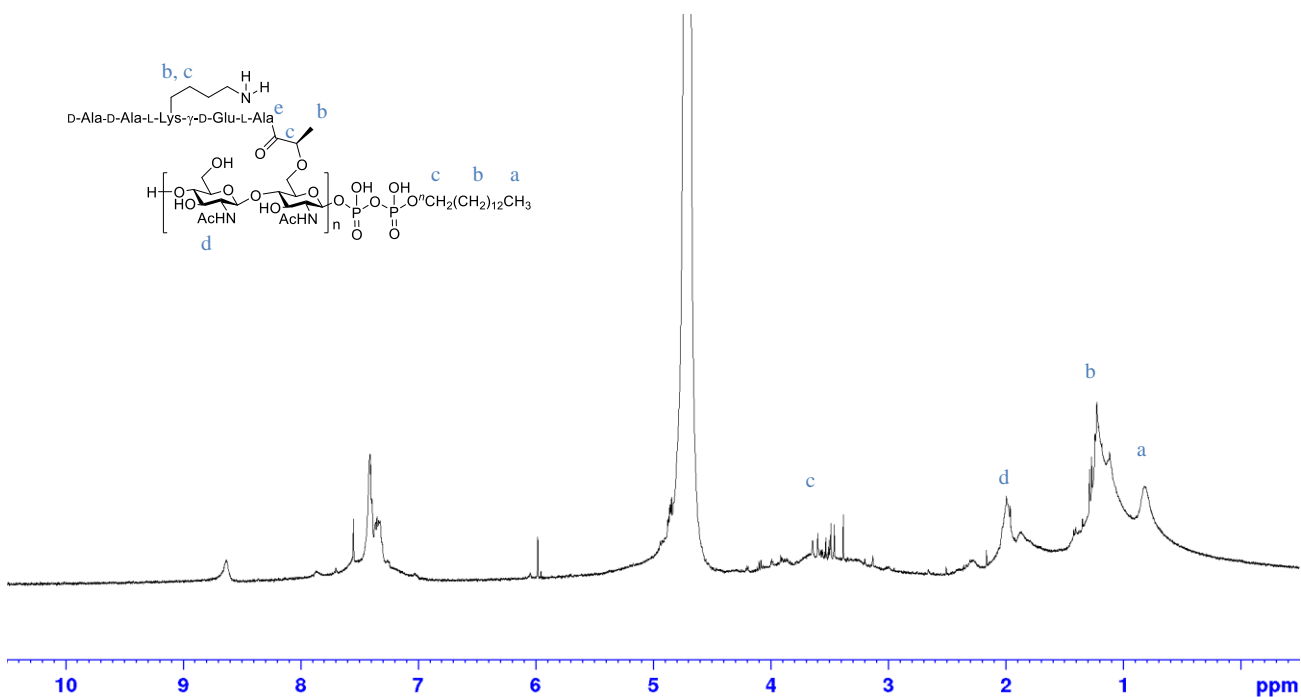


**Figure A3.6** |  $^1\text{H}$  NMR spectrum of **3-14** in D<sub>2</sub>O (500 MHz).

### AIII.3 – Additional Information on the System, 3-1 and 3-1@Rhd

The data recorded herein were obtained from Mr. He Jingxi with regards to the systems **3-1** and **3-1@Rhd** studied. Data included are  $^1\text{H}$  NMR spectrum of **3-1@Rhd** and protected pentapeptide (Boc-L-Ala-D-*iso*-Glu(OBn)-L-Lys(Fmoc)-D-Ala-D-Ala-OMe),  $^{13}\text{C}$  NMR of the protected peptide (Boc-L-Ala-D-*iso*-Glu(OBn)-L-Lys(Fmoc)-D-Ala-D-Ala-OMe), as well as charts recorded from gel permeation chromatography (GPC) and dynamic light-scattering (DLS) of **3-1**.

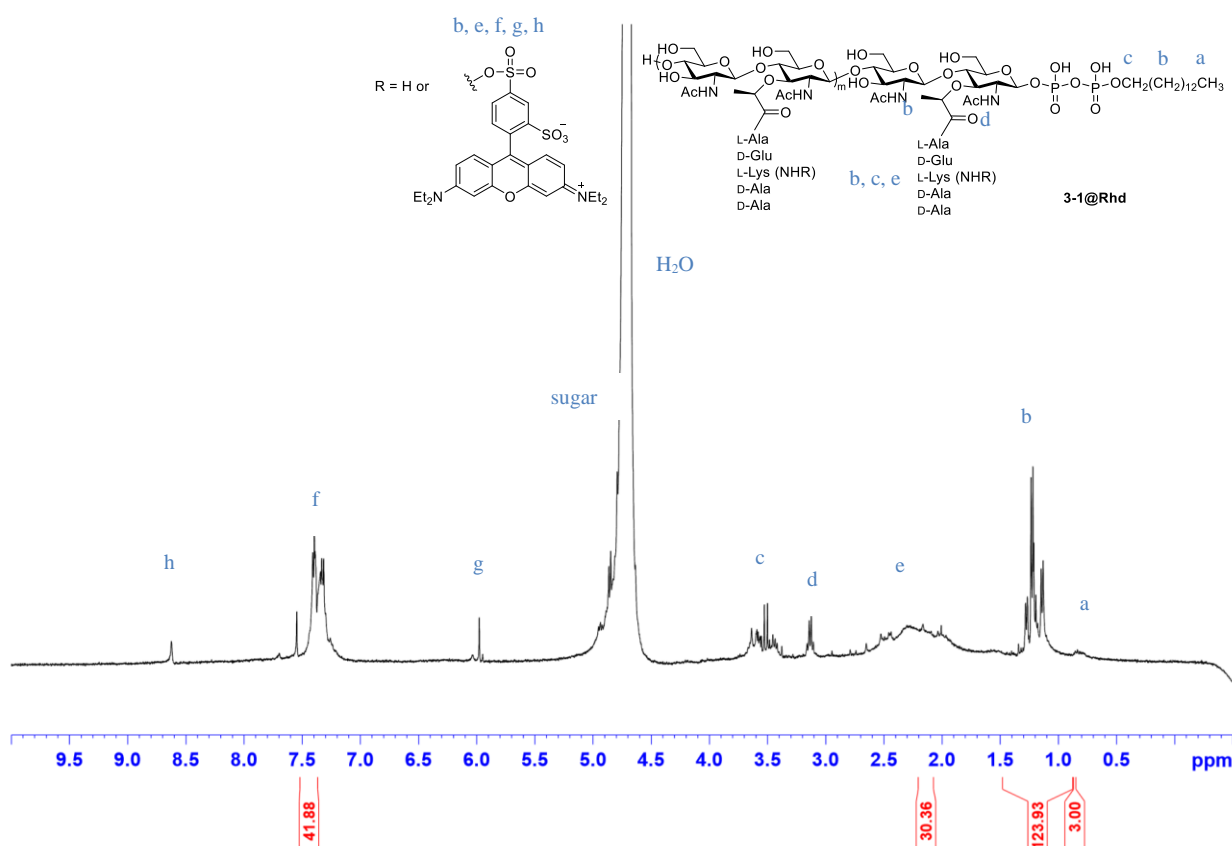
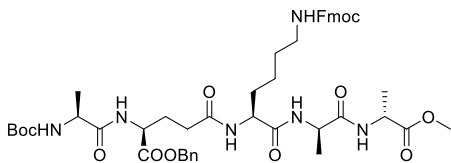


**Figure A3.9** |  $^1\text{H}$  NMR spectrum of **3-1@Rhd** in  $\text{D}_2\text{O}$  (500 MHz)

Proton ratio between f (aromatic, 5H), d (acetyl, 3H) and a (terminal methyl, 3H) suggested average 4.4 rhodamine labeled peptide moieties and 9 acetylated glucosamine units connecting to 1 lipid aglycone.





173.51  
172.90  
172.50  
172.00  
157.79  
155.45  
143.04  
139.89  
137.89  
136.36  
135.86  
134.65  
133.44  
133.19  
127.75  
121.84  
120.49  
110.20  
78.54  
66.39  
53.50  
52.29  
51.14  
50.13  
49.07  
48.03  
31.85  
31.67  
30.06  
29.84  
28.83  
28.71  
28.11  
18.52  
18.40  
17.22

Page | 166

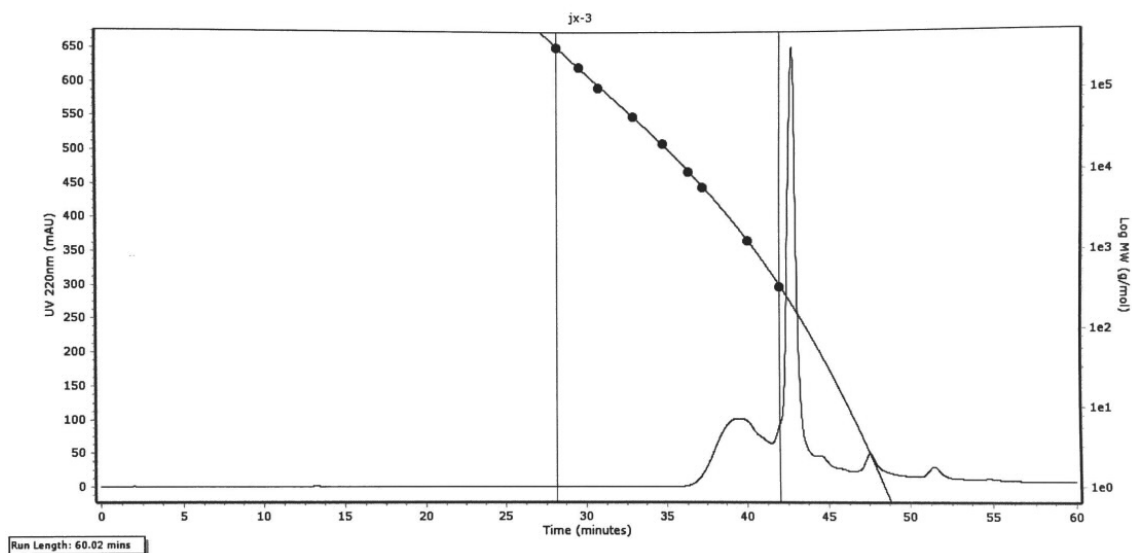


**Figure A3.12** | GPC chromatogram of **3-1** eluted with 0.05 M NaCl in deionized water. Shodex SB-803 HQ and SB-805 HQ columns (Showa Denko, Tokyo, Japan) were connected in series for GPC in Agilent 1260 infinity system (Agilent, CA, USA). Samples were eluted at 0.5 mL/s through columns. Peak broadening observed was from various self-assemblies of the polymer molecules.

### Size distribution of PGOs by number

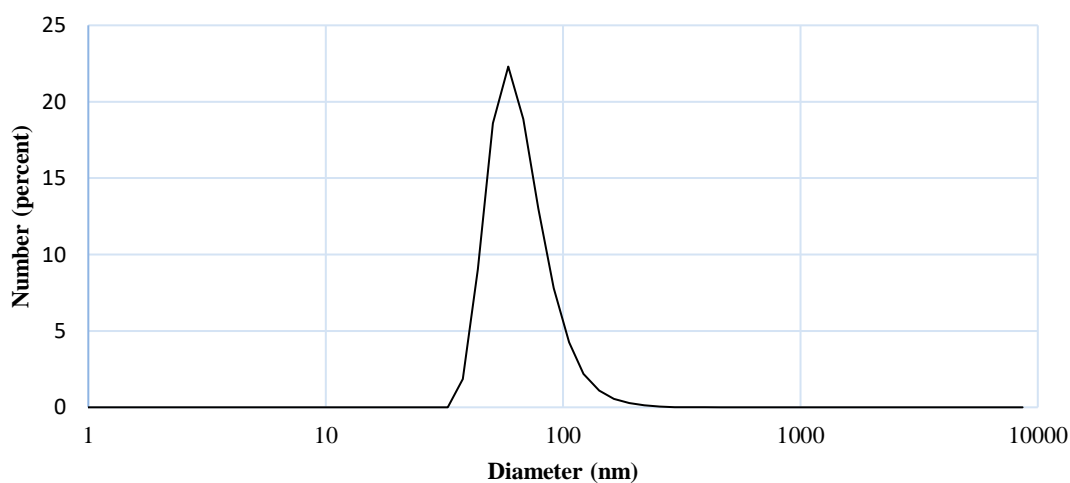


**Figure A3.13** | Size distribution of **3-1** in deionized water with the concentration of 100  $\mu\text{g/mL}$  was obtained from DLS analysis using Malvern zetasizer (Malvern Instruments Ltd, Malvern, UK). Results indicated spontaneous self-assembly of PGOs, probably due to the amphiphilic nature from co-existence of sugar, peptide and lipid moieties in the substrate.